Dissertation

submitted to the

Combined Faculty of Mathematics, Engineering and Natural Sciences of the

Ruperto-Carola University of Heidelberg, Germany

for the degree of

Doctor of Natural Sciences

Put forward by

Oliver Scholer

born in: Trier, Germany

Oral examination: 16. Oct. 2024

On the Implications of a Future Neutrinoless Double Beta Decay Discovery

Referees: Prof. Dr. Dr. h.c. Manfred Lindner

Prof. Dr. Tilman Plehn

Über die Implikationen einer zukünftigen Entdeckung des neutrinolosen doppelten Beta Zerfalls:

Der neutrinolose doppelte Beta Zerfall ($0\nu\beta\beta$) ist der vielversprechendste experimentelle Test von leptonzahlverletzender (LNV) Physik jenseits des Standardmodells. Seine Entdeckung würde tiefgreifende Einblicke in den Mechanismus der Neutrinomassenerzeugung sowie den Ursprung der Baryon-Asymmetry des Universums erlauben. Die einfachste Interpretation eines solchen Signals als LNV Majorana Neutrino Masse vernachlässigt jedoch die Möglichkeit anderer LNV Mechanismen, welche den Prozess dominieren können. Effektive Feldtheorien (EFTs) sind ein effizientes Werkzeug, um die Vielzahl an möglichen LNV Mechanismen auf modellunabhängige Art zu untersuchen. In der vorliegenden Arbeit erforschen wir die Implikationen einer zukünftigen $0\nu\beta\beta$ Entdeckung, indem wir aufzeigen, wie verschiedene LNV Mechanismen anhand der Messung der Halbwertszeit und Elektronkinematik in unterschiedlichen Isotopen unterschieden werden können. Anhand eines Beispielmodells, welches eine nicht triviale $0\nu\beta\beta$ Rate in einem Modell mit leptonzahlerhaltendem Lagrangian generiert, fordern wir das bekannte Black-Box Theorem heraus, welches eine $0\nu\beta\beta$ Entdeckung mit der Majorana Natur der Neutrinos gleichsetzt. Dies wird mithilfe des Einfangs eines leptonzahlgeladenen Skalarfelds aus einem dunklen Hintergrund erreicht. Zu guter Letzt haben wir den verwendeten EFT Ansatz in unserem Python Modul ν`DoBe` automatisiert, welches wir anhand einiger Beispiele beschreiben.

On the Implications of a Future Neutrinoless Double Beta Decay Discovery

Neutrinoless double beta decay ($0\nu\beta\beta$) is the most promising experimental probe of lepton number violating (LNV) physics beyond the Standard Model. Its discovery may provide profound insights into the mechanism of neutrino mass generation as well as the observed baryon asymmetry of the universe. While the most simple interpretation of a $0\nu\beta\beta$ signal is in terms of a LNV Majorana neutrino mass term, other LNV mechanisms may provide the leading contribution to the $0\nu\beta\beta$ transition amplitude. Effective field theories (EFTs) are an efficient tool to describe and study the various LNV mechanisms of $0\nu\beta\beta$ in a model-independent way. In this work, we study the implications of a future $0\nu\beta\beta$ discovery by showcasing how different LNV mechanisms of $0\nu\beta\beta$ can be disentangled via measurements of the half-life and electron kinematics in various isotopes. By providing a proof-of-concept model that generates a non-trivial $0\nu\beta\beta$ half-life in a model with a lepton number conserving vacuum ground-state Lagrangian, we challenge the long-standing black-box theorem, which relates a $0\nu\beta\beta$ observation to the Majorana nature of neutrinos. This is achieved via the capture of a lepton number carrying scalar field from a dark background. Finally, we automated the applied EFT framework in the Python tool ν`DoBe` and showcase example use-cases.

Contents

List of Tables

List of Figures

Disclaimer

The results presented in this work are based on the author's publications which have been performed in collaboration with the other co-authors listed alongside. Specifically,

Chapter 5 presents updated results of Ref. [1]

- [1] L. Gráf, M. Lindner, and O. Scholer, "Unraveling the $0\nu\beta\beta$ decay mechanisms," *Phys. Rev. D* **106** no. 3, (2022) 035022, `arXiv:2204.10845 [hep-ph]`.

In Chapter 6 we present ν`DoBe`, a Python tool developed and published in the context of Ref. [2]

- [2] O. Scholer, J. de Vries, and L. Gráf, "νDoBe — A Python tool for neutrinoless double beta decay," *JHEP* **08** (2023) 043, `arXiv:2304.05415 [hep-ph]`.

The results of

- [3] L. Gráf, S. Jana, O. Scholer, and N. Volmer, "Neutrinoless Double Beta Decay without Vacuum Majorana Neutrino Mass," `arXiv:2312.15016 [hep-ph]`
- [4] L. Gráf, O. Scholer, M. Sen, and N. Volmer, "To be published,",

are discussed in Chapter 7. Finally, in Ref.

- [5] L. Gráf and O. Scholer, "To be published,",

we will discuss an extension to the EFT framework applied in the present work. This discussion enters into chapters 4, 5 and 6.

At the time of writing, Ref. [3] is under peer review, while Refs. [4] and [5] will be finalized and published in the near future.

Conventions

We will use the mostly-minus metric

$$g_{\mu\nu} = (\text{diag}[1, -1, -1, -1])_{\mu\nu},$$

as well as natural units, i.e.,

$$\hbar = k_B = c = 1.$$

Additionally, we use the usual slash notation to contract (covariant) derivatives or, generally, any four-vectors with gamma matrices

$$\not{\partial} = \gamma^\mu \partial_\mu, \qquad \not{D} = \gamma^\mu D_\mu, \qquad \not{p} = \gamma^\mu p_\mu.$$

The Dirac gamma matrices are denoted in the usual way as $\gamma_\mu, \mu \in [0, 3]$ and $\gamma_5 = i\gamma_0\gamma_1\gamma_2\gamma_3$. The Pauli matrices are denoted by both σ_i and $\tau_i, i \in [1, 3]$ where we use the latter to distinguish the Pauli matrices from the spin operator also denoted by σ. Generally, Greek indices $\alpha, \beta, ...$ will run from 0 to 3, representing the Minkowskian space-time indices, while Latin indices $a, b, ...$ may be used in different contexts such as, e.g., Euclidean space, flavor-space or color-space. The latter will be defined each time if their purpose is not clear from the context. We apply the usual sum convention for repeated indices

$$x^\mu y_\mu = \sum_{\mu\nu} g_{\mu\nu} x^\mu y^\nu,$$

which may at times be abbreviated as

$$x \cdot y.$$

Spatial three-vectors in a Euclidean space will usually be denoted as bold or with an arrow on top

$$\begin{pmatrix} x_1 \\ x_2 \\ x_3 \end{pmatrix} = \vec{x} = \mathbf{x}.$$

For convenience, we will often use the abbreviations

$$\int_x = \int \mathrm{d}^d x, \qquad \int_p = \int \frac{\mathrm{d}^d p}{(2\pi)^d},$$

for the d-dimensional integrals over space-time coordinates x and momentum p. Usually, the dimension of the integrals will be clear from the context.

Chapter 1

Introduction

The Nobel-prize-winning discovery of neutrino oscillations in atmospheric neutrinos at Super-Kamiokande [6] and solar neutrinos at the Sudbury Neutrino Observatory (SNO) [7] in combination with subsequent evidence for neutrino oscillations in reactor experiments [8] as well as neutrino beams [9] provides, arguably, the most promising laboratory proof of the requirement for new physics beyond the Standard Model we have today. Indeed, neutrino oscillations require the neutrinos to have non-vanishing mass differences [10, 11], therefore implying at least two of the three neutrino types to be massive, a feature the Standard Model of particle physics [12–14] does not account for. With neutrinos being the only fundamental fermion that is electrically neutral, the question about their intrinsic nature being of Dirac or Majorana type is raised. At the same time, the simplest extensions to the Standard Model able to explain the observed small neutrino masses, the famous seesaw mechanisms [15–20], describe neutrinos as Majorana particles, thereby implying the violation of lepton number. Additionally, Leptogenesis scenarios [21] suggest that the origin of the observed matter-antimatter asymmetry of the Universe might be tightly connected to the origin of the neutrino masses and the nature of the neutrino. Therefore, the unknown origin of neutrino masses is a strong motivation for the search for lepton-number-violating-physics (LNV) beyond the Standard Model.

Neutrinoless double beta decay ($0\nu\beta\beta$) experiments [22–29] are highly sensitive probes of the potential Majorana nature of neutrinos and, additionally, provide the strongest constraints for a variety of LNV physics scenarios [2, 30]. Indeed, there exists a plethora of LNV mechanisms, beyond the most "simple" Majorana neutrino mass scenario, that are testable in $0\nu\beta\beta$ experiments [24, 25]. Despite tremendous efforts in the experimental physics community dedicated towards the discovery of a $0\nu\beta\beta$ signal, it has evaded any detection so far.[1] Next-generation ton-scale experiments [34–38] aim to explore half-lives in the range of $10^{27} - 10^{28}$ yr, thereby covering the so-called inverted hierarchy scenario.

[1] An early claim of a positive signal in ^{76}Ge by parts of the Heidelberg-Moscow collaboration [31, 32] has been ruled out by the follow-up GERDA experiment [33].

A positive signal would have profound implications, as it is, generally, interpreted as showcasing that lepton number conversation is, indeed, violated in Nature, and signaling the Majorana nature of neutrinos [39, 40]. However, as we will discuss in Chapter 7, some subtleties may arise in the interpretation of a $0\nu\beta\beta$ signature requiring additional information from, e.g., cosmology in order to draw definite conclusions. Nevertheless, a positive $0\nu\beta\beta$ detection would, without any doubt, be another Nobel-price-winning achievement, providing valuable information about new physics beyond the Standard Model.

To maximize the scientific return of a future $0\nu\beta\beta$ detection, it is essential to develop a profound understanding of the various underlying LNV mechanisms that can, potentially, trigger $0\nu\beta\beta$. While limits on the $0\nu\beta\beta$ half-life are often interpreted solely in the context of a light Majorana neutrino-exchange mechanism initiating $0\nu\beta\beta$, one has to be more careful and, generally, include all possible LNV scenarios in the analysis. In this way, one may be able to not only observe but also narrow down or identify the new LNV physics causing the $0\nu\beta\beta$ signal. Effective field theories (EFTs) [41–43] allow us to study the relevant LNV scenarios beyond the Standard Model (BSM) in a controlled and model-independent way. Due to the low-energy nature of $0\nu\beta\beta$, with typical decay energies at the MeV scale, EFTs can efficiently describe any LNV mechanism stemming from new physics at some high energy scale. In this work, we will apply the chiral EFT framework developed by Cirigliano et al. [44, 45] to study the implications of a future $0\nu\beta\beta$ detection. To this end, we will discuss the requirement of new BSM physics arising from the observation of neutrino oscillations in Chapter 2. Afterwards, we will give a brief introduction to EFTs in Chapter 3. In Chapter 4, we will provide a comprehensive introduction to the theoretical aspects of $0\nu\beta\beta$. In this context, we will apply the concept of EFTs to $0\nu\beta\beta$ by rederiving and extending the chiral EFT framework of Refs. [44, 45]. This will lay the groundwork for the results presented in the subsequent chapters. We will then study the potential to disentangle the different $0\nu\beta\beta$ mechanisms, that arise in the employed EFT framework, based on the experimental observables available in dedicated $0\nu\beta\beta$ experiments in Chapter 5. The particular focus in this part of our work will be on the possible identification of higher dimensional "non-standard" LNV mechanisms beyond the usual light neutrino-exchange mechanism (LνEM). By utilizing the EFT approach, the calculation of $0\nu\beta\beta$ observables can be described in an algorithmic way. We automated this approach in the open-source Python tool ν`DoBe` [2] which will be briefly described in Chapter 6 where we will provide example use cases of the tool by studying the recent KamLAND-Zen limit on the $0\nu\beta\beta$ half-life in ^{136}Xe [46] and by deriving the corresponding limits on the various LNV mechanisms. Additionally, we will apply ν`DoBe` to the minimal left-right symmetric model [47–50] to showcase its capabilities for model-dependent applications. Finally, we will discuss the famous black-box theorem [39, 40] and its implications and potential shortcomings in Chapter 7.

Chapter 2

Neutrinos in the Standard Model – A Window to New Physics

"*Dear Radioactive Ladies and Gentlemen, [...] because of the "wrong" statistics of the N- and Li-6 nuclei and the continuous beta spectrum, I have hit upon a desperate remedy to save the "exchange theorem" of statistics and the law of conservation of energy.*"
— W. Pauli, 1930

These are the famous first words in Wolfgang Pauli's 1930 letter to the Gauverein meeting in Tübingen [51] in which he proposed the existence of an electrically neutral low-mass fermion, the neutrino[1], to explain the observed continuous energy spectrum of the electrons emitted in a single beta decay, which otherwise would contradict the conservation of energy. This "*desperate*" attempt was finally confirmed by Cowan and Reines in 1956 [53, 54] via the discovery of a neutrino-capture induced beta decay

$$\overline{\nu}_e + p \longrightarrow n + e^+. \tag{2.1}$$

The discovery of neutrinos marked an important milestone in the development of theoretical physics as it paved the path to a deeper understanding of particle physics, culminating in today's formulation of the Standard Model and providing a promising window beyond. In this chapter, we will discuss why our current understanding of neutrinos in the Standard Model, while being tremendously successful in many ways, is still incomplete and, eventually, requires the existence of new physics beyond the Standard Model. More detailed information on the general aspects of neutrino physics can be found, e.g., in Refs. [10, 11], while Ref. [55] provides some historical context.

[1]Strictly speaking, he named it the "neutron" at the time. However, this was before the particle we know today as *the neutron* was discovered in 1932 [52].

2.1 Neutrinos in the Standard Model

2.1.1 The Standard Model Lagrangian

The Standard Model (SM) of particle physics describes the fundamental building blocks and interactions we observe in Nature[2]. It is a relativistic, i.e., Lorentz invariant quantum field theory (QFT) that is characterized by its local $SU(3)_C \times SU(2)_L \times U(1)_Y$ gauge structure. In this way, it unifies Quantum Chromodynamics (QCD) [56, 57], describing the strong nuclear force, with the electroweak theory, which describes electromagnetism and the weak interactions. The dynamical degrees of freedom, and their respective gauge structure, contained in the Standard Model are summarized in Table 2.1. The SM fermions are defined in terms of the left- and right-handed chiral fields

$$\Psi = \Psi_L + \Psi_R, \qquad \Psi_{L,R} = P_{L,R}\Psi, \tag{2.2}$$

via the chiral projectors which obey the following relations

$$P_L = \frac{1-\gamma_5}{2}, \qquad P_R = \frac{1+\gamma_5}{2}, \qquad P_{L,R}P_{L,R} = P_{L,R}, \qquad P_{L,R}P_{R,L} = 0. \tag{2.3}$$

The subscript L in the $SU(2)_L$ symmetry signifies that it only acts onto the left-handed fermions Ψ_L.

It is convenient to split the SM Lagrangian into four different parts [11, 58]

$$\mathcal{L}_{SM} = \mathcal{L}_{\text{Gauge}} + \mathcal{L}_{\text{H}} + \mathcal{L}_{\text{Y}} + \mathcal{L}_{\Psi}. \tag{2.4}$$

The gauge tensor part

$$\mathcal{L}_{\text{Gauge}} = -\sum_{a=1}^{8} \mathcal{G}_{\mu\nu,a}\mathcal{G}^{\mu\nu}_a - \sum_{i=1}^{3} W_{\mu\nu,i}W^{\mu\nu,i} - B_{\mu\nu}B^{\mu\nu}, \tag{2.5}$$

describes the behaviour of the three different gauge fields $B_\mu, W^i_\mu, \mathcal{G}^a_\mu$ corresponding to the $U(1)_Y, SU(2)_L$ and $SU(3)_C$ gauge groups, respectively, with the gauge tensors given by [11, 58]

$$\begin{aligned} B_{\mu\nu} &= \partial_\mu B_\nu - \partial_\nu B_\mu, \\ W^i_{\mu\nu} &= \partial_\mu W^i_\nu - \partial_\nu W^i_\mu - g_2 \epsilon_{ijk} W^j_\mu W^k_\nu, \\ \mathcal{G}^a_{\mu\nu} &= \partial_\mu G^a_\nu - \partial_\nu G^a_\mu - g_3 f_{abc} G^b_\mu G^c_\nu. \end{aligned} \tag{2.6}$$

Here, the $SU(3)$ structure constants f_{abc} are defined via $[\lambda_a, \lambda_b] = 2if_{abc}\lambda^c$ in terms of the eight Gell-Mann matrices $\lambda_a, a \in [1, ..., 8]$. The Higgs sector is described in terms of the $SU(2)_L$ Higgs doublet $H = (h^+, h^0)^T$ as

$$\mathcal{L}_{\text{H}} = (\mathcal{D}_\mu H)^\dagger (\mathcal{D}_\mu H) - \mathcal{V}(H^\dagger H), \qquad \mathcal{V}(H^\dagger H) = \mu^2 H^\dagger H + \lambda \left(H^\dagger H\right)^2, \tag{2.7}$$

[2]except for gravity but this is beyond the scope of this work.

	Fermions of the Standard Model	$SU(3)_C$	$SU(2)_L$	$U(1)_Y$	$U(1)_{EM}$
Quarks	$Q_i = \begin{pmatrix} u_{L,i} \\ d_{L,i} \end{pmatrix}$	**3**	**2**	1/3	+2/3 −1/3
	$u_{R,i}$	**3**	**1**	+4/3	+2/3
	$d_{R,i}$	**3**	**1**	−2/3	−1/3
Leptons	$L_i = \begin{pmatrix} \nu_{L,i} \\ l_{L,i} \end{pmatrix}$	**1**	**2**	−1	0 −1
	$l_{R,i}$	**1**	**1**	−2	−1

	Bosons of the Standard Model	$SU(3)_C$	$SU(2)_L$	$U(1)_Y$	$U(1)_{EM}$
Higgs Boson	$H = \begin{pmatrix} h^+ \\ h^0 \end{pmatrix}$	**1**	**2**	1/2	+1 0
Gauge Bosons	$\mathcal{G}$	**8**	**1**	0	0
	W	**1**	**3**	0	—
	B	**1**	**1**	0	—

Table 2.1: Particle content of the Standard Model and their gauge group representations, including the electric charge in the broken phase of the Standard Model. The index i denotes the existence of three generations of fermions. Due to the mixing of the electroweak gauge bosons W and B in the broken phase of the Standard Model, we do not assign an electric $U(1)_{\text{EM}}$ charge to them here. The bold numbers **1**, **2**, **3** and **8** signify a gauge singlet, doublet, triplet and octet, respectively, while the non-bold numbers represent the relevant $U(1)$ charges.

where $\mathcal{V}(H^\dagger H)$ denotes the famous Higgs potential, with $\mu^2 < 0$ and $\lambda > 0$, that is responsible for the spontaneous symmetry breaking of the electroweak part of the SM to the electromagnetic $U(1)_{\text{EM}}$ subgroup, $SU(2)_L \times U(1)_Y \to U(1)_{\text{EM}}$. Similarly, the fermions and their gauge-interactions are summarized via

$$\mathcal{L}_\Psi = \sum_{i=1}^{3} \sum_{\Psi \in \{Q, L, u_R, d_R, l_R\}} \overline{\Psi}_i i \not{D} \Psi_i, \tag{2.8}$$

where the sum over the index i signifies the existence of three generations of fermions. The gauge-covariant derivative is given in terms of the $SU(3)_C$ and $SU(2)_L$ generators

$\lambda_a/2$, and $\tau_i/2$, respectively, and the weak hypercharge operator Y as [59]

$$\mathcal{D}_\mu = \partial_\mu - ig_3\frac{\lambda_a}{2}G^a_\mu - ig_2\frac{\tau_i}{2}W^i_\mu - ig_1 Y B_\mu, \tag{2.9}$$

where τ_i denote the three Pauli matrices. Finally, the Higgs-fermion Yukawa interactions are given by

$$\mathcal{L}_\mathrm{Y} = -Y^l_{ij}\overline{L}_i H l_{R,j} - Y^u_{ij}\overline{Q}_i\tilde{H}u_{R,j} - Y^d_{ij}\overline{Q}_i H d_{R,j} + \text{h.c.}, \tag{2.10}$$

where we defined $\tilde{H} = i\tau_2 H^* = (h^0, h^-)^T$.

2.1.2 Fermion Masses in the Standard Model

One may notice that, within the fundamental SM Lagrangian, the only physical scale is represented by the tachyonic mass $\mu^2 < 0$, while all other particles remain strictly massless. Indeed, the gauge structure of the SM prohibits the existence of fundamental mass terms for the SM fermions and gauge fields. This is in stark contrast to the observed particle content of the Universe with massive fermions and massive $W^\pm, Z$ gauge bosons. The apparent contradiction between the theoretical description in the SM and the physical reality is solved by the famous Higgs mechanism [60–64] spontaneously breaking the electroweak $SU(2)_L \times U(1)_Y$ symmetry when the neutral component of the Higgs doublet acquires its non-zero vacuum expectation value (vev). In the unitary gauge, we may write the Higgs doublet in the broken phase as [11]

$$H = \frac{1}{\sqrt{2}}\begin{pmatrix} 0 \\ v+h \end{pmatrix}, \qquad v \simeq 246\,\mathrm{GeV}, \tag{2.11}$$

where v is the Higgs vev and h is the physical Higgs boson, i.e., the excitation from the ground-state. In this way, the Yukawa interactions between the Higgs doublet and the SM fermions generate non-vanishing fermion masses of the type

$$\mathcal{L}_\mathrm{Y} \supset \sum_{\Psi\in(l,u,d)} m^\Psi_{ij}\overline{\Psi}_i\Psi_j = m^\Psi_{ij}(\overline{\Psi_{L,i}}\Psi_{R,j} + \overline{\Psi_{R,i}}\Psi_{L,j}), \tag{2.12}$$

with the mass matrices given in terms of the corresponding Yukawa matrices

$$m^l_{ij} = \frac{v}{\sqrt{2}}Y^l_{ij}, \qquad m^u_{ij} = \frac{v}{\sqrt{2}}Y^u_{ij}, \qquad m^d_{ij} = \frac{v}{\sqrt{2}}Y^d_{ij}, \tag{2.13}$$

The neutrino stands out, with respect to the remaining fermions of the SM, as being the only strictly massless fermion. This massless nature of the neutrino within the SM is related to the absence of a right-handed ν_R counterpart, and, consequently, the missing Yukawa interaction with the Higgs field.

2.2 Neutrino Oscillations – Motivating New Physics in the Neutrino Sector

The observation of neutrino oscillations provides definite proof of the existence of new physics beyond the Standard Model as it is described above. In order to understand these implications, we will briefly review the standard quantum mechanical description of neutrino oscillations following chapter 7.1 of Ref. [11]. While the standard textbook description of neutrino oscillations via a quantum mechanical plane-wave approximation [11], strictly speaking, violates energy-momentum conservation [11][3], it generates the correct oscillation probabilities and is thereby sufficient for the purpose of our discussion. For a self-consistent derivation of the neutrino oscillation probabilities, one has to apply a wave packet approach to quantum mechanics or, alternatively, a complete treatment in the context of QFT. The interested reader is referred to Refs. [11, 65–67] and references therein.

Neutrinos are, generally, produced as weak interaction eigenstates $\nu_{L,\alpha}, \alpha \in \{e, \mu, \tau\}$ which are defined in terms of the charged leptons of flavor α via the diagonal charged-current interactions [11]

$$\mathcal{L}_{\mathrm{SM}} \supset -\frac{g_2}{\sqrt{2}} W^-_\mu \overline{l_{L,\alpha}} \gamma^\mu \nu_{L,\alpha} + \text{h.c.}. \tag{2.14}$$

In general, the weak eigenstates $\nu_{L,\alpha}$ do not need to coincide with the Hamiltonian neutrino eigenstates $\nu_{L,i}$ which are defined via

$$\mathcal{H} \left|\nu_{L,i}\right\rangle = E_i \left|\nu_{L,i}\right\rangle, \qquad E_i = \sqrt{\mathbf{p}^2 + m_i^2}, \tag{2.15}$$

but are, instead, related via a unitary 3×3 matrix U

$$\mathcal{L}_{\mathrm{SM}} \supset -\frac{g_2}{\sqrt{2}} W^-_\mu \overline{l_{L,\alpha}} \gamma^\mu \nu_{L,\alpha} = -\frac{g_2}{\sqrt{2}} W^-_\mu \overline{l_{L,\alpha}} \gamma^\mu U^*_{\alpha i} \nu_{L,i}. \tag{2.16}$$

If the interaction and Hamiltonian eigenstates align, U is simply given by the identity matrix. Let us now consider a neutrino of flavor α that is produced via some charged-current weak interaction at time $t = 0$. Its time-evolution is captured by the Schroedinger equation as

$$\left|\nu_{L,\alpha}(t)\right\rangle = \exp\{-i\mathcal{H}t\} \left|\nu_{L,\alpha}\right\rangle = \sum_{\beta,k} U^*_{\alpha k} \exp\{-iE_k t\} U_{\beta k} \left|\nu_{L,\beta}\right\rangle. \tag{2.17}$$

The $\nu_{L,\alpha} \to \nu_{L,\beta}$ transition probability after a certain time t is then given in terms of the absolute square of the corresponding transition amplitude

$$P_{\alpha\to\beta}(t) = \left|\left\langle \nu_{L,\beta} | \nu_{L,\alpha}(t)\right\rangle\right|^2 = \sum_{ij} U^*_{\alpha i} U_{\beta i} U_{\alpha j} U^*_{\beta j} \exp\{-i(E_i - E_j)t\}. \tag{2.18}$$

[3] Also plane-waves are characterized by having a definite momentum and are therefore completely delocalized in position-space making it impossible to define a proper baseline distance.

It is evident that non-trivial transition amplitudes require energy differences between the different Hamiltonian eigenstates $|\nu_{L,i}\rangle$. With typical neutrino energies being at least at the order of a few MeV, we may expand the neutrino energy in terms of small neutrino masses $m_i \ll \mathbf{p}$

$$E_i = \mathbf{p} + \frac{m_i^2}{2\mathbf{p}} + \mathcal{O}\left(\left[\frac{m_i^2}{2\mathbf{p}}\right]^2\right), \tag{2.19}$$

and the energy difference becomes

$$E_i - E_j = \frac{m_i^2 - m_j^2}{2\mathbf{p}}. \tag{2.20}$$

Consequently, in the vacuum, non-zero $\nu_{L,\alpha} \to \nu_{L,\beta}$ transition probabilities require non-trivial mass differences and therefore necessitate the existence of massive neutrinos. The experimental verification of neutrino oscillations is therefore a clear signature requiring physics beyond the SM.

Throughout this section, we applied the so-called same-momentum approach, by assigning a common momentum $\mathbf{p}$ to all propagating neutrino states. Additionally, we assumed the neutrinos to propagate through an empty vacuum. The propagation through a dense medium complicates the discussion, as neutrino-matter interactions have to be considered in the Hamiltonian, thereby changing the in-medium eigenstates of the Hamiltonian. Indeed, one may define an effective or *refractive* mass for neutrinos propagating through a dense and interacting medium. In this way, the famous MSW effect provides a solution to the solar neutrino problem [68–71]. Recently, a refractive neutrino mass generation in the context of neutrino-dark matter interactions was proposed as a potential solution to the observed neutrino oscillations without the necessity for vacuum neutrino masses [72]. In Chapter 7, we will make use of this conceptual idea again.

2.3 Neutrino Masses and the Nature of Neutrinos

Besides its local gauge structure, the SM incorporates several *accidental* global symmetries. These are themselves not a defining feature of the SM, but arise from the given field content and symmetry structure. On the Lagrangian level, both baryon number B and lepton number L as well as their combinations $B - L$ and $B + L$ are conserved. Taking into account non-perturbative effects, so-called anomalies, only $B - L$ survives as an exact *accidental* symmetry of the SM [73–75]. In this section, we will argue that the introduction of neutrino masses into the SM requires either the violation of this *accidental* symmetry or its promotion to a defining feature of the theory.

Basically, we are provided with two possible options for defining a neutrino mass term of the form $m_\nu \overline{\nu}\nu$. First, we may add a $B-L$ conserving Dirac mass term by adding three right-handed neutrinos $\nu_{R,i}$ to the SM and defining the full neutrino field $\nu_i = \nu_{L,i} + \nu_{R,i}$. This allows us to write down a Dirac neutrino mass term of the form

$$\mathcal{L}_{m_\nu} = m_{ij}^D \overline{\nu}_i \nu_j = m_{ij}^D \left(\overline{\nu_{L,i}}\nu_{R,j} + \overline{\nu_{R,i}}\nu_{L,j}\right), \tag{2.21}$$

where the Dirac neutrino mass matrix

$$m_{ij}^D = \frac{v}{\sqrt{2}} Y_{ij}^\nu, \tag{2.22}$$

is generated via the same Yukawa interactions of the neutrino with the Higgs doublet as for the remaining SM neutrinos. Alternatively, instead of adding a dedicated right-handed neutrino field, we may use the CP-conjugate of the left-handed neutrino field

$$\nu_L^C = C\overline{\nu_L}^T = P_R C \overline{\nu}^T, \qquad C = i\gamma_0\gamma_2, \tag{2.23}$$

as the necessary right-handed counterpart and define $\nu = \nu_L + \eta\nu_L^C$ with some complex phase η. This is called a Majorana neutrino. Its defining property is that it requires the neutrino and anti-neutrino to be equivalent up to a complex phase

$$\nu^C = \eta^* \nu. \tag{2.24}$$

The corresponding Majorana mass term is then

$$\mathcal{L}_{m_\nu} = \frac{1}{2} m_{ij}^L \overline{\nu}_i \nu_j = \frac{1}{2} m_{ij}^L \left(\overline{\nu_{L,i}} \nu_{L,j}^C + \overline{\nu_{L,i}^C} \nu_{L,j} \right), \tag{2.25}$$

where we absorbed the complex phase η into the definition of the Majorana mass matrix m_{ij}^L. The conventional factor of $1/2$ accounts for the fact that the left- and right-handed parts of ν are not independent from each other. Evidently, a Majorana neutrino mass term violates lepton number by 2 units. However, a Majorana mass term for the left-handed neutrino is not invariant under the SM gauge structure and requires the extension of the scalar sector by, e.g., an $SU(2)_L$ triplet scalar [17, 18, 20].

In order to save the accidental $B - L$ symmetry of the SM, we have to describe the neutrino as a Dirac particle and, consequently, add right-handed neutrinos to the theory. However, because neutrinos are electrically neutral and do not interact via the strong force, right-handed neutrinos are total singlets under the SM gauge group, $\nu_R \in (\mathbf{1}, \mathbf{1}, 0)$[4]. As a consequence, we may write down a gauge-invariant Majorana mass term for the right-handed neutrino fields

$$\mathcal{L}_{m_\nu} \supset \frac{1}{2} m_{ij}^R \overline{\nu_{R,i}} \nu_{R,j}^C + \text{h.c.}. \tag{2.26}$$

This not only introduces new dimensionful scales given by the right-handed neutrino mass matrix m_{ij}^R into the theory. It also violates $B - L$ by two units, again. Naively, one might argue that the singlet Nature of the right-handed neutrinos will hide the LNV nature of this SM extension, as ν_R does not take part in any gauge interactions. However, as we will see in Chapter 7, the mixing of ν_R with the weakly interacting left-handed neutrinos ν_L via the Dirac mass term, renders the neutrino mass states as Majorana

[4]The electric charge Q of a field is given in terms of the weak hypercharge Y and third component of the weak isospin $I_3 = \tau_3/2$ as $Q = I_3 + Y/2$ [11]. As a right-handed field, ν_R is by definition an $SU(2)_L$ singlet with $I_3 = 0$, therefore requiring $Y = 0$.

particles when diagonalizing the full mass matrix. This is known as the famous seesaw type-I scenario [10, 15–17] which can have significant phenomenological consequences.

We see that in order to save the *accidental* $B - L$ symmetry of the SM, we would have to manually impose it onto the theory when adding right-handed neutrinos. This is a strong motivation for the search for LNV BSM physics and the Majorana nature of neutrinos.

Chapter 3

Effective Field Theories in a Nutshell

Before turning towards $0\nu\beta\beta$ we will briefly introduce and discuss the concepts and relevant aspects of effective field theories (EFTs). For a more comprehensive review the interested reader is referred to the lecture notes of Refs. [41–43] while Ref. [76] offers some interesting insights into the historical contexts and developments. In this chapter, we will mostly follow along the lines of the first two chapters of Penco's lecture notes [43].

3.1 The Purpose of Effective Field Theories

In a general sense, EFTs are approximate solutions to a more fundamental quantum field theory and are valid only under certain conditions, e.g., below a certain energy scale or above a certain length scale. They may be constructed to effectively describe a certain (set of) physical system(s) under consideration. In the context of particle physics, EFTs are used whenever a separation of scales justifies the description of macroscopic (low-energy) phenomena of interest independently of the full microscopic (high-energy) theory.

Depending on the phenomenological context, EFTs may differ from the full microscopic theory in terms of the relevant degrees of freedom under consideration, either by systematically removing "irrelevant" degrees of freedom, such as heavy particles above the energy scale of interest, or by changing to a completely different set of degrees of freedom, such as transitioning from free particles to bound states. In the same way, EFTs can feature different symmetry structures than the underlying fundamental microscopic theory.

In the context of particle physics, the application of EFTs, usually, follows along either of two lines:

1. **Top $\rightarrow$ Down – Simplifying Calculations:** In case the fundamental theory is known we may still encounter problems when trying to do precise calculations of physical observables in certain situations. In such a scenario, EFTs can be a useful

tool to simplify calculations and allow us to make predictions that could not be extracted from the full theory. The most common example in particle physics for such a scenario is QCD at low energies. While the full microscopic theory of QCD is known, it becomes strongly interacting below the energy scale of $\Lambda_\chi \sim 2\,\mathrm{GeV}$ such that perturbation theory breaks down. Chiral perturbation theory [77, 78] offers a systematic way of dealing with QCD in the strongly interacting regime by considering composite mesons and nucleons as the relevant degrees of freedom instead of the fundamental quark and gluon fields.

2. **Bottom → Up – Searching for New Physics:** When searching for new physics we may use EFTs as a model-independent tool to constrain possible scenarios. This can be achieved by either constructing an EFT appropriate to a specific experimental setup using the relevant degrees of freedom and symmetry constraints or by promoting an existing microscopic theory (such as the Standard Model) to an EFT by dropping the renormalizability requirement and systematically adding all (non-renormalizable) terms that can be constructed with the existing degrees of freedom and that are allowed by the symmetries of the theory.

In this work, we will make use of both approaches.

3.2 Constructing an Effective Field Theory

As EFTs are not supposed to be fundamental theories of Nature valid up to arbitrary energy scales, we may drop the requirement of renormalizability in the usual sense. That is, we do not require renormalization via a finite set of counter-terms but settle for an infinite number of counter-terms, instead. While this is, usually, interpreted as a loss of predictive power of a theory, as we introduce an infinite set of free parameters that would need to be fixed experimentally, we will see that one can systematically regain predictability via the introduction of a power-counting scheme. Usually, the construction of an EFT Lagrangian requires the following steps [43]:

1. At the beginning, one has to identify all relevant degrees of freedom and symmetries that are necessary to describe the macroscopic physical system of interest. The EFT will consist of all operators that can be built out of the relevant degrees of freedom consistent with the identified symmetry constraints. In general, this will be an infinite number of terms.

2. In the next step, one has to work out a power-counting scheme that allows us to expand the Lagrangian in terms of some small quantity ϵ. This will enable us to sort the infinite amount of terms in the EFT Lagrangian by their relevance based on a suppression scale. The most common choice in particle physics is an expansion in the ratio E/Λ with the high energy scale Λ representing the scale at which the full microscopic theory and its degrees of freedom become relevant and the low-energy scale E corresponding to the macroscopic phenomena the EFT is supposed

to describe. In D space-time dimensions, we can use such a power-counting scheme to write the effective Lagrangian as [42]

$$\mathcal{L}_{\text{eff}} = \sum_{i,d>0} \frac{C_i^{(d)}}{\Lambda^{d-D}} \mathcal{O}_i^{(d)} = \sum_{d>0} \frac{1}{\Lambda^{d-D}} \mathcal{L}_{\text{eff}}^{(d)}, \tag{3.1}$$

where the operators $\mathcal{O}_i^{(d)}$ are d-dimensional operators allowed by the relevant symmetry constraints and built from the EFT's degrees of freedom, $C_i^{(d)}$ are the corresponding coupling constants or Wilson Coefficients and we have summarized all terms at a certain dimension d in the effective d-dimensional Lagrangian $\mathcal{L}_{\text{eff}}^{(d)}$.

3. By truncating the effective Lagrangian at a certain order in the EFT expansion

$$\mathcal{L}_{\text{eff}} = \mathcal{L}_{\text{eff}}^{(\text{d}\leq\text{D})} + \sum_{k=1}^{k_{\max}} \frac{1}{\Lambda^k} \mathcal{L}_{\text{eff}}^{(D+k)} + \mathcal{O}\left((1/\Lambda)^{k_{\max}}\right), \tag{3.2}$$

one can limit the number of operators to a finite set and, hence, regain predictability up to a certain level of accuracy set by the truncation order $k_{\max}$. Here, we explicitly split the effective Lagrangian into the renormalizable part $\mathcal{L}_{\text{eff}}^{(\text{d}\leq\text{D})}$ and the "non-renormalizable" higher dimensional contributions $\mathcal{L}_{\text{eff}}^{(\text{D+k})}$ suppressed by powers of Λ^{-k}. In this sense, "non-renormalizable" theories are in fact renormalizable as long as we restrict ourselves to some finite accuracy in the EFT expansion.

3.3 Matching Procedure - Integrating Out Heavy Degrees of Freedom

A priori, the Wilson coefficients of an EFT are completely unknown. However, if the microscopic theory is known, we can construct them systematically. This procedure is usually referred to as *matching*. In this section, we will show how the parameters of a given microscopic theory can be matched onto the corresponding macroscopic EFT by *integrating out* the heavy degrees of freedom. This is a valid approach whenever the macroscopic degrees of freedom are a subset of the full microscopic theory.

Let's briefly recall the path integral formulation of Quantum Field Theory [79, 80]. In this formulation, one can derive any n-point correlation function $\langle A \rangle$, from the so-called partition function

$$\mathcal{Z} = \int \prod_n \mathcal{D}\Phi_n \exp\{i\mathcal{S}(\{\Phi_n\}\}, \tag{3.3}$$

either by performing the functional integral

$$\langle A \rangle = \frac{1}{\mathcal{Z}} \int \prod_n \mathcal{D}\Phi_n A \exp\{i\mathcal{S}(\{\Phi_n\}\}, \tag{3.4}$$

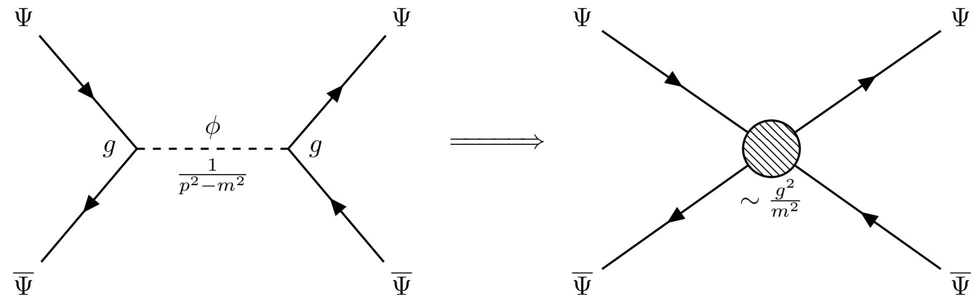

Figure 3.1: Diagrammatic visualization of a tree-level matching procedure. Feynman diagrams offer an intuitive way of understanding the matching procedure from a microscopic theory (left) to a macroscopic EFT (right) by taking the $m \gg p$ limit for internal propagators of heavy particles.

or by introduction of external sources $\mathcal{J}_n$ into the partition function

$$\mathcal{Z}(\{\mathcal{J}_n\}) = \int \prod_n \mathcal{D}\Phi_n \exp\left\{ i\mathcal{S}(\{\Phi_n\} + \int_x \sum_n \mathcal{J}_n^*(x)\Phi_n(x) + \mathcal{J}_n(x)\Phi_n^*(x) \right\}, \tag{3.5}$$

and taking the appropriate functional derivatives with respect to the external sources

$$\langle \Phi_i(x_1)...\Phi_j(x_n) \rangle = \frac{1}{\mathcal{Z}(\{\mathcal{J}_n\})} \frac{\delta^n}{\delta\mathcal{J}_i(x_1)...\delta\mathcal{J}_j(x_n)} \mathcal{Z}(\{\mathcal{J}_n\}) \bigg|_{\mathcal{J}=0} . \tag{3.6}$$

From this point, we can already guess what *integrating out* a certain field means. For simplicity, let us assume a simple Yukawa theory model composed of a heavy real scalar field ϕ and a much lighter fermionic field Ψ with the Lagrangian

$$\mathcal{L} = \overline{\Psi}(i\partial\!\!\!/ - m_\Psi)\Psi - \frac{1}{2}\phi(\partial^\mu\partial_\mu + m_\phi^2)\phi + g\phi\overline{\Psi}\Psi, \tag{3.7}$$

and the partition function given by

$$\mathcal{Z}(J, \overline{\eta}, \eta) = \int \mathcal{D}\phi\mathcal{D}\overline{\Psi}\mathcal{D}\Psi \ \exp\left\{ iS(\phi, \overline{\Psi}, \Psi) + i\int_x J(x)\phi(x) + \overline{\eta}(x)\Psi(x) + \overline{\Psi}(x)\eta(x) \right\},$$

where the action is defined as

$$\mathcal{S} = \int_x \mathcal{L}. \tag{3.8}$$

At energies much lighter than the scalars mass $E \ll m_\phi$ we cannot observe any scattering processes with incoming or outgoing scalars, as there is simply not enough energy to produce them. Hence, we might factor out and perform the path integral over ϕ and define the effective action $\mathcal{S}_{\text{eff}}$ via

$$\begin{aligned}\mathcal{Z}(\mathcal{J}=0,\overline{\eta},\eta) &= \int \mathcal{D}\overline{\Psi}\mathcal{D}\Psi \exp\left\{ i\int_x \overline{\eta}\Psi + \overline{\Psi}\eta \right\} \int \mathcal{D}\phi \exp\{ i\mathcal{S}(\phi,\overline{\Psi},\Psi)\} \\ &= \int \mathcal{D}\overline{\Psi}\mathcal{D}\Psi \exp\left\{ i\mathcal{S}_{\text{eff}}(\overline{\Psi},\Psi) + i\int_x \overline{\eta}\Psi + \overline{\Psi}\eta \right\}. \end{aligned} \tag{3.9}$$

Note that the partition function and effective action obtained in this way exactly describe all scattering amplitudes that do not involve external scalars. For our simple Yukawa theory without scalar self-interactions, we can explicitly calculate the Gaussian integral over ϕ using the relation [79]

$$\int \mathrm{d}^N x \exp\left\{ -\frac{1}{2} x^T A x + j^T x \right\} = \frac{(2\pi)^{(N/2)}}{\sqrt{\det\{A\}}} \exp\left\{ \frac{1}{2} j^T A^{-1} j \right\}, \tag{3.10}$$

yielding

$$\int \mathcal{D}\phi \exp\left\{ i\int_x -\frac{1}{2}\phi(\Box + m_\phi^2)\phi + g\overline{\Psi}\Psi\phi \right\} \propto \exp\left\{ i\int_x g\overline{\Psi}\Psi(\Box + m_\phi^2)^{-1}\overline{\Psi}\Psi \right\}. \tag{3.11}$$

From eq. (3.4) and (3.6) we can see that the prefactor of $(2\pi)^{(N/2)}/\sqrt{\det\{A\}}$ has no physical relevance. Hence, we can simply drop it. In this way, we obtain the effective action

$$\mathcal{S}_{\text{eff}} = \int_x \overline{\Psi}(i\not{\partial} - m_\Psi)\Psi + g\overline{\Psi}\Psi(\Box + m_\phi^2)^{-1}\overline{\Psi}\Psi. \tag{3.12}$$

Turning to momentum space, $\Box \to -p^2$, we may now expand the inverse propagator in the low-energy limit $p^2 \ll m_\phi^2$

$$(\Box + m_\phi^2) = \frac{1}{m_\phi^2} - \frac{\Box}{m_\phi^4} + \mathcal{O}\left(\left(\frac{\Box}{m_\phi^4} \right)^2 \right), \tag{3.13}$$

to obtain our effective action expressed in terms of a power-counting scheme

$$\mathcal{S}_{\text{eff}} = \int_x \overline{\Psi}(i\not{\partial} - m_\Psi)\Psi + \frac{g}{m_\phi^2}\overline{\Psi}\Psi\overline{\Psi}\Psi + \mathcal{O}\left(\frac{\Box}{m_\phi^4} \right). \tag{3.14}$$

As long as we can solve the path integral over ϕ exactly, we do not lose any accuracy in terms of predictive power. However, in most cases, we will not be able to solve the path integral exactly and, instead, will have to resort to good old-fashioned perturbation theory. At tree-level, this just means to solve the Euler-Lagrange equations of motion for ϕ

$$\frac{\partial \mathcal{L}}{\partial \phi} - \partial_\mu \frac{\partial \mathcal{L}}{\partial(\partial_\mu \phi)} = 0, \tag{3.15}$$

and to plug the solution back into the Lagrangian. For our simple toy model with no scalar self-interactions, we expect to recover the same result as obtained by solving the path integral exactly. This is because without self-interactions there are no scalar loop-diagrams that can contribute to any Ψ scattering process. Hence, tree-level is all there is. Indeed, by solving eq. (3.15) we find

$$\phi = g(\Box + m_\phi^2)^{-1}\overline{\Psi}\Psi, \tag{3.16}$$

and by plugging the solution for ϕ back into the action we recover the effective action we found in eq. (3.12).

Diagrammatically, this procedure can be understood quite intuitively by considering all relevant tree-level Feynman diagrams and replacing any internal scalar lines with their respective propagator in the large m limit as visualized in Figure 3.1.

In the following chapter we will apply the concept of EFTs in the context of $0\nu\beta\beta$ utilizing several EFTs each valid at different energy scales. The matching procedure described above can be applied to the matching of a higher energy EFT onto a lower energy EFT as well and we will make use of this when turning towards $0\nu\beta\beta$.

However, in the case of chiral EFT the non-perturbative nature of low-energy QCD does not allow us to apply the above matching procedures. Instead, we will see that we will have to rely on symmetry arguments when matching onto the low-energy bound-state degrees of freedom. The low-energy Wilson coefficients of chiral EFT have to be fixed from experiments or matched via non-perturbative methods such as lattice QCD calculations.

Chapter 4

Theoretical Aspects of Neutrinoless Double Beta Decay – An EFT Perspective

The main purpose of this chapter is to build the foundations necessary for discussing the results of the author's papers [1, 2] which focus on the possibilities of disentangling different mechanisms of $0\nu\beta\beta$ as well as the development of the Python tool ν`DoBe` that automates calculations of $0\nu\beta\beta$ observables for various BSM scenarios. To this end, we will apply the EFT framework developed by Cirigliano et al. [44, 45]. The general idea of this approach is to describe $0\nu\beta\beta$ using a ladder of different EFTs, each valid at a certain energy scale, with the Standard Model EFT (SMEFT) [59, 81–88] describing physics above the scale of electroweak symmetry breaking (EWSB), the $SU(3)_C \times U(1)_{\mathrm{EM}}$-invariant low-energy EFT (LEFT) [89–91] valid below the scale of EWSB, and chiral perturbation theory χPT [78] as well as its multi-nucleon extension, chiral EFT (χEFT) [92] that describe the transition from free quarks to confined nucleons and mesons below $\Lambda_\chi \sim 1\,\mathrm{GeV}$. This EFT ladder is displayed in Figure 4.1.

In the following sections, we will demonstrate that EFTs provide a powerful framework that allows us to study new LNV physics in $0\nu\beta\beta$ both in a model-independent way as well as in the context of individual BSM models that can be mapped onto the EFT framework. We will describe the necessary steps in the transition from a full UV model along the different steps of the EFT ladder to reproduce the $0\nu\beta\beta$ "*master formula*" as derived in Refs. [44, 45]. This will lay the foundation for our results presented in the following chapters. Broader reviews about neutrinoless double beta decay as a probe of new physics can be found in, e.g., Refs. [22–29].

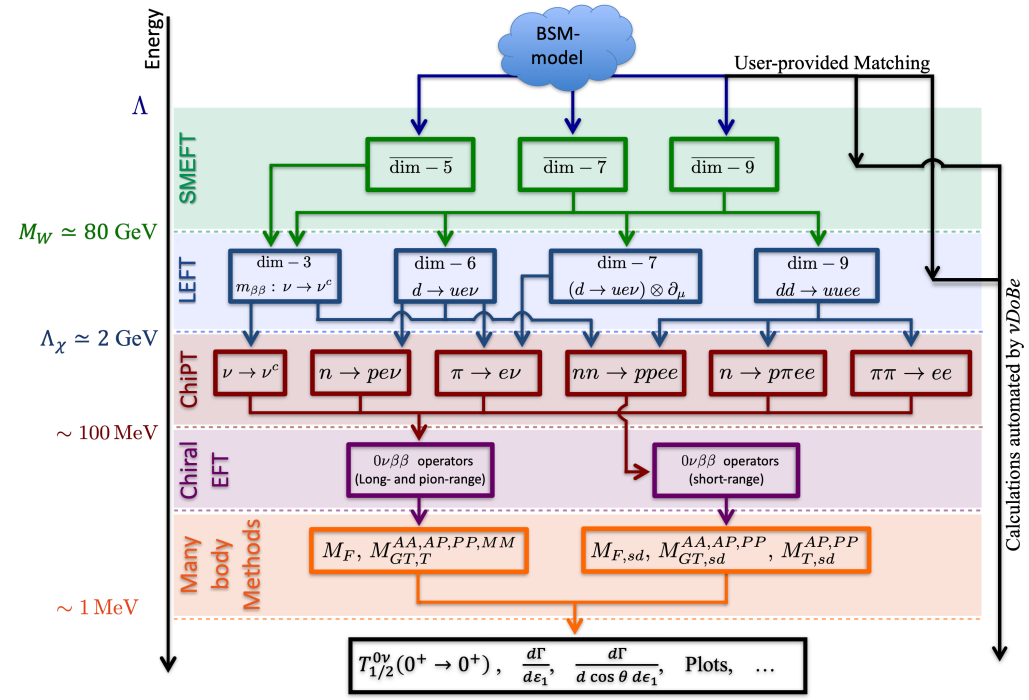

Figure 4.1: Schematic visualization of the applied Effective Field Theory approach to $0\nu\beta\beta$. We utilize a ladder of different EFTs each describing physics at a different energy scale. In this way, $0\nu\beta\beta$ can be studied both in a model-independent way or for specific BSM models via the appropriate matching to the EFT framework. This process was automated in the Python tool νDoBe [2]. The figure is taken from Ref. [2] which is a modified version of Ref. [45].

4.1 A General Introduction to Double Beta Decay

Before we start to dive deeper into the connections between various LNV extensions to the Standard Model and $0\nu\beta\beta$ let us first recall the basics of double beta decay to understand why we even consider its neutrinoless mode. I have, previously, covered a number of the following points within my Master thesis [93].

4.1.1 When and how does Double Beta Decay Occur?

In 1935, just briefly after Fermi's theoretical description of the beta decay in 1934 [94], M. Goeppert-Mayer theorized the existence of a double beta decay process [95] predicting half-lives of $\gtrsim 10^{17}$ yrs. Although double beta decay was initially thought to remain unobserved due to its large half-life [96], it took only about 15 years until the first experimental discovery in geochemical experiments. In 1950, Inghram and Reynolds found a ^{130}Xe excess in tellurium ores extracted from a ~ 240 m deep mine. This excess was attributed to the double beta decay of $^{130}\mathrm{Te} \to ^{130}\mathrm{Xe}$ with an estimated half-live of

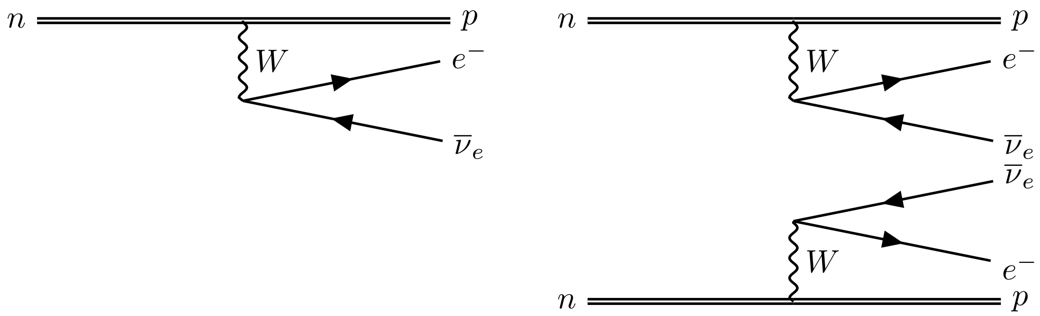

Figure 4.2: Single vs. double beta decay. In the single beta decay (left), a neutron, n, inside some nucleus is turned into a proton, p, by emitting an electron, e^-, and an anti-electron neutrino, $\overline{\nu}_e$. A double beta decay (right) is the occurrence of two simultaneous single beta decays inside the same nucleus.

1.4×10^{21} yrs [97]. Today, double beta decay has been explored and detected in laboratory experiments covering various isotopes (c.f. Table 4.1) with half-lives of up to $\sim 10^{21}$ yrs, while geochemical experiments have uncovered half-lives of up to $\sim 10^{24}$ yrs [98, 99]. Here, we will briefly explain the basics of this process.

The double beta decay, or more precisely the two-neutrino double beta decay ($2\nu\beta\beta$),

$$(A, Z) \longrightarrow (A, Z+2) + 2e^- + 2\overline{\nu}_e, \tag{4.1}$$

as shown in Figure 4.2 is, simply, what its name suggests. That is, the $2\nu\beta\beta$ is the occurrence of two simultaneous beta decays

$$(A, Z) \longrightarrow (A, Z+1) + e^- + \overline{\nu}_e, \tag{4.2}$$

inside a single nucleus of mass number A and charge Z. Both are Standard Model processes that can occur whenever the combined mass of all the final state particles M_f is smaller than the initial state's mass M_i. That is, when the Q-value, i.e. the decay energy

$$Q = M_i - M_f, \tag{4.3}$$

is positive. Naively, one might think that the $2\nu\beta\beta$ mode, being a second order weak interaction, will always be suppressed in comparison to the first order weak interaction single beta mode. However, in certain situations when the single beta decay is energetically forbidden or strongly suppressed, the $2\nu\beta\beta$ can become the dominant mode.

Let's see how such scenarios can be explained. Generally, the mass of a nucleus can be expressed in terms of its constituents, i.e., the protons and neutrons and the relevant binding energy E_B as

$$M(A, Z) = Zm_p + (A - Z)m_n - E_B(A, Z). \tag{4.4}$$

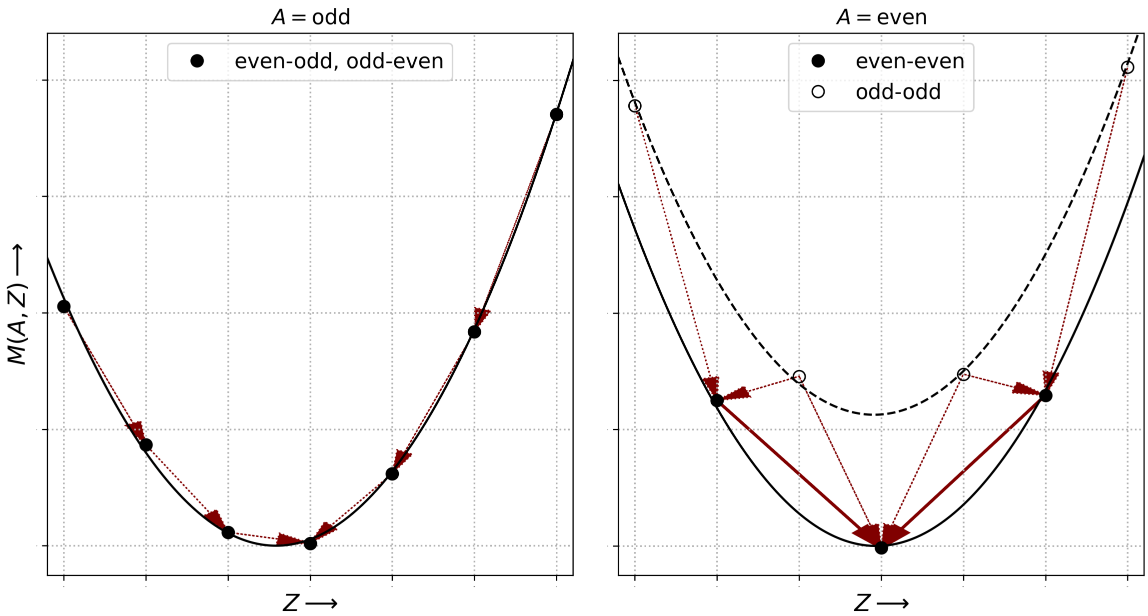

Figure 4.3: Mass parabolas for nuclei with fixed mass number A. For nuclei with an odd mass number (left) all isotopes lie on a single mass parabola. Single beta decays (dotted red arrow) move nuclei down along this parabola. For nuclei with an even mass number (right) two separate mass parabolas exist with single beta decay moving a nucleus from one parabola to the other. If both neighbouring odd-odd isotopes are heavier than the initial state even-even nucleus a single beta decay is energetically forbidden and the $2\nu\beta\beta$ (solid red arrow) can become the dominant decay mode.

The binding energy can be expressed in a semi-empirical formula which was first introduced by Weizsäcker [100] and reformulated by Bethe and Bacher [101] as

$$E_B(A, Z) = \alpha_{\mathrm{V}} A - \alpha_{\mathrm{A}} \frac{(N-Z)^2}{A} - \alpha_{\mathrm{S}} A^{2/3} - \alpha_{\mathrm{C}} \frac{Z^2}{A^{1/3}} + \delta\alpha_{\mathrm{P}} \frac{1}{A^{1/2}}, \tag{4.5}$$

with the constants $\alpha_{\mathrm{V,A,S,C,P}}$ representing the binding energy from nuclear forces proportional to the Volume (V) of the nucleus, the increase in binding energy for asymmetric (A) numbers of neutrons and protons, the surface (S) energy, the repulsive Coulomb (C) energies of the protons, and the spin-pairing (P) energy. In general, these constants have to be determined experimentally. However, we are not interested in the precise values. Instead, we should notice that any beta decay only changes the nuclear charge Z while keeping the mass number A constant. For a constant nuclear mass number A it is convenient to rewrite eq. (4.4) in a parabolic form

$$M_A(Z) = m_A + \alpha Z + \beta(Z - Z_A)^2 + \delta_P, \tag{4.6}$$

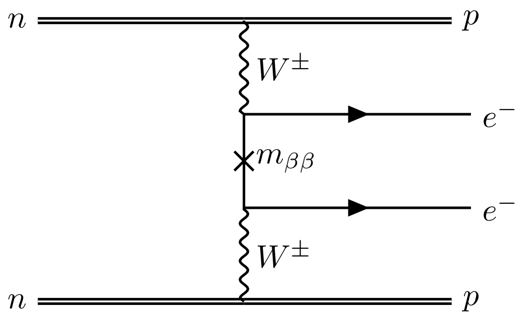

Figure 4.4: The light neutrino-exchange mechanism of $0\nu\beta\beta$. This process can occur if the electron neutrino ν_e is a Majorana fermion. The decay amplitude is proportional to the effective Majorana mass of the electron neutrino $m_{\beta\beta}$.

with the pairing energy

$$\delta_P \propto \begin{cases} 1, & A = \text{even}, N = \text{odd}, Z = \text{odd} \\ 0, & A = \text{odd} \\ -1, & A = \text{even}, N = \text{even}, Z = \text{even} \end{cases} . \tag{4.7}$$

Thus, for fixed A we can see that the masses of isotopes with an odd A form a single parabola such that single beta decays are generally allowed while moving down the parabola. However, isotopes with an even A are positioned on two individual mass parabolas separated by the pairing energy $2\delta_P$ with odd-odd nuclei having larger masses than even-even nuclei. In this case, single beta decays do not move along a single parabola but, instead, move a nucleus from one parabola to the other one. In Figure 4.3 we have visualized this schematically. If the mass splitting between the two parabolas is large enough, the single beta decay mode can be energetically forbidden for some isotopes such that $2\nu\beta\beta$ becomes the leading mode. Overall, there are 35 naturally occuring isotopes that undergo $2\nu\beta\beta$ [1]. The full list is provided in Table A.1.

4.1.2 The Neutrinoless Double Beta Decay

Influenced by E. Majorana's seminal 1937 publication on the description of neutral fermions [102], W. Furry proposed the idea of a neutrinoless double beta decay in 1939 [96]

$$(A, Z) \longrightarrow (A, Z+2) + 2e^-, \tag{4.8}$$

long before any experimental observation of the Standard Model's $2\nu\beta\beta$ process. This hypothetical process can take place if the neutrino and anti-neutrino are the same particle, i.e., if neutrinos are correctly described as Majorana fermions. In this case, one can close the external lines of the two outgoing neutrinos in the $2\nu\beta\beta$ diagram of Figure 4.2

Isotope		Daughter	Q [MeV]	$\overline{N}$[%]	$T_{1/2}^{2\nu\beta\beta}$ [yr]	$T_{1/2}^{0\nu\beta\beta}$ [yr]
^{48}Ca	$\longrightarrow$	^{48}Ti	4.267	0.187	6.4×10^{19} [104]	$> 5.8 \times 10^{22}$ [105]
^{70}Zn	$\longrightarrow$	^{70}Ge	0.997	0.61	$> 3.8 \times 10^{18}$ [106]	$> 1.6 \times 10^{21}$ [107]
^{76}Ge	$\longrightarrow$	^{76}Se	2.039	7.73	2.022×10^{21} [108]	$> 1.8 \times 10^{26}$ [33]
^{82}Se	$\longrightarrow$	^{82}Kr	2.996	8.73	8.69×10^{19} [109]	$> 4.6 \times 10^{24}$ [110]
^{96}Zr	$\longrightarrow$	^{96}Mo	3.349	2.80	2.35×10^{19} [111]	$> 9.2 \times 10^{21}$ [111]
^{100}Mo	$\longrightarrow$	^{100}Ru	3.034	9.82	7.07×10^{18} [112]	$> 1.8 \times 10^{24}$ [113]
^{114}Cd	$\longrightarrow$	^{114}Sn	0.542	28.73	$> 1.3 \times 10^{18}$ [114]	$> 1.6 \times 10^{21}$ [115]
^{116}Cd	$\longrightarrow$	^{116}Sn	2.813	7.49	2.63×10^{19} [116]	$> 2.2 \times 10^{23}$ [116]
^{128}Te	$\longrightarrow$	^{128}Xe	0.867	31.74	2.3×10^{24} [99]$^{(*)}$	$> 3.6 \times 10^{24}$ [117]
^{130}Te	$\longrightarrow$	^{130}Xe	2.528	34.08	7.71×10^{20} [118]	$> 3.2 \times 10^{25}$ [119]
^{134}Xe	$\longrightarrow$	^{134}Ba	0.826	10.436	$> 2.8 \times 10^{22}$ [120]	$> 3.0 \times 10^{23}$ [120]
^{136}Xe	$\longrightarrow$	^{136}Ba	2.458	8.857	2.21×10^{21} [121]	$> 3.8 \times 10^{26}$ [46]
^{150}Nd	$\longrightarrow$	^{150}Sm	3.371	5.638	9.34×10^{18} [122]	$> 2.0 \times 10^{22}$ [122]
^{160}Gd	$\longrightarrow$	^{160}Dy	1.731	21.86	$> 1.9 \times 10^{19}$ [123]	$> 1.3 \times 10^{21}$ [123]
^{186}W	$\longrightarrow$	^{186}Os	0.492	28.43	$> 2.3 \times 10^{19}$ [106]	$> 1.0 \times 10^{21}$ [106]

Table 4.1: List of experimental limits on the $0\nu\beta\beta$ half-life in various isotopes. To our best knowledge, this list provides the strongest limit for each isotope studied in $0\nu\beta\beta$ experiments to this date. In addition, we show the most recent measurements of (limits on) the $2\nu\beta\beta$ half-life for each isotope. Except for the $2\nu\beta\beta$ half-life in ^{128}Te (marked by $^{(*)}$, derived via geochemical methods), all limits are obtained from laboratory experiments. We only included studies of the ground state 0^+ to ground state 0^+ transition. The corresponding Q-values as well as the isotopic abundance $\overline{N} = N(A,Z)/N(Z)$ are given as well and taken from the NIST list of elements [124].

to write down a $0\nu\beta\beta$ diagram as pictured in Figure 4.4. Due to the favourable phase-space in comparison to the $2\nu\beta\beta$ (c.f. Ref. [103]), the $0\nu\beta\beta$ mode was initially expected to be the dominant process with decay rates estimated to exceed the $2\nu\beta\beta$ rates by several orders of magnitude [96]. However, at these early times in history, the structure of the weak interactions was not fully understood. Despite tremendous experimental efforts and ever-increasing half-life sensitivities, the $0\nu\beta\beta$ has evaded detection so far, while, at the same time, $2\nu\beta\beta$ processes have been observed in multiple isotopes.

From today's standpoint and our theoretical understanding of the weak interaction and its $V-A$ structure it is easy to understand why we would expect the $0\nu\beta\beta$ to have much larger half-lives than its Standard Model $2\nu\beta\beta$ cousin. Without going into details on the theoretical aspects of $0\nu\beta\beta$ here, by looking at the Feynman diagram of the $0\nu\beta\beta$ induced via the exchange of light Majorana neutrinos in Figure 4.4 and remembering the left-handed nature of the weak interaction, we can see that the transition amplitude scales with the neutrino propagator as

$$\mathcal{A}_{0\nu\beta\beta} \propto P_L \sum_i U_{ei}^2 \frac{\not{q} + m_i}{q^2 - m_{\nu_i}^2} P_L = \sum_i U_{ei}^2 \frac{m_{\nu_i}}{q^2 - m_i^2} P_L. \tag{4.9}$$

Taking the limit of small neutrino masses $m_i \ll q$ we can see that the transition amplitude is proportional to the small neutrino masses

$$\mathcal{A}_{0\nu\beta\beta} \propto \sum_i U_{ei}^2 m_i = m_{\beta\beta}, \tag{4.10}$$

and the half-life is usually parameterized as

$$\left(T_{1/2}^{0\nu\beta\beta}\right)^{-1} = \left|\frac{m_{\beta\beta}}{m_e}\right|^2 G_{0\nu\beta\beta} \left|\mathcal{M}_{0\nu\beta\beta}\right|^2, \tag{4.11}$$

where $G_{0\nu\beta\beta} \sim \mathcal{O}(10^{-15}\,\mathrm{yr}^{-1})$ is the so-called phase space factor (PSF), $\mathcal{M}_{0\nu\beta\beta} \sim \mathcal{O}(1)$ is the so-called nuclear matrix element (NME) and m_e is, simply, the electron mass. We will go into more details of the $0\nu\beta\beta$ theory in the following sections. For now, we can use the expression in eq. (4.11) to provide a crude estimate of the expected $0\nu\beta\beta$ half-lives as

$$T_{1/2}^{0\nu\beta\beta} \simeq 2.6 \times 10^{26}\,\mathrm{yr} \left(\frac{1\,\mathrm{eV}}{|m_{\beta\beta}|}\right)^2 \left(\frac{10^{-15}\,\mathrm{yr}^{-1}}{G_{0\nu\beta\beta}}\right) \left(\frac{1}{|\mathcal{M}_{0\nu\beta\beta}|}\right)^2, \tag{4.12}$$

to see that we should, indeed, expect very large half-lives suppressed via the smallness of the neutrino masses. Note that the precise values for the NMEs and PSFs are isotope-dependent.

This suppression via the small neutrino masses is a direct consequence of the $V - A$ structure of the weak interaction which fixes the chirality projectors in such a way that the $\not{q}$ part of the neutrino propagator vanishes. In Table 4.1 we present a comprehensive list of $0\nu\beta\beta$ candidate isotopes that have been studied in experiments, together with the corresponding $2\nu\beta\beta$ half-lives and the strongest limits on the $0\nu\beta\beta$ half-life in each isotope up to date. A complete list of all naturally occurring $0\nu\beta\beta$ candidate isotopes is given in the appendix A.

4.1.3 The Experimental Program – Detecting $0\nu\beta\beta$

The key towards identifying a $0\nu\beta\beta$ event and disentangling it from the $2\nu\beta\beta$ background lies in a measurement of the combined kinetic energy carried by the emitted electrons. In a $2\nu\beta\beta$ event, four particles are emitted from the nucleus and the two neutrinos show up as missing energy resulting in a broad electron spectrum with a combined kinetic electron energy T smaller than the decay energy $T < Q$. In contrast, in a $0\nu\beta\beta$ event there are no neutrinos that could carry away any energy and, hence, the two emitted electrons carry all of the decay energy thereby resulting in a delta-peak spectrum with $T = Q$. The recoil energy of the nucleus is typically much smaller than the Q-value, due

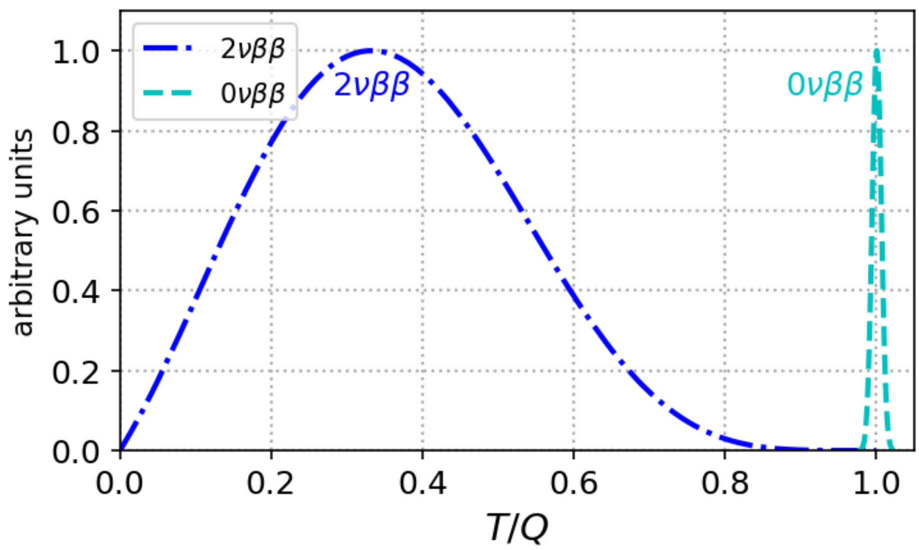

Figure 4.5: Summed electron spectra for the $2\nu\beta\beta$ [103] and $0\nu\beta\beta$. While the $2\nu\beta\beta$ results in a continuous spectrum, the $0\nu\beta\beta$ mode is a simple Gaussian peak at the end of the decay-spectrum with its width given by the experimental energy resolution. Both spectra are in arbitrary and unrelated units to showcase the qualitative behaviour.

to its large mass, and can be ignored in this context. In Figure 4.5 we show the summed electron spectra for both $2\nu\beta\beta$ and $0\nu\beta\beta$.

The experimental program dedicated towards the discovery of $0\nu\beta\beta$ covers various different approaches including high-purity germanium (HPGe) semiconductors [35, 125, 126], cryogenic bolometers [37, 110, 113, 127–129], single- and dual-phase time projection chambers (TPCs) [34, 130–132], organic and inorganic scintillators [38, 46, 133, 134], and tracking calorimeters [111, 135, 136]. Each approach comes with different advantages and disadvantages regarding scalability to maximize exposure, as well as energy resolution and purity of the source. For a comprehensive and recent overview of the experimental program, the interested reader is referred to Ref. [28].

4.1.4 β^+ and Electron Capture Modes

Besides the double-β^- decay we discussed so far, which is inherently characterized by the emission of two electrons and a corresponding increase of the nuclear charge by two units, there are additional decay processes that are connected to the double-β^- decay via crossing symmetry (See Figure 4.6). These are the double-positron emitting $2\nu\beta^+\beta^+$ decay as well as the double-electron capture 2νECEC, and the electron capture accompanied by a positron emission $2\nu\beta^+$EC. All of these decay modes are characterized

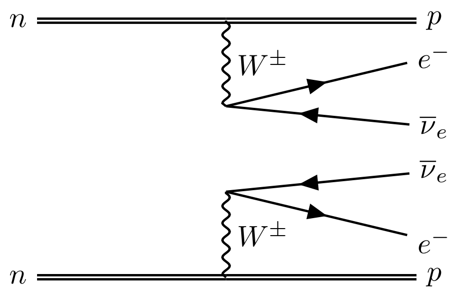

(a) $2\nu\beta^-\beta^-$

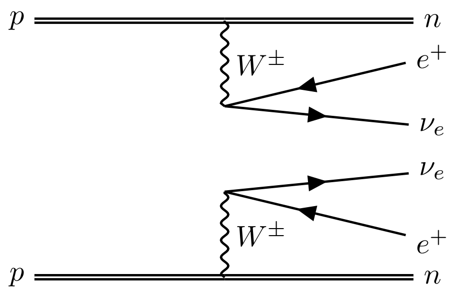

(b) $2\nu\beta^+\beta^+$

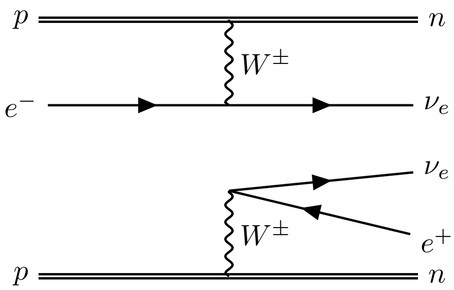

(c) $2\nu\beta^+$EC

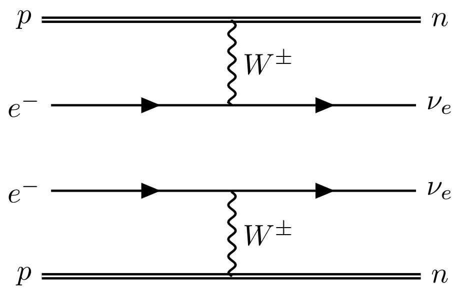

(d) 2νECEC

Figure 4.6: Diagrams of the different double beta decay modes. The standard double-β^- decay diagram is pictured in (a), while the β^+ and electron-capture modes are shown in (b)–(d). The diagrams are related via crossing symmetry.

by a decrease in the nuclear charge by two units

$$\begin{aligned}
&(A,Z) &&\longrightarrow (A,Z-2)+2e^+ + 2\nu_e, &&(2\nu\beta^+\beta^+),\\
&(A,Z)+e^- &&\longrightarrow (A,Z-2)+e^+ + 2\nu_e, &&(2\nu\beta^+\text{EC}),\\
&(A,Z)+2e^- &&\longrightarrow (A,Z-2)+2\nu_e, &&(2\nu\text{ECEC}).
\end{aligned} \tag{4.13}$$

Similar to the usual electron emitting $2\nu\beta\beta$ and $0\nu\beta\beta$ modes, each of these decay modes does have a neutrinoless counterpart that could be studied in dedicated experiments. However, each of these additional modes is phase-space suppressed when compared to the double-β^- mode, making them significantly less attractive from an experimental point of view. This can be understood by investigating the Q-values that are given by

$$\begin{aligned}
&Q(\beta^-\beta^-) = M_i - M_f, && Q(\beta^+\beta^+) = M_i - M_f + 4m_e, &&\\
&Q(\beta^+\text{EC}) = M_i - M_f + 2m_e, && Q(2\nu\text{ECEC}) = M_i - M_f, && Q(0\nu\text{ECEC}) \overset{!}{=} 0,
\end{aligned} \tag{4.14}$$

where $M_{i,f}$ are the masses of the initial- and final-state atoms. We can see that the emission of a positron is related to a suppression of the Q-value by two electron masses when comparing the initial- and final-state atoms. This fact strongly suppresses the corresponding PSFs compared to the standard $0\nu\beta\beta$ process in both the two-neutrino and neutrinoless decays [103, 137]. Therefore, we can expect significantly longer half-lives for the neutrinoless positron emitting β^+ decays. Nevertheless, measurements of the $2\nu\beta\beta$ half-life in positron emitting decays may provide additional data which can help to advance our understanding of the relevant nuclear structure models. Despite the tremendous experimental challenges, the recently proposed NuDoubt^{++} experiment [138] is aiming for a few-kg to ton-scale $2\nu\beta^+\beta^+$ and $0\nu\beta^+\beta^+$ experiment.

While this suppression is not present in the double electron capture, we face a different hurdle here when considering its neutrinoless variant. Looking at the double electron capture diagram in Figure 4.6(d), we can see that, with the removal of the emitted neutrinos, there are no particles that could carry away an excess decay energy, hence, requiring the initial and final state atoms to be of equal mass with $Q = 0$.

Considering that the different double beta decay diagrams are all related via crossing symmetry, we do not expect any enhancement of the β^+ modes from the particle-physics site, independently of the underlying LNV mechanism. In appendix A we provide a complete list of all naturally occurring candidate isotopes for the double β^+ and EC modes.

4.2 Particle Physics Models of $0\nu\beta\beta$

The most commonly studied mechanism of $0\nu\beta\beta$ is the LνEM, or mass mechanism[1], which is mediated via the exchange of light Majorana neutrinos as depicted in Figure 4.4. It is inherently connected to the existence of a non-zero effective Majorana mass for the electron neutrino flavor, with the transition amplitude being proportional to $m_{\beta\beta} = \sum_i U_{ei}^2 m_i$. As discussed in Chapter 2, because the generation of a Dirac neutrino mass term

$$\mathcal{L} \supset m_D \overline{\nu_L} \nu_R + \text{h.c.}, \tag{4.15}$$

requires the addition of gauge-singlet right-handed neutrino fields ν_R, one has to either impose an ad-hoc global lepton number symmetry or a global or gauged $B-L$ symmetry in order to forbid the Majorana mass for the right-handed neutrinos

$$\mathcal{L} \supset \frac{1}{2} m_R \overline{\nu_R} \nu_R^C + \text{h.c.}. \tag{4.16}$$

Consequently, LNV BSM models that aim to explain neutrino masses will, generally, describe the neutrino as a Majorana particle and therefore give rise to the LνEM of $0\nu\beta\beta$. However, the occurrence of Majorana neutrino masses in a given theory does not necessarily imply that the LνEM will be the dominant contribution to the $0\nu\beta\beta$. Instead, we may think of many other particle physics models that can contribute to the $0\nu\beta\beta$ transition amplitude [1] such as vector or scalar leptoquark scenarios [143], neutralino and gluino exchange mechanisms arising in R-parity breaking super symmetric models [141, 142, 144], double-charged scalars coupling to the W-bosons, or right-handed

[1] We will use these two terms interchangeably from here on. The term "*mass mechanism*" will mainly be used when we want to highlight the dependence of the LνEM on the Majorana neutrino mass.

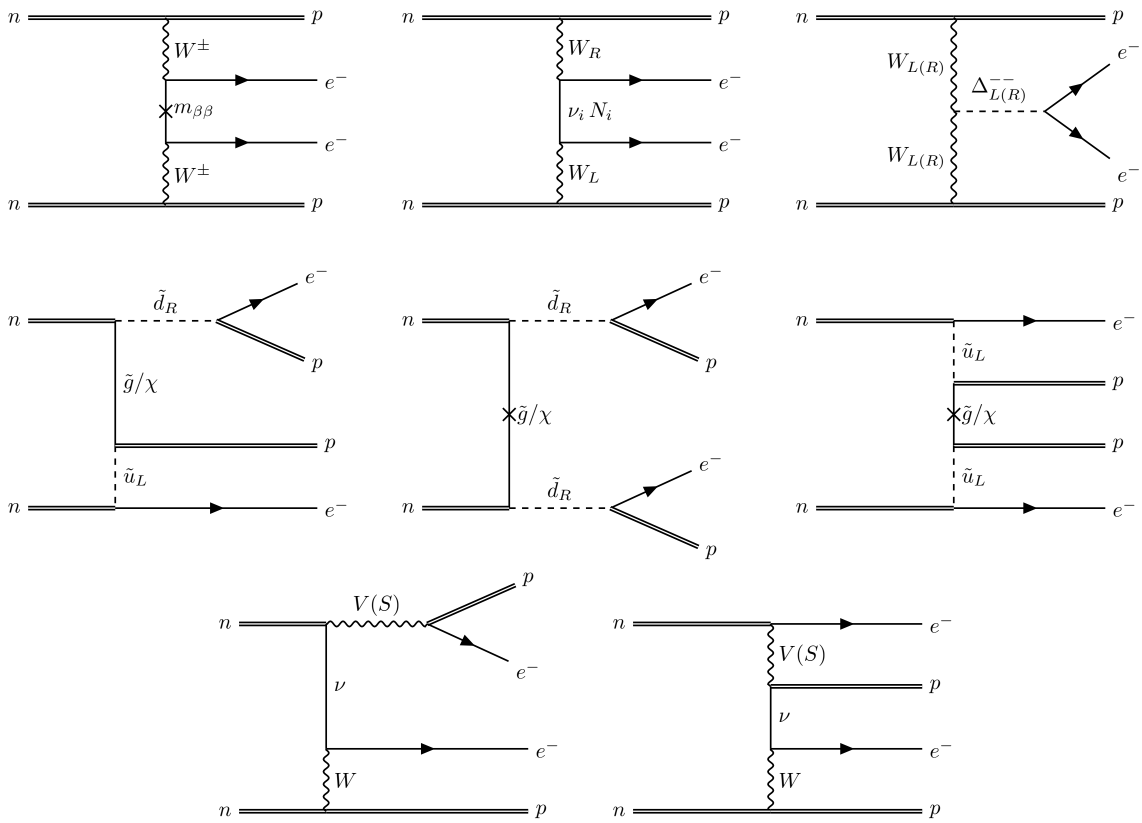

Figure 4.7: Selection of lepton-number-violating mechanisms of neutrinoless double beta decay arising in different BSM scenarios [1]. In the upper row, we present a selection of diagrams appearing in typical left-right symmetric theories which include right-handed W-bosons as well as double-charged scalars $\Delta^{--}_{L,R}$ and heavy neutrinos N [1, 139, 140]. The middle row shows a selection of $0\nu\beta\beta$ diagrams appearing in the R-parity breaking minimal supersymmetric Standard Model ($\not{R}_p$-MSSM) [1, 141, 142]. The $\not{R}_p$-MSSM diagrams are characterized by the exchange of neutralinos χ and gluinos $\tilde{g}$ as well as squarks $\tilde{d}, \tilde{u}$. In the last row, we present diagrams arising in models with scalar (S) and vector (V) leptoquarks [1, 143].

$SU(2)_R$ gauge bosons as they appear in left-right symmetric models [139, 140]. In Figure 4.7 we present a selection of different $0\nu\beta\beta$ diagrams arising in these kinds of LNV BSM models, showcasing the variety of mechanisms that may be the leading cause of a future $0\nu\beta\beta$ detection. The $0\nu\beta\beta$ mechanisms presented in Figure 4.7 represent only a small subset of the possible variations and combinations that are thinkable. Other mechanisms include models with composite neutrinos [145–147], Majoron-emitting models [148–150], spatial extra-dimensions [151, 152], or Standard Model extension with a modified gauge-structure [153, 154]. See Refs. [24, 25] and references therein for a more detailed discussion on the connection of various particle physics models and $0\nu\beta\beta$.

The large variety of possible $0\nu\beta\beta$ realizations from different particle physics models is a strong motivation for a model-independent approach to $0\nu\beta\beta$ via the application of EFTs.

4.3 Lepton Number Violation in the Standard Model EFT

In order to provide a model-independent approach to $0\nu\beta\beta$, let us move to effective field theories now.

The Standard Model is defined by its field content, symmetries, specifically, the symmetry under the local $SU(3)_C \times SU(2)_L \times U(1)_Y$ gauge group as well as invariance under Lorentz transformations, and the requirement of renormalizability. As we have discussed in Chapter 3, in order to study physics beyond the Standard Model in a model-independent way, we can promote the SM to an EFT, the so-called Standard Model EFT (SMEFT) [86], by dropping the requirement of renormalizability and systematically adding all Lorentz invariant terms that can be constructed out of the Standard Model's degrees of freedom while respecting the $SU(3)_C \times SU(2)_L \times U(1)_Y$ gauge structure. The idea of treating the Standard Model as an effective rather than a fundamental field theory was first brought forward by Steven Weinberg [155]. In the context of unresolved problems such as neutrino masses, dark matter [156, 157], or the unification of gravity with the Standard Model, it does indeed appear rather questionable to expect the Standard Model to be a fundamental theory of Nature. As we will see, by promoting the Standard Model to an EFT, we automatically introduce not only a Majorana mass for the neutrino but, indeed, many LNV operators of higher dimensions.

We may then utilize SMEFT, either, for a model-independent approach to $0\nu\beta\beta$ or to study the low-energy effects of some specific BSM model with new physics arising at some high energy scale $\Lambda \gg m_W$ by matching it onto SMEFT.

4.3.1 The SMEFT Operator Basis up to Dimension 9

Lepton number violation by two units ($\Delta L = 2$) in the SMEFT takes place only at odd (5, 7, 9, ...) operator dimensions [158]. On the particle physics level, the $0\nu\beta\beta$ process involves six external fermions, independently of the underlying mechanism. Hence, the "natural" dimension for the $0\nu\beta\beta$ amplitude is dimension 9 and we should include operators up to that dimension in our study. Let us now summarize all the relevant SMEFT operators:

At dimension 5 there exists only one operator that can be constructed out of the Standard Model's degrees of freedom obeying the $SU(3)_C \times SU(2)_L \times U(1)_Y$ gauge symmetry. This is the so-called Weinberg operator [159]

$$\mathcal{O}^{(5)}_{LH} = \epsilon_{ij}\epsilon_{kl}\left[\overline{L^C}_i L_k\right]\left[H_j H_l\right], \tag{4.17}$$

Class 1	$\psi^2 H^4$	Class 5	$\psi^4 D$
$\mathcal{O}^{(\mathbf{7})}_{\mathbf{LH}}$	$\epsilon_{ij}\epsilon_{mn}(L_i^T C L_m) H_j H_n (H^\dagger H)$	$\mathcal{O}^{(\mathbf{7})}_{\mathbf{LL\bar{d}uD1}}$	$\epsilon_{ij}(\bar{d}\gamma_\mu u)(L_i^T C (D^\mu L)_j)$
Class 2	$\psi^2 H^2 D^2$	Class 6	$\psi^4 H$
$\mathcal{O}^{(\mathbf{7})}_{\mathbf{LHD1}}$	$\epsilon_{ij}\epsilon_{mn}(L_i^T C (D_\mu L)_j) H_m (D^\mu H)_n$	$\mathcal{O}^{(7)}_{LL\bar{e}H}$	$\epsilon_{ij}\epsilon_{mn}(\bar{e}L_i)(L_j^T C L_m) H_n$
$\mathcal{O}^{(\mathbf{7})}_{\mathbf{LHD2}}$	$\epsilon_{im}\epsilon_{jn}(L_i^T C (D_\mu L)_j) H_m (D^\mu H)_n$	$\mathcal{O}^{(\mathbf{7})}_{\mathbf{LLQ\bar{d}H1}}$	$\epsilon_{ij}\epsilon_{mn}(\bar{d}L_i)(Q_j^T C L_m) H_n$
Class 3	$\psi^2 H^3 D$	$\mathcal{O}^{(\mathbf{7})}_{\mathbf{LLQ\bar{d}H2}}$	$\epsilon_{im}\epsilon_{jn}(\bar{d}L_i)(Q_j^T C L_m) H_n$
$\mathcal{O}^{(\mathbf{7})}_{\mathbf{LHDe}}$	$\epsilon_{ij}\epsilon_{mn}(L_i^T C \gamma_\mu e) H_j H_m (D^\mu H)_n$	$\mathcal{O}^{(\mathbf{7})}_{\mathbf{LL\bar{Q}uH}}$	$\epsilon_{ij}(\overline{Q}_m u)(L_m^T C L_i) H_j$
Class 4	$\psi^2 H^2 X$	$\mathcal{O}^{(\mathbf{7})}_{\mathbf{Leu\bar{d}H}}$	$\epsilon_{ij}(L_i^T C \gamma_\mu e)(\bar{d}\gamma^\mu u) H_j$
$\mathcal{O}^{(7)}_{LHB}$	$\epsilon_{ij}\epsilon_{mn} g' (L_i^T C \sigma^{\mu\nu} L_m) H_j H_n B_{\mu\nu}$		
$\mathcal{O}^{(\mathbf{7})}_{\mathbf{LHW}}$	$\epsilon_{ij}(\epsilon\tau^I)_{mn} g_2 (L_i^T C \sigma^{\mu\nu} L_m) H_j H_n W^I_{\mu\nu}$		

Table 4.2: Lepton-number-violating operators at SMEFT dimension 7. All operators that contribute to $0\nu\beta\beta$ at tree-level are marked as **bold**. All operators but $\mathcal{O}^{(7)}_{LHB}$ and $\mathcal{O}^{(7)}_{LL\bar{e}H}$ fall into this category. Table taken and adapted from Ref. [44].

which, after electroweak symmetry breaking (EWSB), generates a Majorana mass for the left-handed neutrinos

$$m_\nu = -v^2 C^{(5)}_{LH}. \tag{4.18}$$

In the above equations the Latin indices i, j, k, l represent $SU(2)$ indices and we have suppressed generational indices that would represent the three generations of Standard Model fermions. Note that we, generally, define the SMEFT Wilson coefficients $C_i^{(d)}$ to be dimensionful in this work.

The SMEFT operator basis at dimension 7 was first introduced in Ref. [85]. It contains 12 independent LNV $\Delta L = 2$ operators that we have listed in Table 4.2. In total, 10 out of the 12 dimension-7 operators contribute to the $0\nu\beta\beta$ amplitude at tree-level [2, 44]. The remaining operators, namely $\mathcal{O}^{(7)}_{LHB}$ and $\mathcal{O}^{(7)}_{LLeH}$, can contribute at the 1-loop-level [160, 161].

A complete basis for the SMEFT dimension-9 operators was first derived in Refs. [59, 88] and we will use the basis as presented in Ref. [59]. With growing dimension, the number of operators increases such that there are in total 192 $\Delta L = 2$ operators at dimension 9. In order to reduce the complexity, we will only consider those dimension-9 operators that generate a tree-level contribution to short-range $0\nu\beta\beta$ diagrams at energies below EWSB. We will cover this in more detail in the following section. With this restriction one finds that there are 26 relevant $\Delta L = 2$ operators at dimension 9 [2, 88]. We have listed them in Table 4.3. As only the first generation of quarks (u, d) and leptons (e, ν_e) is relevant for $0\nu\beta\beta$, we will be working in a one-generation approximation. That is, for SMEFT operators of dimension 5 and higher, we only consider the first generation of fermions while setting all Wilson coefficients that involve any of the second or third generation of fermions to zero.

Class 1	ψ^6	Class 3	$\psi^4 H^2 D$
$\mathcal{O}^{(9)}_{ddueue}$	$[\overline{d^\alpha} d^{C\beta}]\,[\overline{u^{C\alpha}} e]\,[\overline{u^{C\beta}} e]$	$\mathcal{O}^{(9)}_{deueH^2D}$	$\epsilon_{ij}\,[\overline{d}\gamma^\mu e]\,[\overline{u^C} e]\,[H_i(iD_\mu H)_j]$
$\mathcal{O}^{(9)}_{dQdueL1}$	$\epsilon_{ij}\,[\overline{d} Q_i]\,[\overline{d}\gamma^\mu u]\,[\overline{e^C}\gamma_\mu L_j]$	$\mathcal{O}^{(9)}_{dQLeH^2D2}$	$\epsilon_{ik}\epsilon_{jl}\,[\overline{d} Q_i]\,[\overline{L^C_j}\gamma^\mu e]\,[H_k(iD_\mu H)_l]$
$\mathcal{O}^{(9)}_{dQdueL2}$	$\epsilon_{ij}\,[\overline{d^\alpha} Q^\beta_i]\,[\overline{d^\beta}\gamma^\mu u^\alpha]\,[\overline{e^C}\gamma_\mu L_j]$	$\mathcal{O}^{(9)}_{dLQeH^2D1}$	$\epsilon_{ik}\epsilon_{jl}\,[\overline{d} L_i]\,[\overline{Q^C_j}\gamma^\mu e]\,[(iD_\mu H)_k H_l]$
$\mathcal{O}^{(9)}_{QudueL1}$	$[\overline{Q} u]\,[\overline{d}\gamma^\mu u]\,[\overline{e^C}\gamma_\mu L]$	$\mathcal{O}^{(9)}_{dLuLH^2D2}$	$\epsilon_{ik}\epsilon_{jl}\,[\overline{d} L_i]\,[\overline{u^C}\gamma_\mu L_j]\,[\tilde{H}_k(iD^\mu H)_l]$
$\mathcal{O}^{(9)}_{QudueL2}$	$[\overline{Q^\alpha} u^\beta]\,[\overline{d^\beta}\gamma^\mu u^\alpha]\,[\overline{e^C}\gamma_\mu L]$	$\mathcal{O}^{(9)}_{duLLH^2D}$	$\epsilon_{ik}\epsilon_{jl}\,[\overline{d}\gamma_\mu u]\,[\overline{L^C}_i(iD^\mu L)_j]\,[\tilde{H}_k H_l]$
$\mathcal{O}^{(9)}_{dQdQLL1}$	$\epsilon_{ik}\epsilon_{jl}\,[\overline{d} Q_i]\,[\overline{d}\gamma^\mu Q_j]\,[\overline{L^C_k}\gamma_\mu L_l]$	$\mathcal{O}^{(9)}_{deQLH^2D}$	$\epsilon_{ik}\epsilon_{jl}\,[\overline{d}\gamma^\mu e]\,[\overline{Q^C_i}(iD_\mu L)_j]\,[H_k H_l]$
$\mathcal{O}^{(9)}_{dQdQLL2}$	$\epsilon_{ik}\epsilon_{jl}\,[\overline{d^\alpha} Q^\beta_i]\,[\overline{d^\beta}\gamma^\mu Q^\alpha_j]\,[\overline{L^C_k}\gamma_\mu L_l]$	$\mathcal{O}^{(9)}_{QueLH^2D2}$	$\epsilon_{jk}\,[\overline{Q}_i u]\,[\overline{u^C}\gamma^\mu L_j]\,[H_i(iD_\mu H)_k]$
$\mathcal{O}^{(9)}_{dQQuLL1}$	$\epsilon_{ij}\,[\overline{d} Q_i]\,[\overline{Q} u]\,[\overline{L^C} L_j]$	$\mathcal{O}^{(9)}_{QeuLH^2D2}$	$\delta_{ik}\epsilon_{jl}\,[\overline{Q}_i e]\,[\overline{u^C}\gamma^\mu L_j]\,[H_k(iD_\mu H)_l]$
$\mathcal{O}^{(9)}_{dQQuLL2}$	$\epsilon_{ij}\,[\overline{d^\alpha} Q^\beta_i]\,[\overline{Q^\beta} u^\alpha]\,[\overline{L^C} L_j]$	$\mathcal{O}^{(9)}_{QLQLH^2D2}$	$\epsilon_{ik}\epsilon_{jl}\,[\overline{Q}\gamma^\mu L]\,[\overline{Q^C_i}\gamma^\mu L_j]\,[H_k(iD_\mu H)_l]$
$\mathcal{O}^{(9)}_{QuQuLL1}$	$[\overline{Q}_i u]\,[\overline{Q}_j u]\,[\overline{L^C_i} L_j]$	$\mathcal{O}^{(9)}_{QLQLH^2D5}$	$\epsilon_{ik}\epsilon_{jl}\,[\overline{Q}\gamma^\mu L_i]\,[\overline{Q^C_j}\gamma^\mu L]\,[(iD_\mu H)_k H_l]$
$\mathcal{O}^{(9)}_{QuQuLL2}$	$[\overline{Q^\alpha_i} u^\beta]\,[\overline{Q^\beta_j} u^\alpha]\,[\overline{L^C_i} L_j]$	$\mathcal{O}^{(9)}_{QQLLH^2D2}$	$\epsilon_{ik}\epsilon_{jl}\,[\overline{Q}\gamma^\mu Q_i]\,[\overline{L^C}(iD_\mu L)_j]\,[H_k H_l]$
Class 2	$\psi^2 H^4 D^2$	Class 4	$\psi^2 H^4 W$
$\mathcal{O}^{(9)}_{eeH^4D^2}$	$\epsilon_{ij}\epsilon_{kl}\,[\overline{e^C} e]\,[H_i(D_\mu H)_j]\,[H_k(D^\mu H)_l]$	$\mathcal{O}^{(9)}_{LLH^4W1}$	$\epsilon_{ij}(\epsilon\tau^I)_{kl} g_2\,[\overline{L^C_i}\sigma^{\mu\nu} L_k]\,[H_j H_l] W^I_{\mu\nu}\,[H^\dagger H]$
$\mathcal{O}^{(9)}_{LLH^4D^23}$	$\epsilon_{ik}\epsilon_{jl}\,[(\overline{D_\mu L^C})_i (D^\mu L)_j]\,[H_k H_l]\,[H^\dagger H]$		
$\mathcal{O}^{(9)}_{LLH^4D^24}$	$\epsilon_{ik}\epsilon_{jl}\,[\overline{L^C}_i (D^\mu L)_j]\,[(D_\mu H)_k H_l]\,[H^\dagger H]$		

Table 4.3: Lepton-number-violating $\Delta L = 2$ operators at SMEFT dimension 9. Here, in order to limit the complexity, we only show those operators that contribute to short-range $0\nu\beta\beta$ diagrams below EWSB.

4.4 Lepton Number Violation Below Electroweak Symmetry Breaking

After EWSB, the Standard Models $SU(3)_C \times SU(2)_L \times U(1)_Y$ symmetry group is spontaneously broken to the subgroup $SU(3)_C \times U(1)_{\text{EM}}$ by the non-zero vacuum expectation value of the Higgs doublet [11]

$$\langle H \rangle = \frac{1}{\sqrt{2}} \begin{pmatrix} 0 \\ v \end{pmatrix}, \qquad v \simeq 246\,\text{GeV}. \tag{4.19}$$

At energies below the mass of the W-Boson, $E \lesssim m_W$, it is convenient to introduce LEFT as a low-energy EFT [89] by dropping all particles heavier than the mass of the W-boson (i.e., we drop the W, Z and H bosons as well as the top quark t) and constructing all operators in agreement with the low-energy $SU(3)_C \times U(1)_{\text{EM}}$ symmetry that can be built out of the remaining Standard Model degrees of freedom. As with any EFT, we can utilize LEFT to simplify calculations by integrating out the heavy Standard Model fields from SMEFT. The operators and Wilson coefficients obtained in this way replicate the low-energy behaviour of SMEFT. Alternatively, we may treat LEFT as an independent EFT by keeping all Wilson coefficients as free parameters that can be constrained from experiments. In this way, one can study new physics beyond the Standard Model that may not be fully captured by the SMEFT. We will utilize both of these approaches in

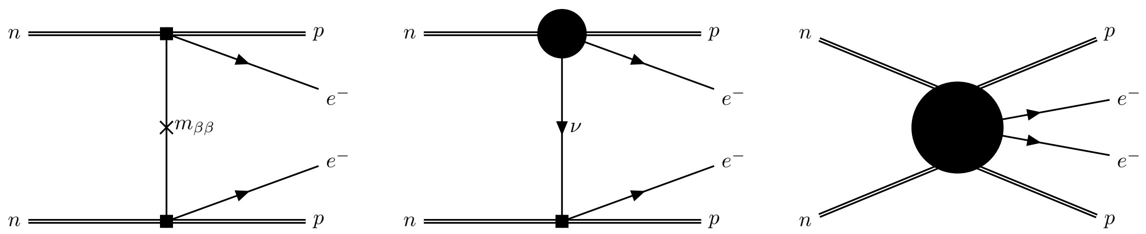

Figure 4.8: Classification of $0\nu\beta\beta$ Feynman diagrams at LEFT level. One may identify three different types of diagrams. These are the usual light neutrino-exchange or mass mechanism (left), long-range mechanisms that include a neutrino exchange and a lepton-number-violating 4-fermion interaction (middle), as well short-range mechanisms based on lepton-number-violating 6-fermion interactions without a neutrino exchange. Here, we represent lepton-number-violating 4- and 6-fermion interactions via black circles, while the standard weak interaction is represented by a black square.

this work.

4.4.1 The LEFT Operator Basis up to Dimension 9

The full operator basis of LEFT up to dimension 6 has been constructed in Ref. [89]. It contains 16 LNV $\Delta L = 2$ operators displayed in Table 4.4, ten of which can contribute to $0\nu\beta\beta$ at tree-level. These are the Majorana neutrino mass operator $\mathcal{O}_\nu^{(3)}$ as well as the charged-current semi-leptonic dimension-6 $\Delta L = 2$ operators $\mathcal{O}^{(6)}_{SL,SR,VL,VR,T}$. Additionally, we will see that also the scalar neutral-current semi-leptonic operators $\mathcal{O}^{(6)}_{SL,SR,\nu u,\nu d}$ contribute to $0\nu\beta\beta$ at tree-level. This feature has been ignored in most of the existing literature, including the original formulation of the EFT approach used in this work [44, 45], and we will discuss it in more detail in Section 4.6.

At dimension 7 there are 15 additional $\Delta L = 2$ operators [91], with four operators generating a tree-level contribution to $0\nu\beta\beta$, summarized in the upper part of Table 4.5. However, as we will see, only two of these operators, namely $\mathcal{O}^{(7)}_{VL,VR}$, are actually relevant. Finally, at dimension 9, LEFT includes 24 different 6-fermion $\Delta L = 2$ operators that contribute to short-range $0\nu\beta\beta$ mechanisms [45]. These are represented in the lower part of Table 4.5.

Based on the various LNV LEFT operators listed in Tables 4.4 and 4.5, we can identify three different types of $0\nu\beta\beta$ mechanisms via their respective topology of the corresponding Feynman diagrams as displayed in Figure 4.8. These are classified as the usual LνEM (or mass mechanism) with lepton number violation being caused by the Majorana nature of the neutrino, other long-range mechanisms that initiate a $0\nu\beta\beta$ via a LNV 4-fermion $qq\nu e$ interaction while still exchanging a neutrino, and the so-called short-range mechanisms which represent 6-fermion $qqqqee$ contact interactions without any neutrino exchange.

Dimension 3		Dimension 5	
Class 1	L	Class 1	LX
$\mathcal{O}_\nu^{(3)}$	$\overline{\nu_L^C}\nu_L$	$\mathcal{O}_{\nu\gamma}^{(5)}$	$\overline{\nu_L}\sigma^{\mu\nu}\nu_L^C F_{\mu\nu}$

Dimension 6			
Class 1	CC – RR	Class 2	CC – RL
$\mathcal{O}_{SR}^{(6)}$	$\left[\overline{e_L}\nu_L^C\right]\left[\overline{u_L}d_R\right]$	$\mathcal{O}_{SL}^{(6)}$	$\left[\overline{e_L}\nu_L^C\right]\left[\overline{u_R}d_L\right]$
$\mathcal{O}_{VR}^{(6)}$	$\left[\overline{e_R}\gamma^\mu\nu_L^C\right]\left[\overline{u_R}\gamma_\mu d_R\right]$	$\mathcal{O}_{VL}^{(6)}$	$\left[\overline{e_R}\gamma^\mu\nu_L^C\right]\left[\overline{u_L}\gamma_\mu d_L\right]$
$\mathcal{O}_{T}^{(6)}$	$\left[\overline{e_L}\sigma^{\mu\nu}\nu_L^C\right]\left[\overline{u_L}\sigma_{\mu\nu}d_R\right]$		
Class 3	NC – RR	Class 4	NC – RL
$\mathcal{O}_{SR,\nu e}^{(6)}$	$\left[\overline{\nu_L}\nu_L^C\right]\left[\overline{e_L}e_R\right]$	$\mathcal{O}_{SL,\nu e}^{(6)}$	$\left[\overline{\nu_L}\nu_L^C\right]\left[\overline{e_R}e_L\right]$
$\mathcal{O}_{SR,\nu u}^{(6)}$	$\left[\overline{\nu_L}\nu_L^C\right]\left[\overline{u_L}u_R\right]$	$\mathcal{O}_{SL,\nu u}^{(6)}$	$\left[\overline{\nu_L}\nu_L^C\right]\left[\overline{u_R}u_L\right]$
$\mathcal{O}_{SR,\nu d}^{(6)}$	$\left[\overline{\nu_L}\nu_L^C\right]\left[\overline{d_L}d_R\right]$	$\mathcal{O}_{SL,\nu d}^{(6)}$	$\left[\overline{\nu_L}\nu_L^C\right]\left[\overline{d_R}d_L\right]$
$\mathcal{O}_{T,\nu e}^{(6)}$	$\left[\overline{\nu_L}\sigma^{\mu\nu}\nu_L^C\right]\left[\overline{e_L}\sigma_{\mu\nu}e_R\right]$		
$\mathcal{O}_{T,\nu u}^{(6)}$	$\left[\overline{\nu_L}\sigma^{\mu\nu}\nu_L^C\right]\left[\overline{u_L}\sigma_{\mu\nu}u_R\right]$		
$\mathcal{O}_{T,\nu d}^{(6)}$	$\left[\overline{\nu_L}\sigma^{\mu\nu}\nu_L^C\right]\left[\overline{d_L}\sigma_{\mu\nu}d_R\right]$		

Table 4.4: Lepton-number-violating $\Delta L = 2$ operators in LEFT at dimensions 3, 5, and 6. We choose to define the operator basis as the complex conjugate of Ref. [89] in order to comply with the definitions of Refs. [44, 45] used to derive the $0\nu\beta\beta$ rates. We provide the complete list for both charged-current (CC) and neutral-current (NC) 4-fermion operators allowing us to extend the Framework of Refs. [44, 45] towards LNV NC operators. However, not all of the NC operators contribute at tree-level to $0\nu\beta\beta$. The same is true for the LNV dimension-5 operator which does not contribute at tree-level. For the CC operators, we used the naming convention of Refs. [44, 45] which were also used within ν`DoBe`.

Ignoring neutral-current operators for now, the relevant LEFT Lagrangians for the LνEM and long-range mechanisms of $0\nu\beta\beta$ are given by [44, 45]

$$\mathcal{L}_{\Delta L=2}^{(3)} = m_{ij}\overline{\nu_{L,i}^C}\nu_{L,j}, \tag{4.20}$$

describing the neutrino mass term at dimension 3, the charged-current scalar, tensor and vector interactions

$$\begin{aligned}\mathcal{L}_{\Delta L=2}^{(6)} = \frac{1}{v^2}\Big[& C_{\mathrm{VL}}^{(6)}\left(\overline{u_L}\gamma^\mu d_L\right)\left(\overline{e_R}\gamma_\mu\nu_L^c\right) + C_{\mathrm{VR}}^{(6)}\left(\overline{u_R}\gamma^\mu d_R\right)\left(\overline{e_R}\gamma_\mu\nu_L^c\right) \\ & + C_{\mathrm{SL}}^{(6)}\left(\overline{u_R}d_L\right)\left(\overline{e_L}\nu_L^c\right) + C_{\mathrm{SR}}^{(6)}\left(\overline{u_L}d_R\right)\left(\overline{e_L}\nu_L^c\right) \\ & + C_{\mathrm{T}}^{(6)}\left(\overline{u_L}\sigma^{\mu\nu}d_R\right)\left(\overline{e_L}\sigma_{\mu\nu}\nu_L^c\right)\Big] + \text{h.c.},\end{aligned} \tag{4.21}$$

at dimension 6, as well as the charged-current dimension-7 vector interactions

$$\mathcal{L}^{(7)}_{\Delta L=2} = \frac{1}{v^3}\left[C^{(7)}_{\mathrm{VL}}\left(\overline{u_L}\gamma^\mu d_L\right)\left(\overline{e_L}\overleftrightarrow{\partial}_\mu \nu^c_L\right) + C^{(7)}_{\mathrm{VR}}\left(\overline{u_R}\gamma^\mu d_R\right)\left(\overline{e_L}\overleftrightarrow{\partial}_\mu \nu^c_L\right)\right] + \text{h.c.}. \tag{4.22}$$

Note that we did not include the two dimension-7 operators $\mathcal{O}^{(7)}_{VL2,VR2}$ which include a derivative term acting on the quark fields. In the initial formulation of this approach [44, 45] they were excluded because no SMEFT operator up to dimension 7 matches onto either of the two operators. However, when including SMEFT dimension-9 operators, $\mathcal{O}^{(9)}_{deQLH^2D}$ does, indeed, generate a contribution to $\mathcal{O}^{(7)}_{VR2}$. Nevertheless, both $\mathcal{O}^{(7)}_{VL2,VR2}$ are significantly suppressed in the chiral power-counting [2] and therefore we will not include them in the calculation of $0\nu\beta\beta$ half-lives. See appendix B.3 for a more detailed discussion on this.

Finally, the relevant short-range dimension-9 terms can be written as

$$\mathcal{L}^{(9)}_{\Delta L=2} = \frac{1}{v^5}\sum_i\left[\left(C^{(9)}_{i,R}\left(\overline{e_R}e^c_R\right) + C^{(9)}_{i,L}\left(\overline{e_L}e^c_L\right)\right)\mathcal{O}_i + C^{(9)}_i\left(\overline{e}\gamma_\mu\gamma_5 e^c\right)\mathcal{O}^\mu_i\right], \tag{4.23}$$

where the operators $\mathcal{O}_i$ represent the baryonic parts of the corresponding dimension-9 operators listed in Table 4.5

$$\mathcal{O}^{(9)}_{i,L,R} = \mathcal{O}_i(\overline{e_{L,R}}e^C_{L,R}), i\in[1,5] \qquad \mathcal{O}^{(9)}_i = \mathcal{O}^\mu_i(\overline{e}\gamma_5\gamma_\mu e^C), i\in[6,9], \tag{4.24}$$

i.e., [1, 45]

$$\begin{aligned}
\mathcal{O}_1 &= \left(\overline{u_L}^\alpha\gamma_\mu d^\alpha_L\right)\left(\overline{u_L}^\beta\gamma^\mu d^\beta_L\right), & \mathcal{O}_1{}' &= \left(\overline{u_R}^\alpha\gamma_\mu d^\alpha_R\right)\left(\overline{u_R}^\beta\gamma^\mu d^\beta_R\right),\\
\mathcal{O}_2 &= \left(\overline{u_R}^\alpha d^\alpha_L\right)\left(\overline{u_R}^\beta d^\beta_L\right), & \mathcal{O}_2{}' &= \left(\overline{u_L}^\alpha d^\alpha_R\right)\left(\overline{u_L}^\beta d^\beta_R\right),\\
\mathcal{O}_3 &= \left(\overline{u_R}^\alpha d^\beta_L\right)\left(\overline{u_R}^\beta d^\alpha_L\right), & \mathcal{O}_3{}' &= \left(\overline{u_L}^\alpha d^\beta_R\right)\left(\overline{u_L}^\beta d^\alpha_R\right),\\
\mathcal{O}_4 &= \left(\overline{u_L}^\alpha\gamma_\mu d^\alpha_L\right)\left(\overline{u_R}^\beta\gamma^\mu d^\beta_R\right), & &\\
\mathcal{O}_5 &= \left(\overline{u_L}^\alpha\gamma_\mu d^\beta_L\right)\left(\overline{u_R}^\beta\gamma^\mu d^\alpha_R\right), & &\\
\\
\mathcal{O}^\mu_6 &= \left(\overline{u_L}\gamma^\mu d_L\right)\left(\overline{u_L}d_R\right), & \mathcal{O}^{\mu\prime}_6 &= \left(\overline{u_R}\gamma^\mu d_R\right)\left(\overline{u_R}d_L\right),\\
\mathcal{O}^\mu_7 &= \left(\overline{u_L}t^A\gamma^\mu d_L\right)\left(\overline{u_L}t^A d_R\right), & \mathcal{O}^{\mu\prime}_7 &= \left(\overline{u_R}t^A\gamma^\mu d_R\right)\left(\overline{u_R}t^A d_L\right),\\
\mathcal{O}^\mu_8 &= \left(\overline{u_L}\gamma^\mu d_L\right)\left(\overline{u_R}d_L\right), & \mathcal{O}^{\mu\prime}_8 &= \left(\overline{u_R}\gamma^\mu d_R\right)\left(\overline{u_L}d_R\right),\\
\mathcal{O}^\mu_9 &= \left(\overline{u_L}t^A\gamma^\mu d_L\right)\left(\overline{u_R}t^A d_L\right), & \mathcal{O}^{\mu\prime}_9 &= \left(\overline{u_R}t^A\gamma^\mu d_R\right)\left(\overline{u_L}t^A d_R\right).
\end{aligned} \tag{4.25}$$

Here, the $SU(3)$ generators $t^A, A\in[1,8]$ are related to the 8 3×3 Gell-Mann matrices λ^A via $t^A = \lambda^A/2$.

4.4.2 Matching SMEFT to LEFT

When transitioning from energies above the scale of EWSB to lower energies, we need to match the relevant SMEFT operators to the corresponding LEFT operators. This

Dimension 7			
Class 1	$\Psi^4\partial$		
$\mathcal{O}^{(7)}_{VL}$	$\left[\overline{e_L}\overleftrightarrow{\partial}_\mu \nu_L^C\right]\left[\overline{u_L}\gamma^\mu d_L\right]$	$\mathcal{O}^{(7)}_{VL2}$	$\left[\overline{e_L}\gamma^\mu \nu_L^C\right]\left[\overline{u_R}\overleftrightarrow{\partial}_\mu d_L\right]$
$\mathcal{O}^{(7)}_{VR}$	$\left[\overline{e_L}\overleftrightarrow{\partial}_\mu \nu_L^C\right]\left[\overline{u_R}\gamma^\mu d_R\right]$	$\mathcal{O}^{(7)}_{VR2}$	$\left[\overline{e_L}\gamma^\mu \nu_L^C\right]\left[\overline{u_L}\overleftrightarrow{\partial}_\mu d_R\right]$

Dimension 9			
Class 1	Scalar Ψ^6	Class 2	Vector Ψ^6
$\mathcal{O}^{(9)}_{1L}$	$\left[\overline{u_L}\gamma_\mu d_L\right]\left[\overline{u_L}\gamma^\mu d_L\right]\left[\overline{e_L}e_L^C\right]$	$\mathcal{O}^{(9)}_{6}$	$\left[\overline{u_L}\gamma_\mu d_L\right]\left[\overline{u_L}d_R\right]\left[\overline{e}\gamma^\mu\gamma_5 e^C\right]$
$\mathcal{O}^{(9)}_{1R}$	$\left[\overline{u_L}\gamma_\mu d_L\right]\left[\overline{u_L}\gamma^\mu d_L\right]\left[\overline{e_R}e_R^C\right]$	$\mathcal{O}^{(9)\prime}_{6}$	$\left[\overline{u_R}\gamma_\mu d_R\right]\left[\overline{u_R}d_L\right]\left[\overline{e}\gamma^\mu\gamma_5 e^C\right]$
$\mathcal{O}^{(9)\prime}_{1L}$	$\left[\overline{u_R}\gamma_\mu d_R\right]\left[\overline{u_R}\gamma^\mu d_R\right]\left[\overline{e_L}e_L^C\right]$	$\mathcal{O}^{(9)}_{7}$	$\left[\overline{u_L}t^A\gamma_\mu d_L\right]\left[\overline{u_L}t^A d_R\right]\left[\overline{e}\gamma^\mu\gamma_5 e^C\right]$
$\mathcal{O}^{(9)\prime}_{1R}$	$\left[\overline{u_R}\gamma_\mu d_R\right]\left[\overline{u_R}\gamma^\mu d_R\right]\left[\overline{e_R}e_R^C\right]$	$\mathcal{O}^{(9)\prime}_{7}$	$\left[\overline{u_R}t^A\gamma_\mu d_R\right]\left[\overline{u_R}t^A d_L\right]\left[\overline{e}\gamma^\mu\gamma_5 e^C\right]$
$\mathcal{O}^{(9)}_{2L}$	$\left[\overline{u_R}d_L\right]\left[\overline{u_R}d_L\right]\left[\overline{e_L}e_R^C\right]$	$\mathcal{O}^{(9)}_{8}$	$\left[\overline{u_L}\gamma_\mu d_L\right]\left[\overline{u_R}d_L\right]\left[\overline{e}\gamma^\mu\gamma_5 e^C\right]$
$\mathcal{O}^{(9)}_{2R}$	$\left[\overline{u_R}d_L\right]\left[\overline{u_R}d_L\right]\left[\overline{e_R}e_R^C\right]$	$\mathcal{O}^{(9)\prime}_{8}$	$\left[\overline{u_R}\gamma_\mu d_R\right]\left[\overline{u_L}d_R\right]\left[\overline{e}\gamma^\mu\gamma_5 e^C\right]$
$\mathcal{O}^{(9)\prime}_{2L}$	$\left[\overline{u_L}d_R\right]\left[\overline{u_L}d_R\right]\left[\overline{e_L}e_L^C\right]$	$\mathcal{O}^{(9)}_{9}$	$\left[\overline{u_L}t^A\gamma_\mu d_L\right]\left[\overline{u_R}t^A d_L\right]\left[\overline{e}\gamma^\mu\gamma_5 e^C\right]$
$\mathcal{O}^{(9)\prime}_{2R}$	$\left[\overline{u_L}d_R\right]\left[\overline{u_L}d_R\right]\left[\overline{e_R}e_R^C\right]$	$\mathcal{O}^{(9)\prime}_{9}$	$\left[\overline{u_R}t^A\gamma_\mu d_R\right]\left[\overline{u_L}t^A d_R\right]\left[\overline{e}\gamma^\mu\gamma_5 e^C\right]$
$\mathcal{O}^{(9)}_{3L}$	$\left[\overline{u_R}^\alpha d_L^\beta\right]\left[\overline{u_R}^\beta d_L^\alpha\right]\left[\overline{e_L}e_L^C\right]$		
$\mathcal{O}^{(9)}_{3R}$	$\left[\overline{u_R}^\alpha d_L^\beta\right]\left[\overline{u_R}^\beta d_L^\alpha\right]\left[\overline{e_R}e_R^C\right]$		
$\mathcal{O}^{(9)\prime}_{3L}$	$\left[\overline{u_L}^\alpha d_R^\beta\right]\left[\overline{u_L}^\beta d_R^\alpha\right]\left[\overline{e_L}e_L^C\right]$		
$\mathcal{O}^{(9)\prime}_{3R}$	$\left[\overline{u_L}^\alpha d_R^\beta\right]\left[\overline{u_L}^\beta d_R^\alpha\right]\left[\overline{e_R}e_R^C\right]$		
$\mathcal{O}^{(9)}_{4L}$	$\left[\overline{u_L}\gamma^\mu d_L\right]\left[\overline{u_R}\gamma_\mu d_R\right]\left[\overline{e_L}e_L^C\right]$		
$\mathcal{O}^{(9)}_{4R}$	$\left[\overline{u_L}\gamma^\mu d_L\right]\left[\overline{u_R}\gamma_\mu d_R\right]\left[\overline{e_R}e_R^C\right]$		
$\mathcal{O}^{(9)}_{5L}$	$\left[\overline{u_L}^\alpha\gamma^\mu d_L^\beta\right]\left[\overline{u_R}^\beta\gamma_\mu d_R^\alpha\right]\left[\overline{e_L}e_L^C\right]$		
$\mathcal{O}^{(9)}_{5R}$	$\left[\overline{u_L}^\alpha\gamma^\mu d_L^\beta\right]\left[\overline{u_R}^\beta\gamma_\mu d_R^\alpha\right]\left[\overline{e_R}e_R^C\right]$		

Table 4.5: Lepton-number-violating $\Delta L = 2$ operators at dimensions 7 and 9 relevant to $0\nu\beta\beta$ in LEFT [2, 45]. The primed operators $\mathcal{O}'$ relate to the unprimed $\mathcal{O}$ via a parity flip in the quark bilinears.

matching procedure includes several steps. As described in Chapter 3, we first need to integrate out the heavy W, H and top-quark fields that cannot be produced on-shell at LEFT scales. Because we will only consider the tree-level matching, this can simply be achieved by solving the equations of motion for the heavy fields as we have shown in Chapter 3. Additionally, several steps are required in order to match the SMEFT operators not onto any but precisely onto the pre-defined basis of LEFT operators. These steps include Fierz identities [162, 163], integration by parts, field redefinitions [164, 165] as well as basic algebraic tools. An explicit example matching calculation is provided in appendix B.

4.4.2.1 Fierz Identities

Fierz identities relate fermion quadrilinears of different Lorentz structures via a set of linear equations. We define the scalar (S), vector (V), tensor (T), axial-vector (A) and pseudo-scalar (P) fermion quadrilinears

$$\begin{aligned} e_S(1234) &= \left[\overline{\Psi}_1\Psi_2\right]\left[\overline{\Psi}_3\Psi_4\right], \\ e_V(1234) &= \left[\overline{\Psi}_1\gamma^\mu\Psi_2\right]\left[\overline{\Psi}_3\gamma_\mu\Psi_4\right], \\ e_T(1234) &= \left[\overline{\Psi}_1\sigma_{\mu\nu}\Psi_2\right]\left[\overline{\Psi}_3\sigma^{\mu\nu}\Psi_4\right], \\ e_A(1234) &= \left[\overline{\Psi}_1\gamma^\mu\gamma_5\Psi_2\right]\left[\overline{\Psi}_3\gamma_\mu\gamma_5\Psi_4\right], \\ e_P(1234) &= \left[\overline{\Psi}_1\gamma_5\Psi_2\right]\left[\overline{\Psi}_3\gamma_5\Psi_4\right], \end{aligned} \tag{4.26}$$

where Ψ_i are *anti-commuting* Dirac spinors. Via the Fierz identities one can express each quadrilinear in terms of a linear equation

$$e_I(1234) = \sum_{J\in\{S,V,T,A,P\}} F_{IJ}e_J(1432), \tag{4.27}$$

where the original sequence of fermions appearing in the order of $\Psi_1, \Psi_2, \Psi_3, \Psi_4$ is rearanged into the sequence $\Psi_1, \Psi_4, \Psi_3, \Psi_2$. The Fierz matrix F is given as

$$F = \begin{pmatrix} -\frac{1}{4} & -\frac{1}{4} & -\frac{1}{8} & \frac{1}{4} & -\frac{1}{4} \\ -1 & \frac{1}{2} & 0 & \frac{1}{2} & 1 \\ -3 & 0 & \frac{1}{2} & 0 & -3 \\ 1 & \frac{1}{2} & 0 & \frac{1}{2} & -1 \\ -\frac{1}{4} & \frac{1}{4} & -\frac{1}{8} & -\frac{1}{4} & -\frac{1}{4} \end{pmatrix}. \tag{4.28}$$

Fierz identities can be especially handy when dealing with chiral fermions $\Psi_i \to \Psi_{i,L,R}$. In this case, we find the explicit identities

$$\begin{aligned} \left[\overline{R_1}L_2\right]\left[\overline{L_3}R_4\right] &= -\frac{1}{2}\left[\overline{R_1}\gamma^\mu R_4\right]\left[\overline{L_3}\gamma_\mu L_2\right], \\ \left[\overline{L_1}R_2\right]\left[\overline{L_3}R_4\right] &= -\frac{1}{2}\left[\overline{L_1}R_4\right]\left[\overline{L_3}R_2\right] - \frac{1}{8}\left[\overline{L_1}\sigma^{\mu\nu}R_4\right]\left[\overline{L_3}\sigma_{\mu\nu}R_2\right], \\ \left[\overline{L_1}\gamma^\mu L_2\right]\left[\overline{L_3}\gamma_\mu L_4\right] &= \left[\overline{L_1}\gamma^\mu L_4\right]\left[\overline{L_3}\gamma_\mu L_2\right], \\ \left[\overline{L_1}\sigma^{\mu\nu}R_2\right]\left[\overline{L_3}\sigma_{\mu\nu}R_4\right] &= -6\left[\overline{L_1}R_4\right]\left[\overline{L_3}R_2\right] + \frac{1}{2}\left[\overline{L_1}\sigma^{\mu\nu}R_4\right]\left[\overline{L_3}\sigma_{\mu\nu}R_2\right] \\ &= -8\left[\overline{L_1}R_4\right]\left[\overline{L_3}R_2\right] - 4\left[\overline{L_1}R_2\right]\left[\overline{L_3}R_4\right], \\ \left[\overline{L_1}\sigma^{\mu\nu}R_2\right]\left[\overline{R_3}\sigma_{\mu\nu}L_4\right] &= 0, \end{aligned} \tag{4.29}$$

giving other helpful relations like

$$\begin{aligned} \left[\overline{L_1}\sigma^{\mu\nu}\gamma^\rho L_2\right]\left[\overline{L_3}\sigma_{\mu\nu}R_4\right] &= -4\left[\overline{L_1}\gamma^\rho L_2\right]\left[\overline{L_3}R_4\right] - 8\left[\overline{L_1}R_4\right]\left[\overline{L_3}\gamma^\rho L_2\right], \\ \left[\overline{R_1}\gamma^\rho\sigma^{\mu\nu}R_2\right]\left[\overline{L_3}\sigma_{\mu\nu}R_4\right] &= -4\left[\overline{R_1}\gamma^\rho R_2\right]\left[\overline{L_3}R_4\right] - 8\left[\overline{R_1}\gamma^\rho R_4\right]\left[\overline{L_3}R_2\right]. \end{aligned} \tag{4.30}$$

Switching $L_i \rightleftharpoons R_i$ results in the same identities.

Let us take the opportunity to briefly point out a minor subtlety that arises in the construction of the LEFT dimension-6 basis. Notice that at LEFT dimension 6 only a single charged-current $\Delta L = 2$ tensor operator is present. In some previous literature [166], an additional LEFT tensor operator

$$\mathcal{O}_{TL}^{(6)} = \left[\overline{e_L}\sigma^{\mu\nu}\nu_L^C\right]\left[\overline{u_R}\sigma_{\mu\nu}d_L\right], \tag{4.31}$$

was considered in the context of $0\nu\beta\beta$. By utilizing the chiral Fierz identities for tensor currents, we can directly see that this operator, being of the type $\left[\overline{L_1}\sigma^{\mu\nu}R_2\right]\left[\overline{R_3}\sigma^{\mu\nu}L_4\right]$ is identically zero and, hence, does not need to be considered. The same is, obviously, true for neutral-current tensor operators of the same chirality structure.

4.4.2.2 Field Redefinitions

Although the dynamical degrees of freedom in a QFT, the fields, are supposed to represent physical particles such as the neutrino, electron, etc., their choice is, actually, not unique. Indeed, the fields that are present in the action of a QFT are themselves not physically observable quantities. Instead, the experimentally observable quantities of a QFT are the S-matrix elements, and we are free to define the fields in any way as long as they result in the same S-matrix elements. To put it in the famous words of S. Weinberg: "*You may use any degrees of freedom you like to describe a physical system, but if you use the wrong ones, you'll be sorry*" [43, 167].

The proof of the invariance of the S-matrix under local field redefinitions $\Phi \to \Phi'$

$$\Phi = F(\Phi'), \tag{4.32}$$

has been derived in Refs. [164, 165]. In the path integral formulation of QFT, such a field redefinition can be understood as a substitution of the integration variable (c.f. [42]). The S-matrix is invariant under a field redefinition if

$$\langle p|F[\Phi]|0\rangle \neq 0. \tag{4.33}$$

Field redefinitions are convenient tools that can significantly reduce the complexity of an EFT Lagrangian by removing redundancies. When matching a theory onto some EFT, field redefinitions are usually required to match onto a minimal EFT operator basis. Primarily, we apply redefinitions of fields to remove derivative terms of the type

$$\mathcal{O}\partial\!\!\!/\Psi_{L,R}, \tag{4.34}$$

where $\Psi_{L,R}$ is a chiral fermion and $\mathcal{O}$ is some operator built from the EFT's degrees of freedom. The removal of such derivative terms via field redefinitions comes at the cost of introducing higher dimensional interaction terms. To leading order, field redefinitions are related to the equations of motion [41, 168]. Taking

$$\Psi \to \Psi + \delta\Psi, \qquad \overline{\Psi} \to \overline{\Psi} + \delta\overline{\Psi}, \tag{4.35}$$

induces a change in the action [168]

$$\mathcal{S} \to \mathcal{S} + \delta\mathcal{S}, \qquad \delta\mathcal{S} = \frac{\delta\mathcal{S}}{\delta\Psi}\delta\Psi + \delta\overline{\Psi}\frac{\delta\mathcal{S}}{\delta\overline{\Psi}} + \mathcal{O}(\delta\Psi^2, \delta\overline{\Psi}^2). \tag{4.36}$$

We can see that to leading order in $\delta\Psi$, this is equivalent to adding some operator multiplied by the fields equations of motion $\delta\mathcal{S}/\delta\Psi$ to the Lagrangian.

4.4.2.3 The Matching Relations

After integrating out the heavy fields with masses $\geq m_W$ and applying the appropriate algebraic steps (c.f. appendix B) one finds the matching relations that map the SMEFT Wilson coefficients onto the relevant LEFT coefficients. These have been derived in Refs. [1, 2, 44] and we replicate these results here. For the neutrino mass we find the usual contribution from the SMEFT dimension-5 Weinberg operator and its dimension-7 extension via

$$m_{\beta\beta} = -v^2 C_{LH}^{(5)} - \tfrac{v^4}{2} C_{LH}^{(7)}, \tag{4.37}$$

while the relevant $\Delta L = 2$ four-fermion Wilson coefficients receive contributions from operators at SMEFT dimensions 7 and 9

$$\begin{aligned}
C_{SL}^{(6)} &= v^3\left(\tfrac{1}{\sqrt{2}}C_{LLQuH1}^{(7)*} + \tfrac{m_u}{v}\tfrac{V_{ud}}{2}C_{LHD2}^{(7)*}\right) \\
&\quad + v^4\left(m_u\tfrac{V_{ud}}{2}C_{LLH^4D^23}^{(9)*} - m_u\tfrac{V_{ud}}{4}C_{LLH^4D^24}^{(9)*} - m_u\tfrac{1}{4}C_{QQLLH^2D2}^{(9)*} - m_d\tfrac{1}{4}C_{duLLH^2D}^{(9)*}\right), \\
C_{SR}^{(6)} &= v^3\left(\tfrac{1}{2\sqrt{2}}C_{LLQdH1}^{(7)*} - \tfrac{V_{ud}}{2}\tfrac{m_d}{v}C_{LHD2}^{(7)*}\right) \\
&\quad + v^4\left(-m_d\tfrac{V_{ud}}{2}C_{LLH^4D^23}^{(9)*} + m_d\tfrac{V_{ud}}{4}C_{LLH^4D^24}^{(9)*} + \tfrac{m_d}{4}C_{QQLLH^2D2}^{(9)*} + \tfrac{m_u}{4}C_{duLLH^2D}^{(9)} + \tfrac{m_e}{8}C_{deQLH^2D}^{(9)*}\right), \\
C_{VL}^{(6)} &= v^3\left(-\tfrac{i}{\sqrt{2}}V_{ud}C_{LHDe}^{(7)*} + 4\tfrac{m_e}{v}C_{LHW}^{(7)*}\right) + v^4\left(2m_eV_{ud}C_{LLH^4W1}^{(9)*} - \tfrac{m_d}{4}C_{deQLH^2D}^{(9)*}\right), \\
C_{VR}^{(6)} &= v^3\tfrac{1}{\sqrt{2}}C_{LeudH}^{(7)*} - v^4\tfrac{m_u}{4}C_{deQLH^2D}^{(9)*}, \\
C_{T}^{(6)} &= v^3\left(\tfrac{1}{8\sqrt{2}}C_{LLQdH1}^{(7)*} + \tfrac{1}{4\sqrt{2}}C_{LLQdH2}^{(7)*}\right) + v^4\tfrac{m_e}{16}C_{deQLH^2D}^{(9)*}, \\
C_{VL}^{(7)} &= v^3\left(V_{ud}C_{LHD1}^{(7)*} - \tfrac{V_{ud}}{2}C_{LHD2}^{(7)*} + 4V_{ud}C_{LHW}^{(7)*}\right) \\
&\quad + v^5\left(2V_{ud}C_{LLH^4W1}^{(9)*} + \tfrac{V_{ud}}{2}C_{LLH^4D^23}^{(9)*} - \tfrac{V_{ud}}{4}C_{LLH^4D^24}^{(9)*} - \tfrac{1}{4}C_{QQLLH^2D2}^{(9)*}\right), \\
C_{VR}^{(7)} &= v^3\left(-iC_{LLduD1}^{(7)*}\right) + v^5\left(\tfrac{1}{4}C_{duLLH^2D}^{(9)*}\right).
\end{aligned} \tag{4.38}$$

In a similar fashion, the short-range LEFT dimension-9 operators receive contributions from both dimension-7 and -9 SMEFT operators. The SMEFT-to-LEFT matching onto the scalar LEFT dimension-9 operators is then given by

$$
\begin{aligned}
C_{1L}^{(9)} &= v^3\Big(2V_{ud}^2 C_{LHD1}^{(7)*} + 8V_{ud}^2 C_{LHW}^{(7)*}\Big)\\
&\quad + v^5\Big(4V_{ud}^2 C_{LLH^4W1}^{(9)*} - V_{ud}^2 C_{LLH^4D^23}^{(9)*} - V_{ud}^2 C_{LLH^4D^24}^{(9)*} - V_{ud} C_{QQLLH^2D2}^{(9)*}\\
&\qquad - \frac{V_{ud}}{2} C_{QLQLH^2D2}^{(9)*} - \frac{V_{ud}}{2} C_{QLQLH^2D5}^{(9)*}\Big),\\
C_{1R}^{(9)} &= -v^5 V_{ud}^2 C_{eeH^4D^2}^{(9)*}, \quad C_{1R}^{(9)\prime} = \frac{v^5}{4} C_{ddueue}^{(9)*},\\
C_{2L}^{(9)} &= -v^5 C_{QuQuLL1}^{(9)*}, \quad C_{2L}^{(9)\prime} = -v^5 C_{dQdQLL1}^{(9)*},\\
C_{3L}^{(9)} &= -v^5 C_{QuQuLL2}^{(9)*}, \quad C_{3L}^{(9)\prime} = -v^5 C_{dQdQLL2}^{(9)*},\\
C_{4L}^{(9)} &= -v^3 i2V_{ud} C_{LLduD1}^{(7)*} + v^5\Big(V_{ud} C_{duLLH^2D}^{(9)*} - \frac{V_{ud}}{2} C_{dLuLH^2D2}^{(9)*} - \frac{1}{2} C_{dQQuLL2}^{(9)*}\Big),\\
C_{4R}^{(9)} &= -v^5 \frac{V_{ud}}{2} C_{deueH^2D}^{(9)*},\\
C_{5L}^{(9)} &= -\frac{1}{2} v^5 C_{dQQuLL1}^{(9)*},
\end{aligned}
\tag{4.39}
$$

while the matching onto the vector LEFT dimension-9 operators is given as

$$
\begin{aligned}
C_6^{(9)} &= v^5\Big(-\frac{2}{3} V_{ud} C_{dLQeH^2D1}^{(9)*} + \frac{V_{ud}}{2} C_{dQLeH^2D2}^{(9)*} - \frac{5}{12} V_{ud} C_{deQLH^2D}^{(9)*}\Big),\\
C_6^{(9)\prime} &= v^5\Big(\frac{1}{6} C_{QudueL2}^{(9)*} + \frac{1}{2} C_{QudueL1}^{(9)*}\Big),\\
C_7^{(9)} &= v^5\Big(-V_{ud} C_{dLQeH^2D1}^{(9)} - V_{ud} C_{deQLH^2D}^{(9)*}\Big), \quad C_7^{(9)\prime} = v^5 C_{QudueL2}^{(9)*},\\
C_8^{(9)} &= v^5\Big(-\frac{V_{ud}}{2} C_{QueLH^2D2}^{(9)*} + \frac{V_{ud}}{6} C_{QeuLH^2D2}^{(9)*}\Big), \quad C_8^{(9)\prime} = v^5\Big(\frac{1}{6} C_{dQdueL2}^{(9)*} + \frac{1}{2} C_{dQdueL1}^{(9)*}\Big),\\
C_9^{(9)} &= v^5 V_{ud} C_{QeuLH^2D2}^{(9)*}, \quad C_9^{(9)\prime} = v^5 C_{dQdueL2}^{(9)*}.
\end{aligned}
\tag{4.40}
$$

In the above relations, we ignored a matching contribution from $\mathcal{O}_{deQLH^2D}$ onto the LEFT dimension-7 vector operator $\mathcal{O}_{VR2}^{(7)}$ as it is suppressed in the chiral power counting (c.f. appendix B.3).

4.5 Chiral EFT - $0\nu\beta\beta$ at the Nuclear Level

Of course, our main interest lies in the realm of particle physics and the previous sections have equipped us with the necessary tools to describe the transition from a high-energy microscopic particle physics model with possible new degrees of freedom and/or new symmetry structures to the low-energy EFT valid at energies below EWSB, via a subsequent matching chain onto SMEFT and LEFT.[2] However, $0\nu\beta\beta$ is a nuclear decay process and we need to consider the effects of nuclear physics as well. In this section, we will describe the transition from the particle physics level with free quarks at the LEFT scale to the nuclear level with quarks being confined within mesons and nucleons and, finally, to complex nuclei composed of protons and neutrons. In this context, we will utilize chiral perturbation theory (χPT) [78] as well as its few-nucleon extension chiral EFT (χEFT) [92, 169] as the effective low-energy theory of QCD. For a more general review, the interested reader is referred to Refs. [170–174].

We will start by describing the quark-to-nucleon transition via χPT which can be used to effectively describe the LNV 4-fermion $n \to p$ interactions as well as LNV pion interactions. Afterwards, we will apply χEFT to describe the short-range LNV nucleon-nucleon interactions.

4.5.1 QCD with External Fields

Because we are only interested in the first generation of quarks we restrict ourselves to the two flavor formalism of chiral perturbation theory. The Standard Model QCD Lagrangian is then given by [171]

$$\mathcal{L}^0_{\text{QCD}} = \overline{q}\left(i\not{D} - M\right)q - \frac{1}{4}\mathcal{G}_{a\mu\nu}G^{\mu\nu}_a, \tag{4.41}$$

with the quark doublet

$$q = \begin{pmatrix} u \\ d \end{pmatrix}, \quad M = \text{diag}(m_u, m_d), \tag{4.42}$$

and the gluon gauge field tensors $\mathcal{G}^{\mu\nu}_a$. In the massless quark limit, taking $m_d = m_u = 0$, two flavor QCD obeys a global $SU(2)_L \times SU(2)_R$ symmetry on the classical level. Interactions other than QCD, including symmetry-breaking effects, can be studied by adding external fields to the Lagrangian [78, 172]

$$\mathcal{L} = \mathcal{L}^0_{\text{QCD}} + \mathcal{L}_{\text{ext}}, \tag{4.43}$$

defined as

$$\mathcal{L}_{\text{ext}} = \overline{q}\gamma_\mu\left(v^\mu + \frac{1}{3}v^\mu_{(s)} + \gamma_5 a^\mu\right)q - \overline{q}\left(s - i\gamma_5 p\right)q + \overline{q}\sigma_{\mu\nu}\overline{t}^{\mu\nu}q, \tag{4.44}$$

[2]Strictly speaking, we still require the renormalization group equations of the relevant SMEFT and LEFT operators, in order to correctly describe the transition from a high-energy particle physics model to the LEFT scales. We shift this discussion to Section 4.8.

with the hermitian and color-neutral vector, singlet-vector, axial-vector, scalar, pseudo-scalar and tensor fields [172, 175]

$$
\begin{aligned}
v^\mu &= \sum_{a=1}^{3} v_a^\mu \frac{\tau_a}{2}, \quad v_{(s)}^\mu = v_s^\mu \mathbb{1}, \quad a^\mu = \sum_{a=1}^{3} a_a^\mu \frac{\tau_a}{2}, \quad s = \sum_{a=0}^{3} s_a \tau_a, \quad p = \sum_{a=0}^{3} p_a \tau_a, \\
\bar{t}^{\mu\nu} &= \sum_{a=0}^{3} \bar{t}_a^{\mu\nu} \frac{\tau_a}{2}.
\end{aligned} \tag{4.45}
$$

Here, τ_a are the Pauli matrices and we defined $\tau_0 = \mathbb{1}$. As usual, we can define the left- and right-handed chiral fields l^μ and r^μ as linear combinations of the vector and axial-vector fields

$$
l^\mu = \frac{1}{2}\left(v^\mu - i a^\mu\right), \quad r^\mu = \frac{1}{2}\left(v^\mu + i a^\mu\right). \tag{4.46}
$$

and write the external Lagrangian in terms of chiral fields as [172, 175]

$$
\begin{aligned}
\mathcal{L}_{\text{ext}} =& \bar{q}_L \gamma_\mu \left(l^\mu + \frac{1}{3} v_{(s)}^\mu\right) q_L + \bar{q}_R \gamma_\mu \left(r^\mu + \frac{1}{3} v_{(s)}^\mu\right) q_R \\
&+ \bar{q}_R \left(s - ip\right) q_L + \bar{q}_L \left(s + ip\right) q_R \\
&+ \bar{q}_R \sigma_{\mu\nu} t_L^{\mu\nu} q_L + \bar{q}_L \sigma_{\mu\nu} t_R^{\mu\nu} q_R,
\end{aligned} \tag{4.47}
$$

with the chiral tensor fields

$$
t_R^{\mu\nu} = P_R^{\mu\nu\sigma\rho} \bar{t}_{\sigma\rho}, \quad t_{\mu\nu,L} = t_{\mu\nu,R}^\dagger, \quad P_R^{\mu\nu\sigma\rho} = \frac{1}{4}\left(g^{\mu\sigma} g^{\nu\rho} - g^{\nu\sigma} g^{\mu\rho} + i\epsilon^{\mu\nu\sigma\rho}\right). \tag{4.48}
$$

We can now promote the global $\mathrm{SU}(2)_L \times \mathrm{SU}(2)_R$ symmetry to a local one by requiring that the external fields transform as [172, 175, 176]

$$
\begin{array}{rclrcl}
l^\mu & \longrightarrow & L l^\mu L^\dagger - i L \partial L^\dagger, & r^\mu & \longrightarrow & R r^\mu R^\dagger - i R \partial R^\dagger, \\
(s + ip) & \longrightarrow & R(s + ip) L^\dagger, & (s - ip) & \longrightarrow & L(s - ip) R^\dagger, \\
t_L^{\mu\nu} & \longrightarrow & R t_L^{\mu\nu} L^\dagger, & t_R^{\mu\nu} & \longrightarrow & L t_R^{\mu\nu} R^\dagger,
\end{array} \tag{4.49}
$$

where L and R represent gauge transformations under the corresponding $SU(2)_{L,R}$ symmetries.

4.5.1.1 Defining the External Fields

We have already identified the relevant 4-fermion $\Delta L = 2$ LEFT operators up to dimension 7 in Tables 4.4 and 4.5. From there, we can simply read off the external source terms required to describe LNV 4-fermion interactions together with the standard charged-current weak interactions in χPT as (c.f. Ref. [44])

$$
\begin{aligned}
l^\mu =& \frac{1}{v^2}\Big(-2V_{ud}\Big[\overline{e_L}\gamma^\mu\nu_L\Big]\tau^+ + C^{(6)}_{VL}\Big[\overline{e_R}\gamma^\mu\nu_L^C\Big]\tau^+\Big) + \frac{1}{v^3}\Big(C^{(7)}_{VL}\Big[\overline{e_L}i\overleftrightarrow{\partial}^\mu\nu_L^C\Big]\tau^+\Big) + \text{h.c.},\\
r^\mu =& \frac{1}{v^2}\Big(C^{(6)}_{VR}\Big[\overline{e_R}\gamma^\mu\nu_L^C\Big]\tau^+\Big) + \frac{1}{v^3}\Big(C^{(7)}_{VR}\Big[\overline{e_L}i\overleftrightarrow{\partial}^\mu\nu_L^C\Big]\tau^+\Big) + \text{h.c.},\\
(s-ip) =& \frac{1}{v^2}\Big(C^{(6)}_{SL}\Big[\overline{e_L}\nu_L^C\Big]\tau^+ + (C^{(6)}_{SR})^\dagger\Big[\overline{\nu_L^C}e_L\Big]\tau^-\\
&+ C^{(6)}_{SL,\nu u}\Big[\overline{\nu_L}\nu_L^C\Big]\tau^u + (C^{(6)}_{SR,\nu u})^\dagger\Big[\overline{\nu_L^C}\nu_L\Big]\tau^u\\
&+ C^{(6)}_{SL,\nu d}\Big[\overline{\nu_L}\nu_L^C\Big]\tau^d + (C^{(6)}_{SR,\nu d})^\dagger\Big[\overline{\nu_L^C}\nu_L\Big]\tau^d\Big),\\
(s+ip) =& \frac{1}{v^2}\Big(C^{(6)}_{SR}\Big[\overline{e_L}\nu_L^C\Big]\tau^+ + (C^{(6)}_{SL})^\dagger\Big[\overline{\nu_L^C}e_L\Big]\tau^-\\
&+ C^{(6)}_{SR,\nu u}\Big[\overline{\nu_L}\nu_L^C\Big]\tau^u + (C^{(6)}_{SL,\nu u})^\dagger\Big[\overline{\nu_L^C}\nu_L\Big]\tau^u\\
&+ C^{(6)}_{SR,\nu d}\Big[\overline{\nu_L}\nu_L^C\Big]\tau^d + (C^{(6)}_{SL,\nu d})^\dagger\Big[\overline{\nu_L^C}\nu_L\Big]\tau^d\Big),\\
t_R^{\mu\nu} =& \frac{1}{v^2}\Big(C^{(6)}_{T}\Big[\overline{e_L}\sigma^{\mu\nu}\nu_L^C\Big]\tau^+ + C^{(6)}_{T,\nu u}\Big[\overline{\nu_L}\sigma^{\mu\nu}\nu_L^C\Big]\tau^u + C^{(6)}_{T,\nu d}\Big[\overline{\nu_L}\sigma^{\mu\nu}\nu_L^C\Big]\tau^d\Big),\\
t_L^{\mu\nu} =& (t_R^{\mu\nu})^\dagger,
\end{aligned}
\tag{4.50}
$$

with

$$
\tau^\pm = \frac{1}{2}(\tau_1 \pm i\tau_2), \quad \tau^u = \frac{1}{2}(\tau_0+\tau_3), \quad \tau^d = \frac{1}{2}(\tau_0-\tau_3). \tag{4.51}
$$

For completeness and in contrast to Refs. [44, 45], we have included the LNV neutral-current dimension-6 operators in the above definitions. While they are usually not considered to be of greater relevance for $0\nu\beta\beta$, we will see later on in Section 4.6 that the scalar NC interactions do provide a significant tree-level contribution to the $0\nu\beta\beta$ amplitude. Additionally, NC interactions may become relevant in the high-density neutrino environments of core-collapse supernovae [177].

In the next two sections, we will follow the procedure outlined in Refs. [44, 45, 178] and derive the LNV meson and nucleon interactions in χPT.

4.5.2 Chiral Perturbation Theory for Mesons

Within the two flavour χPT approach one introduces three scalar mesons, the pions, described via [44, 172, 176]

$$
U = u^2 = \exp\left\{\frac{i\vec{\tau}\cdot\vec{\pi}}{F_0}\right\} = 1 + \frac{i}{F_0}\begin{pmatrix}\pi^0 & \sqrt{2}\pi^+\\ \sqrt{2}\pi^- & \pi^0\end{pmatrix} + \mathcal{O}(\pi^2), \tag{4.52}
$$

which under the chiral $\mathrm{SU}(2)_L \times \mathrm{SU}(2)_R$ symmetry transforms as

$$U \longrightarrow LUR^\dagger, \quad u \longrightarrow LuK^\dagger = KuR^\dagger, \tag{4.53}$$

where K is a function of L, R, and U. Here, F_0 is the so-called pion decay constant and we use $F_0 = F_\pi = 92.2\,\mathrm{MeV}$ [44]. In order to write down a local gauge invariant Lagrangian as well as to include the above external source terms we need to define a covariant derivative $\mathcal{D}_\mu$ acting on U as [176]

$$\mathcal{D}_\mu U = \partial_\mu U - il_\mu U + iUr_\mu, \tag{4.54}$$

which transforms as

$$\mathcal{D}_\mu U \longrightarrow L(\mathcal{D}_\mu U)R^\dagger. \tag{4.55}$$

The external scalar and pseudoscalar sources are described via the linear combination [44, 172, 176]

$$\chi = 2B(M + s - ip), \qquad \chi \longrightarrow L\chi R^\dagger, \qquad B = \frac{m_\pi^2}{m_u + m_d} \simeq 2.7\,\mathrm{GeV}. \tag{4.56}$$

Here, we choose not to include the quark mass matrix M in the scalar field s and, instead, separate it from the LNV interactions. One should, however, keep in mind that M would usually be included in the scalar external field s and, hence, follows the same symmetry transformation as s. The quantity B is related to the formation of a non-zero quark condensate $\langle \overline{q}q \rangle$ [172].

Assigning the standard power-counting scheme [172, 175]

$$\begin{aligned} &U \sim \mathcal{O}(1), \quad \mathcal{D}_\mu U \sim \mathcal{O}(p), \quad l_\mu \sim \mathcal{O}(p), \quad r_\mu \sim \mathcal{O}(p), \quad v^\mu_{(s)} \sim \mathcal{O}(p), \\ &\chi \sim \mathcal{O}(p^2), \quad t^{\mu\nu}_{L,R} \sim \mathcal{O}(p^2), \end{aligned} \tag{4.57}$$

allows for an expansion in terms of the small parameter

$$\epsilon_\chi = \frac{p}{\Lambda_\chi}, \qquad \Lambda_\chi \sim 1\,\mathrm{GeV}, \qquad p \sim m_\pi, \tag{4.58}$$

for the meson operators of χPT. In the context of $0\nu\beta\beta$, we will also encounter powers of quark masses, as well as electron masses and energies. Therefore, we assign [45]

$$m_u \sim m_d \sim \mathcal{O}(\epsilon_\chi^2 \Lambda_\chi), \qquad Q \sim E_e \sim m_e \sim \mathcal{O}(\epsilon_\chi^3 \Lambda_\chi). \tag{4.59}$$

We will see later on that the introduction of nucleons will require a different counting scheme, due to the appearance of nucleon masses $m_N \sim \Lambda_\chi$, but for now let us stick to this one to follow the standard χPT reviews [171, 172].

The leading order χPT Lagrangian for pions in a p/Λ_χ expansion is then given by [44, 172]

$$\mathcal{L}_\pi^{(0)} = \frac{F_0^2}{4}\mathrm{Tr}\Big[(\mathcal{D}_\mu U)^\dagger(\mathcal{D}^\mu U)\Big] + \frac{F_0^2}{4}\mathrm{Tr}\Big[U^\dagger\chi + U\chi^\dagger\Big]. \tag{4.60}$$

Considering the LNV $\Delta L = 2$ dimension-6 LEFT operators of interest, it is convenient to express the external fields in terms proportional to τ^+, τ^u and τ^d

$$\begin{aligned} l^\mu &= l^\mu_+ \tau^+ + \text{h.c.}, \qquad r^\mu = r^\mu_+ \tau^+ + \text{h.c.} \\ s &= (s^+ \tau^+ + \text{h.c.}) + s^u \tau^u + s^d \tau^d, \\ p &= (p^+ \tau^+ + \text{h.c.}) + p^u \tau^u + p^d \tau^d, \\ t_{\mu\nu} &= (t^+_{\mu\nu} \tau^+ + \text{h.c.}) + t^u_{\mu\nu} \tau^u + t^d_{\mu\nu} \tau^d. \end{aligned} \tag{4.61}$$

This allows us to separate the charged-current interactions acting via $\tau^\pm$ from the neutral-current interactions acting via $\tau^{u,d}$. We can then expand eq. (4.60) in powers of the pion and external fields as

$$\begin{aligned} \mathcal{L}^{(0)}_\pi =& -\frac{\sqrt{2}F_0}{2}\Big[(\partial_\mu \pi^-)(l^\mu_+ - r^\mu_+) + \text{h.c.}\Big] + \frac{F_0^2}{4}\text{Tr}\Big[4Bs - \frac{4B}{F_0}\begin{pmatrix} \pi^0 & \sqrt{2}\pi^+ \\ \sqrt{2}\pi^- & \pi^0 \end{pmatrix} p\Big] \\ &+ \mathcal{O}\Big(\pi^2, l^2, r^2, lr\Big) \\ =& \frac{\sqrt{2}F_0}{2}\Big[(\partial_\mu \pi^-)(l^\mu_+ - r^\mu_+) + \text{h.c.}\Big] \\ &+ \frac{F_0^2}{4}\Big(4B(s^u + s^d) - \frac{4B}{F_0}\Big[(p^u + p^d)\pi^0 + (\sqrt{2}\pi^- p^+ + \text{h.c.})\Big]\Big) + \mathcal{O}\Big(\pi^2, l^2, r^2, lr\Big), \end{aligned} \tag{4.62}$$

to arrive at the relevant interactions contributing to the $0\nu\beta\beta$ amplitude.

4.5.3 Chiral Perturbation Theory for Nucleons

4.5.3.1 The Power-Counting Problem in Baryon-χPT

Next, we want to consider the χPT single-nucleon interactions in the presence of the external fields. Let us, therefore, introduce the nucleon doublet [44, 172]

$$N = \begin{pmatrix} p \\ n \end{pmatrix}, \qquad N \longrightarrow KN. \tag{4.63}$$

Keeping the power-counting scheme of the external fields introduced in eq. (4.57), the pion-nucleon Lagrangian at leading order (LO) with the lowest number of derivatives is given by [172]

$$\mathcal{L}^{(1)}_{\pi N} = \overline{N}\Big(i\not{D} - m_N + \frac{g_A}{2}\gamma^\mu\gamma_5 u_\mu\Big)N, \tag{4.64}$$

and at next-to-leading order (NLO) one finds [172]

$$\begin{aligned} \mathcal{L}^{(2)}_{\pi N} =& c_1 \,\text{Tr}\left[\chi_+\right]\overline{N}N - \frac{c_2}{4m^2}\,\text{Tr}\left[u_\mu u_\nu\right]\Big(\overline{N}\mathcal{D}^\mu\mathcal{D}^\nu N + \text{h.c.}\Big) + \frac{c_3}{2}\,\text{Tr}\left[u^\mu u_\mu\right]\overline{N}N \\ &- \frac{c_4}{4}\overline{N}\gamma^\mu\gamma^\nu\left[u_\mu, u_\nu\right]N + c_5\overline{N}\hat{\chi}_+ N + \overline{N}\Big(\frac{c_6}{2}f^+_{\mu\nu} + \frac{c_7}{2}v^{(s)}_{\mu\nu}\Big)\sigma^{\mu\nu}N \qquad (4.65) \\ &+ \overline{N}\Big(c_8 \hat{t}^{\mu\nu}_+ + c_9\,\text{Tr}\left[\hat{t}^{\mu\nu}_+\right]\Big)\sigma_{\mu\nu}N. \qquad (4.66) \end{aligned}$$

In the above Lagrangians, we defined

$$\hat{\chi}_+ = \chi_+ - \frac{1}{2}\mathrm{Tr}(\chi_+), \quad \chi_\pm = u^\dagger \chi u^\dagger \pm u\chi^\dagger u. \tag{4.67}$$

Similarly, we summarize the tensor fields $t^{\mu\nu}_{L,R}$ in

$$\hat{t}^{\mu\nu}_\pm = u^\dagger t^{\mu\nu}_R u^\dagger \pm u t^{\mu\nu}_L u. \tag{4.68}$$

The covariant derivative acting on the nucleons is then defined as

$$\mathcal{D}_\mu N = \left(\partial_\mu + \Gamma_\mu - i v^{(s)}_\mu\right) N, \tag{4.69}$$

with the vector field

$$\Gamma_\mu = \frac{1}{2}\Big[u^\dagger(\partial_\mu - i l_\mu)u + u(\partial_\mu - i r_\mu)u^\dagger\Big], \tag{4.70}$$

and the axial-vector field

$$u_\mu = -i\Big[u^\dagger(\partial_\mu - i l_\mu)u - u(\partial_\mu - i r_\mu)u^\dagger\Big]. \tag{4.71}$$

The tensor fields $f^+_{\mu\nu}$ and $v^{(s)}_{\mu\nu}$ are associated with the external vector fields $l_\mu, r_\mu, v^{(s)}_\mu$ via [172]

$$\begin{aligned}
f^\pm_{\mu\nu} &= u f^L_{\mu\nu} u \dagger \pm u^\dagger f^R_{\mu\nu} u, \\
f^L_{\mu\nu} &= \partial_\mu l_\nu - \partial_\nu l_\mu - i\left[l_\mu, l_\nu\right], \\
f^R_{\mu\nu} &= \partial_\mu r_\nu - \partial_\nu r_\mu - i\left[r_\mu, r_\nu\right], \\
v^{(s)}_{\mu\nu} &= \partial_\mu v^{(s)}_\nu - \partial_\nu v^{(s)}_\mu.
\end{aligned} \tag{4.72}$$

In the above expansion, we come across two problems associated with the applied power-counting scheme. The first problem is that, due to the nucleon mass being of the order of the chiral scale

$$m_N \sim \Lambda_\chi, \tag{4.73}$$

we have to count derivatives acting on the nucleon fields as order one

$$\mathcal{D}_\mu N \sim \mathcal{D}_0 N \sim \mathcal{O}(m_N/\Lambda_\chi) \sim \mathcal{O}(1). \tag{4.74}$$

In this way, we could construct LO nucleon operators with an arbitrary number of derivatives and the derivative expansion of χPT would break down. Secondly, in order to accommodate the nucleon-to-nucleus transition and calculation of NMEs, we need to switch to a non-relativistic expansion of the nuclear operators used in the numerical many-body simulations.

4.5.3.2 Heavy Baryon Chiral Perturbation Theory

We can solve these problems by applying the heavy baryon chiral perturbation theory (HBχPT) developed by Manohar and Jenkins [179] which allows for a non-relativistic derivative expansion of baryon-χPT. Additionally, we will be switching to Weinbergs power-counting scheme characterized by the (tree-level) chiral index [169]

$$\Delta = d + \frac{1}{2}n - 2, \tag{4.75}$$

where n is the number of nucleons, and d is the number of derivatives involved in the operator.

While Weinbergs power counting does lift some operators from the NLO Lagrangian in eq. (4.66) to the leading order, we will stick to the LO Lagrangian of eq. (4.64) for now and use it as an example to show how to derive the non-relativistic HBχPT Lagrangian from the relativistic theory. Following along the lines of Ref. [171], we introduce the velocity projectors

$$P_v^{\pm} = \frac{1 \pm \not{v}}{2}, \tag{4.76}$$

splitting the nucleon field N into velocity dependent light and heavy nucleon fields

$$N_v = \exp\{im_N v_\mu x^\mu\} P_v^+ N, \quad H_v = \exp\{im_N v_\mu x^\mu\} P_v^- N, \tag{4.77}$$

which are orthogonal eigenstates of the velocity operator

$$\not{v} N_v = N_v, \quad \not{v} H_v = -H_v, \quad \overline{N}_v H_v = \overline{H}_v N = 0. \tag{4.78}$$

We can write the pion-nucleon Lagrangian in terms of these light and heavy nucleon fields by replacing

$$N = \exp\{-im_N v_\mu x^\mu\}(N_v + H_v). \tag{4.79}$$

Explicitly, the πN Lagrangian of eq. (4.64) can then be written as

$$\begin{aligned}
L_{\pi N}^{(1)} &= \left(\overline{N}_v + \overline{H}_v\right) \exp\{im_N v_\mu x^\mu\} \Big(i\not{D} - m_N + \frac{g_A}{2}\gamma^\mu\gamma_5 u_\mu\Big) \exp\{-im_N v_\mu x^\mu\}(N_v + H_v) \\
&= \left(\overline{N}_v + \overline{H}_v\right)\Big(m_N \not{v} + i\not{D} - m_N + \frac{g_A}{2}\gamma^\mu\gamma_5 u_\mu\Big)(N_v + H_v) \\
&= \left(\overline{N}_v + \overline{H}_v\right)\Big(i\not{D} + \frac{g_A}{2}\gamma^\mu\gamma_5 u_\mu\Big)(N_v + H_v) - 2m_N \overline{H}_v H_v.
\end{aligned} \tag{4.80}$$

That is, only the heavy nucleon field H_v remains massive, with a mass of $2m_N$, while the mass term of the light nucleon field N_v cancels, justifying the naming convention of N_v and H_v. We can now integrate out the heavy nucleon field H_v exactly by performing a Gaussian integral of the type [79]

$$\mathcal{Z}(\overline{\eta}, \eta) = \int \mathcal{D}\overline{\Psi}\mathcal{D}\Psi \, \exp\big\{-\overline{\Psi} M \Psi + \overline{\eta}\Psi + \overline{\Psi}\eta\big\} = \det\{M\} \exp\big\{\overline{\eta} M^{-1} \eta\big\}. \tag{4.81}$$

Rewriting eq. (4.80) as

$$\begin{aligned}L_{\pi N}^{(1)} =&\overline{N}_v\Big(i\not{D} + \frac{g_A}{2}\gamma^\mu\gamma_5 u_\mu\Big)N_v + \overline{H}_v\Big(i\not{D} - 2m_N + \frac{g_A}{2}\gamma^\mu\gamma_5 u_\mu\Big)H_v \\ &+ \overline{N}_v\Big(i\not{D} + \frac{g_A}{2}\gamma^\mu\gamma_5 u_\mu\Big)H_v + \overline{H}_v\Big(i\not{D} + \frac{g_A}{2}\gamma^\mu\gamma_5 u_\mu\Big)N_v,\end{aligned} \tag{4.82}$$

the Gaussian structure becomes obvious and we find

$$\begin{aligned}\hat{L}_{\pi N}^{(1)} =&\overline{N}_v\Big(i\not{D} + \frac{g_A}{2}\gamma^\mu\gamma_5 u_\mu\Big)N_v \\ &- \overline{N}_v\Big(i\not{D} + \frac{g_A}{2}\gamma^\mu\gamma_5 u_\mu\Big)\Big(i\not{D} - 2m_N + \frac{g_A}{2}\gamma^\mu\gamma_5 u_\mu\Big)^{-1}\Big(i\not{D} + \frac{g_A}{2}\gamma^\mu\gamma_5 u_\mu\Big)N_v.\end{aligned} \tag{4.83}$$

We can see that we have successfully removed operators proportional to the nucleon mass m_N from the Lagrangian at the cost of introducing higher-order operators that are suppressed by powers of $1/m_N$ as represented in the second term of eq. (4.83). Hence, for the light nucleon field N_v the power-counting rule is $D_\mu N_v \sim \mathcal{O}(p)$ such that we can expand the Lagrangian in terms of p/m_N and therefore recover a working derivative expansion. Finally, the HBχPT approach allows us to write the nucleon operators in a non-relativistic form. The light nucleon fields N_v obey the following equalities [171, 179]

$$\begin{gathered}\overline{N}_v\gamma_5 N_v = 0, \quad \overline{N}_v\gamma^\mu N_v = \overline{N}_v v^\mu N_v, \quad \overline{N}_v\gamma^\mu\gamma_5 N_v = 2\overline{N}_v\mathcal{S}_v^\mu N_v, \\ \overline{N}_v\sigma^{\mu\nu}N_v = 2\epsilon^{\mu\nu\alpha\beta}v_\alpha\overline{N}_v S_{v\beta}N_v, \quad \overline{N}_v\sigma^{\mu\nu}\gamma_5 N_v = 2i\Big(v^\mu\overline{N}_v S_v^\nu N_v - v^\nu\overline{N}_v\mathcal{S}_v^\mu N_v\Big),\end{gathered} \tag{4.84}$$

where the spin matrix S_v^μ is given by

$$S_v^\mu = \frac{i}{2}\gamma_5\sigma^{\mu\nu}v_\nu. \tag{4.85}$$

In this way, we finally end up at the non-relativistic HBχPT expression of eq. (4.64) as

$$\hat{\mathcal{L}}_{\pi N}^{(1)} = \overline{N}_v\Big(p^\mu v_\mu + g_A S_v^\mu u_\mu\Big)N_v + \mathcal{O}\left(\frac{p}{m_N}\right). \tag{4.86}$$

Note that from here on, we will drop the index v from the light nucleon fields N_v as well as the spin operator S_v^μ and use the non-relativistic approximation $v = (1,0,0,0)^T$, $S = (0, \sigma_1/2, \sigma_2/2, \sigma_3/2)^T$ valid in the rest-frame of the nucleon [45].

4.5.3.3 The Heavy Baryon Lagrangian at Leading and Next-to-Leading Order

The HBχPT expansion of the πN Lagrangian in the presence of the external fields $l_\mu, r_\mu, s, p, t_{\mu\nu}$ has been derived to LO and NLO in Ref. [44]. The relevant LO terms for $0\nu\beta\beta$ are

$$\hat{\mathcal{L}}_{\pi N}^{(1)} =i\overline{N}v_\mu\mathcal{D}^\mu N + g_A\overline{N}\mathcal{S}_\mu u^\mu N - \overline{N}c_5\chi_+ N - \Big[2g_T\epsilon_{\mu\nu\alpha\beta}v^\alpha\overline{N}\mathcal{S}^\beta t_+^{\mu\nu}N\Big]. \tag{4.87}$$

Note that terms involving $\mathrm{Tr}[\chi_+]$ and $\mathrm{Tr}\big[\hat{t}_+^{\mu\nu}\big]$ do not contribute to $n \leftrightarrow p$ transitions and can be ignored in the context of $0\nu\beta\beta$. At zeroth order in the pion fields this can be expanded as

$$\begin{aligned}\hat{\mathcal{L}}_{\pi N}^{(1)} =& \overline{N} v_\mu \Big[i\partial^\mu + \frac{1}{2}(l^\mu + r^\mu) + v^\mu_{(s)} \Big] N - g_A \overline{N} \mathcal{S}_\mu (l^\mu - r^\mu) N \\ & - g_S \overline{N} \begin{pmatrix} s^u & s^+ \\ s^- & s^d \end{pmatrix} N - 2 g_T \epsilon^{\mu\nu\alpha\beta} v_\alpha \overline{N} \mathcal{S}_\beta \left[\begin{pmatrix} t^u_{R\mu\nu} & t^+_{R\mu\nu} \\ t^-_{R\mu\nu} & t^d_{R\mu\nu} \end{pmatrix} + \text{h.c.} \right] N + \mathcal{O}(\pi). \end{aligned} \tag{4.88}$$

Additionally, we will need the πN coupling to zeroth order in the external fields which is given by

$$\hat{\mathcal{L}}_{\pi N}^{(1)} \supset + \frac{g_A}{F_0} \overline{N} \mathcal{S}_v^\mu \partial_\mu \begin{pmatrix} \pi^0 & \sqrt{2}\pi^+ \\ \sqrt{2}\pi^- & \pi^0 \end{pmatrix} N. \tag{4.89}$$

In this way, the LNV LEFT operators associated with the pseudo-scalar external field p^+ can generate a $0\nu\beta\beta$ via their coupling to the charged pion which allows for a transition of the type

$$\pi^- \longrightarrow e^- + \nu_e. \tag{4.90}$$

The corresponding $0\nu\beta\beta$ diagram is shown on the right side of Figure 4.10.

As the parity and spin structure of the LO nucleon-pion Lagrangian does not provide a contribution to the ground-state to ground-state $0^+ \to 0^+$ $0\nu\beta\beta$ transition for the LNV vector and tensor operators $\mathcal{O}^{(6)}_{VL,VR}$ and $\mathcal{O}^{(6)}_T$, one has to include the NLO Lagrangian [44]

$$\begin{aligned}\mathcal{L}_{\pi N}^{(2)} =& \frac{1}{2m_N} \big(v^\mu v^\nu - g^{\mu\nu} \big) \big(\overline{N} \mathcal{D}_\mu \mathcal{D}_\nu N \big) - \frac{i g_A}{2m_N} \overline{N} \big\{ S \cdot \mathcal{D}, v \cdot u \big\} N \\ & - \frac{g_M}{4mN} \epsilon^{\mu\nu\alpha\beta} v_\alpha \overline{N} S_\beta f^+_{\mu\nu} N - \frac{g_T}{m_N} \epsilon_{\mu\nu\alpha\beta} \overline{N} S_\beta \big\{ t_+^{\mu\nu}, i\mathcal{D}^\alpha \big\} N + \frac{g_T'}{m_N} v_\mu \overline{N} \big\{ t_+^{\mu\nu}, i\mathcal{D}_\nu \big\} N. \end{aligned} \tag{4.91}$$

4.5.4 The $n \to pe\nu_e$ Transition Amplitude in χPT

With these building blocks defined in $\mathcal{L}_\pi^{(0)}, \mathcal{L}_{\pi N}^{(1)}, \mathcal{L}_{\pi N}^{(2)}$ we can write down the lepton-number violating and conserving $n \to pe\nu_e$ amplitudes that arise from the Standard Model's charged-current weak interactions as well as the LNV BSM interactions as summarized in the external fields defined in eq. (4.50). The calculation of the $n \to pe\nu_e$ transition amplitudes involves 4-fermion contact interactions as seen on the left side of Figure 4.9 as well as pion-exchange diagrams as visualized on the right side of Figure 4.9. It can be written as [44]

$$\mathcal{A}_{n\to pe\nu_e} = \overline{N} \tau^+ \left[\frac{l_\mu + r_\mu}{2} J_V^\mu + \frac{l_\mu - r_\mu}{2} J_A^\mu - s J_S + i p J_P + t_{R,\mu\nu} J_T^{\mu\nu} \right] N, \tag{4.92}$$

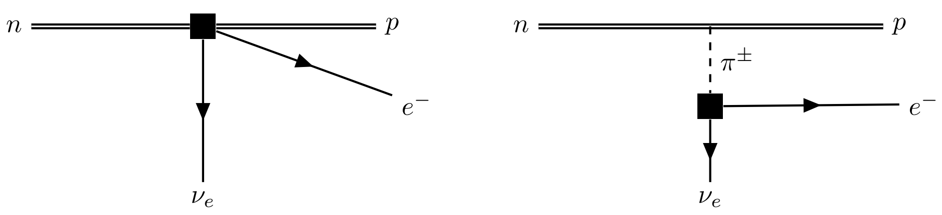

Figure 4.9: Feynman diagrams of the single-β decay in chiral perturbation theory. The square denotes a LNV BSM $qqe\nu$ interaction. The diagrams of the Standard Model single-β decay in χPT are obtained by replacing $\nu_e \to \overline{\nu}_e$.

with the nuclear currents

$$
\begin{aligned}
J_V^\mu &= g_V(\mathbf{q}^2)\left(v^\mu + \frac{p^\mu + p'^\mu}{2m_N}\right) + \frac{i g_M(\mathbf{q}^2)}{m_N}\epsilon^{\mu\nu\alpha\beta} v_\alpha S_\beta q_\nu, \\
J_A^\mu &= -g_A(\mathbf{q}^2)\left(2S^\mu - \frac{v^\mu}{2m_N} 2S\cdot(p+p')\right) + \frac{g_P(\mathbf{q}^2)}{2m_N} 2q^\mu S\cdot q, \\
J_S &= g_S(\mathbf{q}^2), \\
J_P &= B\frac{g_P(\mathbf{q}^2)}{m_N} S\cdot q, \\
J_T^{\mu\nu} &= -2g_T(\mathbf{q}^2)\epsilon^{\mu\nu\alpha\beta}\left(v_\alpha + \frac{p_\alpha + p'_\alpha}{2m_N}\right)S_\beta - i\frac{g'_T(\mathbf{q}^2)}{2m_N}(v^\mu q^\nu - v^\nu q^\mu),
\end{aligned} \tag{4.93}
$$

defined as functions of the incoming neutron and outgoing proton momenta p and p', respectively, and the momentum transfer $q^\mu = (q^0, \mathbf{q})^T = p^\mu - p'^\mu$. The momentum-dependent form factors relate to the low-energy constants (LECs) of the χPT Lagrangians via [44]

$$
\begin{aligned}
g_V(\mathbf{q}^2) =& 1, \qquad g_A(\mathbf{q}^2) = g_A, \qquad g_M(\mathbf{q}^2) = g_M, \qquad g_S(\mathbf{q}^2) = -4Bc_5, \\
g_P(\mathbf{q}^2) =& -g_A\frac{2m_N}{\mathbf{q}^2 + m_\pi^2}, \qquad g_T(\mathbf{q}^2) = g_T, \qquad g'_T(\mathbf{q}^2) = g'_T,
\end{aligned} \tag{4.94}
$$

where the $1/(\mathbf{q}^2 + m_\pi^2)$ dependence of the pseudo-scalar form factor $g_P(\mathbf{q}^2)$ arises from the pion propagator as shown on the right side of Figure 4.9. Hence, up to NLO in χPT all form factors except for $g_P(\mathbf{q})$ are constant.

We can use these $n \to pe\nu_e$ amplitudes in combination with the appropriate neutrino propagators to construct the long-range $0\nu\beta\beta$ amplitudes that are induced via the dimension-3, -6 and -7 LEFT operators. The corresponding Feynman diagrams are displayed in Figure 4.10.

4.5.5 Nucleon-Nucleon Contact Interactions and Chiral EFT

In order to include short-range interactions into our description, we need to consider direct nucleon-nucleon interactions $nn \to ppee$ as well as nucleon-pion interactions of

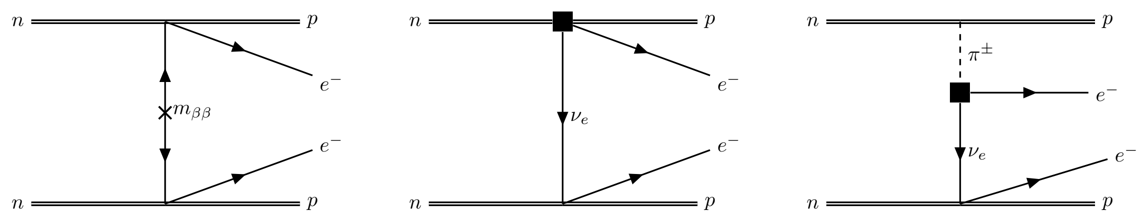

Figure 4.10: Feynman diagrams of $0\nu\beta\beta$ in chiral perturbation theory. The lepton-number-violating interactions are denoted by a black square. At leading order in the χPT expansion, there are three different tree-level topologies associated with the standard light neutrino-exchange mechanism (left), a LNV 4-fermion $npe\nu_e$ interaction (middle), and a LNV lepton-pion $e\nu_e\pi$ interaction (right).

the type $n\pi \to pee$ and pion-lepton interactions $\pi\pi \to ee$. Because these originate from non-renormalizable 6-fermion $\bar{q}q\bar{q}qee$ interactions at the LEFT scale, we cannot simply add them to the renormalizible QCD Lagrangian in the same external field formalism we used before[3]. The relevant $0\nu\beta\beta$ diagrams generated by these dimension-9 LEFT operators are shown in Figure 4.11.

Instead, one has to resort towards matching the short-range dimension-9 LEFT operators to the corresponding chiral $NNNNee$, $NN\pi ee$ and $\pi\pi ee$ operators based on symmetry arguments alone. As the hadronization from quarks to nucleons is caused by QCD interactions, each quark level operator should match onto chiral operators that follow the same parity as well as $SU(2)_L \times SU(2)_R$ symmetry structure in the massless quark limit. This matching procedure has first been done for a LEFT dimension-9 operator basis of parity eigenstates in Ref. [180] and redone for our choice of LEFT basis in Ref. [45]. In this section, we will summarize the relevant equations identified in Ref. [45].

4.5.5.1 $\pi\pi$ee

The relevant scalar $\pi\pi ee$ operators that induce $0\nu\beta\beta$ diagrams of the type shown in the left part of Figure 4.11 are summarized in Ref. [45]

$$\begin{aligned}\mathcal{L}^{(s)}_{\pi\pi ee} = \frac{F_0^4}{4v^5}\Bigg[&\frac{5}{3}g_1^{\pi\pi}\left(C_{1L}^{(9)} + C_{1L}^{(9)\prime}\right)\partial_\mu\pi^-\partial^\mu\pi^- \\ &+ \left(g_4^{\pi\pi}C_{4L}^{(9)} + g_5^{\pi\pi}C_{5L}^{(9)} - g_2^{\pi\pi}\left(C_{2L}^{(9)} + C_{2L}^{(9)\prime}\right) - g_3^{\pi\pi}\left(C_{3L}^{(9)} + C_{3L}^{(9)\prime}\right)\right)\pi^-\pi^-\Bigg]\overline{e_L}e_L^C \\ &+ (L \leftrightarrow R). \end{aligned} \tag{4.95}$$

[3] If we did so, we would have put quark-containing operators into the external fields, thus defying their purpose and missing the quark to nucleon and meson transition.

4.5.5.2 NNπee

LNV nucleon-pion interactions of the type $NN\pi ee$ are generated by the scalar $\mathcal{O}_{1L}^{(9)}, \mathcal{O}_{1L}^{(9)\prime}$ operators in

$$\mathcal{L}_{NN\pi ee}^{(s)} = \frac{1}{v^5}\sqrt{2} g_A g_1^{\pi N} F_0 \big(C_{1L}^{(9)} + C_{1L}^{(9)\prime}\big) \big[\overline{p} S \cdot (\partial \pi^-) n\big] \overline{e_L} e_L^C + (L \leftrightarrow R), \tag{4.96}$$

as well as the vector operators $\mathcal{O}_{6,7,8,9}^{(9)}, \mathcal{O}_{6,7,8,9}^{(9)\prime}$ generating

$$\mathcal{L}_{NN\pi ee}^{(v)} = \frac{1}{v^5}\sqrt{2} g_A F_0 \big[\overline{p} S \cdot (\partial \pi^-)\big] \big(g_V^{\pi N} C_V^{(9)} + \tilde{g}_V^{\pi N} \tilde{C}_V^{(9)}\big) v^\mu \overline{e} \gamma_\mu \gamma_5 e^C, \tag{4.97}$$

with

$$\begin{aligned} C_V^{(9)} &= C_6^{(9)} + C_6^{(9)\prime} + C_8^{(9)} + C_8^{(9)\prime}, \qquad & g_V^{\pi N} &= g_6^{\pi N} + g_8^{\pi N}, \\ \tilde{C}_V^{(9)} &= C_7^{(9)} + C_7^{(9)\prime} + C_9^{(9)} + C_9^{(9)\prime}, \qquad & \tilde{g}_V^{\pi N} &= g_7^{\pi N} + g_9^{\pi N}. \end{aligned} \tag{4.98}$$

4.5.5.3 NNNNee

Similarly to the scalar (s) and vector (v) $\pi\pi ee$ and $NN\pi ee$ Lagrangians, the relevant scalar $NNNNee$ Lagrangian is given by

$$\begin{aligned} \mathcal{L}_{NNNNee}^{(s)} = \frac{1}{v^5}\Big[& g_1^{NN}\big(C_{1L}^{(9)} + C_{1L}^{(9)\prime}\big) + g_2^{NN}\big(C_{2L}^{(9)} + C_{2L}^{(9)\prime}\big) + g_3^{NN}\big(C_{3L}^{(9)} + C_{1L}^{(9)\prime}\big) \\ & + g_4^{NN} C_{4L}^{(9)} + g_5^{NN} C_{5L}^{(9)}\Big] \big[\overline{p} n\big] \big[\overline{p} n\big] \overline{e_L} e_L^C + (L \leftrightarrow R), \end{aligned} \tag{4.99}$$

while the corresponding vector operators are

$$\mathcal{L}_{NNNNee}^{(v)} = \frac{1}{v^5}\Big[g_6^{NN} C_V^{(9)} + g_7^{NN} \tilde{C}_V^{(9)}\Big] \big[\overline{p} n\big] \big[\overline{p} n\big] v^\mu \overline{e} \gamma_\mu \gamma_5 e^C. \tag{4.100}$$

4.5.5.4 Leading Order Counter Terms

Additionally, renormalization of the neutrino-exchanging $0\nu\beta\beta$ diagrams associated with the neutrino mass $m_{\beta\beta}$ as well as the LEFT dimension-6 operators $\mathcal{O}_{VL}^{(6)}, \mathcal{O}_{VR}^{(6)}, \mathcal{O}_T^{(6)}$ requires the introduction of $NNNNee, NN\pi ee$ and $\pi\pi ee$ counter terms to the LO Lagrangian [45, 181, 182]. These contact interactions arising from hard-neutrino ex-

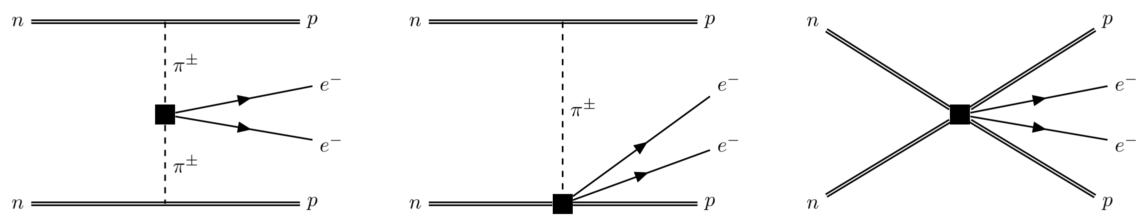

Figure 4.11: The chiral EFT $0\nu\beta\beta$ diagrams originating from the dimension-9 $qqqqee$ LEFT operators [45]. The $0\nu\beta\beta$ can be induced via interactions of the type $\pi^-\pi^- \to e^-e^-$ (left), $\pi^- n \to pe^-\nu_e$ (center), and $nn \to ppe^-e^-$ (right).

change [181, 182] are given by [45]

$$\begin{aligned}
\mathcal{L}^{(ct)}_{NNNNee} =& 2G_F^2 V_{ud}^2 m_{\beta\beta} g_\nu^{NN} \left[\overline{N} u^\dagger \tau^+ u N\right] \left[\overline{N} u^\dagger \tau^+ u N\right] \overline{e_L} e_L^C \\
&+ iV_{ud} \frac{1}{v^4} \left[\frac{g^E_{VL}}{m_\pi^2} C^{(6)}_{VL} + \frac{g^E_{VR}}{m_\pi^2} C^{(6)}_{VR}\right] \left[\overline{p} n\right] \left[\overline{p} n\right] v^\mu v^\nu \overline{e} \gamma_\mu \overleftrightarrow{\partial}_\nu e^C \\
&+ V_{ud} \frac{m_e}{v^4} \left[\frac{g^{m_e}_{VL}}{m_\pi^2} C^{(6)}_{VL} + \frac{g^{m_e}_{VR}}{m_\pi^2} C^{(6)}_{VR}\right] \left[\overline{p} n\right] \left[\overline{p} n\right] \overline{e} e^C \\
&+ \frac{V_{ud}}{v^4} \left[\frac{g^{NN}_{VL}}{m_N} C^{(6)}_{VL} v^\mu \overline{e} \gamma_\mu \gamma_5 e^C + \frac{g^{NN}_T}{m_N} C^{(6)}_T \overline{e_L} e_L^C\right] \left[\overline{p} n\right] \left[\overline{p} n\right]. \qquad (4.101)
\end{aligned}$$

Similarly, one has to introduce LO $\pi\pi ee$ and $NN\pi ee$ interactions given by [45]

$$\begin{aligned}
\mathcal{L}^{(ct)}_{\pi\pi ee} =& V_{ud} \frac{F_0^2}{2m_N v^4} \partial_\mu \pi^- \partial^\mu \pi^- g_T^{\pi\pi} C_T^{(6)} \overline{e_L} e_L^C, \\
\mathcal{L}^{(ct)}_{NN\pi ee} =& \sqrt{2} V_{ud} \frac{g_A F_0}{v^4} \left[\overline{p} S \cdot (\partial \pi^-) n\right] \left[\frac{g^{\pi N}_{VL}}{m_N} C^{(6)}_{VL} v^\mu \overline{e} \gamma_\mu \gamma_5 e^C + \frac{g^{\pi N}_T}{m_N} C^{(6)}_T \overline{e_L} e_L^C\right]. \qquad (4.102)
\end{aligned}$$

4.5.6 Estimating the Low Energy Constants of Chiral EFT

The above chiral Lagrangians introduce new LECs which are the coupling constants of χPT and χEFT. Due to the non-perturbative nature of QCD, we cannot simply derive these couplings by the same matching procedure we employed for the SMEFT-to-LEFT matching. Instead, the LECs of χEFT have to be derived either on experimental grounds, by relating the LECs to certain physical observables, such as, e.g., masses or scattering amplitudes. Alternatively, one can use non-perturbative methods such as lattice QCD to calculate the LECs from first principles. When neither of these options is available, the best remaining option is to estimate the order of magnitude of the unknkown LECs g_i that appear in some operator $\mathcal{O}_i$ via a naive dimensional analysis

(NDA) [183, 184] as

$$g_i \sim f^2\Lambda^2 \left(\frac{1}{f}\right)^{N_{\phi,i}} \left(\frac{1}{f\sqrt{\Lambda}}\right)^{N_{\Psi,i}} \left(\frac{g_X}{\Lambda^2}\right)^{N_{X,i}} \left(\frac{1}{\Lambda}\right)^{N_{D,i}}, \tag{4.103}$$

where $N_{\phi,\Psi,X,D,i}$ are the numbers of scalars, fermions, gauge field tensors and covariant derivatives in the corresponding operator, g_X is the gauge coupling related to the gauge field tensor X and $\Lambda \sim 4\pi f$ is the suppression scale.

While this simple NDA estimate does give quite reliable projections of the LECs in the mesonic and single-nucleon sector of χPT, it is known to fail in the multi-nucleon regime of χEFT [182, 185–187]. Instead, the corresponding LECs were estimated based on renormalization arguments in Refs. [45, 182]. The relevant LECs obtained in these ways are summarized in Table 4.6. Nevertheless, in what follows we will refer to all order of magnitude estimates of unknown LECs as NDA estimates. It should be noted that precise values of these short-range LECs such as g_ν^{NN} depend on the applied renormalization scheme which in turn affects the size of the relevant nuclear forces that enter the calculation of NMEs. Hence, the numerical values of the short-range LECs have to be determined in the same regularization scheme used in the NME calculations. The pathway towards a reliable determination of the short-range LECs has been worked out in Refs. [176, 188] and applied to the LνEM in Ref. [189] which provided the value given for g_ν^{NN} in Table 4.6. Strictly speaking, the numerical value of g_ν^{NN} given in Table 4.6 only applies to the NMEs calculated in Ref. [189]. It is for this reason that we assign an uncertainty of $\pm 50\%$ to g_ν^{NN} [2].

Obviously, the $0\nu\beta\beta$ half-life is highly sensitive to the precise values of the currently unknown LECs. In order to provide conservative numerical estimates of the expected $0\nu\beta\beta$ half-lives, we will generally be using a benchmark scenario with all unknown LECs being put to zero except for the short-range LECs that enter the calculation of the $0\nu\beta\beta$ transition amplitude generated by the short-range vector operators where we take $g_6^{NN} = g_7^{NN} = g_V^{\pi N} = \tilde{g}_V^{\pi N} = 1$. Keeping these LECs non-zero is necessary in order not to completely omit the contributions of the short-range vector operators $\mathcal{O}_i^{(9)(\prime)}, i \in [6, ..., 9]$.

4.6 Neutral-Current Contributions to Neutrinoless Double Beta Decay

Within the χEFT formalism derived in Refs. [44, 45] as well as in most of the general literature the contribution of neutral-current LNV operators to the $0\nu\beta\beta$ amplitude is generally ignored. At first sight, this is done for good reason as there are simply no tree-level $0\nu\beta\beta$ diagrams that can be drawn from neutral-current LNV interactions. However, as was first noted by Babič et al. [193] the formation of a non-vanishing quark condensate $\langle\overline{q}q\rangle$ in combination with LNV neutral-current $\overline{\nu}\nu^C\overline{q}q$ operators can induce a non-zero Majorana mass for the neutrinos.

This feature is easy to see in the χPT framework. Indeed, the leading order meson

$n \to pe\nu$, $\pi \to e\nu$			$\pi\pi \to ee$		
g_A	1.271 ± 0.002	[190]	$g_1^{\pi\pi}$	0.36 ± 0.02	[191]
g_S	0.97 ± 0.13	[192]	$g_2^{\pi\pi}$	2.0 ± 0.2 GeV^2	[191]
g_M	4.7	[190]	$g_3^{\pi\pi}$	$-(0.62 \pm 0.06)$ GeV^2	[191]
g_T	0.99 ± 0.06	[192]	$g_4^{\pi\pi}$	$-(1.9 \pm 0.2)$ GeV^2	[191]
$\lvert g_T' \rvert$	$\mathcal{O}(1)$		$g_5^{\pi\pi}$	$-(8.0 \pm 0.6)$ GeV^2	[191]
B	2.7 GeV		$\lvert g_T^{\pi\pi} \rvert$	$\mathcal{O}(1)$	
$n \to p\pi ee$			$nn \to pp\, ee$		
$\lvert g_1^{\pi N} \rvert$	$\mathcal{O}(1)$		$\lvert g_1^{NN} \rvert$	$\mathcal{O}(1)$	
$\lvert g_{6,7,8,9}^{\pi N} \rvert$	$\mathcal{O}(1)$		$\lvert g_{6,7}^{NN} \rvert$	$\mathcal{O}(1)$	
$\lvert g_{VL}^{\pi N} \rvert$	$\mathcal{O}(1)$		$\lvert g_{VL}^{NN} \rvert$	$\mathcal{O}(1)$	
$\lvert g_T^{\pi N} \rvert$	$\mathcal{O}(1)$		$\lvert g_T^{NN} \rvert$	$\mathcal{O}(1)$	
			$\lvert g_\nu^{NN} \rvert$	$-92.9\,\text{GeV}^{-2} \pm 50\%$	[176, 188, 189]
			$\lvert g_{VL,VR}^{E,m_e} \rvert$	$\mathcal{O}(1)$	
			$\lvert g_{2,3,4,5}^{NN} \rvert$	$\mathcal{O}((4\pi)^2)$	

Table 4.6: The low-energy constants of chiral EFT. The table is taken from Ref. [2], which is an updated version of the values given in Ref. [45].

Lagrangian of χPT of eq. (4.60) contains the term

$$\mathcal{L}_\pi^{(0)} \supset BF_0^2\big(s^u + s^d\big), \tag{4.104}$$

with the scalar external fields $s^{u,d}$ given by eq. (4.50)

$$\begin{aligned} s^u &= \frac{1}{2v^2}\Big[C_{SL,\nu u}^{(6)} + C_{SR,\nu u}^{(6)}\Big]\big[\overline{\nu_L}\nu_L^C\big] + \text{h.c.},\\ s^d &= \frac{1}{2v^2}\Big[C_{SL,\nu d}^{(6)} + C_{SR,\nu d}^{(6)}\Big]\big[\overline{\nu_L}\nu_L^C\big] + \text{h.c.}, \end{aligned} \tag{4.105}$$

and the quark condensate being parameterized by $3F_0^2 B = -\langle\overline{q}q\rangle$ [172]. By relating B to the pion mass $m_\pi^2 = B(m_u + m_d)$ one finds that $B \simeq 2.7\,\text{GeV}$ [44, 45]. Consequently, in the low-energy realm of χPT the neutral-current LNV scalar operators $C_{SL,SR,\nu,u,d}^{(6)}$ generate a Majorana neutrino mass of

$$m_\nu = -\frac{BF_0^2}{v^2}\Big[C_{SL,\nu u}^{(6)} + C_{SR,\nu u}^{(6)} + C_{SL,\nu d}^{(6)} + C_{SR,\nu d}^{(6)}\Big] \simeq 9.3 \times 10^4\,\text{eV} \times C_{S,NC}^{(6)}, \tag{4.106}$$

where we define the neutral-current LNV coefficient

$$C_{S.NC}^{(6)} = -\Big[C_{SL,\nu u}^{(6)} + C_{SR,\nu u}^{(6)} + C_{SL,\nu d}^{(6)} + C_{SR,\nu d}^{(6)}\Big]. \tag{4.107}$$

As already stated, this contribution has been ignored in the original formulation of Refs. [44, 45] as well as within our earlier publications [1, 2] but will be included in this work. Notice that the SMEFT-to-LEFT matching relations were obtained in Refs. [2, 44] which did not consider neutral-current contributions to $0\nu\beta\beta$ and consequently did not derive the matching relations onto the neutral-current LEFT operators. The same is true for the LEFT RGEs derived in Refs. [44, 45]. The full matching relations will be published in a future work. However, we do not expect a significant correction to the $0\nu\beta\beta$ half-life from the inclusion of the neutral-current operators when considering SMEFT operators that also map onto charged-current LEFT operators. This is because of the relatively small contribution of the neutral-current dimension-6 LEFT operators to the $0\nu\beta\beta$ amplitude in comparison to the charged-current dimension-6 operators. As we will see in the following chapter, the current best limit on the $0\nu\beta\beta$ half-life in ^{136}Xe set by the KamLAND-Zen collaboration [46] constraints the charged-current LNV dimension-6 LEFT operators to be smaller than $10^{-7} - 10^{-9}$ while the upper limit on the neutral-current operators is "only" at around 10^{-4}. Nevertheless, to our knowledge this bound represents the most stringent limit on BSM neutral-current neutrino-quark interactions available to this date. In Ref. [5] we will discuss the impacts of LNV neutral-current interactions on $0\nu\beta\beta$ in more detail.

4.7 Calculating the $0\nu\beta\beta$ Half-Life

4.7.1 The Light Neutrino-Exchange Mechanism

We are now equipped with the necessary tools to calculate the $0\nu\beta\beta$ transition amplitude at the nuclear scale. The general transition amplitude including all relevant operators and interference terms has been derived in Ref. [182] which we will summarize at the end of this section. Here, we will rederive the $0\nu\beta\beta$ transition amplitude of the standard LνEM without the recently discovered contact interaction as an example.

4.7.1.1 Transition Amplitude

The transition amplitude for the LνEM of $0\nu\beta\beta$ can be read from the two diagrams in Figure 4.12. It is simply given by two single-beta decay amplitudes connected via a Majorana neutrino propagator. In momentum-space, the $0^+ \to 0^+$ ground-state to ground-state transition amplitude is defined as

$$\mathcal{A} = \left\langle 0^+ \right| \mathcal{V}(\mathbf{q}^2) \left| 0^+ \right\rangle, \tag{4.108}$$

with the so-called neutrino-potential defined as

$$\begin{aligned}\mathcal{V} =& 2G_F^2 V_{ud}^2 \big(J_V^\mu(1) + J_A^\mu(1)\big)\tau_1^+ \overline{e_L}(k_1)\gamma_\mu \sum_{i=1}^{3} U_{ei} \frac{\not{q} + m_i}{q^2 - m_i^2} (U_{ie})^T \gamma_\nu e_L^C(k_2) \big(J_V^\nu(2) + J_A^\nu(2)\big)\tau_2^+ \\ &- (k_1 \leftrightarrow k_2),\end{aligned} \tag{4.109}$$

where the $(k_1 \leftrightarrow k_2)$ part arises from the right diagram in Figure 4.12. Assuming that the electron momenta are small, $k_{1,2} \simeq \mathcal{O}(\text{MeV}) \ll m_\pi$, we can take the momentum exchange carried in the neutrino propagator to be equal in both diagrams. The relative

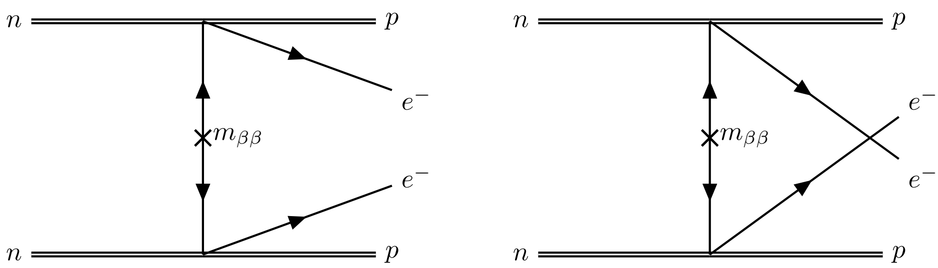

Figure 4.12: Relevant diagrams for the standard light neutrino-exchange mechanism of $0\nu\beta\beta$.

minus sign between the two contributions arises due to the anti-symmetric nature of fermions. Noticing that

$$P_L(\not{q} + m_i)P_L = m_i P_L, \tag{4.110}$$

and taking the limit of small neutrino masses $m_i^2 \ll q^2$, as well as ignoring the nuclear recoil energy $q^0 \ll |\mathbf{q}|$, we can separate the nuclear and leptonic parts and write

$$\begin{aligned}\mathcal{V} =& 2G_F^2 V_{ud}^2 m_{\beta\beta} \frac{1}{-\mathbf{q}^2}\Big[(J_V^\mu(1) + J_A^\mu(1))(J_V^\nu(2) + J_A^\nu(2))\tau_1^+\tau_2^+\Big]\Big[\overline{e}(k_1)\gamma_\mu\gamma_\nu P_R e^C(k_2)\Big] \\ &- (k_1 \leftrightarrow k_2),\end{aligned} \tag{4.111}$$

with the effective Majorana mass $m_{\beta\beta}$ defined as

$$m_{\beta\beta} = \sum_{i=1}^{3} U_{ei}^2 m_i. \tag{4.112}$$

Using the property (c.f. appendix B.1)

$$\overline{\Psi}_1\gamma^\mu\gamma^\nu\Psi_2^C = -\overline{\Psi}_2\gamma^\mu\gamma^\nu\Psi_1^C, \tag{4.113}$$

we can see that the second ($k_1 \leftrightarrow k_2$) diagram gives the same contribution as the first diagram resulting in

$$\mathcal{V} = -4G_F^2 V_{ud}^2 m_{\beta\beta} \frac{1}{\mathbf{q}^2}\Big[(J_V^\mu(1) + J_A^\mu(1))(J_V^\nu(2) + J_A^\nu(2))\tau_1^+\tau_2^+\Big]\Big[\overline{e}(k_1)\gamma_\mu\gamma_\nu P_R e^C(k_2)\Big]. \tag{4.114}$$

With the anti-commutator relation for the gamma matrices

$$\{\gamma^\mu, \gamma^\nu\} = 2g^{\mu\nu}, \tag{4.115}$$

we can rewrite the leptonic current as

$$\overline{e}(k_1)\gamma_\mu\gamma_\nu P_R e^C(k_2) = \overline{e}(k_1)\left(g^{\mu\nu} + \frac{1}{2}(\gamma^\mu\gamma^\nu - \gamma^\nu\gamma^\mu)\right)P_R e^C(k_2), \tag{4.116}$$

and notice that due to the symmetric nature of the nuclear currents, only the symmetric part of the leptonic currents survives. Hence, the potential simplifies to

$$\mathcal{V} = -4G_F^2 V_{ud}^2 m_{\beta\beta}\frac{1}{\mathbf{q}^2}\Big[g_{\mu\nu}(J_V^\mu(1)+J_A^\mu(1))(J_V^\nu(2)+J_A^\nu(2))\tau_1^+\tau_2^+\Big]\Big[\overline{e}(k_1)P_R e^C(k_2)\Big]. \tag{4.117}$$

4.7.1.2 Nuclear Matrix Elements

Let us first focus on the nuclear part of the transition amplitude. The leading order ground state $0\nu\beta\beta$ is of the type $0^+ \to 0^+$, i.e., it is parity even and spin conserving. Therefore, only even powers of $\mathbf{q}$ contribute to the $0^+ \to 0^+$ amplitude. Because the leptonic part of the transition amplitude in eq. (4.117) is independent of $\mathbf{q}$, only the parity even parts of the nuclear currents contribute to the $0^+ \to 0^+$ transition. These are given by [178]

$$\begin{aligned}
J_V^\mu(1)J_{V\mu}(2) &= g_V^2(\mathbf{q}^2) - g_M^2(\mathbf{q}^2)\frac{\mathbf{q}^2}{6m_N}\left(\boldsymbol{\sigma}_1\cdot\boldsymbol{\sigma}_2 + \frac{1}{2}S^{(12)}\right),\\
J_A^\mu(1)J_{A\mu}(2) &= -g_A^2\Bigg[\boldsymbol{\sigma}_1\cdot\boldsymbol{\sigma}_2\left(\frac{g_A^2(\mathbf{q^2})}{g_A^2} + \frac{g_A(\mathbf{q}^2)g_P(\mathbf{q}^2)\mathbf{q}^2}{3g_A^2 m_N} + \frac{g_P^2(\mathbf{q^2})\mathbf{q}^4}{12g_A^2m_N^2}\right)\\
&\qquad - S^{(12)}\left(\frac{g_A(\mathbf{q}^2)g_P(\mathbf{q}^2)\mathbf{q}^2}{3g_A^2m_N} + \frac{g_P^2(\mathbf{q^2})\mathbf{q}^4}{12g_A^2m_N^2}\right)\Bigg],
\end{aligned} \tag{4.118}$$

with the tensor operator

$$S^{(12)} = \boldsymbol{\sigma}_1\cdot\boldsymbol{\sigma}_2 - 3(\boldsymbol{\sigma}_1\cdot\hat{\boldsymbol{q}})(\boldsymbol{\sigma}_2\cdot\hat{\boldsymbol{q}}), \qquad \hat{\boldsymbol{q}} = \frac{\boldsymbol{q}}{|\boldsymbol{q}|}. \tag{4.119}$$

The form factors in the nuclear currents can be summarized in the Fermi (F), Gamow-Teller (GT), and Tensor (T) contributions as [44, 45]

$$\begin{aligned}
&h_F(\mathbf{q}^2) = g_V(\mathbf{q}^2), \qquad h_{GT}^{AA}(\mathbf{q}^2) = \frac{g_A^2(\mathbf{q}^2)}{g_A^2}, \qquad h_{GT}^{AP}(\mathbf{q}^2) = \frac{g_P(\mathbf{q}^2)g_A(\mathbf{q}^2)}{g_A^2}\frac{\mathbf{q}^2}{3m_N},\\
&h_{GT}^{PP} = \frac{g_P^2(\mathbf{q}^2)}{g_A^2}\frac{\mathbf{q}^4}{12m_N^2}, \qquad h_{GT}^{MM}(\mathbf{q}^2) = \frac{g_M^2(\mathbf{q}^2)}{g_A^2}\frac{\mathbf{q}^2}{6m_N^2}, \qquad h_T^{AA}(\mathbf{q}^2) = h_{GT}^{AA}(\mathbf{q}^2),\\
&h_T^{AP}(\mathbf{q}^2) = -h_{GT}^{AP}(\mathbf{q}^2), \qquad h_T^{PP}(\mathbf{q}^2) = -h_{GT}^{PP}(\mathbf{q}^2), \qquad h_T^{MM}(\mathbf{q}^2) = \frac{1}{2}h_{GT}^{MM}(\mathbf{q}^2),
\end{aligned} \tag{4.120}$$

such that we can write the relevant parts of the nuclear currents as

$$\begin{aligned}
J_V^\mu(1)J_{V\mu}(2) &= -g_A^2\left[-\frac{1}{g_A^2}h_F(\mathbf{q}^2) + h_{GT}^{MM}(\mathbf{q}^2)\boldsymbol{\sigma}_1\cdot\boldsymbol{\sigma}_2 + h_T^{MM}(\mathbf{q}^2)S^{(12)}\right],\\
J_A^\mu(1)J_{A\mu}(2) &= -g_A^2\Bigg[\boldsymbol{\sigma}_1\cdot\boldsymbol{\sigma}_2\Big(h_{GT}^{AA}(\mathbf{q}^2) + h_{GT}^{AP}(\mathbf{q}^2) + h_{GT}^{PP}(\mathbf{q}^2)\Big)\\
&\qquad + S^{(12)}\Big(h_T^{AP}(\mathbf{q}^2) + h_T^{PP}(\mathbf{q}^2)\Big)\Bigg].
\end{aligned} \tag{4.121}$$

Summarizing the Gamow-Teller and Tensor contributions in

$$\begin{aligned} h_{GT}(\mathbf{q}^2) &= h_{GT}^{AA}(\mathbf{q}^2) + h_{GT}^{AP}(\mathbf{q}^2) + h_{GT}^{PP}(\mathbf{q}^2) + h_{GT}^{MM}(\mathbf{q}^2), \\ h_{T}(\mathbf{q}^2) &= h_{T}^{AP}(\mathbf{q}^2) + h_{T}^{PP}(\mathbf{q}^2) + h_{T}^{MM}(\mathbf{q}^2), \end{aligned} \tag{4.122}$$

we can write the potential as

$$\begin{aligned} \mathcal{V} =& 4G_F^2 V_{ud}^2 g_A^2 m_{\beta\beta} \frac{1}{\mathbf{q}^2} \Big[-\frac{1}{g_A^2} h_F(\mathbf{q}^2) + h_{GT}(\mathbf{q}^2) \boldsymbol{\sigma}_1 \cdot \boldsymbol{\sigma}_2 + h_T(\mathbf{q}^2) S^{(12)} \Big] \tau_1^+ \tau_2^+ \\ & \times \Big[\bar{e}(k_1) P_R e^C(k_2) \Big]. \end{aligned} \tag{4.123}$$

The numerical many-body calculations of the nuclear matrix elements that describe the transition at the level of composite nuclei are oftentimes performed in position-space (c.f. [194]). Hence, we define the position-space amplitude for the ground-state $0^+ \to 0^+$ transition as the Fourier transform of the momentum-space amplitude [182]

$$\mathcal{A}_r = \langle 0^+ | \sum_{m,n} \int \frac{\mathrm{d}^3 q}{(2\pi)^3} \exp\{i\mathbf{q} \cdot \mathrm{r}_{nm}\} \mathcal{V}(\mathbf{q}^2) \, |0^+\rangle \,, \tag{4.124}$$

where the sum is taken over all combinations of nucleons inside the nucleus with $m \neq n$ and we defined the spatial distance between the nuclei n, m as $\mathbf{r}_{nm} = \mathbf{r}_n - \mathbf{r}_m$. The $0\nu\beta\beta$ rate Γ is then related to the spin-summed and averaged transition amplitude via [23, 44, 195]

$$\mathrm{d}\Gamma = \frac{2\pi}{8} \sum_{\text{spins}} |\mathcal{A}_r|^2 \delta\big(\epsilon_1 + \epsilon_2 + E_f - E_i\big) F(Z, \epsilon_1) F(Z, \epsilon_2) \frac{\mathrm{d}^3 k_1}{(2\pi)^3 2\epsilon_1} \frac{\mathrm{d}^3 k_2}{(2\pi)^3 2\epsilon_2}, \tag{4.125}$$

where ϵ_j, k_j are the energy and momentum of the j-th electron, $E_{i,f}$ are the energies (masses) of the initial and final state nuclei, and the Fermi function for a point-like nucleus [196]

$$F(Z, E) = \frac{2\pi\eta}{1 - \exp\{(-2\pi\eta)\}}, \qquad \eta = Z\alpha \frac{m_e}{p}, \tag{4.126}$$

accounts for the effects of the Coulomb potential generated by the positively charged final-state nucleus on the emitted electrons.[4]

We can now switch to spherical coordinates and perform the integration over the angles ϕ, θ

$$\mathcal{A}_r = \langle 0^+ | \sum_{m,n} \int_0^{2\pi} \mathrm{d}\phi \int_0^{\pi} \mathrm{d}\theta \int_0^{\infty} \frac{\mathrm{d}|\mathbf{q}|}{(2\pi)^3} \, \mathbf{q}^2 \sin\theta \exp\{i|\mathbf{q}||\mathrm{r}_{nm}|\cos\theta\} \mathcal{V}(\mathbf{q}^2) \, |0^+\rangle \,. \tag{4.127}$$

[4] Note that the Fermi function has a pole at $p = 0$.

Noticing that the factor of $\mathbf{q}^2$ resulting from the Fourier transformation cancels with the $1/\mathbf{q}^2$ of the neutrino propagator we can define the position-space NMEs

$$\begin{aligned} M_F &= \langle 0^+ | \sum_{m,n} h_F(r) \tau^+_{(m)} \tau^+_{(n)} | 0^+ \rangle , \\ M^{ij}_{GT} &= \langle 0^+ | \sum_{m,n} h^{ij}_{GT}(r) \boldsymbol{\sigma}_{(m)} \cdot \boldsymbol{\sigma}_{(n)} \tau^+_{(m)} \tau^+_{(n)} | 0^+ \rangle , \\ M^{ij}_{T} &= \langle 0^+ | \sum_{m,n} h^{ij}_{T}(r) S^{(mn)}(\hat{\mathbf{r}}) \tau^+_{(m)} \tau^+_{(n)} | 0^+ \rangle . \end{aligned} \tag{4.128}$$

via the quantities [182, 194]

$$h^{ij}_K(r) = \frac{2}{\pi} R_A \int_0^\infty \mathrm{d}|\boldsymbol{q}|\, h^{ij}_K(\mathbf{q}^2) j_\lambda(|\mathbf{q}|r), \tag{4.129}$$

where $R_A = 1.2\,\mathrm{fm} \times A^{1/3}$ is the nuclear radius, and j_λ are the spherical bessel functions which arise from the spherical part of the Fourier transformation with $\lambda = 0$ for $K \in [F, GT]$, i.e. for the Fermi and Gamow-Teller transitions which are independent of $\cos\theta$, and $\lambda = 2$ for $K = T$, i.e. for the Tensor transitions.

Similarly, one can define the short-range NMEs that arise in the context of the dimension-9 LEFT operators not involving a neutrino exchange as [45]

$$\begin{aligned} h^{ij}_{K,sd}(r) &= \frac{2}{\pi} \frac{R_A}{m_\pi^2} \int_0^\infty \mathrm{d}|\boldsymbol{q}|\, \boldsymbol{q}^2 h^{ij}_K(\mathbf{q}^2) j_\lambda(|\mathbf{q}|r), \\ M_{F,sd} &= \langle 0^+ | \sum_{m,n} h_{F,sd}(r) \tau^+_{(m)} \tau^+_{(n)} | 0^+ \rangle , \\ M^{ij}_{GT,sd} &= \langle 0^+ | \sum_{m,n} h^{ij}_{GT,sd}(r) \boldsymbol{\sigma}_{(m)} \cdot \boldsymbol{\sigma}_{(n)} \tau^+_{(m)} \tau^+_{(n)} | 0^+ \rangle , \\ M^{ij}_{T,sd} &= \langle 0^+ | \sum_{m,n} h^{ij}_{T,sd}(r) S^{(mn)}(\hat{\mathbf{r}}) \tau^+_{(m)} \tau^+_{(n)} | 0^+ \rangle . \end{aligned} \tag{4.130}$$

With the normalization factor R_A/m_π^2 the short-range NMEs are typically of the same order as the long-range NMEs. Note that within the literature, oftentimes a different normalization factor of $R_A/(m_e m_p)$ is used [194, 197, 198]. Hence, when implementing the results of numerical NME calculations from the literature, one has to be careful to use the same conventions and apply possible rescalings appropriately when necessary.

In Table 4.7 we provide a comprehensive set of NMEs calculated in the Interacting Boson Model 2 (IBM2) [197] covering most $0\nu\beta\beta$ candidate isotopes. Throughout this work, we will use this set of NMEs. Exceptions from this will be stated explicitly. For a comparison and review of the various different approaches to NMEs see Ref. [199].

4.7.1.3 Phase-Space Factor

The last remaining part of the half-life calculation for the LνEM is the leptonic PSF. With the definition of the NMEs above we can write the spin-summed absolute square

	M_F	M_{GT}^{AA}	M_{GT}^{AP}	M_{GT}^{PP}	M_{GT}^{MM}	M_T^{AA}	M_T^{AP}	M_T^{PP}	M_T^{MM}	M_{Fsd}	M_{GTsd}^{AA}	M_{GTsd}^{AP}	M_{GTsd}^{PP}	M_{Tsd}^{AP}	M_{Tsd}^{PP}
^{76}Ge	-0.78	6.06	-0.86	0.17	0.20	0.0	0.24	-0.06	0.04	-1.20	4.18	-1.24	0.29	-0.77	0.23
^{82}Se	-0.67	4.93	-0.71	0.14	0.17	0.0	0.24	-0.06	0.04	-1.01	3.46	-1.03	0.25	-0.73	0.22
^{96}Zr	-0.36	4.32	-0.64	0.13	0.15	0.0	-0.21	0.05	-0.04	-0.87	3.06	-0.89	0.21	0.64	-0.20
^{100}Mo	-0.51	5.55	-0.90	0.20	0.22	0.0	-0.29	0.07	-0.05	-1.28	4.48	-1.33	0.30	0.93	-0.28
^{110}Pd	-0.42	4.43	-0.76	0.17	0.18	0.0	-0.21	0.06	-0.04	-1.07	3.72	-1.11	0.25	0.79	-0.24
^{116}Cd	-0.34	3.17	-0.55	0.12	0.13	0.0	-0.12	0.04	-0.03	-0.80	2.72	-0.81	0.18	0.49	-0.16
^{124}Sn	-0.57	3.37	-0.50	0.11	0.12	0.0	0.12	-0.03	0.02	-0.82	2.56	-0.77	0.19	-0.42	0.13
^{128}Te	-0.72	4.32	-0.64	0.13	0.15	0.0	0.12	-0.04	0.03	-1.03	3.24	-0.98	0.24	-0.52	0.16
^{130}Te	-0.65	3.89	-0.57	0.12	0.14	0.0	0.14	-0.04	0.02	-0.94	2.95	-0.89	0.22	-0.47	0.15
^{134}Xe	-0.69	4.21	-0.62	0.13	0.15	0.0	0.12	-0.04	0.03	-0.97	3.07	-0.92	0.22	-0.48	0.15
^{136}Xe	-0.52	3.20	-0.45	0.09	0.11	0.0	0.12	-0.03	0.02	-0.73	2.32	-0.69	0.17	-0.36	0.12
^{148}Nd	-0.36	2.52	-0.48	0.11	0.12	0.0	-0.12	0.02	-0.02	-0.78	2.54	-0.79	0.19	0.30	-0.09
^{150}Nd	-0.51	3.75	-0.76	0.17	0.19	0.0	-0.12	0.04	-0.03	-0.74	2.46	-0.76	0.18	0.34	-0.10
^{154}Sm	-0.34	2.98	-0.52	0.11	0.13	0.0	-0.12	0.03	-0.02	-0.78	2.64	-0.79	0.19	0.39	-0.13
^{160}Gd	-0.42	4.22	-0.71	0.15	0.17	0.0	-0.21	0.05	-0.03	-1.02	3.52	-1.04	0.24	0.60	-0.19
^{198}Pt	-0.33	2.27	-0.50	0.11	0.12	0.0	-0.12	0.03	-0.02	-0.78	2.57	-0.78	0.18	0.37	-0.12
^{232}Th	-0.44	4.17	-0.76	0.17	0.18	0.0	-0.21	0.05	-0.04	-1.08	3.80	-1.11	0.25	0.69	-0.22
^{238}U	-0.52	4.96	-0.90	0.20	0.21	0.0	-0.21	0.06	-0.04	-1.29	4.51	-1.32	0.30	0.82	-0.25

Table 4.7: A comprehensive set of NMEs covering most $0\nu\beta\beta$ candidate isotopes. These NMEs have been calculated in Ref. [197] and have been rescaled to fit the conventions used in this work. This table was published in Ref. [1].

of the transition amplitude as

$$|\mathcal{A}|^2 = 16G_F^4 V_{ud}^4 \, |m_{\beta\beta}|^2 \, \frac{\pi^2}{4R_A^2} \, |\mathcal{M}|^2 \sum_{\text{spins}} |\overline{e}(k_1) P_R e^C(k_2)|^2, \tag{4.131}$$

with the NMEs summarized in

$$\begin{aligned} \mathcal{M} &= -\frac{1}{g_A^2} M_F + \mathcal{M}_{GT} + \mathcal{M}_T, \\ \mathcal{M}_{GT} &= M_{GT}^{AA} + M_{GT}^{AP} + M_{GT}^{PP} + M_{GT}^{MM}, & (4.132) \\ \mathcal{M}_T &= M_T^{AP} + M_T^{PP} + M_T^{MM}. & (4.133) \end{aligned}$$

We can perform the sum over the electron spins via the usual trace techniques

$$\sum_{\text{spin}} |\overline{e}(k_1) P_R e^C(k_2)|^2 = 2k_1^\mu k_{2\mu} = 2\big(\epsilon_1\epsilon_2 - |\mathbf{k}_1||\mathbf{k_2}|\cos\theta\big), \tag{4.134}$$

and by defining the PSF as

$$G_{01} = \frac{1}{\log 2}\frac{G_F^4 m_e^2}{64\pi^5 R_A^2}\int \mathrm{d}\cos(\theta)\mathrm{d}\epsilon_1\mathrm{d}\epsilon_2\,|\mathbf{k}_1||\mathbf{k}_1|(\epsilon_1\epsilon_2 - |\mathbf{k}_1||\mathbf{k_2}|\cos\theta) \\ F(Z,\epsilon_1)F(Z,\epsilon_2)\delta\big(\epsilon_1+\epsilon_2+E_f-E_i\big), \tag{4.135}$$

the half-life can be written as

$$\left(T_{1/2}^{0\nu}\right)^{-1} = \frac{\Gamma}{\log 2} = g_A^4 G_{01}\left|V_{ud}^2\mathcal{M}\right|^2\left|\frac{m_{\beta\beta}}{m_e}\right|^2. \tag{4.136}$$

It should be noted that, in contrast to most of the literature, we follow Refs. [44, 45, 178] in not including V_{ud} in the definition of the PSF but rather shift it towards the nuclear part of the amplitude. This is done in order to have a common prefactor for the PSFs of the LνEM (with two weak interaction vertices), other long-range mechanism (with one single weak interaction vertex), and short-range mechanisms without any weak interaction vertices.

The above definition of the PSF is a rather crude one which tries to capture the deformation of the electron wave functions generated from the nuclear Coulomb potential via the introduction of the Fermi functions $F(Z,E)$. Indeed, more sophisticated treatments exist that calculate the electron wave functions by solving the radial Dirac equations for point-like [200] or finite-size nuclei assuming either a uniform nuclear charge distribution [103] or a Woods-Saxon potential [201]. Additionally, screening effects resulting from the surrounding electron shells of the atom have been included in these calculations [103, 200, 201].

If we want to study also the remaining $0\nu\beta\beta$ mechanisms including interference scenarios of different mechanisms, we have to consider different leptonic currents and, hence, different PSFs as well. Using the formalism described in Ref. [200], it is convenient to define the general PSFs by splitting the leptonic currents into a radial part g as well as an angular dependent part h via

$$G_{0k} = C_k\frac{G_F^4 m_e^2}{64\pi^5\ln 2R^2}\int\delta\Big(\epsilon_1+\epsilon_2+E_f-E_i\Big) \\ \times\Big(h_{0k}(\epsilon_1,\epsilon_2,R)\cos\theta + g_{0k}(\epsilon_1,\epsilon_2,R)\Big) \\ \times k_1k_2\epsilon_1\epsilon_2\,\mathrm{d}\epsilon_1\,\mathrm{d}\epsilon_2\,\mathrm{d}(\cos\theta). \tag{4.137}$$

Again, k_i and ϵ_i denote the absolute values of the momentum and energy of the i-th electron. The angular-dependent and independent functions h, g depend on the approximations used in the calculations of the electron wave functions as described in Ref. [200] and exact solutions require numerical methods [103]. We have calculated the PSFs by analytically solving the radial electron wave functions to the lowest order assuming a uniform charge distribution (see Ref. [200] scheme “A”) as well as via the analytic solution of the electron wave functions for a point-like nucleus (see Ref. [200] scheme “B”) while exact solutions for a uniform or Woods-Saxon charge distribution including the

	Q	$\overline{N}$	$G_{01}[10^{-14}\mathrm{yr}^{-1}]$		$G_{02}[10^{-14}\mathrm{yr}^{-1}]$		$G_{03}[10^{-14}\mathrm{yr}^{-1}]$		$G_{04}[10^{-14}\mathrm{yr}^{-1}]$		$G_{06}[10^{-14}\mathrm{yr}^{-1}]$		$G_{09}[10^{-14}\mathrm{yr}^{-1}]$	
Isotope	[MeV]	[%]	A	B	A	B	A	B	A	B	A	B	A	B
^{46}Ca	0.989	0.004	0.017	0.016	0.006	0.006	0.005	0.005	0.012	0.012	0.036	0.035	0.042	0.041
^{48}Ca	4.267	0.187	2.910	2.780	19.000	18.100	2.250	2.110	2.786	2.696	2.688	2.524	6.092	5.805
^{70}Zn	0.997	0.610	0.027	0.026	0.010	0.010	0.009	0.008	0.020	0.019	0.060	0.055	0.070	0.066
^{76}Ge	2.039	7.730	0.290	0.271	0.474	0.449	0.164	0.149	0.253	0.244	0.442	0.400	0.654	0.607
^{80}Se	0.134	49.610	0.001	0.000	0.000	0.000	0.000	0.000	0.000	0.000	0.002	0.002	0.002	0.002
^{82}Se	2.996	8.730	1.270	1.170	4.400	4.070	0.893	0.791	1.179	1.116	1.526	1.343	2.739	2.502
^{86}Kr	1.258	17.279	0.075	0.070	0.047	0.045	0.030	0.027	0.059	0.057	0.149	0.133	0.184	0.169
^{94}Zr	1.142	17.380	0.074	0.068	0.038	0.036	0.027	0.024	0.056	0.054	0.153	0.134	0.184	0.166
^{96}Zr	3.349	2.800	2.680	2.390	11.600	10.400	2.010	1.700	2.511	2.336	2.981	2.512	5.721	5.053
^{98}Mo	0.110	24.390	0.001	0.001	0.000	0.000	0.000	0.000	0.000	0.000	0.003	0.002	0.003	0.002
^{100}Mo	3.034	9.820	2.100	1.860	7.540	6.760	1.510	1.270	1.940	1.804	2.496	2.077	4.505	3.959
^{104}Ru	1.301	18.620	0.142	0.128	0.096	0.090	0.059	0.051	0.111	0.107	0.275	0.234	0.343	0.304
^{110}Pd	2.017	11.720	0.641	0.567	1.060	0.960	0.375	0.311	0.558	0.522	0.990	0.819	1.447	1.264
^{114}Cd	0.542	28.730	0.020	0.018	0.002	0.002	0.003	0.003	0.011	0.011	0.053	0.045	0.057	0.049
^{116}Cd	2.813	7.490	2.290	1.980	7.230	6.340	1.620	1.300	2.097	1.930	2.872	2.296	4.963	4.233
^{122}Sn	0.373	4.630	0.010	0.009	0.000	0.000	0.001	0.001	0.005	0.005	0.031	0.026	0.032	0.028
^{124}Sn	2.291	5.790	1.250	1.080	2.680	2.370	0.800	0.640	1.116	1.030	1.798	1.426	2.786	2.366
^{128}Te	0.867	31.740	0.081	0.071	0.023	0.022	0.023	0.019	0.055	0.054	0.187	0.151	0.212	0.180
^{130}Te	2.528	34.080	2.000	1.700	5.200	4.510	1.360	1.060	1.809	1.656	2.700	2.094	4.400	3.681
^{134}Xe	0.826	10.436	0.083	0.073	0.021	0.020	0.023	0.018	0.056	0.055	0.197	0.157	0.221	0.185
^{136}Xe	2.458	8.857	2.090	1.760	5.150	4.440	1.400	1.080	1.876	1.710	2.861	2.182	4.592	3.800
^{142}Ce	1.417	11.114	0.506	0.428	0.419	0.374	0.234	0.178	0.407	0.380	0.949	0.715	1.209	0.986
^{146}Nd	0.070	17.189	0.002	0.002	0.000	0.000	0.000	0.000	0.000	0.001	0.008	0.006	0.008	0.006
^{148}Nd	1.928	5.756	1.510	1.240	2.340	2.000	0.881	0.649	1.300	1.179	2.392	1.743	3.426	2.750
^{150}Nd	3.371	5.638	9.790	7.750	44.600	35.900	7.770	5.480	9.135	7.965	10.899	7.621	20.861	16.293
^{154}Sm	1.251	22.750	0.489	0.406	0.313	0.279	0.204	0.150	0.380	0.355	0.975	0.709	1.193	0.951
^{160}Gd	1.731	21.860	1.480	1.200	1.860	1.580	0.808	0.574	1.246	1.130	2.497	1.755	3.423	2.676
^{170}Er	0.656	14.910	0.168	0.137	0.026	0.025	0.035	0.025	0.103	0.103	0.430	0.300	0.467	0.353
^{176}Yb	1.089	12.996	0.685	0.544	0.329	0.290	0.253	0.171	0.509	0.472	1.443	0.974	1.715	1.284
^{186}W	0.492	28.430	0.168	0.132	0.013	0.013	0.024	0.016	0.089	0.094	0.469	0.307	0.493	0.350
^{192}Os	0.408	40.780	0.145	0.113	0.007	0.007	0.016	0.010	0.069	0.076	0.425	0.272	0.441	0.305
^{198}Pt	1.049	7.356	1.360	1.020	0.606	0.520	0.488	0.299	0.999	0.914	2.926	1.775	3.445	2.395
^{204}Hg	0.419	6.870	0.234	0.178	0.012	0.013	0.027	0.016	0.113	0.125	0.683	0.413	0.710	0.472
^{232}Th	0.838	100	2.990	2.050	0.811	0.689	0.848	0.432	2.025	1.836	7.047	3.533	7.923	4.805
^{238}U	1.144	99.274	7.720	5.090	4.210	3.260	3.060	1.470	5.850	4.950	15.986	7.569	19.197	11.500

Table 4.8: Summary of the different phase space factors for each double beta decaying isotop. We show the values obtained for both PSF approximation schemes "A" and "B" [2, 200]. In addition, we present the corresponding Q-values as well as the relative isotopic abundance $\overline{N}$. The PSFs are rounded to 3 digits and entries denoted by 0.000 are not exactly zero.

effects of electron screening were obtained in Refs. [103, 201]. Generally, the approximation scheme "A" results in PSFs that, in comparison to the exact numerical solutions, are larger by about $\sim 10\% - 60\%$ depending on the exact PSF and isotope of interest, while the approximation scheme "B" tends to overestimate the exact solutions by $\sim 2\% - 10\%$ [200]. In order to comply with different conventions used in Refs. [45]

and [200] we defined the rescaling constants

$$C_k = \begin{cases} 9/2 & , k = 4 \\ m_e R_A/2 & , k = 6 \\ (m_e R_A/2)^2 & , k = 9 \\ 1 & , \text{else} \end{cases} . \tag{4.138}$$

The different PSFs for all naturally occuring $0\nu\beta\beta$ candidate isotopes are given in Table 4.8.

4.7.2 The $0\nu\beta\beta$ Half-Life Master Formula

The example of the LνEM presented in the previous section highlights the methodology of the $0\nu\beta\beta$ half-life calculation and can be extended to the full LEFT basis of LNV operators as has been done in Refs. [44, 45] with the exception of the neutral-current dimension-6 LEFT operators. The contributions from the latter to the $0\nu\beta\beta$ amplitude have been derived in this work, particularly in Section 4.6, for the first time. By separating the different leptonic currents that arise in the context of the various operators, the general transition amplitude can be written as [45]

$$\mathcal{A} = \frac{g_A^2 G_F^2 m_e}{\pi R_A}\Bigg(\Big[\overline{e}(k_1)P_R e^C(k_2)\Big]\mathcal{A}_\nu + \Big[\overline{e}(k_1)P_L e^C(k_2)\Big]\mathcal{A}_R + \frac{\epsilon_1 - \epsilon_2}{m_e}\Big[\overline{e}(k_1)\gamma_0 e^C(k_2)\Big]\mathcal{A}_E$$
$$+ \Big[\overline{e}(k_1)e^C(k_2)\Big]\mathcal{A}_{m_e} + \Big[\overline{e}(k_1)\gamma_0\gamma_5 e^C(k_2)\Big]\mathcal{A}_M\Bigg), \tag{4.139}$$

with the different sub-amplitudes $\mathcal{A}_i(\{C_i^{(d)}\})$ defined in terms of the nuclear matrix elements $\mathcal{M}_i$ and the corresponding Wilson coefficients $C_i^{(d)}$ as

$$\begin{aligned}
\mathcal{A}_\nu =& \left(\frac{m_{\beta\beta}}{m_e} + \frac{BF_0^2}{v^2 m_e}C^{(6)}_{S,NC}\right)\mathcal{M}_\nu^{(3)} + \frac{m_N}{m_e}\mathcal{M}_\nu^{(6)}\left(C^{(6)}_{\mathrm{SL}}, C^{(6)}_{\mathrm{SR}}, C^{(6)}_{\mathrm{T}}, C^{(7)}_{\mathrm{VL}}, C^{(7)}_{\mathrm{VR}}\right) \\
&+ \frac{m_N^2}{m_e v}\mathcal{M}_\nu^{(9)}\left(C^{(9)}_{1\mathrm{L}}, C^{(9)\prime}_{1\mathrm{L}}, C^{(9)}_{2\mathrm{L}}, C^{(9)\prime}_{2\mathrm{L}}, C^{(9)}_{3\mathrm{L}}, C^{(9)\prime}_{3\mathrm{L}}, C^{(9)}_{4\mathrm{L}}, C^{(9)}_{5\mathrm{L}}\right), \\
\mathcal{A}_R =& \frac{m_N^2}{m_e v}\mathcal{M}_R^{(9)}\left(C^{(9)}_{1\mathrm{R}}, C^{(9)\prime}_{1\mathrm{R}}, C^{(9)}_{2\mathrm{R}}, C^{(9)\prime}_{2\mathrm{R}}, C^{(9)}_{3\mathrm{R}}, C^{(9)\prime}_{3\mathrm{R}}, C^{(9)}_{4\mathrm{R}}, C^{(9)}_{5\mathrm{R}}\right), \\
\mathcal{A}_E =& \mathcal{M}^{(6)}_{E,L}\left(C^{(6)}_{\mathrm{VL}}\right) + \mathcal{M}^{(6)}_{E,R}\left(C^{(6)}_{\mathrm{VR}}\right), \\
\mathcal{A}_{m_e} =& \mathcal{M}^{(6)}_{m_e,L}\left(C^{(6)}_{\mathrm{VL}}\right) + \mathcal{M}^{(6)}_{m_e,R}\left(C^{(6)}_{\mathrm{VR}}\right), \\
\mathcal{A}_M =& \frac{m_N}{m_e}\mathcal{M}_M^{(6)}\left(C^{(6)}_{\mathrm{VL}}\right) + \frac{m_N^2}{m_e v}\mathcal{M}_M^{(9)}\left(C^{(9)}_6, C^{(9)\prime}_6, C^{(9)}_7, C^{(9)\prime}_7, C^{(9)}_8, C^{(9)\prime}_8, C^{(9)}_9, C^{(9)\prime}_9\right).
\end{aligned} \tag{4.140}$$

Here, we explicitly state the different Wilson coefficients involved in each sub-amplitude. The corresponding NMEs $\mathcal{M}_i$ are defined in terms of the relevant LECs, the individual

NMEs $M_F, M_{F,sd}, ...$ as well as the LEFT Wilson coefficients. The sub-amplitude $\mathcal{A}_\nu$, which covers the standard LνEM including the new LO contact term proportional to g_ν^{NN}, is given in terms of the NMEs

$$
\begin{aligned}
\mathcal{M}_\nu^{(3)} &= -V_{ud}^2\left(-\frac{1}{g_A^2}M_F + \mathcal{M}_{GT} + \mathcal{M}_T + 2\frac{m_\pi^2 \mathbf{g}_\nu^{\mathbf{NN}}}{g_A^2}M_{F,sd}\right),\\
\mathcal{M}_\nu^{(6)} &= V_{ud}\left(\frac{B}{m_N}\left(C_{SL}^{(6)} - C_{SR}^{(6)}\right) + \frac{m_\pi^2}{m_N v}\left(C_{VL}^{(7)} - C_{VR}^{(7)}\right)\right)\mathcal{M}_{PS} + V_{ud}C_{\mathrm{T}}^{(6)}\mathcal{M}_{T6},\\
\mathcal{M}_\nu^{(9)} &= -\frac{1}{2m_N^2}C_{\pi\pi L}^{(9)}\left(M_{GT,sd}^{AP} + M_{T,sd}^{AP}\right) - \frac{2m_\pi^2}{g_A^2 m_N^2}C_{NNL}^{(9)}M_{F,sd}.
\end{aligned}
\tag{4.141}
$$

Further, $\mathcal{A}_R$, which describes right-handed short-range interactions arising in the context of, e.g., left-right symmetric models [139, 140], is simply given by

$$
\mathcal{M}_R^{(9)} = \mathcal{M}_\nu^{(9)}\big|_{L\to R}. \tag{4.142}
$$

The sub-amplitude $\mathcal{A}_E$ summarizes contributions proportional to the electron energies with

$$
\begin{aligned}
\mathcal{M}_{E,L}^{(6)} &= -\frac{V_{ud}C_{VL}^{(6)}}{3}\left(\frac{g_V^2}{g_A^2}M_F + \frac{1}{3}\left(2M_{GT}^{AA} + M_T^{AA}\right) + \frac{6\mathbf{g}_{\mathbf{V\,L}}^{\mathbf{E}}}{g_A^2}M_{F,sd}\right),\\
\mathcal{M}_{E,R}^{(6)} &= -\frac{V_{ud}C_{VR}^{(6)}}{3}\left(\frac{g_V^2}{g_A^2}M_F - \frac{1}{3}\left(2M_{GT}^{AA} + M_T^{AA}\right) + \frac{6\mathbf{g}_{\mathbf{V\,R}}^{\mathbf{E}}}{g_A^2}M_{F,sd}\right),
\end{aligned}
\tag{4.143}
$$

while terms proportional to the electron mass m_e are described by the sub-amplitude $\mathcal{A}_{m_e}$ which is determined by

$$
\begin{aligned}
\mathcal{M}_{m_e,L}^{(6)} = \frac{V_{ud}C_{VL}^{(6)}}{6}\Bigg(&\frac{g_V^2}{g_A^2}M_F - \frac{1}{3}\left(M_{GT}^{AA} - 4M_T^{AA}\right) - 3\left(M_{GT}^{AP} + M_{GT}^{PP} + M_T^{AP} + M_T^{PP}\right)\\
&- \frac{12\mathbf{g}_{\mathbf{V\,L}}^{\mathbf{m_e}}}{g_A^2}M_{F,sd}\Bigg),\\
\mathcal{M}_{m_e,R}^{(6)} = \frac{V_{ud}C_{VR}^{(6)}}{6}\Bigg(&\frac{g_V^2}{g_A^2}M_F + \frac{1}{3}\left(M_{GT}^{AA} - 4M_T^{AA}\right) + 3\left(M_{GT}^{AP} + M_{GT}^{PP} + M_T^{AP} + M_T^{PP}\right)\\
&- \frac{12\mathbf{g}_{\mathbf{V\,R}}^{\mathbf{m_e}}}{g_A^2}M_{F,sd}\Bigg).
\end{aligned}
\tag{4.144}
$$

Finally, $\mathcal{A}_M$ is given by

$$
\begin{aligned}
\mathcal{M}_M^{(6)} = V_{ud}C_{VL}^{(6)}\Bigg[&2\frac{g_A}{g_M}\left(M_{GT}^{MM} + M_T^{MM}\right)\\
&+ \frac{m_\pi^2}{m_N^2}\left(-\frac{2}{g_A^2}\mathbf{g}_{\mathbf{VL}}^{\mathbf{NN}}M_{F,sd} + \frac{1}{2}\mathbf{g}_{\mathbf{VL}}^{\pi\mathbf{N}}\left(M_{GT,sd}^{AP} + M_{T,sd}^{AP}\right)\right)\Bigg],\\
\mathcal{M}_M^{(9)} = \frac{m_\pi^2}{m_N^2}\Bigg[&-\frac{2}{g_A^2}\left(\mathbf{g}_{\mathbf{6}}^{\mathbf{NN}}C_V^{(9)} + \mathbf{g}_{\mathbf{7}}^{\mathbf{NN}}\tilde{C}_V^{(9)}\right)M_{F,sd}\\
&+ \frac{1}{2}\left(\mathbf{g}_{\mathbf{V}}^{\pi\mathbf{N})}C_V^{(9)} + \tilde{\mathbf{g}}_{\mathbf{V}}^{\pi\mathbf{N}}\tilde{C}_V^{(9)}\right)\left(M_{GT,sd}^{AP} + M_{T,sd}^{AP}\right)\Bigg].
\end{aligned}
\tag{4.145}
$$

While the individual Fermi, Gamow-Teller and Tensor NMEs of the long- and short-range mechanisms, $M_F, \mathcal{M}_{GT}, \mathcal{M}_T, M_{GT}^{ij}, \mathcal{M}_T^{ij}$, have been defined in Section 4.7.1.2, the remaining pseudo-scalar and tensor NMEs are defined as

$$
\begin{aligned}
\mathcal{M}_{PS} &= \frac{1}{2}M_{GT}^{AP} + M_{GT}^{PP} + \frac{1}{2}M_T^{AP} + M_T^{PP}, \\
\mathcal{M}_{T6} &= 2\frac{\mathbf{g_T'} - \mathbf{g_T^{NN}}}{g_A^2}\frac{m_\pi^2}{m_N^2}M_{F,sd} - \frac{8g_T}{g_M}\left(M_{GT}^{MM} + M_T^{MM}\right) \\
&\quad + \mathbf{g_T^{\pi N}}\frac{m_\pi^2}{4m_N^2}\left(M_{GT,sd}^{AP} + M_{T,sd}^{AP}\right) + \mathbf{g_T^{\pi\pi}}\frac{m_\pi^2}{4m_N^2}\left(M_{GT,sd}^{PP} + M_{T,sd}^{PP}\right). \qquad (4.146)
\end{aligned}
$$

With these definitions, the general $0\nu\beta\beta$ half-life "*master formula*" is given as [45]

$$
\boxed{
\begin{aligned}
\left(T_{1/2}^{0\nu}\right)^{-1} = g_A^4\Big[&G_{01}\left(|\mathcal{A}_\nu|^2 + |\mathcal{A}_R|^2\right) - 2\left(G_{01} - G_{04}\right)\mathrm{Re}\left[\mathcal{A}_\nu^*\mathcal{A}_R\right] \\
&+ 4G_{02}|\mathcal{A}_E|^2 + 2G_{04}\left(|\mathcal{A}_{m_e}|^2 + \mathrm{Re}\left[\mathcal{A}_{m_e}^*\left(\mathcal{A}_\nu + \mathcal{A}_R\right)\right]\right) \\
&- 2G_{03}\,\mathrm{Re}\left[\left(\mathcal{A}_\nu + \mathcal{A}_R\right)\mathcal{A}_E^* + 2\mathcal{A}_{m_e}\mathcal{A}_E^*\right] \\
&+ G_{09}|\mathcal{A}_M|^2 + G_{06}\,\mathrm{Re}\left[\left(\mathcal{A}_\nu - \mathcal{A}_R\right)\mathcal{A}_M^*\right]\Big].
\end{aligned}
} \qquad (4.147)
$$

4.8 Renormalization Group Equations

In order to describe the transition from the high-energy scale of new physics to the low-energy scale of $0\nu\beta\beta$ described in terms of χEFT, one has to take the running of the different Wilson coefficients into account.

4.8.1 RGE Running at LEFT Level

The LEFT QCD RGEs are covered in Ref. [45] and we repeat the results here for convenience. The RGEs for the scalar and tensor long-range operators $\mathcal{O}_{SL,SR,T}^{(6)}$ are given as [45]

$$
\frac{\mathrm{d}}{\mathrm{d}\log\mu}C_{SL,SR}^{(6)} = -6C_F\frac{\alpha_s(\mu)}{4\pi}C_{SL,SR}^{(6)}, \qquad \frac{\mathrm{d}}{\mathrm{d}\log\mu}C_T^{(6)} = 2C_F\frac{\alpha_s(\mu)}{4\pi}C_T^{(6)}, \qquad (4.148)
$$

with the constant C_F given in terms of the number of colors N_c as

$$
C_F = \frac{N_c^2 - 1}{2N_c}. \qquad (4.149)
$$

The RGEs for the short-range scalar dimension-9 operators $\mathcal{O}_i^{(9)(\prime)}, i \in [1, ..., 5]$ have been derived as [45]

$$\begin{aligned}
\frac{\mathrm{d}}{\mathrm{d}\log\mu} C_{1L,R}^{(9)(\prime)} &= 6\left(1 - \frac{1}{N_c}\right)\frac{\alpha_s(\mu)}{4\pi} C_{1L,R}^{(9)(\prime)}, \\
\frac{\mathrm{d}}{\mathrm{d}\log\mu}\begin{pmatrix} C_{2L,R}^{(9)(\prime)} \\ C_{3L,R}^{(9)(\prime)} \end{pmatrix} &= \frac{\alpha_s(\mu)}{4\pi}\begin{pmatrix} 8 + \frac{2}{N_c} - 6N_c & -4 - \frac{8}{N_c} + 4N_c \\ 4 - \frac{8}{N_c} & 4 + \frac{2}{N_c} + 2N_c \end{pmatrix}\begin{pmatrix} C_{2L,R}^{(9)(\prime)} \\ C_{3L,R}^{(9)(\prime)} \end{pmatrix}, \\
\frac{\mathrm{d}}{\mathrm{d}\log\mu}\begin{pmatrix} C_{4L,R}^{(9)} \\ C_{5L,R}^{(9)} \end{pmatrix} &= \frac{\alpha_s(\mu)}{4\pi}\begin{pmatrix} \frac{6}{N_c} & 0 \\ -6 & -12C_F \end{pmatrix}\begin{pmatrix} C_{4L,R}^{(9)} \\ C_{5L,R}^{(9)} \end{pmatrix},
\end{aligned} \tag{4.150}$$

and, finally, the RGEs for the short-range vector operators $\mathcal{O}_i^{(9)(\prime)}, i \in [6, .., 9]$ are given by [45]

$$\frac{\mathrm{d}}{\mathrm{d}\log\mu}\begin{pmatrix} C_6^{(9)(\prime)} \\ C_7^{(9)(\prime)} \end{pmatrix} = \frac{\alpha_s(\mu)}{4\pi}\begin{pmatrix} -2C_F\frac{3N_c-4}{N_c} & 2C_F\frac{(N_c+2)(N_c-1)}{N_c^2} \\ 4\frac{N_c-2}{N_c} & \frac{4-N_c+2N_c^2+N_c^3}{N_c^2} \end{pmatrix}\begin{pmatrix} C_6^{(9)(\prime)} \\ C_7^{(9)(\prime)} \end{pmatrix}. \tag{4.151}$$

Importantly, the RGEs introduce a mixing between different operators when evolving them from the SMEFT-to-LEFT matching scale, m_W, down to the chiral scale $\mu \sim 2\,\mathrm{GeV}$. Therefore, when extracting limits on the different Wilson coefficients from experimental $0\nu\beta\beta$ half-life limits, it is essential to define the scale at which the Wilson coefficients are given. As already stated, the above RGEs only represent those that arise from QCD, i.e., that are proportional to the strong coupling constant g_s. The full LEFT RGEs up to dimension 6 have been calculated in Refs. [90, 202]. However, the full set of RGEs is quite complex and not yet included in neither ν`DoBe` [2] nor in Ref. [1] or this work. In contrast to the QCD RGEs presented above, the complete RGE running would induce a loop-level neutrino mass generated from neutral-current $\Delta L = 2$ $\nu\nu ee, \nu\nu qq$ as well as $\nu\nu F_{\mu\nu}$ operators and the $\Delta L = 4$ $\nu\nu\nu\nu$ operator. While this is a qualitatively new feature, these RGEs are proportional to the small masses of e, ν, u, d with $\mathrm{d}m_\nu/\mathrm{d}(\log\mu) \propto G_F m_{e,u,d,\nu}^3 \sim 10^{-5}\,\mathrm{eV}(m_{e,u,d,\nu}/\mathrm{MeV})^3$ [90] and we expect their contribution to be of little relevance in the one-generation approximation which we apply. The full LEFT RGEs will be added to ν`DoBe` in a future update.

4.8.2 RGE Running at SMEFT Level

The RGEs for the SMEFT dimension-7 operators have been worked out in Ref. [87] which covered the RGE effects generated by Standard Model interactions, while Refs. [160, 161] have calculated the full set of SMEFT RGEs up to dimension 7 including the mixing of dimension-5, -6, and -7 operators. Within our code ν`DoBe`, we have included both approaches. Again, the full set of SMEFT RGEs as derived in Refs. [160, 161] does induce a mixing between different LNV operators. Due to the complexity and length of the RGEs, we will not repeat the full set of RGEs here. Instead, we will focus on the loop generation of the Weinberg operator via other LNV dimension-7 SMEFT operators. In our simple one-generation approximation we can write the relevant terms for the dimension-5 Weinberg operator as [160, 161, 203]

$$\begin{aligned}\frac{\mathrm{d}}{\mathrm{d}\log\mu}C_{LH}^{(5)} =& \frac{1}{16\pi^2}\Big(-3g_2^2+2\lambda+2T\Big)C_{LH}^{(5)}\\ &+\frac{2m_H^2}{16\pi^2}\Bigg[8C_{LH}^{(7)\dagger}+\frac{3}{2}g_2^2\Big(2C_{LHD1}^{(7)\dagger}+C_{LHD2}^{(7)\dagger}\Big)+\Big(Y_lY_l^\dagger\Big)_{ee}\Big(C_{LHD1}^{(7)\dagger}-\frac{1}{2}C_{LHD2}^{(7)\dagger}\Big)\\ &\qquad+i\Big(Y_l\Big)_{ee}C_{LHDe}^{(7)\dagger}-3\Big(Y_l^\dagger\Big)_{ee}C_{LLeH}^{(7)\dagger}-3\Big(Y_d^\dagger\Big)_{dd}C_{LLQdH1}^{(7)\dagger}\\ &\qquad+6\Big(Y_u\Big)_{uu}C_{LLQuH}^{(7)\dagger}\Bigg],\end{aligned}\tag{4.152}$$

where we ignored contributions from any dimension-6 SMEFT operators that we do not include in our study. In eq. (4.152), g_2 and λ denote the weak gauge coupling and the quartic Higgs coupling, respectively, while $Y_{l,u,d}$ represent the charged-lepton, up-quark and down-quark Yukawa matrices (c.f. Chapter 2). Further, we defined the trace [160, 161, 203]

$$T=\mathrm{Tr}\Big\{Y_l^\dagger Y_l+3Y_d^\dagger Y_d+3Y_u^\dagger Y_u\Big\}.\tag{4.153}$$

While the dimension-7 version of the Weinberg operator $\mathcal{O}_{LH}^{(7)}$ unsurprisingly contributes to the neutrino mass at both tree- and loop-level, we can see that we expect an additional loop-level contribution to the neutrino mass from the dimension-7 SMEFT operators $\mathcal{O}_{LHD1}^{(7)}, \mathcal{O}_{LHD2}^{(7)}, \mathcal{O}_{LHDe}^{(7)}, \mathcal{O}_{LLQdH1}^{(7)}, \mathcal{O}_{LLQuH}^{(7)}$ as well as $\mathcal{O}_{LLeH}^{(7)}$. In fact, for the latter operator $\mathcal{O}_{LLeH}^{(7)}$ this represents the leading contribution to $0\nu\beta\beta$ as it does not generate any relevant diagram at tree-level. In contrast to the RGEs at LEFT level, the loop contributions to the neutrino mass operator are generally less suppressed. While the renormalization of the SMEFT up to dimension 7 is fully available within the literature, the dimension-9 operators have not been covered, yet. Hence, if not stated otherwise, we will ignore the RGE running in the SMEFT sector and always define the LEFT and SMEFT Wilson coefficients right at the SMEFT-to-LEFT matching scale.

Chapter 5

Unraveling the $0\nu\beta\beta$ Decay Mechanisms

As we have seen in the previous chapter, from an EFT point of view there are numerous mechanisms that can induce a non-zero $0\nu\beta\beta$ rate. It is by no means clear that a future observation of a $0\nu\beta\beta$ signal can be interpreted as the widely considered "standard" LνEM scenario. Instead, further information is required in order to determine the underlying mechanism of a future $0\nu\beta\beta$ signal. In this chapter, we will discuss the possibilities how to experimentally distinguish the different $0\nu\beta\beta$ mechanisms and, in an optimal case, identify the underlying particle physics scenario. This chapter summarizes the results published in Ref. [1]. All numerical calculations within this chapter have been carried out using the ν`DoBe` Python tool [2], which will be described in the following Chapter 6. In Ref. [1], we utilized electron wave functions approximated by the leading order solution to a uniform nuclear charge distribution (Scheme "A"). At the time of publication, this was the only approximation of the electron wave functions implemented in ν`DoBe`. However, the analytic solution to a point-like nucleus (Scheme "B") is known to give more robust results and we will update the results of Ref. [1] accordingly in this chapter. Nevertheless, one should notice that this is only a very minor correction to the results published in Ref. [1].

5.1 Distinguishing the Leptonic Phase Space

As we have discussed in Section 4.1.3, $0\nu\beta\beta$ experiments will generally aim to identify $0\nu\beta\beta$ events by measuring the combined electron spectrum. As such, these experiments are sensitive only to the half-life of the $0\nu\beta\beta$ process. However, experiments that apply tracking calorimeters, such as NEMO [111, 135] or its next-generation successor SuperNEMO [136], are sensitive to the kinematics of each individual electron that is emitted. Therefore, they can detect the single electron spectrum as well as the angular correlation of the two outgoing electrons.

5.1.1 Single Electron Spectra

For convenience let us repeat here the definition of the PSFs as given in eq. (4.137)

$$\begin{aligned}G_{0k} = C_k \frac{G_F^4 m_e^2}{64\pi^5 \ln 2 R_A^2} \int \delta\Big(\epsilon_1 + \epsilon_2 + E_f - E_i\Big) \\ \times \Big(h_{0k}(\epsilon_1, \epsilon_2, R)\cos\theta + g_{0k}(\epsilon_1, \epsilon_2, R)\Big) \\ \times k_1 k_2 \epsilon_1 \epsilon_2 \, \mathrm{d}\epsilon_1 \, \mathrm{d}\epsilon_2 \, \mathrm{d}(\cos\theta).\end{aligned} \tag{5.1}$$

The single electron spectrum is defined as the derivative of the decay rate with respect to the electron energy. With the half-life being parameterized in the form

$$T_{1/2}{}^{-1} = g_A^4 \sum_i G_{0i} |\mathcal{A}_i(\{C_k\})|^2, \tag{5.2}$$

the single electron spectrum becomes

$$\frac{\mathrm{d}\Gamma}{\mathrm{d}\epsilon_1} = \frac{G_F^4 m_e^2}{32\pi^5 R_A^2} \left(\sum_k C_k g_{0k} |\mathcal{A}_k|^2\right) k_1 k_2 \epsilon_1 \epsilon_2, \tag{5.3}$$

with the energy and momentum of the second electron being fixed by the condition

$$Q = \epsilon_1 + \epsilon_2 - 2m_e. \tag{5.4}$$

By defining the normalized electron energy

$$\bar{\epsilon}_1 = \frac{\epsilon_1 - m_e}{Q}, \qquad \bar{\epsilon}_1 \in [0, 1], \tag{5.5}$$

we can determine the normalized spectrum as

$$\frac{1}{\Gamma}\frac{\mathrm{d}\Gamma}{\mathrm{d}\bar{\epsilon}_1} = \frac{Q}{\Gamma}\frac{\mathrm{d}\Gamma}{\mathrm{d}\epsilon_1}. \tag{5.6}$$

Before we dive deeper into the precise spectra for each mechanism, let us first try to gain some intuitive understanding of the expected spectral shapes. We can understand the kinematics of the emitted electrons on a qualitative level by solving the corresponding absolute square of the electron currents, again, via the usual trace techniques [44]

$$\begin{aligned}
&g_{01} \sim \epsilon_1\epsilon_2, && h_{01} \sim -k_1 k_2 \cos\theta, \\
&g_{02} \sim \left(\tfrac{\epsilon_1 - \epsilon_2}{m_e}\right)^2 \left(\epsilon_1\epsilon_2 - m_e^2\right), && h_{02} \sim +k_1 k_2 \cos\theta, \\
&g_{03} \sim \left(\epsilon_1 - \epsilon_2\right)^2, && h_{03} \sim 0, \\
&g_{04} \sim \left(\epsilon_1\epsilon_2 - m_e^2\right), && h_{04} \sim -k_1 k_2 \cos\theta, \\
&g_{06} \sim 2m_e(\epsilon_1 + \epsilon_2), && h_{06} \sim 0, \\
&g_{09} \sim \left(\epsilon_1\epsilon_2 + m_e^2\right), && h_{09} \sim +k_1 k_2 \cos\theta.
\end{aligned} \tag{5.7}$$

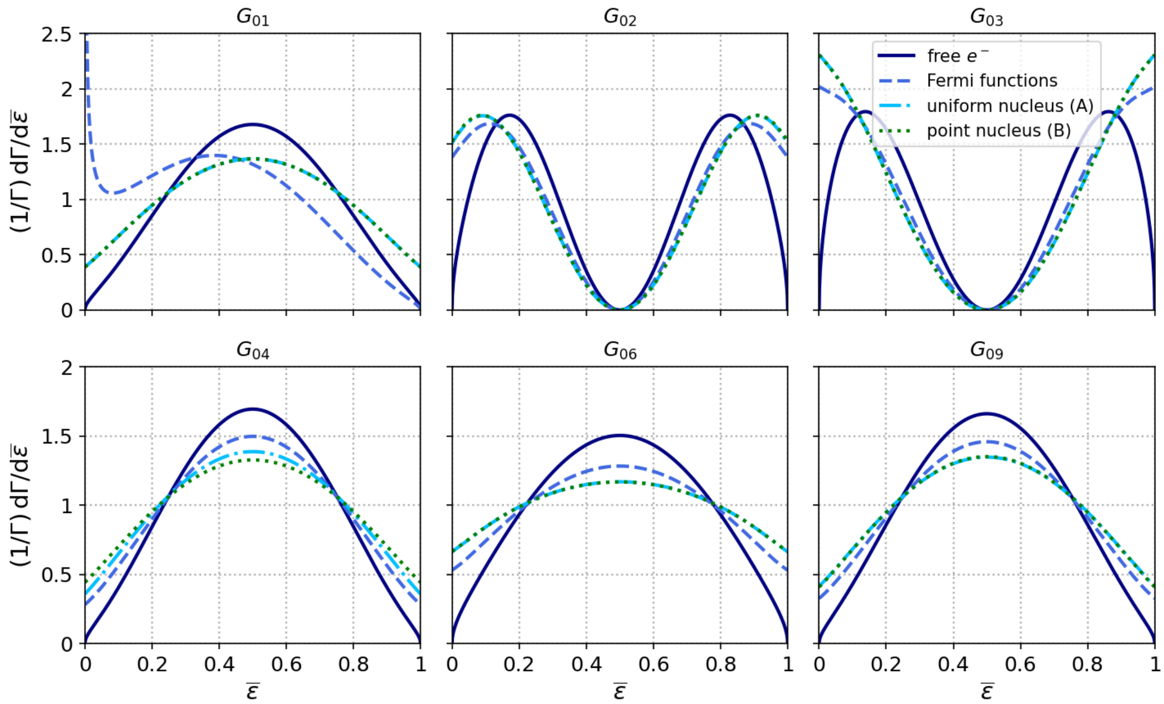

Figure 5.1: Comparison of the normalized single electron spectra arising from different approximation schemes of the electron wave functions. The solid line describes the case of free electrons calculated by taking the usual trace techniques, the dashed line adds the correction in terms of the Fermi function $F(Z, E)$, the dashed-dotted line shows the approximate leading order solution for a uniform nucleus (scheme "A" in Ref. [200]), and lastly the dotted line represents the exact solution to the radial electron wave functions for a point-like nucleus (scheme "B" in Ref. [200]). The spectra are all shown for ^{136}Xe.

Hence, we expect two qualitative behaviours in the single electron spectra. The PSFs with $g_{0k} \propto \epsilon_1\epsilon_2$ will result in a single electron spectrum peaked at $\epsilon_1 = \epsilon_2$, i.e., they will favour an even energy distribution among the emitted electrons, while those PSFs with $g_{0k} \propto \epsilon_1 - \epsilon_2$ will favour an uneven distribution.

As we have mentioned earlier in Section 4.7.1.3, this simple approximation, treating electrons as free particles, does not account for deformations of the electron wave functions caused by the positively charged nucleus. Instead, one can try to model the effects of the nuclear potential via the addition of the Fermi functions $F(Z, E)$, by analytically solving the radial Dirac equations for a nucleus of uniform charge distribution to leading order (scheme "A"), by solving the exact radial electron wave functions for a point-like nucleus (scheme "B"), or by numerically calculating the exact radial electron wave functions for a uniform or Woods-Saxon nuclear potential including electron screening from the atomic shell. In Figure 5.1 we showcase the spectra as calculated in the first three

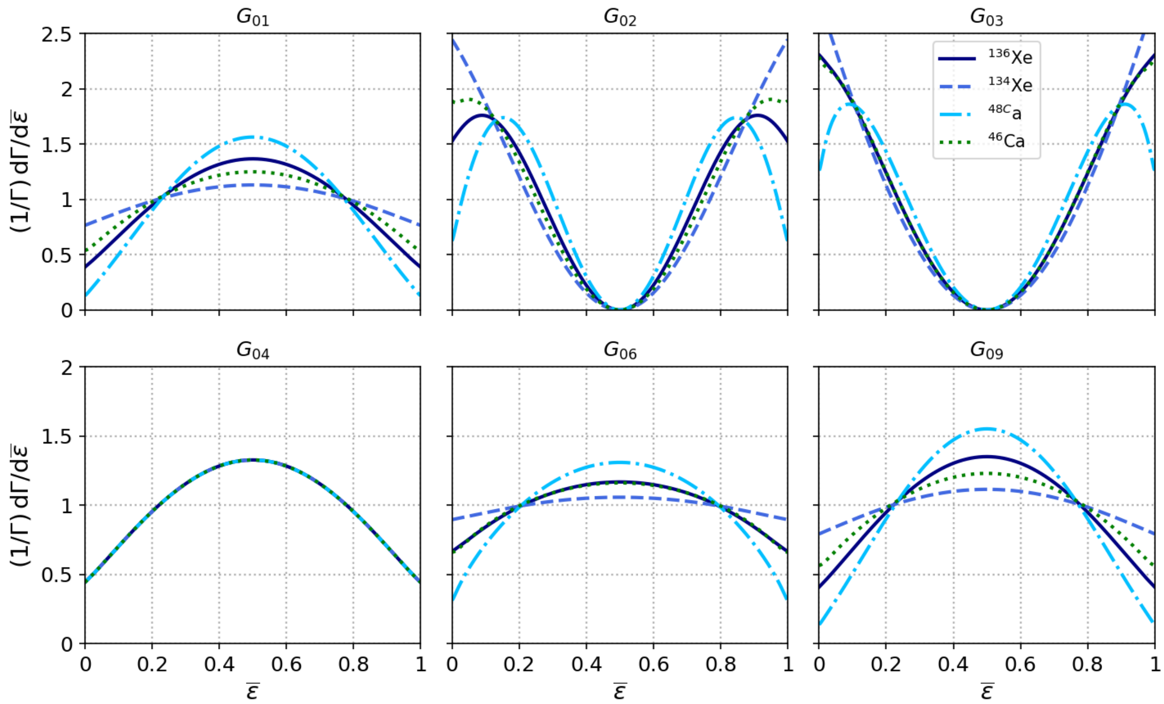

Figure 5.2: Comparison of the normalized single electron spectra in different $0\nu\beta\beta$ candidate isotopes. The normalized spectra are presented for the large Z isotopes ^{136}Xe ($Z = 54, Q \sim 2.5\,\mathrm{MeV}$) and ^{134}Xe ($Z = 54, Q \sim 0.8\,\mathrm{MeV}$) with large and small Q-values, and the small Z isotopes ^{48}Ca ($Z = 20, Q \sim 4.3\,\mathrm{MeV}$) and ^{46}Ca ($Z = 20, Q \sim 1\,\mathrm{MeV}$), again, with a larger and smaller $Q-$value.

approximation schemes of the electron wave functions. Except for G_{01}, the qualitative behaviour is similar among the different schemes. The same is true when considering the exact numerical solutions to the electron wave functions as was shown in Ref. [200].

In Figure 5.2 we show the spectral dependence on the chosen isotope by comparing two large Z isotopes with a larger and smaller Q-value, ^{136}Xe ($Z = 54, Q \sim 2.5\,\mathrm{MeV}$) and ^{134}Xe ($Z = 54, Q \sim 0.8\,\mathrm{MeV}$), with two small Z isotopes, again, with a larger and smaller $Q-$value in ^{48}Ca ($Z = 20, Q \sim 4.3\,\mathrm{MeV}$) and ^{46}Ca ($Z = 20, Q \sim 1\,\mathrm{MeV}$) using the point-like nucleus wave functions "B". Again, we see that the qualitative behaviour is similar among the different isotopes with quantitative differences being attributed mainly to the different $Q-$values.

5.1.2 Angular Correlation

To study the angular correlation of the two emitted electrons we can define the differential decay rate with respect to the normalized energy $\bar{\epsilon}$ and the opening angle θ

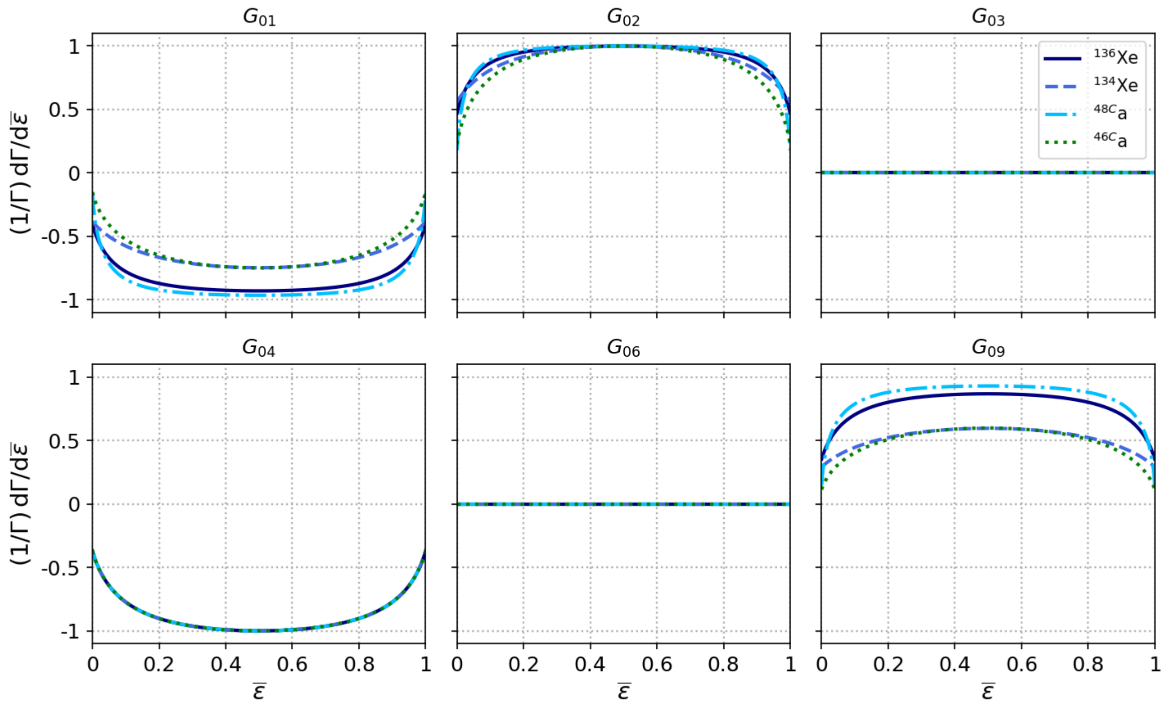

Figure 5.3: Comparison of the angular correlation coefficient in different $0\nu\beta\beta$ candidate isotopes. Again, we present the angular correlation coefficient for large Z isotopes ^{136}Xe ($Z = 54, Q \sim 2.5\,\mathrm{MeV}$) and ^{134}Xe ($Z = 54, Q \sim 0.8\,\mathrm{MeV}$) with comparatively small and large Q-values as well as low Z isotopes ^{48}Ca ($Z = 20, Q \sim 4.3\,\mathrm{MeV}$) and ^{46}Ca ($Z = 20, Q \sim 1\,\mathrm{MeV}$).

as

$$\frac{\mathrm{d}\Gamma}{\mathrm{d}\cos\theta \mathrm{d}\bar{\epsilon}_1} = a_0 \left(1 + \frac{a_1}{a_0}\cos\theta\right). \tag{5.8}$$

The angular correlation coefficient

$$\frac{a_1}{a_0}(\bar{\epsilon}) = \frac{\sum_i |\mathcal{A}_i|^2 h_{0i}}{\sum_j |\mathcal{A}_j|^2 g_{0j}}, \tag{5.9}$$

then describes the angular kinematics of the emitted electrons. Qualitatively, a positive angular correlation describes a scenario with the two electrons being preferably emitted towards the same hemisphere with $\theta < \pi/2$, while a negative angular correlation represents scenarios with the two electrons preferably being emitted back-to-back with an opening angle $\theta > \pi/2$. A vanishing angular correlation coefficient corresponds to a scenario with no preferred angular distribution.

The qualitative behaviour of the angular correlation described in terms of the functions h_{0k} can be read of eq. (5.7). We see that we would expect a negative angular correlation for $k \in [1, 4]$, a positive correlation for $k \in [2, 9]$, and no correlation for $k \in [3, 6]$. In

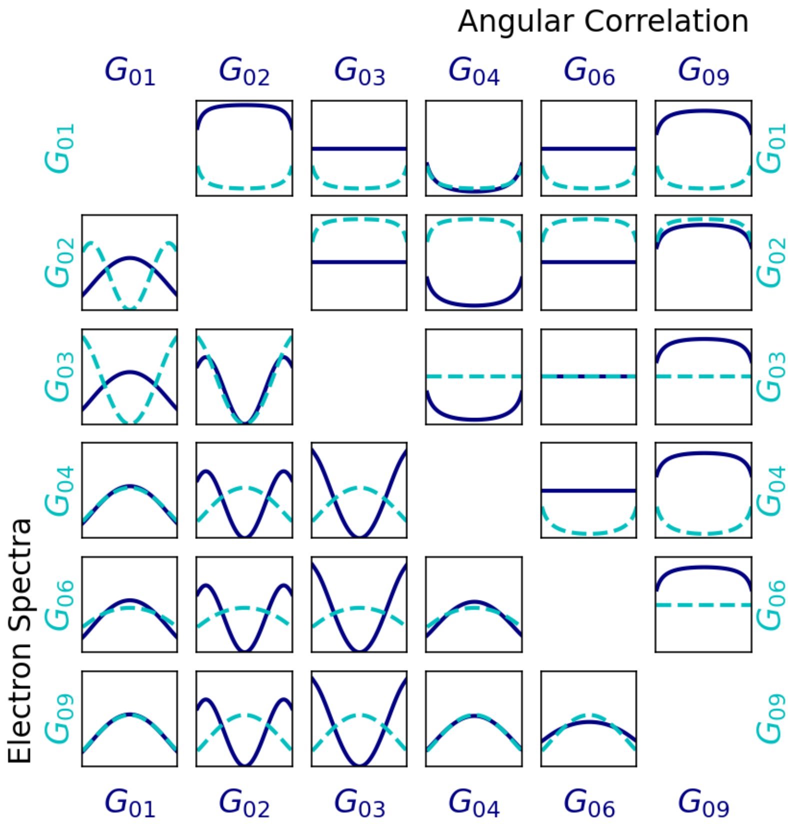

Figure 5.4: Comparison of the normalized single electron spectra (lower left triangle) and angular correlation coefficients (upper right triangle) associated with the different phase space factors. The isotope is chosen to be ^{136}Xe. The dark blue solid lines correspond to the equally coloured PSFs labelled on the x-axis, while the dashed cyan lines represent the equally coloured PSFs on the vertical axis. Again, the plots are with respect to the normalized electron energy in the range $\bar{\epsilon} \in [0-1]$. This is an update of the figure published in Ref. [1].

Figure 5.3 we present the angular correlation coefficients corresponding to each of the six PSFs as calculated in the point-like nucleus approximation.

5.1.3 LEFT Operators

In Figure 5.4 we show a comparison of the normalized single electron spectra and the angular correlation coefficients that arise from the six different PSFs involved in the $0\nu\beta\beta$ half-life calculation. Indeed one finds that operators associated with different PSFs generate kinematic signatures that are in principle distinguishable in the spectra and/or the angular correlation, despite some combinations requiring precise experimental accuracy with high statistics. However, considering each PSF on its own is only meaningful in a

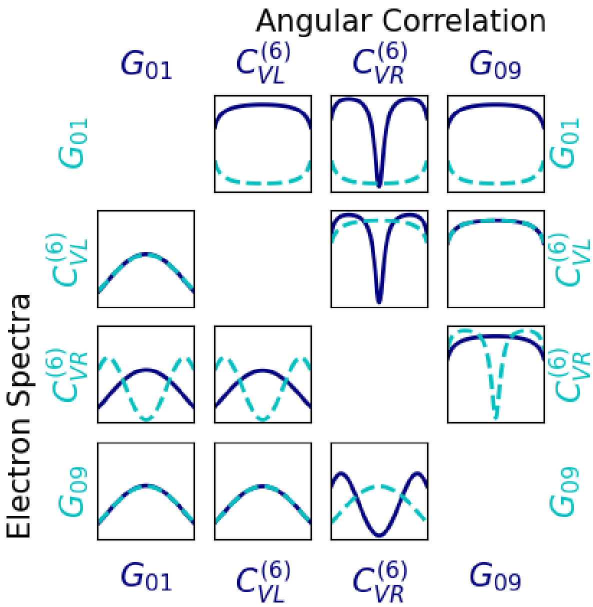

Figure 5.5: Comparison of the normalized single electron spectra (lower left triangle) and angular correlation coefficients (upper right triangle) for each of the 4 groups of LEFT operators related to different phase space factors. Again, the isotope is chosen to be ^{136}Xe and the dark blue solid lines correspond to the equally coloured PSFs labelled on the x-Axis, while the dashed cyan lines represent the equally coloured PSFs on the vertical axis. As before, the plots are shown with respect to the normalized electron energy in the range $\bar{\epsilon} \in [0-1]$. The operators represented by G_{01} are the neutrino mass $m_{\beta\beta}$, the long-range operators $,\mathcal{O}^{(6)}_{SL,SR,T}, \mathcal{O}^{(7)}_{VL,VR}$ and the scalar short-range operators, $\mathcal{O}^{(9)}_{i,L,R}, {\mathcal{O}^{(9)}_{i,L,R}}', i = 1...5$. Similarly, the short-range vector operators, $\mathcal{O}^{(9)}_i, \mathcal{O}^{(9)\prime}_i, i = 6...9$, belong to G_{09}, while the long-range vector operators $\mathcal{O}^{(6)}_{VL,VR}$ have separate kinematic signatures. This is an update of the figure published in Ref. [1].

limited set of scenarios. The reason for this is that, assuming only one operator at a time, the long-range dimension-6 vector operators $C^{(6)}_{VL,VR}$ contribute not only to a single sub-amplitude with a single electron current but, instead, trigger several PSFs ($G_{02,03,04,09}$). The remaining operators $\left(m_{\beta\beta}, C^{(6)}_{SL,SR,T}, C^{(7)}_{VL,VR} \text{ and } C^{(9)}_{i,L,R}, {C^{(9)}_{i,L,R}}', i = 1...5\right)$ all have half-lives proportional to G_{01}, while the short-range vector operators $C^{(9)}_i, C^{(9)\prime}_i, i = 6...9$ are proportional to G_{09}. At the same time, the PSF G_{06} is only generated via interference terms.

In Figure 5.5 we provide a comparison of the leptonic phase space observables in these 4 groups of operators. Consequently, one finds that at LEFT scale, only the dimension-6 long-range vector operators $\mathcal{O}^{(6)}_{VL,VR}$ as well as the short-range vector operators $\mathcal{O}^{(9)(\prime)}_i, i \in [6,..,9]$ generate electron kinematics which are different from the LνEM. The remaining

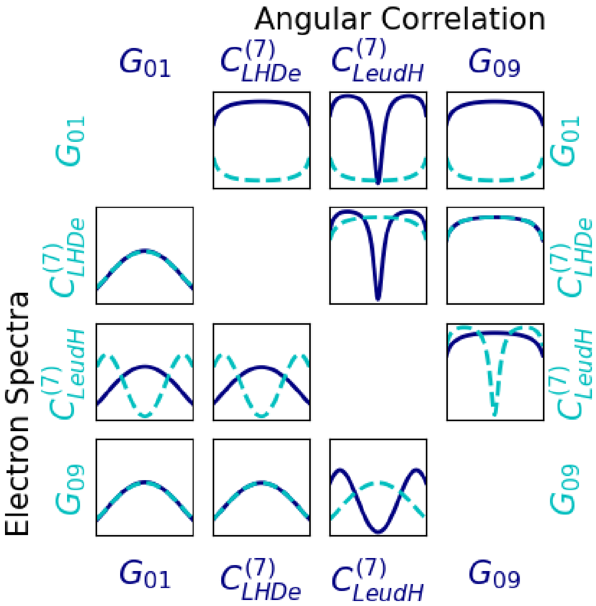

Figure 5.6: Comparison of the normalized single electron spectra (lower left triangle) and angular correlation coefficients (upper right triangle) for each of the 4 groups of SMEFT operators related to different phase space factors similar to Figure 5.5. The operators represented by G_{09} are the Ψ^6 operators $\mathcal{O}^{(9)}_{dQdueL1,2}$ and $\mathcal{O}^{(9)}_{QudueL1,2}$ as well as the Ψ^4H^2D operators $\mathcal{O}^{(9)}_{dQLeH^2D2}, \mathcal{O}^{(9)}_{QueLH^2D2}, \mathcal{O}^{(9)}_{QeuLH^2D2}, \mathcal{O}^{(9)}_{dLQeH^2D1}$ and $\mathcal{O}^{(9)}_{deQLH^2D}$. The dimension-7 operators $\mathcal{O}^{(7)}_{LHDe}$ and $\mathcal{O}^{(7)}_{LeudH}$ result in the same kinematics as the LEFT dimension-6 vector operators $\mathcal{O}^{(6)}_{VL,VR}$. The remaining SMEFT operators, including the neutrino mass generating Weinberg operator, are summarized in the contributions proportional to G_{01}.

LEFT operators are not distinguishable from this scenario via a comparison of the kinematic signatures of the emitted electrons.

5.1.4 SMEFT Operators

While we did not cover a comparison of the different SMEFT operators in Ref. [1], we will include a brief discussion here, in order to provide a comprehensive overview.

Taking into account the leading order SMEFT-to-LEFT matching relations, i.e. ignoring contributions proportional to the small quark or electron masses, we find that, except for $\mathcal{O}^{(7)}_{LHDe}$ and $\mathcal{O}_{LeudH(7)}$, all SMEFT dimension-7 operators give half-life contributions proportional to the PSF G_{01} and, as such, result in the same electron kinematics as the LνEM. The remaining two operators map onto the two long-range dimension-6 vector operators, $\mathcal{O}^{(6)}_{VL}$ ($\mathcal{O}^{(7)}_{LHDe}$) and $\mathcal{O}^{(6)}_{VR}$ ($\mathcal{O}^{(7)}_{LeudH}$). At SMEFT dimension 9, the 6-fermion Ψ^6 operators $\mathcal{O}^{(9)}_{dQdueL1,2}$ and $\mathcal{O}^{(9)}_{QudueL1,2}$ as well as the Ψ^4H^2D operators $\mathcal{O}^{(9)}_{dQLeH^2D2}, \mathcal{O}^{(9)}_{QueLH^2D2}$,

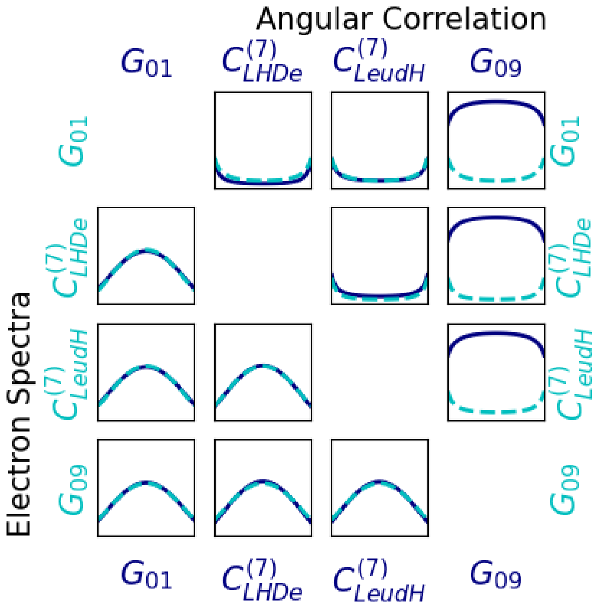

Figure 5.7: Effect of the Renormalization Group Equations on the electron kinematics generated by different SMEFT operators. The setting is the same is in Figure 5.6. However, here we define each operator at the scale $\Lambda = 1\,\text{TeV}$ before running it down to the SMEFT-to-LEFT matching scale m_W. As one can see, the operator mixing induced via the 1-loop RGEs significantly changes the expected signatures of the SMEFT dimension-7 operators.

$\mathcal{O}^{(9)}_{QeuLH^2D2}$, $\mathcal{O}^{(9)}_{dLQeH^2D1}$ and $\mathcal{O}^{(9)}_{deQLH^2D}$ map onto the short-range vector LEFT operators that contribute via G_{09}. The remaining SMEFT dimension-9 operators all map onto LEFT operators that contribute via G_{01} and hence have the same kinematics as the usual mass mechanism. In Figure 5.6 we provide a comparison of the expected electron kinematics for these four different sets of SMEFT operators. Unsurprisingly, the SMEFT operators $\mathcal{O}^{(7)}_{LHDe}$ and $\mathcal{O}^{(7)}_{LeudH}$ generate the same kinematics as the LEFT operators $\mathcal{O}^{(6)}_{VL,VR}$.

5.1.5 Renormalization Group Equations and Operator Mixing

In the previous sections, we assumed only a single operator with a non-vanishing Wilson coefficient at a time, each defined at the SMEFT-to-LEFT matching scale m_W. Therefore, we have ignored the potential effects of the RGE running in the SMEFT sector. Considering the SMEFT RGEs that arise solely from the Standard Model interactions as calculated by Liao and Ma [87], the induced operator mixing does not alter the results discussed in the previous section. However, when considering the full SMEFT RGEs up to dimension 7 as calculated by Zhang [160, 161], the 1-loop contribution of the dimension-7 SMEFT operators to the neutrino mass generating dimension-5 Weinberg operator can have a significant impact on the expected electron kinematics. To study the effects of the operator mixing induced via the 1-loop renormalization we apply the RGEs as calculated by Zhang [160, 161] and define each SMEFT operator at the scale $\Lambda = 1\,\mathrm{TeV}$ before running it down to the SMEFT-to-LEFT matching scale m_W. We present the corresponding kinematic signatures in Figure 5.7 showcasing that the 1-loop contribution to the neutrino mass generating Weinberg operator does significantly change the kinematics of the emitted electrons for the SMEFT dimension-7 operators. After applying the RGE, the signatures of the SMEFT dimension-7 operators all resemble that of the LνEM. This finding signifies the importance of loop contributions to $0\nu\beta\beta$ in the SMEFT regime.

Conversely, as we have discussed in Section 4.8, we do not expect the full set of LEFT RGEs calculated by Jenkins et al. [90] to be of similar importance as long as we stick to the one-generation approximation.

5.2 Half-Life Ratios – Measuring $0\nu\beta\beta$ in Different Isotopes

While only tracking calorimeter $0\nu\beta\beta$ experiments are sensitive to the kinematics of the emitted electrons, the major experimental observable is of course the half-life of the $0\nu\beta\beta$ process. In contrast to the electron kinematics which are only able to distinguish operators via the leptonic phase-space, i.e., they can only distinguish operators with different leptonic currents, the half-life is sensitive to the full $0\nu\beta\beta$ transition amplitude. As such the half-life carries information about both the leptonic currents as well as the hadronic structures of different operators and the corresponding NMEs. In order to study the isotopic dependence of the various NMEs that arise in the context of different LNV mechanisms, we define the half-life ratios [1]

$$R^{\mathcal{O}_i}(^{\mathrm{A}}\mathrm{X}) \equiv \frac{T_{1/2}^{\mathcal{O}_i}(^{\mathrm{A}}\mathrm{X})}{T_{1/2}^{\mathcal{O}_i}(^{76}\mathrm{Ge})} = \frac{\sum_j |\mathcal{A}_j^{\mathcal{O}_i}(^{76}\mathrm{Ge})|^2 G_j^{\mathcal{O}_i}(^{76}\mathrm{Ge})}{\sum_k |\mathcal{A}_k^{\mathcal{O}_i}(^{\mathrm{A}}\mathrm{X})|^2 G_k^{\mathcal{O}_i}(^{\mathrm{A}}\mathrm{X})}, \tag{5.10}$$

by normalizing the half-life $T_{1/2}^{\mathcal{O}_i}(^{\mathrm{A}}\mathrm{X})$ in a certain isotope $^{\mathrm{A}}\mathrm{X}$ with mass number A, generated by some LNV operator $\mathcal{O}_i$, with respect to the benchmark isotope $^{76}\mathrm{Ge}$. In the above equation, we take the sums $\sum_{j,k}$ with respect to all PSFs $G_{0j,k}$ generated by the operator $\mathcal{O}_i$, and we denote the corresponding sub-amplitudes by $\mathcal{A}_i^{\mathcal{O}_i}$. Conveniently, in a single-operator scenario, the Wilson coefficient of the LNV operator drops out when taking the ratios of half-lives, thereby eliminating any dependence on the magnitude of the new physics couplings. This feature was first discussed in Refs. [204, 205]. Obviously, this is only true in scenarios dominated by a single operator, while half-life ratios derived from multi-operator scenarios will still depend on the precise parameter settings. By comparing the expected ratios resulting from two different operators $\mathcal{O}_{i,j}$ via the ratio

$$R_{ij}(^{A}X) = \frac{R^{\mathcal{O}_i}(^{\mathrm{A}}\mathrm{X})}{R^{\mathcal{O}_j}(^{\mathrm{A}}\mathrm{X})}, \tag{5.11}$$

Groups:	$m_{\beta\beta}$	$C_{VL}^{(6)}$	$C_{VR}^{(6)}$	$C_{T}^{(6)}$	$C_{S,V}^{(6,7)}$	$C_{S1}^{(9)}$	$C_{S2}^{(9)}$	$C_{S3}^{(9)}$	$C_{S4}^{(9)}$	$C_{S5}^{(9)}$	$C_{V}^{(9)}$	$\tilde{C}_{V}^{(9)}$
	$m_{\beta\beta}$	$C_{VL}^{(6)}$	$C_{VR}^{(6)}$	$C_{T}^{(6)}$	$C_{SL}^{(6)}$	$C_{1L}^{(9)}$	$C_{2L}^{(9)}$	$C_{3L}^{(9)}$	$C_{4L}^{(9)}$	$C_{5L}^{(9)}$	$C_{6}^{(9)}$	$C_{7}^{(9)}$
	$C_{SL,\nu u}^{(6)}$	-	-	-	$C_{SR}^{(6)}$	$C_{1R}^{(9)}$	$C_{2R}^{(9)}$	$C_{3R}^{(9)}$	$C_{4R}^{(9)}$	$C_{5R}^{(9)}$	$C_{6}^{(9)\prime}$	$C_{7}^{(9)\prime}$
	$C_{SL,\nu d}^{(6)}$	-	-	-	$C_{VL}^{(7)}$	$C_{1L}^{(9)\prime}$	$C_{2L}^{(9)\prime}$	$C_{3L}^{(9)\prime}$	-	-	$C_{8}^{(9)}$	$C_{9}^{(9)}$
	$C_{SR,\nu u}^{(6)}$	-	-	-	$C_{VR}^{(7)}$	$C_{1R}^{(9)\prime}$	$C_{2R}^{(9)\prime}$	$C_{3R}^{(9)\prime}$	-	-	$C_{8}^{(9)\prime}$	$C_{9}^{(9)\prime}$
	$C_{SR,\nu d}^{(6)}$	-	-	-	-	-	-	-	-	-	-	-

Table 5.1: LEFT Operator groups that can be distinguished via taking decay rate ratios. Operators within a certain group result in the same half-life ratios while operators of different groups are, in principle, distinguishable via the half-life ratios. The precise composition of the distinguishable groups does depend on the currently unknown LECs. This table assumes there is no fine-tuning among the unknown LECs. If, instead, the unknown LECs are taken to be zero or equal to their NDA estimates, the short-range scalar operator groups $C_{S2-S5}^{(9)}$ will result in the same ratios rendering them indistinguishable. The same is true for the short-range vector operator groups $\tilde{C}_V^{(9)}$ and $\tilde{C}_V^{(9)}$. This table was published in Ref. [1] and is, here, updated with the neutral-current LEFT operators.

we can determine how well these operators are distinguishable via half-life measurements in multiple isotopes. In the following, we will calculate the ratios of all possible operator combinations, to estimate if one can pinpoint the exact underlying mechanism. However, our main focus will be put on the possibility of an experimental identification of exotic higher-dimensional operators in contrast to the LνEM which is widely considered to be the *"standard"* scenario. That is, we will focus on the ratios $R_{im_{\beta\beta}}$ which compare the half-life ratios expected for the LνEM with those originating from more exotic scenarios parameterized in the operator $\mathcal{O}_i$.

As a potential benefit, taking half-life ratios in different isotopes may help to decrease numerical uncertainties connected to correlated systematic relative errors that may arise in the calculation of NMEs via the different many-body methods. This is because systematic relative errors that, e.g., tend to over/underestimate NMEs by a certain amount should drop out or cancel, at least to a certain extent, when taking the ratio of half-lives.

5.2.1 LEFT Operators

At LEFT scale, we can sort the 36 different operators into 12 different groups, such that all operators within a certain group depend on the same combinations of PSFs, NMEs and LECs and, as such, result in the same half-life ratios. In Table 5.1 we present these operator groups and the corresponding operators. Notably, the LνEM is,

Groups:	$m_{\beta\beta}$	$C_{VL}^{(6)}$	$C_{VR}^{(6)}$	$C_{T}^{(6)}$	$C_{S,V}^{(6,7)}$	$C_{S1}^{(9)}$	$C_{S2}^{(9)}$	$C_{S3}^{(9)}$	$C_{S4}^{(9)}$	$C_{S5}^{(9)}$
	$C_{LH}^{(5)}$	$C_{LHDe}^{(7)}$	$C_{LeudH}^{(7)}$	$C_{LLQdH2}^{(7)}$	$C_{LHD2}^{(7)}$	$C_{ddueue}^{(9)}$	$C_{QuQuLL1}^{(9)}$	$C_{QuQuLL2}^{(9)}$	$C_{dQQuLL2}^{(9)}$	$C_{dQQuLL1}^{(9)}$
	$C_{LH}^{(7)}$	-	-	-	$C_{LLQuH}^{(7)}$	$C_{QLQLH^2D2}^{(9)}$	$C_{dQdQLL1}^{(9)}$	$C_{dQdQLL2}^{(9)}$	$C_{deueH^2D}^{(9)}$	-
	-	-	-	-	-	$C_{QLQLH^2D5}^{(9)}$	-	-	$C_{dLuLH^2D2}^{(9)}$	-
	-	-	-	-	-	$C_{eeH4D2}^{(9)}$	-	-	-	-
Groups:	$C_{V}^{(9)}$	$C_{V\tilde{V}}^{(9)}$	C_{LHW}	$C_{LHD1}^{(7)}$	$C_{LLQdH1}^{(7)}$	$C_{duLLH^2D}^{(9)}$	$C_{dLQeH^2D1}^{(9)}$	$C_{deQLH^2D}^{(9)}$	$C_{LLH^4D^23}^{(9)}$	$C_{QQLLH^2D2}^{(9)}$
	$C_{dQdueL1}^{(9)}$	$C_{dQdueL2}^{(9)}$	$C_{LHW}^{(7)}$	$C_{LHD1}^{(7)}$	$C_{LLQdH1}^{(7)}$	$C_{duLLH^2D}^{(9)}$	$C_{dLQeH^2D1}^{(9)}$	$C_{deQLH^2D}^{(9)}$	$C_{LLH^4D^23}^{(9)}$	$C_{QQLLH^2D2}^{(9)}$
	$C_{QudueL1}^{(9)}$	$C_{QudueL2}^{(9)}$	$C_{LLH^4W1}^{(9)}$	-	-	-	-	-	-	$C_{LLH^4D^24}^{(9)}$
	$C_{dQLeH^2D2}^{(9)}$	$C_{QeuLH^2D2}^{(9)}$	-	-	-	-	-	-	-	-
	$C_{QueLH^2D2}^{(9)}$	-	-	-	-	-	-	-	-	-

Table 5.2: SMEFT operator groups that generate different decay rate ratios. Again, operators within a certain group result in the same half-life ratios while operators of different groups are, in principle, distinguishable via the half-life ratios (c.f. Table 5.1). Whenever the half-life ratios are the same as for a certain LEFT operator group, we have labelled the group by the same name.

in principle, distinguishable from all other operators[1]. The same is true for the long-range dimension-6 tensor and vector operators $C_{SL,SR,T}^{(6)}$, each of which differs when taking half-life ratios. At the same time, we have identified 5 different groups for the short-range scalar operators. However, the operator groups $C_{S2,3,4,5}^{(9)}$ only result in distinct half-life ratios if the currently unknown LECs $g_{2,3,4,5}^{NN}$ are taken into account. Similarly, the operator groups $C_V^{(9)}, \tilde{C}_V^{(9)}$ corresponding to the short-range vector operators are only distinguishable from each other if the unknown LECs $g_{6,7}^{NN}, g_V^{\pi N}$ and $\tilde{g}_V^{\pi N}$ turn out to be different from each other.

5.2.2 SMEFT Operators

Considering only tree-level contributions to $0\nu\beta\beta$, within the SMEFT we identify the Weinberg operator at dimension 5, 10 different dimension-7 operators, and 26 dimension-9 operators giving rise to $0\nu\beta\beta$. That is, in total we find 37 different SMEFT operators contributing to the $0\nu\beta\beta$ amplitude at tree-level. Analogously to the LEFT case, we can arrange these operators into different groups with operators within a given group generating the same half-life ratios. However, due to the more complex SMEFT-to-LEFT matching relations, the number of groups with potentially different half-life ratios is larger. Indeed, we find that we can arrange the different SMEFT operators into 20 operator groups displayed in Table 5.2.

[1] Except of course from the scalar LNV NC operators which generate a neutrino mass directly and therefore trigger the same mechanism.

5.2.3 A Parameter Scan over the Unknown LECs

The major source of uncertainty within the chiral EFT approach results from the currently unknown LECs (c.f. Table 4.6). As a baseline scenario, we will set all unknown LECs to zero, except for $g_{6,7}^{NN} = g_V^{\pi N} = \tilde{g}_V^{\pi N} = 1$ which are taken to their NDA estimates in order not to omit the short-range vector operators. One can examine the sensitivity of the half-life ratios towards variations of the unknown LECs g_i via a parameter scan in the range of $\pm[1/\sqrt{10}, \sqrt{10}] \times |g_i|$. That is, we randomize the sign of the unknown LECs and vary them within their respective order of magnitude estimate as given in Table 4.6. At the same time, we assign a variation of $\pm 50\%$ to g_ν^{NN} which parameterizes the contact interaction arising from the LνEM to account for uncertainties arising due to an inconsistent usage of regularization schemes (c.f. the discussion in Section 4.5.6). In the following, we will consider all $0\nu\beta\beta$ candidate isotopes with $Q > 2\,\mathrm{eV}$ that are currently or have previously been used in laboratory $0\nu\beta\beta$ experiments with NMEs available in the IBM2 framework, namely ^{76}Ge, ^{82}Se, ^{96}Zr, ^{100}Mo, ^{116}Cd, ^{130}Te, ^{136}Xe and ^{150}Nd. Additionally, we consider the low Q-value isotopes ^{128}Te and ^{134}Xe which, due to their large natural isotopic abundance, are oftentimes present in experiments searching for $0\nu\beta\beta$ in ^{130}Te and ^{136}Xe, respectively, if no isotopic enrichment techniques are applied.

In order to study the sensitivity of the half-life ratios with respect to the unknown LECs, we have performed a parameter scan by simulating 1000 different LEC parameter settings drawing each LEC randomly from the defined parameter ranges using a uniform probability distribution. In Figures 5.8 and 5.9 we present the resulting half-life ratios $R^{\mathcal{O}_i}$ (upper panel) and $R_{im_{\beta\beta}}$ (lower panel) obtained via this parameter scan for the LEFT and SMEFT operator groups. The ratios resulting from the parameter scan are visualized via the coloured points and we use ^{76}Ge as the reference isotope. Additionally, in Figures 5.8 and 5.9, we also display the ratios resulting from the benchmark scenario with most of the unknown LECs turned off (by a dot for the low Q-values isotopes and by a star for all other isotopes). The central (median) ratios arising from the variation of the LECs are marked by a cross.

We can see that the variation of the contact term g_ν^{NN} does not generate a significant uncertainty in the half-life ratios of the LνEM. Indeed, they are too small to be visible on the log-scale of Figures 5.8 and 5.9. However, the contribution arising from the contact interaction g_ν^{NN} cannot be disregarded when calculating the magnitude of the $0\nu\beta\beta$ half-life as it decreases the expected $0\nu\beta\beta$ half-lives by approximately $\sim 50\%$. We have displayed a parameter scan over g_ν^{NN} of the $0\nu\beta\beta$ half-life for the normal and inverted hierarchy scenarios in Figure 5.10, where we also provide a comparison to the $g_\nu^{NN} = 0$ scenario. We can see that the variation of g_ν^{NN} does not generate a significant uncertainty in the expected half-lives, especially when compared to the uncertainty arising from the unknown Majorana CP phases. This behaviour supports the observed stability of the half-life ratios with respect to a variation of g_ν^{NN}.

For the more exotic higher dimensional operators, the introduction of non-zero values for the unknown LECs generates half-life ratios that differ, by a considerable margin, from the ratios resulting from the baseline scenario with the unknown LECs mostly switched off (c.f. the upper half of Figure 5.8). This is especially true for the short-

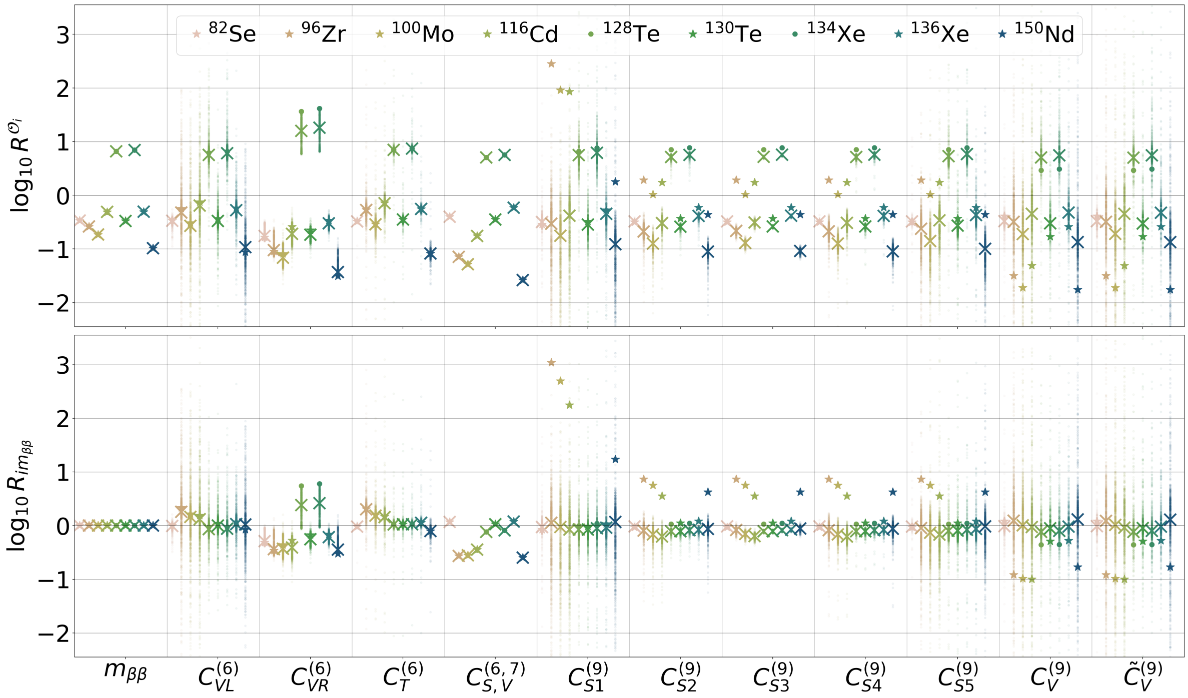

Figure 5.8: Parameter scan of the half-life ratios $R^{\mathcal{O}_i}$ and the normalized ratios $R_{im_{\beta\beta}}$ for each LEFT operator group over the unknown LECs. The unknown LECs are varied within their respective order of magnitude NDA estimates with a randomized sign, while the contact interaction LEC g_ν^{NN} is varied at $\pm 50\%$. The baseline scenario with all unknown LECs turned off is marked by a star for isotopes with $Q > 2\,\mathrm{MeV}$ and a point for those with $Q < 2\,\mathrm{MeV}$. Additionally, we mark the central (median) values of the LEC variation by a cross. This figure was published in Ref. [1] and is recalculated here with updated PSFs.

range LEFT operators $C_i^{(9)}$ as well as most of the SMEFT operators that cannot be associated to a LEFT operator group (c.f. Figure 5.9). For these operators, the central values given by the LEC parameter scan differ significantly from the baseline scenario. At the same time, the parameter scans can show large variations in both $R^{\mathcal{O}_i}$ and $R_{im_{\beta\beta}}$ ranging over several orders of magnitude. This signifies the importance of a precise determination of the unknown LECs.

Some of the parameter scans in Figures 5.8 and 5.9 display gaps which can result from the fact that we did not fix the sign of the unknown LECs. As we have stated previously, we are mostly concerned with the identification of exotic higher dimensional operators contrasting the standard light neutrino-exchange scenario. The relevant parameter here is $R_{im_{\beta\beta}}$. From Figures 5.8 and 5.9 we can see that, besides the large uncertainty arising from the parameter scan, the introduction of the unknown LECs tends to push the ratio $R_{im_{\beta\beta}}$ towards 1 (indistinguishable) when considering the central values of the variation.

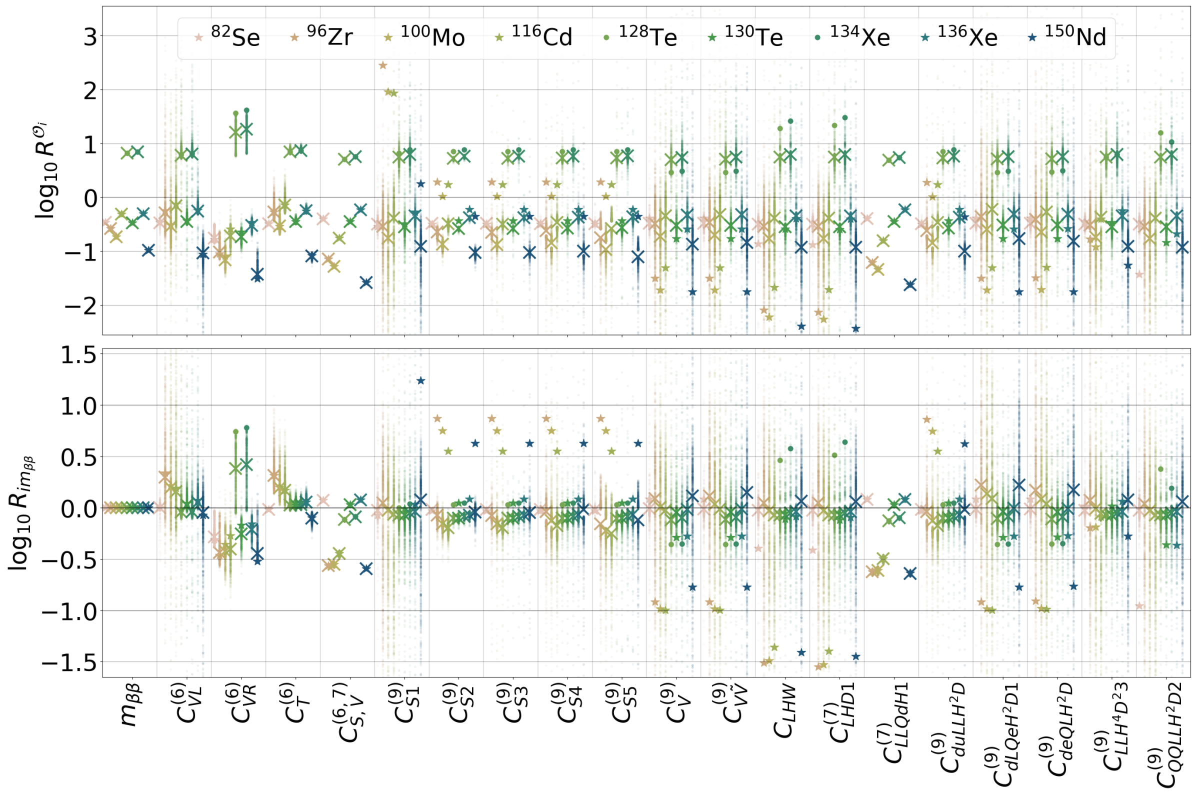

Figure 5.9: Parameter scan of the half-life ratios $R^{\mathcal{O}_i}$ and the normalized ratios $R_{im_{\beta\beta}}$ for each SMEFT operator group over the unknown LECs. See Figure 5.8 for details. The SMEFT operators were not studied in Ref. [1] and we add them here for completeness.

5.2.4 Distinguishing Different Operators

As we have demonstrated, the uncertainties introduced by the unknown LECs are substantial. Nevertheless, we will attempt to provide a further analysis regarding the distinguishability of different $0\nu\beta\beta$ mechanisms, again, with a focus on the identification of exotic scenarios in contrast to the LνEM. In this context, we define two benchmark scenarios. First, we try to provide a *representative* scenario with half-life ratios given by the central (median) values arising from the parameter scan. Secondly, we will provide a *worst-case* scenario given by the ratios R_{ij} that are closest to unity within the parameter scan. For both scenarios, we can then identify the optimal combination of isotopes that maximizes the expected half-life ratios R_{ij} and, hence, provides the best chance to distinguish different operators from each other via a multi-isotope measurement. In Figure 5.11 we provide a comprehensive overview of the best combinations of isotopes and the corresponding expected half-life ratios for each operator combination R_{ij}. The figure is divided along the diagonal with the representative scenario derived from the central values of the parameter scan being showcased in the upper right triangle, while the ratios R_{ij} arising from the worst-case scenario are given in the lower left triangle.

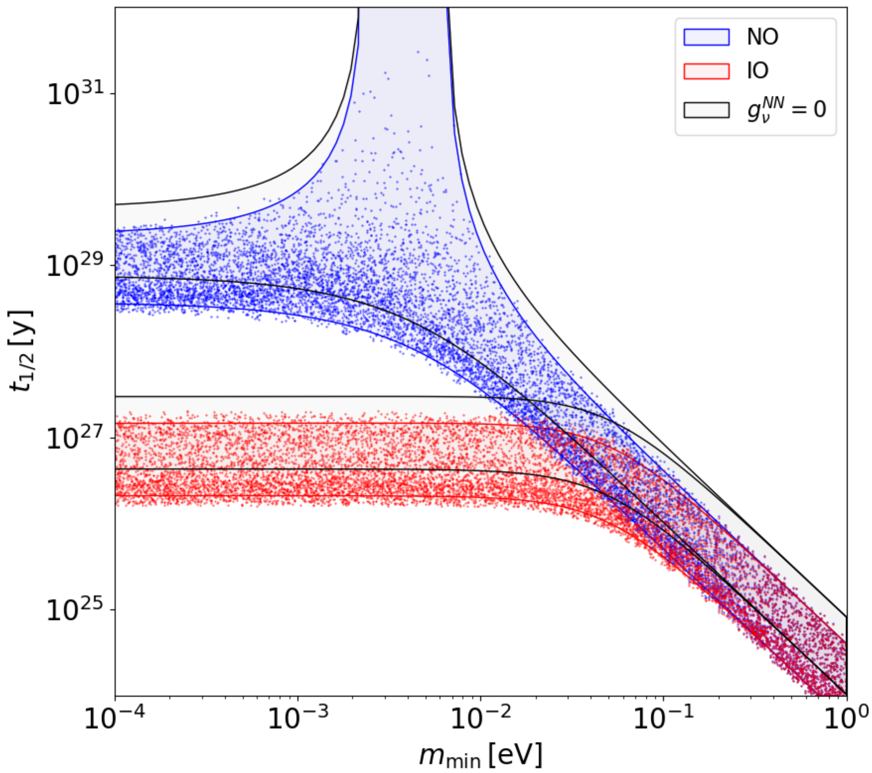

Figure 5.10: Impact of the contact LEC g_ν^{NN} on the $0\nu\beta\beta$ half-life. We show the expected half-life in the light neutrino-exchange mechanism in dependency on the minimal neutrino mass m_{min} for normal mass ordering (NO, blue) and inverted mass ordering (IO, red). The shaded regions display the expected $0\nu\beta\beta$ half-lives with g_ν^{NN} (coloured) and for $g_\nu^{NN} = 0$ (gray) when marginalizing over the unknown Majorana CP phases. The dots show a parameter scan of 10000 variations of the unknown Majorana phase as well as the LEC g_ν^{NN} within a range of $\pm 50\%$. The isotope chosen here is ^{136}Xe. This figure was published in Ref. [1] and is recalculated here with updated PSFs.

Let us focus on the identification of exotic higher-dimensional operators in contrast to the "standard" LνEM proportional to the effective Majorana neutrino mass $m_{\beta\beta}$. In the *representative* scenario derived from the central values of the parameter scan, we can see from the first row of Figure 5.11 that the long-range right-handed vector operator $C_{VR}^{(6)}$ (as well as the SMEFT operator $\mathcal{O}_{LeudH}^{(7)}$ which matches onto $C_{VR}^{(6)}$, c.f. Table 5.2) generates the half-life ratios that differ from the ones associated with the neutrino mass mechanism the most, specifically by a factor of $R_{im_{\beta\beta}} \sim 7.5$, closely followed by the SMEFT operator $\mathcal{O}_{LLQdH1}^{(7)}$ and the operators associated with $C_{S,V}^{(6,7)}$. However, while the latter operators give the most distinct ratios compared to the LνEM by utilizing the isotopic combinations of ^{136}Xe and ^{150}Nd or ^{82}Se and ^{150}Nd, the best ratio for the operators associated with $C_{VR}^{(6)}$ is achieved by comparing the half-lives in ^{134}Xe to those in ^{150}Nd. While ^{134}Xe does appear in experiments utilizing natural (i.e., not enriched) xenon with a natural abundance of $\overline{N}(^{134}\mathrm{Xe}) \sim 10.4\%$ (c.f. Table 4.1), its Q-value of $Q(^{134}\mathrm{Xe}) \sim 0.8\,\mathrm{MeV}$ is significantly smaller resulting in a considerable phase-space suppression by about 2 orders of magnitude (c.f. Table 4.8), thereby complicating its experimental detection. Therefore, in Figure 5.12 we provide the same overview as in Figure 5.11 but only considering isotopes of experimental interest with $Q > 2\,\mathrm{MeV}$. In this case, the best ratios obtainable for the operators associated with $C_{VR}^{(6)}$ reduce to 2.3 when comparing half-lives in ^{76}Ge to those in ^{150}Nd. This is in a similar range as for the remaining long-range LEFT operators $C_{VL,T}^{(6)}$ and the SMEFT operators matching onto them. At the same time, the short-range dimension-9 LEFT operators as well as the remaining SMEFT operators tend to give best values for $R_{im_{\beta\beta}}$ in the range of $\sim 1.5...2$. While some of these are achieved by utilizing the low Q-value isotope ^{128}Te, considering only isotopes with $Q > 2\,\mathrm{MeV}$ does decrease these ratios only slightly as we can read off from the first rows of Figures 5.11 and 5.12. In addition to the half-life ratios R_{ij} we have marked each operator combination distinguishable via the leptonic phase-space by a dashed background in Figures 5.11 and 5.12.

Conversely, when considering the worst-case scenario the best achievable values of $R_{im_{\beta\beta}}$ drop significantly for most of the operators, with many becoming (almost) indistinguishable from the LνEM. Only the operators associated with $C_{S,V}^{(6,7)}$ as well as the SMEFT operator $\mathcal{O}_{LLQdH1}^{(7)}$ remain mostly unchanged. This feature can be attributed to the fact that the operators associated with $C_{S,V}^{(6,7)}$ do, indeed, not depend on any unknown LECs and, as such, are not influenced by the parameter scan. In this context, it should be noted that the operator $\mathcal{O}_{LLQdH1}^{(7)}$ matches onto the operators $\mathcal{O}_{SR,T}^{(6)}$ and hence generates ratios similar to $\mathcal{O}_{SR}^{(6)}$. Nevertheless, if nature chooses to realize a parameter setting best represented by our worst-case scenario, the identification of exotic $0\nu\beta\beta$ mechanisms will have to rely mostly on the observables related to the leptonic phase space and may be declared hopeless in many cases.

Of course, the final goal is to exactly determine and identify the underlying mechanism once a $0\nu\beta\beta$ detection is realized. Taking our *representative* central value scenario as a baseline, we can see that the LNV right-handed vector currents represented by $C_{VR}^{(6)}$, as well as operators associated with $C_{S,V}^{(6,7)}$ and the SMEFT operator $\mathcal{O}_{LLQdH1}^{(7)}$ exhibit the best potential for a clear identification, as they, generally, provide large values of $R_{ij} > 4.7$[2] when comparing them to all other operators.

[2]Except for the combination of the operators associated with $C_{S,V}^{(6,7)}$ and the SMEFT dimension-7 operator $\mathcal{O}_{LLQdH1}^{(7)}$, which are hardly distinguishable from each other with $R_{ij} = 1.2$.

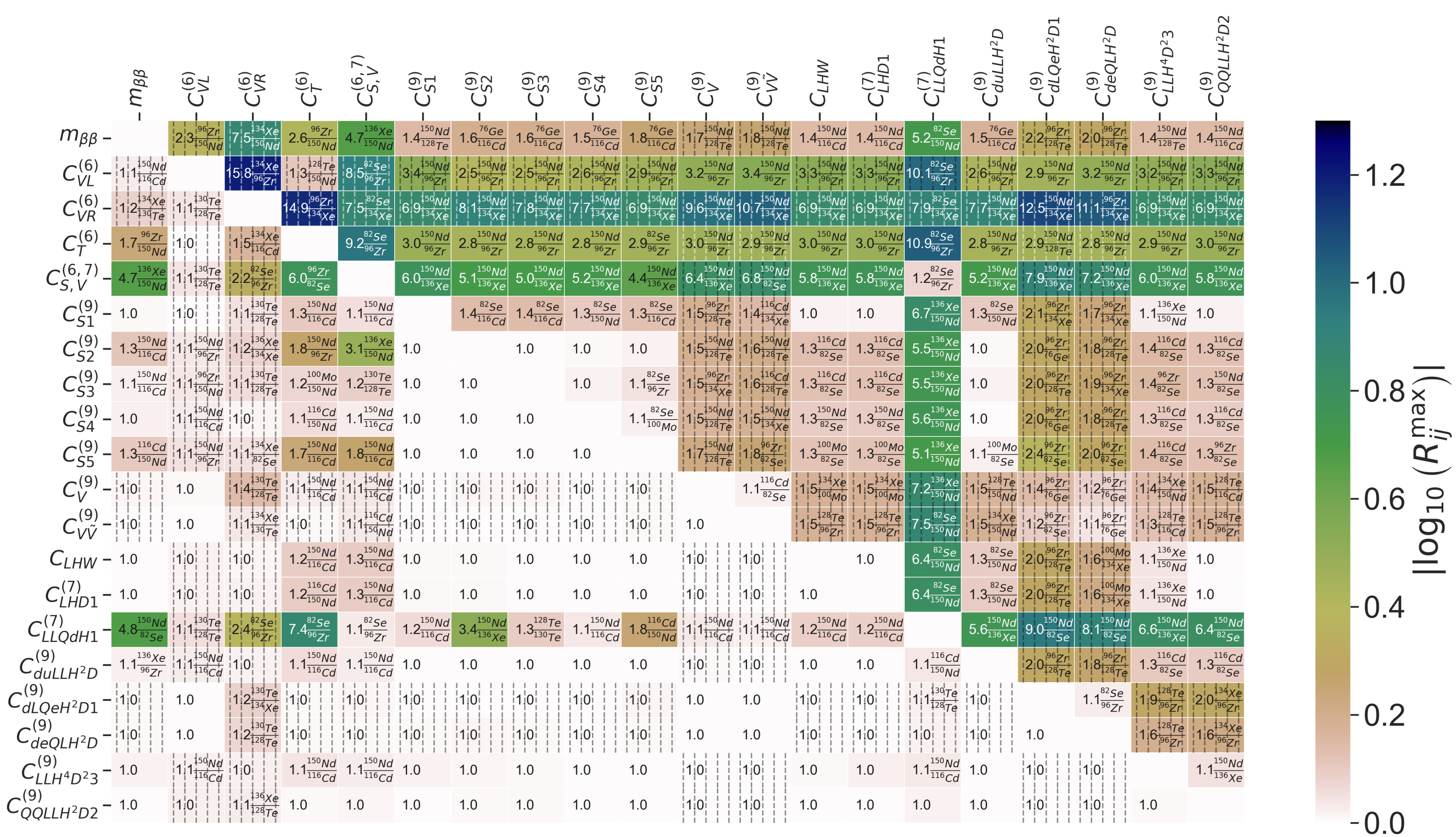

Figure 5.11: Maximal ratios R_{ij} for all SMEFT and LEFT operator combinations. The maximum ratios R_{ij} and the corresponding isotopes are shown in each tile. The figure is divided along the diagonal with ratios in the upper right triangle corresponding to a *representative* scenario derived from the central (median) ratios generated in the parameter scan. Conversely, the ratios in the lower left triangle represent the *worst-case* scenario. In addition, operator combinations that are distinguishable in the electron kinematics are marked by a dashed background. The SMEFT operators were not studied in Ref. [1] and we add them here for completeness.

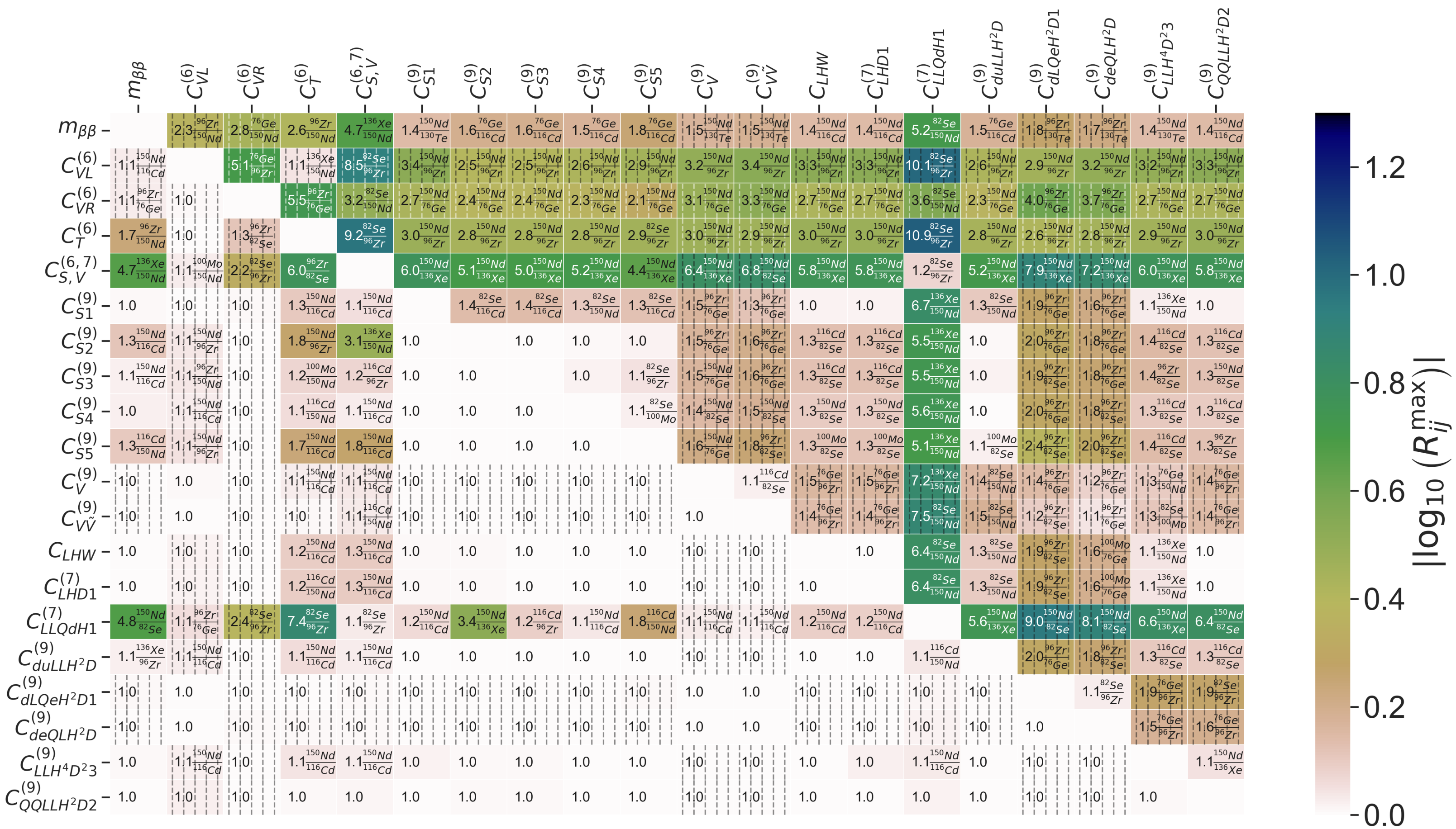

Figure 5.12: Maximal ratios R_{ij} for all SMEFT and LEFT operator combinations with isotopes of experimental interest and $Q > 2\,\mathrm{MeV}$. See Figure 5.11 for further details.

5.2.5 Estimating the Required Accuracy in the Nuclear Theory

As we have seen in the previous section, the uncertainty related to the currently unknown LECs is significant. Similarly, NMEs derived from distinct many-body methods often vary by factors of two to three from each other, thereby inducing a variance in the half-lives of about an order of magnitude when using NMEs derived from different approaches. These uncertainties, related to the nuclear theory, strongly limit the conclusions that can be drawn from a potential future $0\nu\beta\beta$ discovery concerning the identification of the underlying mechanism via half-life ratios.

Again, we write the half-life in terms of the new physics coupling C, the phase space factor G and an *effective* NME $\mathcal{M}_{\text{eff}}$ that summarizes the contributions from the different individual NMEs as well as the relevant LECs

$$\left(T_{1/2}^{0\nu\beta\beta}\right)^{-1} = |C|^2 G |\mathcal{M}_{\text{eff}}|^2. \tag{5.12}$$

Strictly speaking, the effective NME $\mathcal{M}_{\text{eff}}$ is a weighted sum of different NMEs and LECs, with the weight also (for some operators) including the individual PSFs G_i normalized with respect to G.

Because the PSFs can be calculated exactly [103], we can safely associate the theoretical uncertainties on the $0\nu\beta\beta$ half-life with the uncertainties in the nuclear theory parameterized by $\mathcal{M}_{\text{eff}}$. In Figure 5.13 we provide an overview of the NMEs for the LνEM obtained via various many-body methods. Typically, one finds a variation of the NMEs of about a factor ~ 3 with some outliers generated by the rEDF/CDFT NMEs of Ref. [210]. For the higher-dimensional operators, the unknown LECs induce additional uncertainties. Clearly, the identification of the underlying $0\nu\beta\beta$ mechanism via half-life ratios requires a substantial improvement in the nuclear theory. We can estimate the required accuracy by relating the uncertainty on the effective NME $\Delta\mathcal{M}_{\text{eff}}$ to the uncertainty on the half-life ratios ΔR_{ij}. For simplicity, we assume $\Delta\mathcal{M}_{\text{eff}}$ to be independent of the choice of isotopes [1]

$$\frac{\Delta M_{\text{eff}}}{M_{\text{eff}}}(^A Z) = \frac{\Delta M_{\text{eff}}}{M_{\text{eff}}} = \text{const.}. \tag{5.13}$$

Two operators $\mathcal{O}_{i,j}$ can be considered to be distinguishable via half-life measurements in multiple isotopes if the theoretical uncertainty on the expected ratio ΔR_{ij} is small enough to separate it from unity, i.e., we require

$$\Delta R_{ij} \overset{!}{<} |R_{ij} - 1|. \tag{5.14}$$

This criterion can be translated into an upper limit on the required theoretical uncertainty on the effective NME $\mathcal{M}_{\text{eff}}$ as

$$\frac{\Delta M_{\text{eff}}}{M_{\text{eff}}} \overset{!}{<} \frac{1}{4}\frac{|R_{ij} - 1|}{R_{ij}}. \tag{5.15}$$

Taking the *representative* central value scenario as a baseline, the identification of any higher dimensional exotic mechanism in contrast to the “standard” mass mechanism

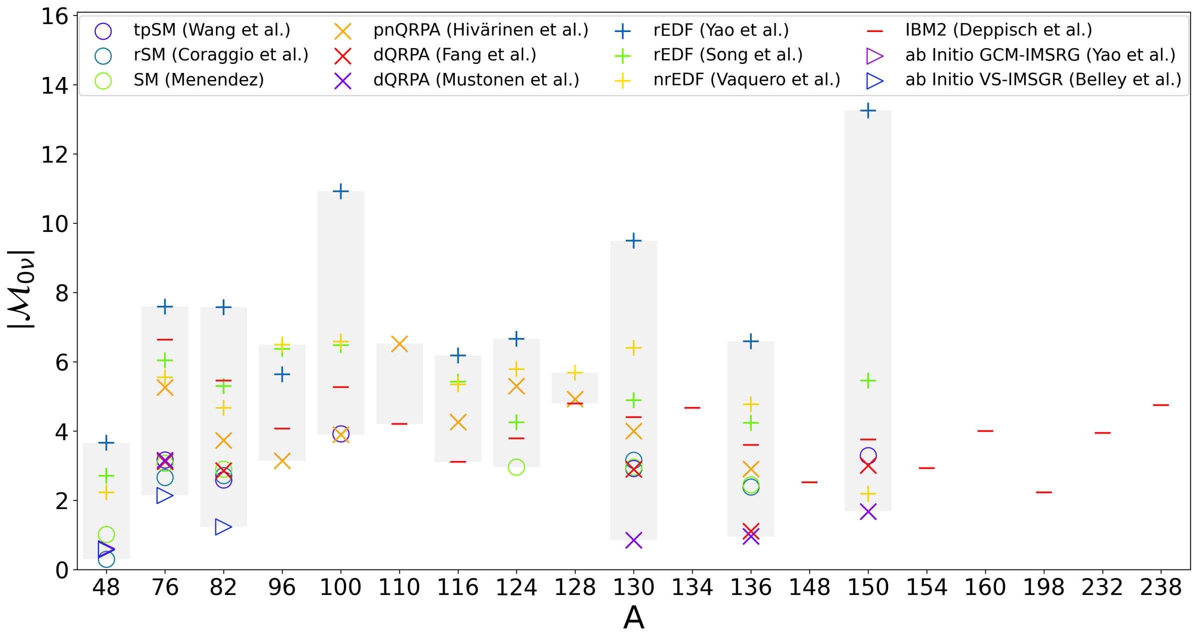

Figure 5.13: Comparison of NMEs related to the light neutrino-exchange mechanism as derived in various many-body methods. We plot the NME $\mathcal{M}_{0\nu} = -\frac{1}{g_A^2}M_F + M_{GT} + M_T$, i.e., without the contact term, calculated via different many-body methods. These include the interacting shell model (SM) [198], the triaxial projected shell model (tpSM) [206] or realistic shell model (rSM) [207], the proton-neutron quasiparticle random phase approximation (pnQRPA) [194], the deformed QRPA (dQRPA) [208, 209], the relativistic energy density functional method (rEDF) or covariant density functional theory (CDFT) [210, 211], the non-relativistic energy density functional method (nrEDF) [212], the interacting boson model (IBM2) [197] and state-of-the-art ab initio approaches calculating NMEs from basic principles of χPT [213, 214]. As one can see, there is a significant spread when comparing the different approaches, and we highlight the range of NMEs in grey. This figure was published in Ref. [1].

of light neutrino-exchange would require a theoretical accuracy in the nuclear theory calculations of $\Delta\mathcal{M}_{\rm eff}/\mathcal{M}_{\rm eff} \sim 7\%$, when considering all $0\nu\beta\beta$ candidate isotopes of experimental interest with $Q > 2\,\text{MeV}$. While the inclusion of the low Q-value isotopes ^{128}Te and ^{134}Xe does improve the distinguishability from the LνEM for some operators, as discussed in the previous section, it does not influence the $R_{im_{\beta\beta}}$ values that limit the identification of the short-range operators which set the most stringent requirement on the accuracy of the nuclear theory calculations.

The operators easiest to disentangle from the LνEM are the long-range vector SMEFT and LEFT operators associated with $C_{VR}^{(6)}$ as well as operators associated with $C_{S,V}^{(6,7)}$ and the dimension-7 SMEFT operator $\mathcal{O}_{LLQdH1}^{(7)}$. Taking, again, the central value scenario as a baseline, these operators would require an accuracy of $\Delta\mathcal{M}_{\rm eff}/\mathcal{M}_{\rm eff} \sim 22\%$ to 20%

to become distinguishable from the LνEM.

Considering the current status of NME calculations, the required accuracy signifies the necessity for a substantial improvement on the nuclear-theory side. Taking into account more than two isotopes might help to improve the potential of identifying non-standard operators [215].

5.3 Getting Creative: What About Other $0\nu\beta\beta$ Modes?

Up to this point, we have been concerned only with the leading $0^+ \to 0^+$ ground-state to ground-state transition of the $0\nu\beta^-\beta^-$ decay. However, as discussed in Chapter 4 one may consider $0\nu\beta\beta$-modes related to either the emission of positrons or the capture of electrons. This raises the question whether the consideration of more exotic decay modes would allow for an improved distinguishability among the various $0\nu\beta\beta$ mechanisms. For the sake of this discussion, let us ignore the fact that one can expect a significant phase-space suppression for all these modes in comparison to the more standard $0\nu\beta^-\beta^-$ decay (c.f. Refs. [103, 137, 216, 217]), and instead focus on their potential for an improvement in the distinguishability of $0\nu\beta\beta$ mechanisms.

5.3.1 Beta Plus and Electron Capture Modes

Even when ignoring the phase-space suppression, it is hard to imagine a significant advantage in the consideration of the $0\nu\beta^+\beta^+, 0\nu\beta^+$EC, and 0νECEC modes from a particle physics point of view due to their relation to the $0\nu\beta^-\beta^-$ mode via crossing symmetry. Obviously, the β^+ and electron capture modes differ with regards to the final state nuclei from the usual β^- decay mode and as such they may offer some improvement with regards to half-life ratios in the same way as the inclusion of additional $\beta^-\beta^-$ isotopes would do. Without a proper numerical evaluation, however, the potential benefit is hard to quantify. At the current time, the relevant NMEs are, to our best knowledge, not available within the literature.

While the positron-emitting modes are, in general, highly phase space suppressed, we want to point out that the 0νECEC may be enhanced via a resonance of the initial and final state nuclei [216, 217], potentially leading to expected half-lives smaller than those for the $0\nu\beta^-\beta^-$. While the current estimates of the expected 0νECEC half-lives do not suggest the existence of a significant resonance enhancement [216, 217], the uncertainties connected to the mass measurement of the initial and final state nuclei are still considerable [216]. A more recent finding suggests an additional enhancement of the 0νECEC rate via a non-resonant shake mechanism [218] in which the double capture of two electrons is accompanied by the emission of another electron from the atomic shell. The emitted electron can carry away any excess decay energy, thereby lowering the resonance requirement on the 0νECEC decay and enhancing the expected half-lives. See Ref. [219] for a recent review on the physics of the 0νECEC decay.

5.3.2 Excited Final State Nuclei

Similarly to positron-emitting $0\nu\beta\beta$ modes, the $0\nu\beta\beta$ to excited final-state nuclei is typically phase-space suppressed due to a smaller Q-value compared to the ground-state-to-ground-state transition. However, the suppression can be substantially smaller when considering the lowest order 2^+ excited final state [23] making the search for the $0\nu\beta\beta$ to an excited state much more compelling.

In contrast to the β^+ and EC modes, the decay to an excited 2^+ state may offer some intriguing opportunities. The most promising feature, from the point of distinguishing different $0\nu\beta\beta$ mechanisms experimentally, lies in the fact that the decay to the lowest lying 2^+ ground state is associated with a spin flip of a nucleon inside the nucleus $0^+ \to 2^+$. This spin-flip requires the inclusion of (parity-odd) P-states of the electron wave functions. This, in turn, allows for the long-range LEFT operators $\mathcal{O}^{(6)}_{VL,VR,T}$ and the associated SMEFT operators to contribute at LO in the chiral power counting, instead of their NLO contribution in the $0^+ \to 0^+$ transition [23]. In contrast, mechanisms such as the LνEM contributing at LO to the $0^+ \to 0^+$ transition can move to the NLO in the $0^+ \to 2^+$ transition due to the different parity structure. Therefore, it can expected that the half-life ratios $R_{im_{\beta\beta}}$, associated with these operators, will be significantly enhanced, thereby providing the potential to identify these exotic mechanisms more easily. While the decay to an excited state suffers from a higher background of $2\nu\beta\beta$ events, the subsequent de-excitation of the nucleus via the emission of a fixed-energy γ provides a smoking-gun signature of this process, which should allow for a high detection efficiency. The additional benefit of studying two decay modes (to the ground and the excited states) within a single experiment as an internal consistency check has been previously pointed out in Ref. [220].

Chapter 6

νDoBe - A Python Tool for Neutrinoless Double Beta Decay

In this chapter, we present ν`DoBe`, an open-source Python tool for $0\nu\beta\beta$ calculations originally published in Ref. [2]. ν`DoBe` is accessible via GitHub under the URL:

https://github.com/OScholer/nudobe

and a comprehensive code documentation is given in Ref. [2]. Here, we will refrain from repeating the tool's documentation and instead provide specific examples of possible use cases of ν`DoBe`. The Python code used to derive the results of most of the following sections can be found on GitHub in the `ExampleNotebooks` directory.[1]

6.1 Features

ν`DoBe` automates the chiral EFT approach developed in Refs. [44, 45] and described in Chapter 3. As such it is able to perform all necessary steps in evolving any LNV SMEFT model down to the scale of chiral EFT where the $0\nu\beta\beta$ observables such as half-lives, electron energy spectra and angular correlations can be extracted. Vice-versa, given an experimental limit on the $0\nu\beta\beta$ half-life in a certain isotope, ν`DoBe` can be used to derive the corresponding limits on the relevant SMEFT and LEFT operators as well as on the parameter space that is spanned by any pair of two SMEFT or LEFT operators.

Its most important features are [2]:

- ν`DoBe` contains all relevant LNV SMEFT and LEFT operators up to dimension 9.
- Calculating the $0\nu\beta\beta$ half-lives in all isotopes of experimental interest from any given EFT model.

[1]Please note that ν`DoBe` is an ongoing project under constant development. Therefore, all files on the ν`DoBe` GitHub are subject to change.

- Calculating the electron kinematics, i.e., the single electron spectrum and the angular correlation in all isotopes of experimental interest from any given EFT model.
- ν`DoBe` can perform the full tree-level SMEFT-to-LEFT matching procedure.
- Solving the 1-loop QCD RGEs of the LEFT operators up to dimension 9.
- Solving the full 1-loop RGEs of the SMEFT operators up to dimension 7.
- An easy extraction of the limits on the effective Majorana neutrino mass as well as the higher-dimensional LNV SMEFT or LEFT operators given an experimental bound on the $0\nu\beta\beta$ half-life for a certain isotope.
- ν`DoBe` can be used to constrain the parameter space that is spanned by any set of two LNV BSM operators given an experimental bound on the $0\nu\beta\beta$ half-life for a certain isotope.
- ν`DoBe` incorporates NMEs calculated in different state-of-the-art many-body schemes such as the nuclear shell model (SM) [198], the quasi-random-phase-approximation (QRPA) [194], the interacting boson model 2 (IBM2) [197] and the recently added covariant density functional theory approach (CDFT) [221].

Additionally, ν`DoBe` provides several quality-of-life features such as

- Highly customizable plotting functions to visualize all relevant and interesting $0\nu\beta\beta$ observables as well as operator limits, etc.
- Automated parameter scans over the unknown LECs
- LaTeX and HTML outputs of analytical expressions of the $0\nu\beta\beta$ half-life for any EFT model.

ν`DoBe` utilizes the following third-party Python packages

1. `NumPy` [222] [v. 1.19.2]
2. `Pandas` [223, 224] [v. 1.1.3]
3. `Matplotlib` [225] [v. 3.3.2]
4. `SciPy` [226] [v. 1.5.2]
5. `mpmath` [227] [v. 1.1.0]

6.2 Reanalyzing the Recent KamLAND-Zen Results with νDoBe

In Ref. [2] we have used νDoBe to reanalyze the results published by the KamLAND-Zen collaboration [228] which, at the date of publication, provided the strongest limit on both the $0\nu\beta\beta$ half-life as well as the effective Majorana mass $m_{\beta\beta}$. By including the effect of the contact interaction proportional to g_ν^{NN} generated in the LνEM, which was ignored in the KamLAND-Zen results, we were able to improve their limits by about 50% [2]. Additionally, we provided limits on the more exotic higher dimensional LNV SMEFT and LEFT operators, thereby offering a more complete picture.

With the KamLAND-Zen collaboration just recently providing an updated limit on the $0\nu\beta\beta$ half-life in ^{136}Xe of 3.8×10^{26} yr [46], we will repeat our reanalysis procedure here. In doing so, we will, again, provide a comparison of the impact of the contact interaction proportional to g_ν^{NN} which was ignored by the KamLAND-Zen collaboration. Additionally, we will provide the corresponding limits for each of the higher dimensional LNV SMEFT and LEFT operators.

6.2.1 The Light Neutrino-Exchange Scenario

When only the LνEM is considered, the half-life simplifies to

$$T_{1/2}^{-1} = g_A^4 \left|\frac{m_{\beta\beta}}{m_e}\right|^2 G_{01} V_{ud}^4 \left|\left(-\frac{1}{g_A^2} M_F + M_{GT} + M_T + 2\frac{m_\pi^2 g_\nu^{NN}}{g_A^2} M_{F,sd}\right)\right|^2. \tag{6.1}$$

Following our approach in Ref. [2], we will use the exact numerical solutions to the PSFs provided in Ref. [103] by using

$$V_{ud}^4 G_{01}(^{136}\mathrm{Xe}) = 1.458 \times 10^{-14}\,\mathrm{yr}^{-1}, \tag{6.2}$$

where the factor of V_{ud}^4 accounts for the conventionally different definition of the PSFs as described in Chapter 3. As the exact PSFs are only available for the LνEM within the literature, we will resort to the PSFs calculated by νDoBe via the point-like nucleus approximation when dealing with the higher dimensional operators in the following sections. In the literature, the individual NMEs M_F, M_{GT}^{ij} and M_T^{ij} are often not given and instead, only the overall NME

$$M_\nu = -\frac{1}{g_A} M_F + M_{GT} + M_T, \tag{6.3}$$

is provided. At the same time, the contact interaction arising from hard neutrino-exchange and the corresponding NMEs have only been considered in a limited number of publications with NMEs being available in the QRPA [194], IBM2 [197], SM [198] and CDFT [221] frameworks. In Table 6.1 we provide a comprehensive list of NMEs calculated in various many-body schemes as well as the corresponding limits on the effective Majorana mass $m_{\beta\beta}$ with and without the inclusion of the contact interaction

	M_ν	$M_{F,sd}$	$M_{F,sd}/M_\nu$	$\langle M_{F,sd}/M_\nu \rangle$	$m_{\beta\beta}$ [meV]	$\tilde{m}_{\beta\beta}$ [meV]
QRPA [194]*	3.009	$-61.8\frac{m_e m_p}{m_\pi^2}$	-0.51	-0.68 ± 0.10	45	21
QRPA [229]	3.384	–	–	–	40	27
QRPA [230]	2.460	–	–	–	55	38
QRPA [209]	1.89	–	–	–	71	49
QRPA [208]	1.18	$-28.8\frac{m_e m_p}{m_\pi^2}$	-0.60	–	114	49
EDF [212]	4.773	–	–	–	28	19
EDF [210]	4.32	–	–	–	31	21
EDF [231]	4.20	–	–	–	32	22
EDF [221]*	4.40	$-65.3\frac{m_e m_p}{m_\pi^2}$	-0.37	-0.36 ± 0.01	31	17
IBM2 [197]*	3.387	$-29.8\frac{m_e m_p}{m_\pi^2}$	-0.22	-0.25 ± 0.05	40	27
IBM2 [232]	3.05	$-29.7\frac{m_e m_p}{m_\pi^2}$	-0.24	–	44	29
SM [207]	2.39	–	–	–	56	39
SM [233]	1.76	–	–	–	76	53
SM [234]	1.77	–	–	–	76	52
SM [198]*	2.45	$-52\frac{m_e m_p}{m_\pi^2}$	-0.52	-0.53 ± 0.06	55	25

Table 6.1: A list of various nuclear matrix elements for ^{136}Xe. The list is taken from Ref. [2] and updated with the addition of the CDFT NMEs (labelled as EDF) of Ref. [221]. We assume $g_A \sim 1.271$ and apply the proper rescaling whenever necessary. NME sets that are marked with an asterisk (*) come pre-installed in ν`DoBe`. The limits on the effective Majorana mass are given in the columns labelled by $m_{\beta\beta}$ and $\tilde{m}_{\beta\beta}$, which represent the results without ($m_{\beta\beta}$) and including ($\tilde{m}_{\beta\beta}$) the contact terms of the light neutrino-exchange mechanism proportional to g_ν^{NN}. Additionally, we provide the ratio of the long-range and short-range NMEs $M_{F,sd}/M_\nu$ in ^{136}Xe as well as the average ratio of the NMEs $\langle M_{F,sd}/M_\nu \rangle$ and its standard deviation when considering all isotopes for a given scheme.

proportional to g_ν^{NN}. With the recent update of the $0\nu\beta\beta$ half-life limit in ^{136}Xe by the KamLAND-Zen collaboration we can put an upper limit on the effective Majorana mass of $m_{\beta\beta} < [28, 114]\,\mathrm{meV}$ when ignoring the contact interaction.

Most of the sets of NMEs given in Table 6.1 do not include the short-range NME $M_{F,sd}$. Nevertheless, we want to make a conservative estimate of the half-life limit as it would be obtained had the short-range NME $M_{F,sd}$ been calculated in all of the many-body schemes. In order to achieve this, we can take a look at the ratios of the long-range NME M_ν and the short-range NME $M_{F,sd}$ in ^{136}Xe as well as the average taken over all isotopes covered by each NME method. The corresponding values are displayed in Table 6.1. We then find that the ratios of the long- and short-range NMEs are generally larger than about $|M_{F,sd}|/|M_\nu| \gtrsim 0.2$ in ^{136}Xe with the smallest ratio resulting from the IBM2 NMEs while the QRPA NMEs result in the largest short-range NMEs when compared to M_ν. Generally, the ratio of $M_{F,sd}/M_\nu$ tends to be relatively stable among different isotopes for a given NME method with standard deviations ranging from 0.01 in the CDFT NMEs of Ref. [221] to 0.10 in the QRPA NMEs of Ref. [194]. While we could estimate the short-range NMEs for each method based on the $M_{F,sd}/M_\nu$ ratios of NMEs derived within a similar scheme, we will settle for a more conservative estimate and simply fix the ratio $M_{F,sd}/M_\nu = -0.2$ for all methods that do not provide their own calculation of the short-range NME. In doing so we are able to include the short-range contribution to the $0\nu\beta\beta$ transition amplitude, while, at the same time, minimizing the probability of overestimating its significance. Note that due to the negative sign of g_ν^{NN} the short-range contribution to the LνEM's transition amplitude is constructive, and therefore, results in tighter bounds on the effective Majorana mass. By including the short-range contribution in this way, we find an upper limit of $m_{\beta\beta} < [17, 53]$ meV when taking the full transition amplitude into account, with the strongest limit being provided by the CDFT NMEs of Ref. [221].

In Figure 6.1 we provide a comparison of the corresponding half-life limits in the $m_{\min}-m_{\beta\beta}$ plane, spanned by the minimal neutrino mass $m_{\min}$ and the effective Majorana mass, with the allowed parameter space for the inverted (IO) and normal (NO) mass ordering displayed in green and red, respectively. Additionally, we provide the same information with respect to the summed neutrino masses $\sum_i m_i \lesssim 260\,\mathrm{meV}$ [235, 236]. While the limit on the sum of the neutrino masses already puts strong constraints on the parameter space of the inverted mass ordering, most of the $0\nu\beta\beta$ limits put even more stringent bounds with the strongest limits obtained by using the NMEs of Ref. [221] ruling out almost all of the remaining parameter space of the IO scenario when considering the full $0\nu\beta\beta$ transition amplitude.

6.2.2 Higher Dimensional Operators

Let us now also take the higher dimensional LNV operators into account. As mentioned previously, the exact numerical solutions to the electron wave functions for a uniform charge distribution including electron screening effects are to this date only available for the LνEM within the literature. Instead, we will use the analytic solution for a point-like nucleus, again, which is known to be a precise approximation of the exact results, overestimating the PSFs only by about $\sim 2\% - 10\%$ [200].

Generally, in scenarios with a single LNV BSM operator dominating the $0\nu\beta\beta$ transition amplitude, the half-life can be parameterized as

$$\left(T_{1/2}^{0\nu\beta\beta}\right)^{-1}(^AZ) = |C_i|^2 G_i(^AZ)|M_i(^AZ)|^2, \tag{6.4}$$

where G_i and M_i represent the PSF and NME corresponding to the BSM operator $\mathcal{O}_i$ for the isotope ^AZ. The proportionality of the decay rate to the absolute square of the Wilson coefficient $|C_i|^2$ allows us to easily translate any experimental lower limit on the

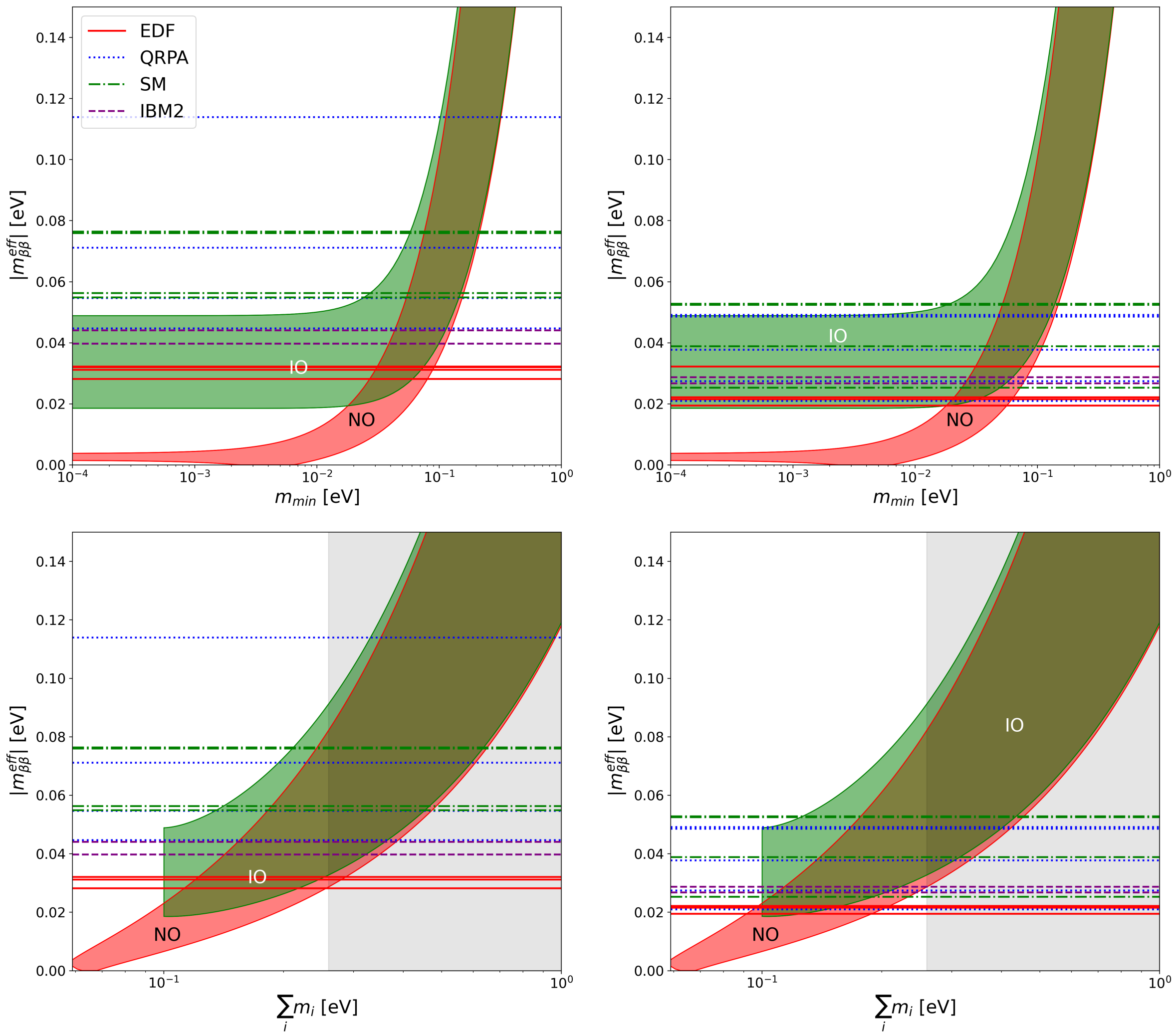

Figure 6.1: Limits on the effective Majorana mass $m_{\beta\beta}$ as obtained from the recent half-life limit by the KamLAND-Zen experiment [46]. The parameter space of the normal neutrino mass ordering (NO) and the inverted ordering (IO) are given in red and green. In the upper two plots, we present the limits obtained from the set of NMEs by setting $g_\nu^{NN} = 0$ (left) and by using $g_\nu^{NN} = -92.9\,\mathrm{GeV}^2$ (right). Additionally, we provide a comparison to the cosmological limit on the sum of neutrino masses in the lower two plots. This is an updated version of the figure published in Ref. [2].

half-life given in a certain isotope $({}^AZ)$ to an upper limit on the absolute value of the Wilson coefficient $|C_{i,\mathrm{max}}|$ via the relation

$$|C_{i,\mathrm{max}}| = \sqrt{\frac{T_{1/2}^{0\nu\beta\beta}(C_i = 1, {}^A Z)}{T_{1/2,\mathrm{min}}^{0\nu\beta\beta}({}^A Z)}}, \tag{6.5}$$

$m_{\beta\beta}$	$C_S^{(6)}$	$C_{S,NC}^{(6)}$	$C_T^{(6)}$	$C_{VL}^{(6)}$	$C_{VR}^{(6)}$	$C_V^{(7)}$	$C_{S1}^{(9)}$	$C_{S2}^{(9)}$	$C_{S3}^{(9)}$	$C_{S4}^{(9)}$	$C_{S5}^{(9)}$	$C_V^{(9)}$	$C_{\tilde{V}}^{(9)}$
$m_{\beta\beta}$	$C_{SL}^{(6)}$	$C_{SL,\nu u}^{(6)}$	$C_T^{(6)}$	$C_{VL}^{(6)}$	$C_{VR}^{(6)}$	$C_{VL}^{(7)}$	$C_{1L}^{(9)}$	$C_{2L}^{(9)}$	$C_{3L}^{(9)}$	$C_{4L}^{(9)}$	$C_{5L}^{(9)}$	$C_6^{(9)}$	$C_7^{(9)}$
	$C_{SR}^{(6)}$	$C_{SR,\nu u}^{(6)}$				$C_{VR}^{(7)}$	$C_{1R}^{(9)}$	$C_{2R}^{(9)}$	$C_{3R}^{(9)}$	$C_{4R}^{(9)}$	$C_{5R}^{(9)}$	$C_8^{(9)}$	$C_9^{(9)}$
		$C_{SL,\nu d}^{(6)}$					$C_{1L}^{(9)\prime}$	$C_{2L}^{(9)\prime}$	$C_{3L}^{(9)\prime}$			$C_6^{(9)\prime}$	$C_7^{(9)\prime}$
		$C_{SR,\nu d}^{(6)}$					$C_{1R}^{(9)\prime}$	$C_{2R}^{(9)\prime}$	$C_{3R}^{(9)\prime}$			$C_8^{(9)\prime}$	$C_9^{(9)\prime}$

Table 6.2: Groups of LEFT operators that result in the same half-lives.

where $T_{1/2,\min}^{0\nu\beta\beta}(^AZ)$ is the lower experimental limit on the half-life in an isotope ^AZ and $T_{1/2}^{0\nu\beta\beta}(C_i = 1, ^A Z)$ is the half-life that would result from the theory when setting $C_i = 1$. From a naturalness perspective, it is reasonable to connect a limit on the dimensionful Wilson coefficients to an expected scale Λ, at which the effective operator is generated by integrating out the heavy new-physics fields, by defining [2]

$$C_i = \frac{\tilde{C}_i}{\Lambda^{(d-4)}}, \tag{6.6}$$

and assuming that the dimensionless coupling $\tilde{C}_i$ should be of order 1. Hence, for an operator of dimension d we can estimate the new-physics scale as

$$\Lambda \simeq \left(C_{i,\max}\right)^{(1/(4-d))}. \tag{6.7}$$

Notice that in the definitions of the LEFT Wilson coefficients, we have already factored out factors of G_F in such a way that the LEFT Wilson coefficients are defined to be dimensionless and the new-physics scale can, instead, be derived via

$$\Lambda \simeq v\left(C_{i,\mathrm{mac}}^{\mathrm{LEFT}}\right)^{(1/(4-d))}. \tag{6.8}$$

6.2.2.1 LEFT Operators

From the half-life formula given in eq. (4.147) we can arrange the 36 different LEFT operators into 14 different groups such that each operator within a given group results in the same numerical value for the $0\nu\beta\beta$ half-life. We present these 14 groups of operators in Table 6.2. Extracting the numerical limits on the corresponding Wilson coefficients as well as the related new-physics scale can be achieved with the help of `νDoBe` within a single line of code by using the provided `get_limits_LEFT()` function. The corresponding lower limits on the new-physics scale Λ for each operator groups are presented in Figure 6.2. In Table 6.3 we provide a comprehensive overview of the numerical limits on the dimensionless couplings C_i as well as the estimated scales of new physics as derived from the recent KamLAND-Zen limit [46]. The limits are given, individually, as derived from each of the four NME methods that are available within `νDoBe`. To our

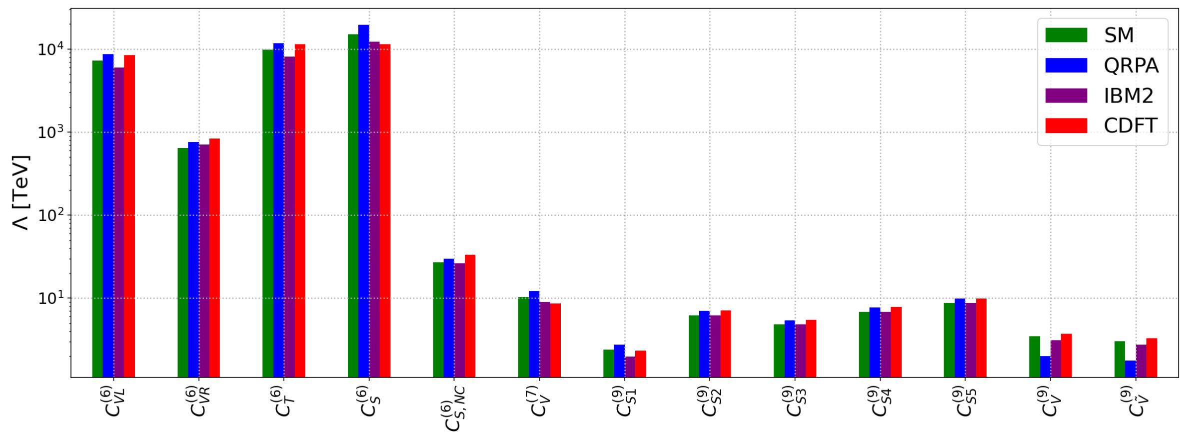

Figure 6.2: Lower limits on the new-physics scale for each LEFT operator group as derived from the recent KamLAND-Zen results [46].

best knowledge, the limits obtained for the neutral-current LNV dimension-6 LEFT operators summarized in $C^{(6)}_{S,NC}$ represent the strongest constraints available in the current literature exceeding the limits obtained from coherent elastic neutrino-nucleus scattering (CEνNS) experiments by about 2 orders of magnitude [237].

In Figure 6.3 we provide a comparison of the limits derived from the recent KamLAND-Zen results providing a lower half-life limit in ^{136}Xe of $T^{0\nu\beta\beta}_{1/2} > 3.8 \times 10^{26}$ yr [46] and the final results of the GERDA experiment giving a lower limit on the $0\nu\beta\beta$ half-life in ^{76}Ge of $T^{0\nu\beta\beta}_{1/2} > 1.8 \times 10^{26}$ yr [33]. We can see that despite the different isotopes being used and the corresponding difference in the NMEs, the KamLAND-Zen experiment provides the strongest constraints on all the LEFT operators. For the comparison we use the shell model NMEs of Ref. [198]. However, the statement remains true for all of the NMEs provided in ν`DoBe`.

6.2.2.2 SMEFT Operators

Due to the complex SMEFT-to-LEFT matching relations (c.f. Section 4.4.2) there are rarely any SMEFT operators that result in precisely the same $0\nu\beta\beta$ half-lives. The only exceptions out of the 36 relevant SMEFT operators are the operator pairs $\mathcal{O}^{(9)}_{QLQLH^2D2}$ and $\mathcal{O}^{(9)}_{QLQLH^2D5}$, $\mathcal{O}^{(9)}_{QueLH^2D2}$ and $\mathcal{O}^{(9)}_{dQLeH^2D2}$, $\mathcal{O}^{(9)}_{dLuLH^2D2}$ and $\mathcal{O}^{(9)}_{deueH^2D}$, $\mathcal{O}^{(9)}_{dQdQLL1}$ and $\mathcal{O}^{(9)}_{QuQuLL1}$, $\mathcal{O}^{(9)}_{dQdQLL2}$ and $\mathcal{O}^{(9)}_{QuQuLL2}$, $\mathcal{O}^{(9)}_{QudueL1}$ and $\mathcal{O}^{(9)}_{dQdueL1}$, as well as the pair $\mathcal{O}^{(9)}_{QudueL2}$ and $\mathcal{O}^{(9)}_{dQdueL2}$, and we refrain from organizing the SMEFT operators into several groups as we did for the LEFT operators. We extract the limits on the SMEFT coefficients at the SMEFT-to-LEFT matching scale m_W. The corresponding new-physics scales are displayed in Figure 6.4. To save space here, we do not show the precise numerical values but instead refer to the corresponding notebook in the ν`DoBe` GitHub with which they can be easily derived.

NMEs:	Operator:	$C_{VL}^{(6)}$	$C_{VR}^{(6)}$	$C_{T}^{(6)}$	$C_{S}^{(6)}$	$C_{S,NC}^{(6)}$	$C_{V}^{(7)}$
SM [198]	C_i	1.2×10^{-9}	1.5×10^{-7}	6.2×10^{-10}	2.7×10^{-10}	8.3×10^{-5}	1.4×10^{-5}
	Λ [TeV]	7.3×10^{3}	645	9.9×10^{3}	1.5×10^{4}	27.1	10.3
QRPA [194]	C_i	8.1×10^{-10}	1.0×10^{-7}	4.4×10^{-10}	1.6×10^{-10}	6.8×10^{-5}	8.2×10^{-6}
	Λ [TeV]	8.6×10^{3}	761	1.2×10^{4}	1.9×10^{4}	29.8	12.2
IBM2 [197]	C_i	1.7×10^{-9}	1.2×10^{-7}	9.3×10^{-10}	4.0×10^{-10}	8.7×10^{-5}	2.0×10^{-5}
	Λ [TeV]	5.9×10^{3}	707	8.1×10^{3}	1.2×10^{4}	26.4	9.0
CDFT [221]	C_i	8.60×10^{-10}	8.57×10^{-8}	4.65×10^{-10}	4.58×10^{-10}	5.47×10^{-5}	2.35×10^{-5}
	Λ [TeV]	8.4×10^{3}	840	1.1×10^{4}	1.1×10^{4}	33.3	8.6

NMEs:	Operator:	$C_{S1}^{(9)}$	$C_{S2}^{(9)}$	$C_{S3}^{(9)}$	$C_{S4}^{(9)}$	$C_{S5}^{(9)}$	$C_{V}^{(9)}$	$C_{\tilde{V}}^{(9)}$
SM [198]	C_i	1.1×10^{-5}	9.6×10^{-8}	3.4×10^{-7}	5.9×10^{-8}	1.7×10^{-8}	1.8×10^{-6}	3.5×10^{-6}
	Λ [TeV]	2.4	6.2	4.8	6.9	8.8	3.5	3.0
QRPA [194]	C_i	5.8×10^{-6}	5.4×10^{-8}	1.9×10^{-7}	3.3×10^{-8}	9.7×10^{-9}	2.7×10^{-5}	5.1×10^{-5}
	Λ [TeV]	2.7	7.0	5.4	7.7	9.8	2.0	1.8
IBM2 [197]	C_i	2.9×10^{-5}	9.7×10^{-8}	3.5×10^{-7}	6.0×10^{-8}	1.8×10^{-7}	3.0×10^{-6}	5.7×10^{-6}
	Λ [TeV]	2.0	6.2	4.8	6.9	8.8	3.1	2.8
CDFT [221]	C_i	1.3×10^{-5}	5.1×10^{-8}	1.8×10^{-7}	3.1×10^{-8}	9.2×10^{-9}	1.3×10^{-6}	2.4×10^{-6}
	Λ [TeV]	2.3	7.1	5.5	7.8	10.0	3.7	3.3

Table 6.3: Numerical limits on the different higher dimensional LEFT operators as derived from the recent KamLAND-Zen results. We present both the limits on the dimensionless couplings C_i as well as the corresponding scale of new physics Λ for the four different sets of NMEs that are included in ν`DoBe`.

6.2.3 Multi-Operator Scenarios

The above limits on the SMEFT and LEFT operators all assume the $0\nu\beta\beta$ half-life to be dominated by a single operator. However, the $0\nu\beta\beta$ amplitude might be driven by multiple operators at the same time, with the possibility of constructive and destructive interference terms adding another layer of complexity to the analysis. Again, ν`DoBe` is equipped with tools that allow us to easily analyze the parameter space of scenarios dominated by two operators at a time. In a scenario with the $0\nu\beta\beta$ amplitude being dominated by two operators $\mathcal{O}_{x,y}$, the half-life can be parameterized in terms of the corresponding Wilson coefficients $C_{x,y}$ as well as the relative complex phase ϕ between the two operators as [2]

$$\left(T_{1/2}^{0\nu\beta\beta}\right)^{-1} = C_x^2 M_{xx} + C_y^2 M_{yy} + 2\mathrm{Re}[C_x C_y \exp\{(i\phi)\}]M_{xy}, \tag{6.9}$$

where the matrix M depends on the relevant PSFs, NMEs and LECs involved. Solving for C_y, we get the expression

$$C_y = -C_x \frac{\cos(\phi) M_{xy}}{M_{yy}} \pm \sqrt{C_x^2 \frac{\cos(\phi) M_{xy}^2 - M_{xx} M_{yy}}{M_{yy}^2} + \frac{1}{T_{1/2}^{0\nu\beta\beta} M_{yy}}}, \tag{6.10}$$

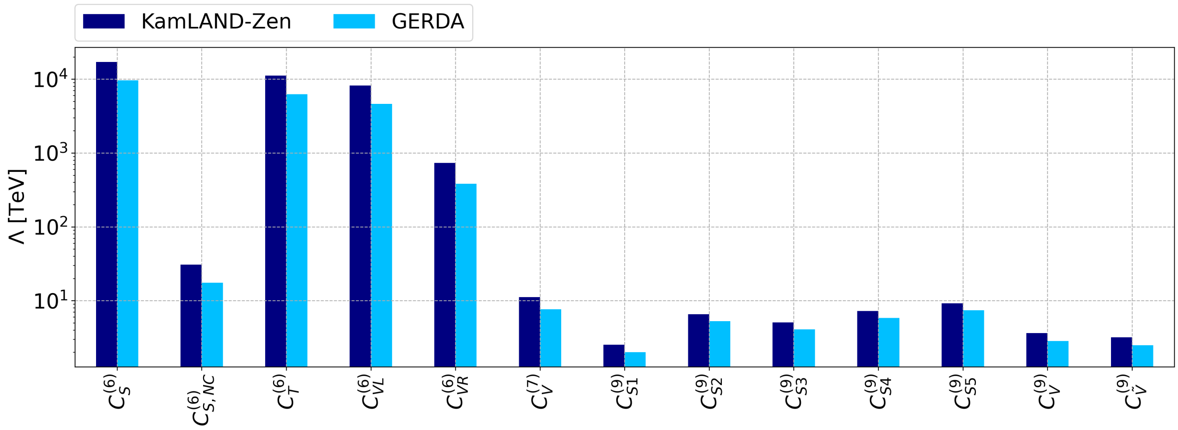

Figure 6.3: Comparison of the LEFT constraints obtained from the half-life limit of $T_{1/2}^{0\nu\beta\beta} > 3.8 \times 10^{26}\,\mathrm{yr}$ in ^{136}Xe set by the KamLAND-Zen collaboration [46] and the half-life limit of $T_{1/2}^{0\nu\beta\beta} > 1.8 \times 10^{26}\,\mathrm{yr}$ in ^{76}Ge set by the GERDA experiment [33]. The limits are obtained using the shell model NMEs of Ref. [198].

which we can use to constrain the allowed parameter space in the $C_x - C_y$ plane from experimental half-life limits. Notably, depending on the precise values of the matrix entries M the possibility of a cancellation between the two operators $\mathcal{O}_{x,y}$ exists, such that the allowed parameter space contains unrestricted directions. In Figure 6.5 we provide a summary of the allowed parameter space in the $m_{\beta\beta} - C_y$ plane for all relevant LEFT operators $\mathcal{O}_y$ by considering the half-life limits given in ^{76}Ge set by GERDA [33], ^{100}Mo obtained by CUPID-Mo [113], ^{130}Te given by the CUORE experiment [119], as well as ^{136}Xe as set by KamLAND-Zen [46] (c.f. Table 4.1). The limits on the parameter space are obtained by using the IBM2 set of NMEs [197] and we varied the relative phase ϕ. We can see that, except for the long- and short-range vector operators $\mathcal{O}_{VL,VR,6,7}^{(9)}$, the $m_{\beta\beta} - C_y$ plane generally has a direction of cancellation such that the magnitude of the coefficients cannot be fully constrained from a half-life limit in a single isotope. However, an important feature displayed in Figure 6.5 is the relative tilt of the parameter space regions constrained within different $0\nu\beta\beta$ candidate isotopes. Specifically, the allowed parameter space resulting from half-life limits in ^{100}Mo tends to be substantially tilted with respect to the remaining isotopes. While this feature might be a remnant resulting from the numerical many-body methods used to derive the relevant NMEs, it is prominent not only within the IBM2 approach [197], but also in the QRPA NMEs of Ref. [194], though to a different extent. While the shell model NMEs of Ref. [198] available in ν`DoBe` do not support the ^{100}Mo isotope, the tilt is far less prominent within the CDFT NMEs of Ref. [221], showcasing, again, the importance of precise and reliable nuclear theory calculations. Nevertheless, this feature makes a strong case for next generation $0\nu\beta\beta$ experiments utilizing ^{100}Mo, such as CUPID [37] or AMoRE [238] aiming to significantly improve the $0\nu\beta\beta$ half-life limit in ^{100}Mo.

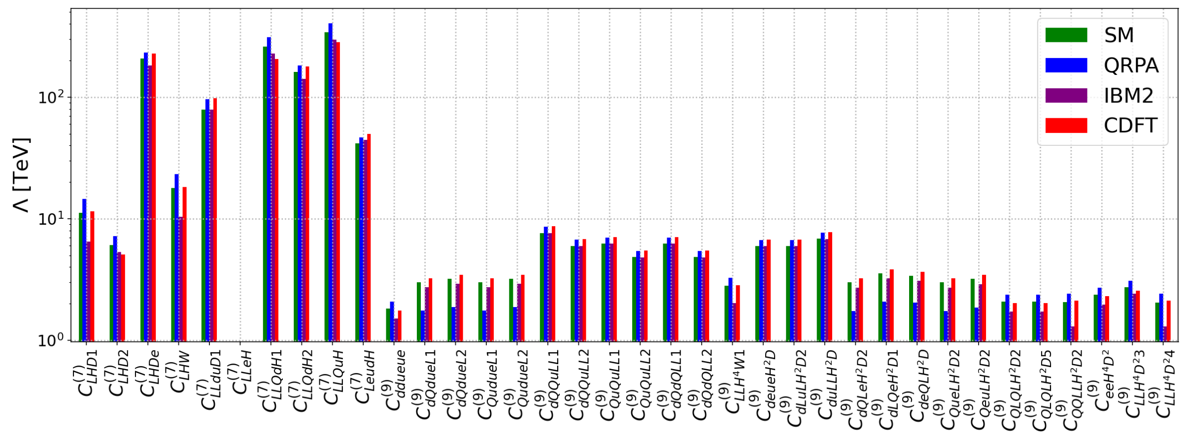

Figure 6.4: Lower limits on the new-physics scale for each of the 36 SMEFT operators of dimension-7 and 9 as derived from the recent KamLAND-Zen results [46]. The limits are extracted at the SMEFT-to-LEFT matching scale m_W and therefore do not include RGE effects.

6.3 Studying the Minimal Left-Right Symmetric Model with νDoBe

Besides model-independent studies of new LNV physics in $0\nu\beta\beta$ experiments, the EFT framework described in Chapter 4 allows for model-dependent approaches as well by matching specific LNV high-energy models onto the appropriate SMEFT or LEFT operators. In this section, we will study the minimal left-right symmetric model (mLRSM) [47–50] following along the lines of Refs. [1, 2, 45]. This will serve as an example how νDoBe can facilitate model-dependent studies of $0\nu\beta\beta$ observables.

As described in Chapter 2, the Standard Model is a chiral theory that, due to its $SU(2)_L$ gauge symmetry, maximally violates parity in the weak interaction sector. On an intuitive level, this parity violation and the explicit distinction between left- and right-handed fields seems rather unnatural. Of course, in the end Nature does not need to care what we deem as natural or unnatural. Nevertheless, it is tempting to extend the SM to a left-right symmetric theory which is only spontaneously broken to the observed left-handed symmetry structure. The easiest way to achieve this is via the mLRSM. It extends the SM symmetry structure to a left-right symmetric $SU(3)_C \times SU(2)_L \times SU(2)_R \times U(1)_{B-L}$ gauge model with the field content of the SM enlarged to include three right-handed neutrino fields ν_R acting as a counterpart to the left-handed neutrinos. At the same time, the mLRSM includes two scalar $SU(2)_{L,R}$ triplets $\Delta_L \in (\mathbf{1}, \mathbf{3}, \mathbf{1}, 2)$ and $\Delta_R \in (\mathbf{1}, \mathbf{1}, \mathbf{3}, 2)$ as well as a scalar bidoublet $\Phi \in (\mathbf{1}, \mathbf{2}, \mathbf{2}^*, 0)$ which replaces the standard Higgs doublet [50]. The neutral components of the scalar fields

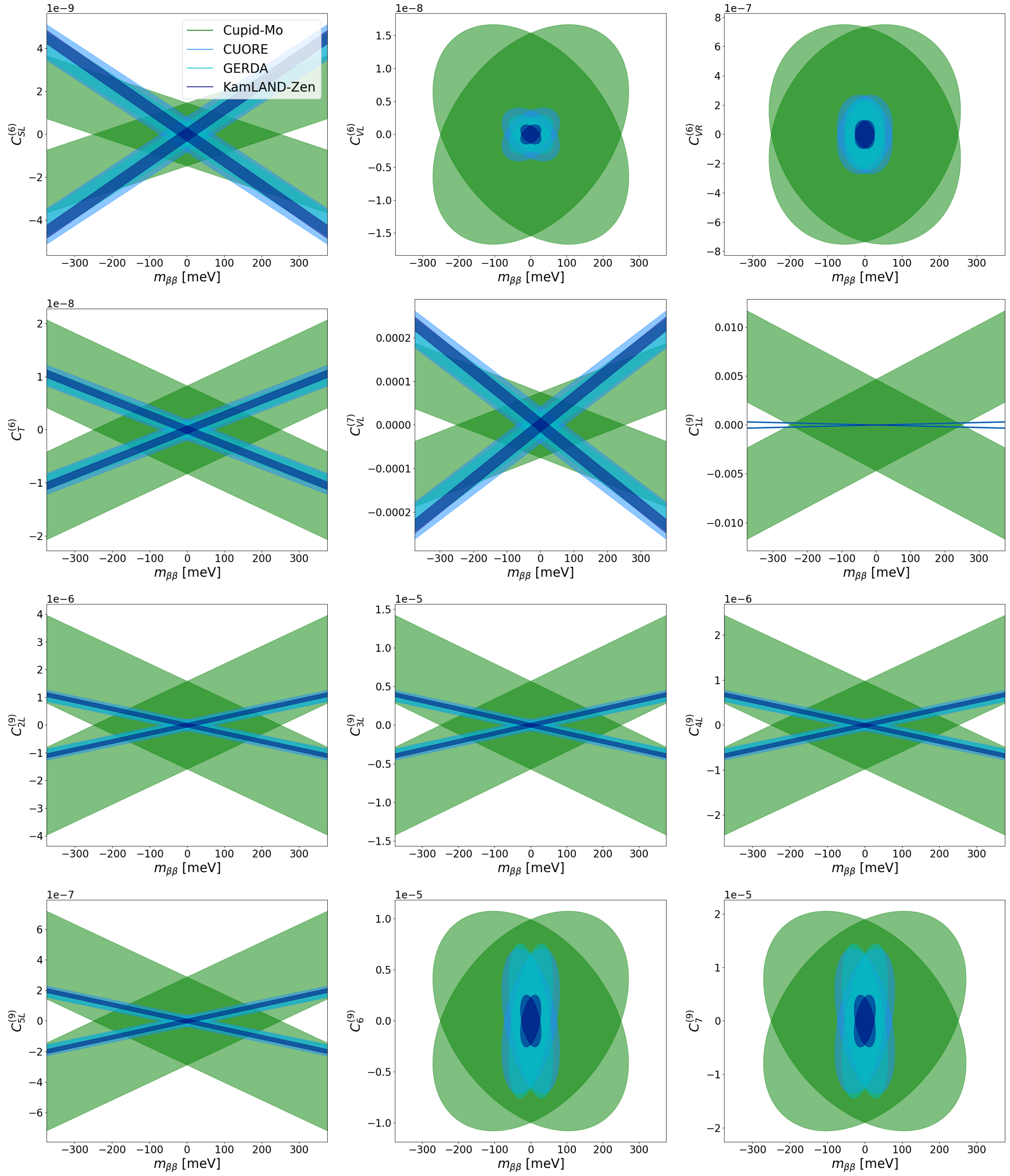

Figure 6.5: Parameter space constraints for the effective Majorana mass $m_{\beta\beta}$ with an additional higher-dimensional contribution. The parameter space is obtained from the half-life limits set by the KamLAND-Zen [46], GERDA [33], CUORE [119] and CUPID-Mo [113] experiments (c.f. Table 4.1).

acquire non-trivial vevs [1, 2, 45, 50]

$$\langle \Phi \rangle = \frac{1}{\sqrt{2}} \begin{pmatrix} \kappa & 0 \\ 0 & \kappa' e^{i\alpha} \end{pmatrix}, \qquad \langle \Delta_L \rangle = \frac{1}{\sqrt{2}} \begin{pmatrix} 0 & 0 \\ v_L e^{i\theta_L} & 0 \end{pmatrix}, \qquad \langle \Delta_R \rangle = \frac{1}{\sqrt{2}} \begin{pmatrix} 0 & 0 \\ v_R & 0 \end{pmatrix}, \tag{6.11}$$

subsequently breaking the mLRSM gauge structure down to the SM gauge group and the broken phase of the SM, $SU(2)_L \times SU(2)_R \times U(1)_{B-L} \to SU(2)_L \times U(1)_Y \to U(1)_{\mathrm{EM}}$. The relevant LNV terms in the broken phase of the mLRSM are given by the Yukawa interactions [1, 2, 45, 50]

$$\mathcal{L}_y = \sum_{ij} \left[Y^l_{ij} \overline{L_{Li}} \Phi L_{R,j} + \tilde{Y}^l_{ij} \overline{L_{Li}} \tilde{\Phi} L_{R,j} + Y^L_{ij} L^T_{L,i} C i\tau_2 \Delta_L L_{L,j} + Y^{R\dagger}_{ij} L^T_{R,i} C i\tau_2 \Delta_R L_{R,j} \right] + \text{h.c.}, \tag{6.12}$$

where we defined the $SU(2)_L$ and $SU(2)_R$ fermion doublets [1, 2, 45, 50]

$$\begin{aligned} L_L &= \begin{pmatrix} \nu_L \\ e_L \end{pmatrix} \in (1,2,1,-1)\,, \qquad & Q_L &= \begin{pmatrix} u_L \\ d_L \end{pmatrix} \in (3,2,1,1/3)\,, \\ L_R &= \begin{pmatrix} \nu_R \\ e_R \end{pmatrix} \in (1,1,2,-1)\,, \qquad & Q_R &= \begin{pmatrix} u_R \\ d_R \end{pmatrix} \in (3,1,2,1/3)\,. \end{aligned} \tag{6.13}$$

These Yukawa interactions generate a Dirac neutrino mass matrix as well as a left-handed and right-handed Majorana mass matrix given by [1, 2, 45, 50]

$$\begin{aligned} M^\nu_{D,ij} &= \frac{1}{\sqrt{2}} \left[Y^l_{ij} \kappa + \tilde{Y}^l_{ij} \kappa' \exp\{-i\alpha\} \right], \\ M^{\nu}_{L,ij}{}^\dagger &= \sqrt{2} Y^L_{ij} v_L \exp\{i\theta_L\}, \\ M^\nu_{R,ij} &= \sqrt{2} Y^R_{ij} v_R. \end{aligned} \tag{6.14}$$

The matching of the mLRSM onto the relevant SMEFT operators has been obtained in Ref. [45] and the correspinding LNV parts of the Lagrangian may be written as

$$\begin{aligned} \mathcal{L}_{\Delta L=2} =& C^{(5)} \left(\left(L^T C i\tau_2 H \right) \left(\tilde{H}^\dagger L \right) \right) \\ & + \left(L^T \gamma^\mu e_R \right) i\tau_2 H \left[C^{(7)}_{Leu\bar{d}\Phi} \overline{d_R} \gamma_\mu u_R + C^{(7)}_{L\Phi De} H^T i\tau_2 (D_\mu \Phi_{SM}) \right] \\ & + \overline{e_R} e^c_R \left[C^{(9)}_{eeud} \overline{u_R} \gamma^\mu d_R \overline{u_R} \gamma_\mu d_R + C^{(9)}_{ee\Phi ud} \overline{u_R} \gamma^\mu d_R \left([iD_\mu H]^\dagger \tilde{H} \right) \right. \\ & \left. + C^{(9)}_{ee\Phi D} \left([iD_\mu H]^\dagger \tilde{H} \right)^2 \right]. \end{aligned} \tag{6.15}$$

The SM Higgs vev is connected to the bidoublet's vevs by $v = \sqrt{\kappa^2 + \kappa'^2}$. The relevant

Wilson coefficients are given in terms of the mLRSM parameters as

$$\begin{aligned}
C^{(5)} &= \frac{1}{v^2}\left(M_D^{\nu\,T} M_R^{\nu\,-1} M_D^{\nu} - M_L^{\nu}\right), \\
C^{(7)}_{Leu\bar{d}\Phi} &= \frac{\sqrt{2}}{v}\frac{1}{v_R^2}\left(V_R^{ud}\right)^*\left(M_D^{\nu T} M_R^{\nu\,-1}\right)_{ee}, \qquad & C^{(7)}_{L\Phi De} &= \frac{2i\xi\exp\{i\alpha\}}{(1+\xi^2)\,V_R^{ud*}} C^{(7)}_{Leu\bar{d}\Phi}, \\
C^{(9)}_{eeud} &= -\frac{1}{2v_R^4} V_R^{ud2}\left[\left(M_R^{\nu\dagger}\right)^{-1} + \frac{2}{m^2_{\Delta_R}} M_R^{\nu}\right], \qquad & C^{(9)}_{ee\Phi ud} &= -4\frac{\xi\exp\{-i\alpha\}}{(1+\xi^2)\,V_R^{ud}} C^{(9)}_{eeud}, \\
C^{(9)}_{ee\Phi D} &= 4\frac{\xi^2\exp\{-2i\alpha\}}{(1+\xi^2)^2\,V_R^{ud2}} C^{(9)}_{eeud},
\end{aligned} \tag{6.16}$$

where $\xi = \kappa'/\kappa$ represents the left-right mixing. However, the operators in the LNV Lagrangian of eq. (6.15) as obtained in Ref. [45] are defined in a different operator basis than the one used in ν`DoBe`. Therefore, we have to perform one final step and match these operators onto the set defined in Tables 4.2 and 4.3. The corresponding Wilson coefficients are easily obtained and read

$$\begin{aligned}
&C^{(5)}_{LH} = \left(C^{(5)}\right)_{ee}, \qquad C^{(7)}_{LeudH} = C^{(7)}_{Leu\bar{d}\Phi}, \qquad C^{(7)}_{LHDe} = C^{(7)}_{L\Phi De}, \\
&C^{(9)}_{ddueue} = 4\left(C^{(9)}_{eeud}\right)^*, \qquad C^{(9)}_{deueH^2D} = -2\left(C^{(9)}_{ee\Phi ud}\right)^*, \qquad C^{(9)}_{eeH^4D} = -\left(C^{(9)}_{ee\Phi D}\right)^*.
\end{aligned} \tag{6.17}$$

These matching relations given in eq. 6.16 and 6.17, will serve as the relevant input to ν`DoBe` and enable us to study the $0\nu\beta\beta$ in the context of the mLRSM.

To this end, we will utilize the `EFT.SMEFT` module of ν`DoBe` which takes the relevant SMEFT Wilson coefficients as input to calculate $0\nu\beta\beta$ half-lives as well as electron kinematics in various isotopes. In addition, it is convenient to define a function that translates the free parameters of the mLRSM to the relevant SMEFT coefficients. In this context, the free parameters of the mLRSM are the masses of the three heavy sterile neutrinos, $m_{\nu_{R,i}}, i \in [1,2,3]$, the minimal active neutrino mass $m_{\min}$, the left- and right-handed neutrino mixing matrices $U_{L,R}$, the vevs of the scalar triplets $v_{L,R}$ as well as the phases θ_L, α, the right-handed triplets mass m_{Δ_R} and, finally, the left-right mixing ξ [1, 2, 45]. We provide a Python notebook with the relevant functions in the `ExampleNotebooks` folder on the ν`DoBe` GitHub. In this way, ν`DoBe` can be utilized to study specific mLRSM settings as well as extensive multi-dimensional parameter scans in the context of $0\nu\beta\beta$.

In Figure 6.6 we present a parameter scan over the minimal light neutrino mass $m_{\min}$ of the expected $0\nu\beta\beta$ half-life in ^{136}Xe parameterized in terms of the effective mass parameter [2, 45]

$$m_{\beta\beta}^{eff} = \frac{m_e}{g_A^2 V_{ud}^2 \mathcal{M}_3^{(\nu)} G_{01}^{1/2}} T_{1/2}^{-1/2}. \tag{6.18}$$

Additionally, we varied the complex vev phases θ_L, α as well as the unknown neutrino Majorana phases of the mixing matrix U (c.f. eq. 7.105). The effective mass parameter

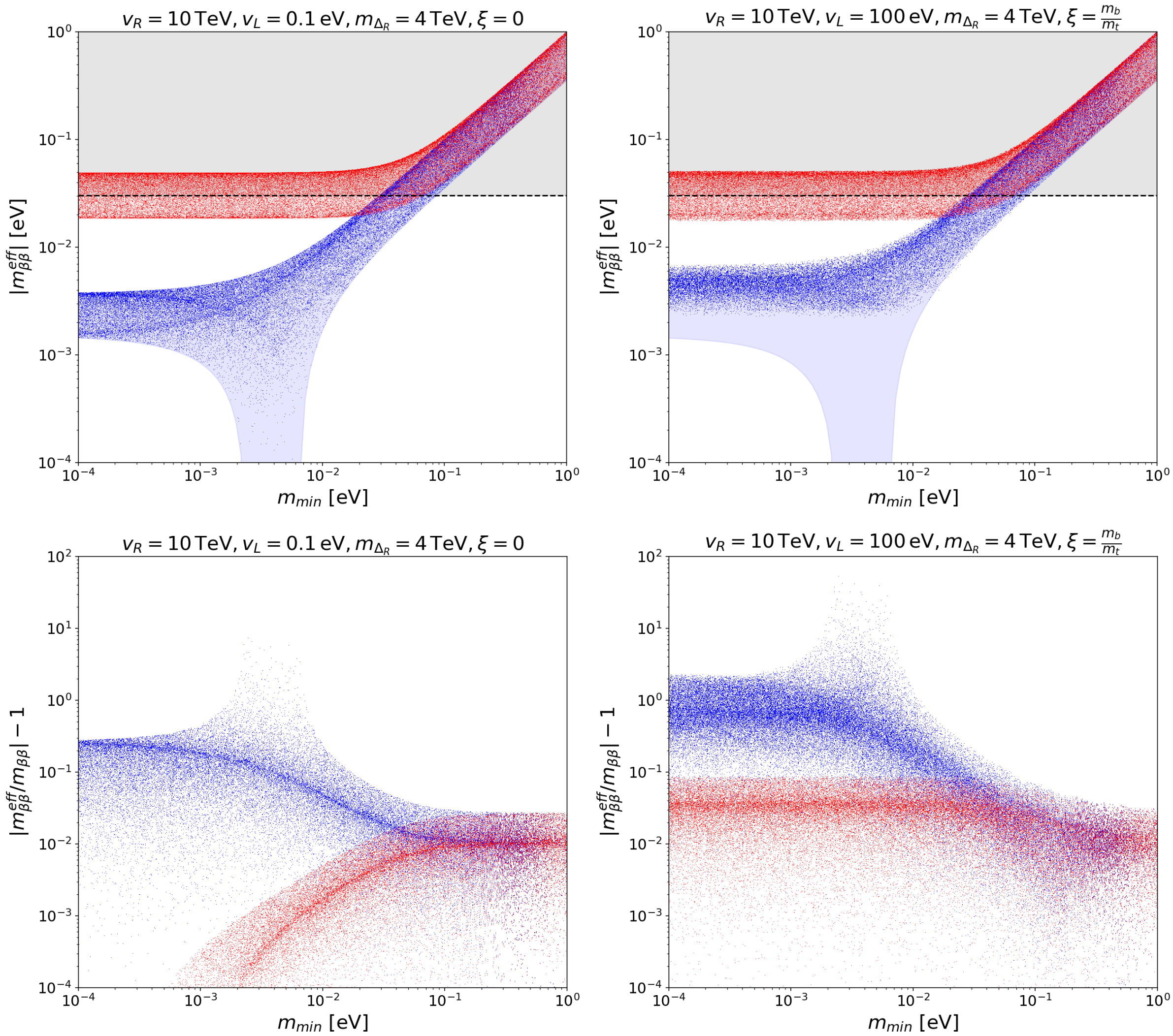

Figure 6.6: A parameter scan of the effective mass parameter $m_{\beta\beta}^{eff}$ in the mLRSM. In the upper half, we present the effective mass parameter $m_{\beta\beta}^{eff}$ scanned over the minimal neutrino mass $m_{\min}$ on the x-axis, while varying the unknown complex phases of the model. In the lower half, we have normalized the effective mass parameter to the LνEM. We present two parameter settings with a small left-handed vev and small left-right mixing on the left, and a large vev and mixing on the right. The blue and red dots represent the parameter scan in the normal and inverted hierarchy scenarios, respectively, while the shaded areas represent the parameter space of the standard LνEM. The isotope is ^{136}Xe. For comparison, we showcase the current best experimental limit set by the KamLAND-Zen collaboration [46] via the dashed line. This figure was published in Ref. [2].

$m_{\beta\beta}^{eff}$ serves as a convenient comparison to the standard LνEM scenario parameterized in terms of $m_{\beta\beta}$. The parameter scan is presented for two parameter settings by taking [2, 45]

$$m_{\nu_{R1}} = 10\,\text{TeV}, \quad m_{\nu_{R2}} = 12\,\text{TeV}, \quad m_{\nu_{R3}} = 13\,\text{TeV},$$
$$m_{\Delta_R} = 4\,\text{TeV}, \quad v_R = 10\,\text{TeV}, \quad V_{ud}^R = V_{ud}^L, \quad U_R = U_L = U, \tag{6.19}$$

for both models and varying the left-right mixing ξ as well as the left-handed vev v_L. Specifically, we take $v_L = 0.1\,\text{eV}, \xi = 0$ for the model presented in the left panels of Figure 6.6 and $v_L = 100\,\text{eV}, \xi = m_b/m_t$ for the one presented on the right panels. In the upper panels of Figure 6.6, we present the effective mass parameter $m_{\beta\beta}^{eff}$ for both settings alongside the expected ranges for the LνEM while the lower panels are normalized with respect to $m_{\beta\beta}$, providing a better comparison to the standard LνEM. As we can see, for the two parameter settings, the inverted hierarchy scenario differs at most at a few % level of ca. 10% from the simple LνEM scenario. For the larger left-right mixing scenario with $\xi = m_b/m_t$, however, the normal mass ordering differs at the $\mathcal{O}(100\%)$ level when considering smaller minimal neutrino masses, $m_{\text{min}} \lesssim 10\,\text{meV}$. At the same time, the famous funnel region of cancellation in the normal hierarchy scenario is closed due to the additional LNV contributions in the mLRSM with large left-right mixing, thereby providing an upper limit on the $0\nu\beta\beta$ half-life not only in the inverted but also in the normal ordered scenario. Again, we utilized the IBM2 NMEs of Ref. [197].

The application of ν`DoBe` to the mLRSM scenario showcases its potential to the model-building community by largely simplifying and automating the tedious computational steps in deriving the $0\nu\beta\beta$ observables for a specific LNV BSM model.

Chapter 7

Neutrinoless Double Beta Decay without Vacuum Majorana Neutrino Mass

In this chapter, we will discuss possible new-physics scenarios beyond the Standard Model that can generate a non-zero $0\nu\beta\beta$ signal while, at the same time, preserving the Dirac nature of neutrinos on a fundamental level. This is an intriguing scenario that has been given little attention in the existing literature. In this context, we will review the well-known black-box theorem in Section 7.1 and, subsequently, explain the general ideas that could lead to a potential loophole scenario in Section 7.2. In Section 7.3, we will briefly revisit $0\nu\beta\beta$ in the Standard Model. The proof-of-concept model that we propose in Section 7.4 introduces a new complex scalar field carrying two units of lepton number with a $0\nu\beta\beta$ signal being generated by a proposed high-density scalar background. In Section 7.4 we study the possible impacts of such a scalar background on $0\nu\beta\beta$ experiments assuming the scalar background to be in a free phase. As it will turn out, a $0\nu\beta\beta$ rate in the range of current and next-generation $0\nu\beta\beta$ experiments requires a substantial number density of the scalar background. In this case, one should expect the scalar field to undergo a phase transition to a Bose-Einstein condensed state. To build the theoretical foundations for the description of such a high-density scalar field, we will provide a brief introduction to quantum field theory at finite densities and temperatures in Section 7.5. Afterwards, we will revisit the $0\nu\beta\beta$ in the condensate phase in Section 7.6.

This chapter is based on Refs. [3] (under review) and [4] (to be published).

7.1 The Schechter-Valle Black-Box Theorem Revisited

The famous $0\nu\beta\beta$ black-box theorem, as proposed by Schechter and Valle [39] and later refined by E. Takasugi [40], provides a deep connection between the Majorana nature of

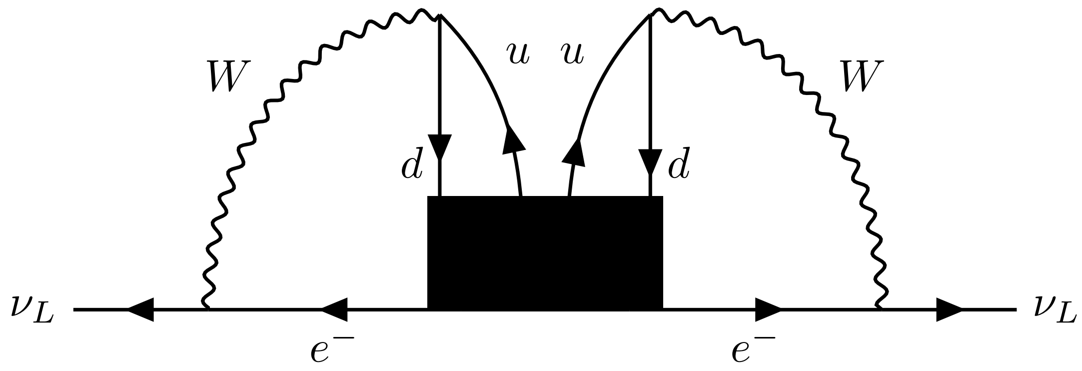

Figure 7.1: The $0\nu\beta\beta$ black-box diagram. Independently of the underlying lepton-number-violating mechanism, represented by the black-box, the $0\nu\beta\beta$ can be employed to generate a contribution to the Majorana mass of the electron neutrino at 4-loop-level.

neutrinos and a non-zero $0\nu\beta\beta$ rate. While it is obvious that a non-zero effective Majorana mass for the electron neutrino will generate a non-zero $0\nu\beta\beta$ rate, we have seen that also other LNV mechanisms can do the job. Hence, without further information, the observation of a future $0\nu\beta\beta$ signal would not tell us anything about the nature of neutrinos. This gap is filled by the black-box theorem as depicted in Figure 7.1. It provides a simple proof that a non-zero $0\nu\beta\beta$ rate does, indeed, verify that the electron neutrino is of Majorana type by generating a 4-loop contribution to the effective Majorana mass of the electron neutrino. This loop contribution is present, independently of the underlying LNV mechanism that triggers the $0\nu\beta\beta$.

Several years after the introduction of the black-box theorem, Duerr et al. [239] studied its quantitative aspects finding a contribution to the neutrino mass of $\delta m_{ee} \lesssim 10^{-28}$ eV. Therefore, the observation of $0\nu\beta\beta$ does tell us about the nature of the neutrino. However, the extraction of the effective Majorana mass from the $0\nu\beta\beta$ half-life is not valid, if the underlying mechanism turns out to be different from the LνEM. Additionally, while a future observation of $0\nu\beta\beta$ does, indeed, imply the Majorana nature of the neutrino, it may be, in fact, an almost degenerate pseudo-Dirac scenario.

In this context, the black-box theorem, while still widely referenced within today's literature, may be no more than an academic statement lacking physical consequences. In this chapter, we will discuss possibilities of avoiding the remaining essence of the black-box theorem by providing proof-of-concept scenarios in which a non-zero $0\nu\beta\beta$ rate can be achieved with Dirac neutrinos.

7.2 Avoiding the Black-Box Theorem

Let us discuss the general idea of how to avoid the consequences of the black-box theorem in order to find mechanisms of $0\nu\beta\beta$ in Dirac neutrino models. As can be seen from Figure 7.1, the black-box theorem holds if a transition of the form

$$2d \longrightarrow 2u + 2e^-, \tag{7.1}$$

is observed. This is, obviously, the case for the standard $0\nu\beta\beta$

$$(A, Z) \longrightarrow (A, Z \pm 2) + 2e^{\mp}, \tag{7.2}$$

and its β^+ and electron capture variants. However, avoiding the applicability of the black-box theorem is simply achieved by adding external lepton-number-carrying fields that may be emitted or absorbed in the process. Within the literature, examples of such models are given in the emission of lepton-number-carrying Majorons χ via the process

$$(A, Z) \longrightarrow (A, Z \pm 2) + 2e^{\mp} + n\chi, \tag{7.3}$$

where n signals the possibility of the emission of multiple Majorons [148, 149, 240]. If lepton number is strictly conserved, such models may account for a non-zero $0\nu\beta\beta$ rate while simultaneously describing neutrinos as Dirac fields. However, the experimental signature of such Majoron-emission models is structurally different from the conventional $0\nu\beta\beta$ signature. This is obviously the case, as the emission of additional particles will change the energy spectrum of the emitted electrons, i.e., not all of the decay energy will be carried by the electrons anymore.

While the emission of additional particles does cause a change in the observed electron spectrum, we may instead consider the absorption of additional lepton-number-carrying fields χ from a dark background

$$(A, Z) + n\chi \longrightarrow (A, Z \pm 2) + 2e^{\mp}. \tag{7.4}$$

If the energy of the captured particle(s) is smaller than the energy resolution of the $0\nu\beta\beta$ detector, it will mimic the standard $0\nu\beta\beta$ signature in the electron spectrum. In Figure 7.2 we provide a comparison of the expected summed electron spectra for the standard $2\nu\beta\beta$ and $0\nu\beta\beta$ modes, the spectrum for the $0\nu\beta\beta$ accompanied by the emission of a single massless scalar, and the expected spectrum for a $0\nu\beta\beta$ induced via the capture of a low-energy scalar. This is the general idea behind this chapter and the corresponding publication [3].

7.3 Neutrinoless Double Beta Decay in the Standard Model

Indeed, we do not have to consider any physics beyond the Standard Model in order to obtain a non-trivial $0\nu\beta\beta$ signal as, despite the strict conservation of lepton number

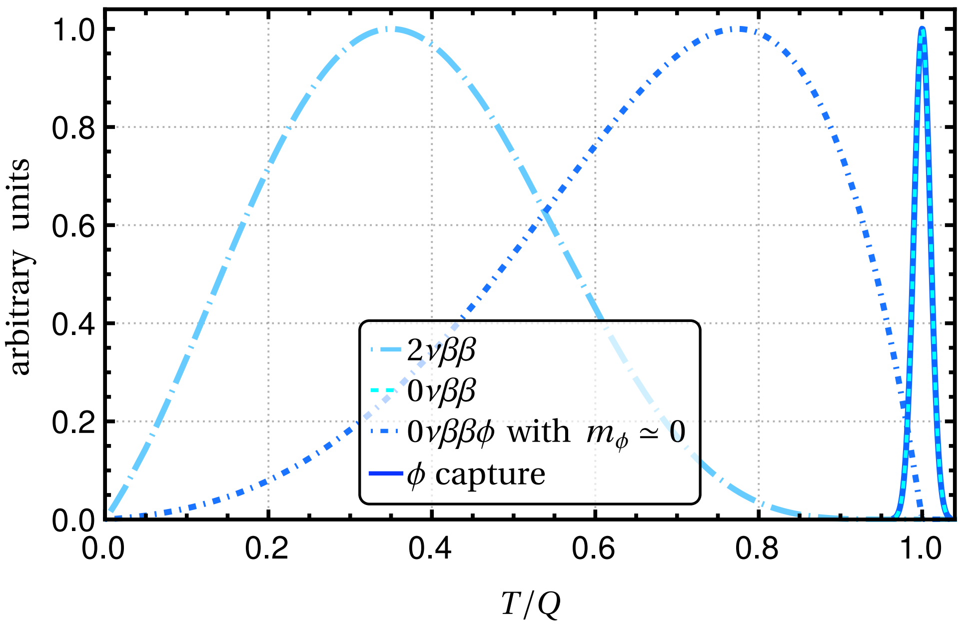

Figure 7.2: Comparison of the summed electron spectra expected in the usual two-neutrino double beta decay ($2\nu\beta\beta$), neutrinoless double beta decays ($0\nu\beta\beta$), a neutrinoless double beta decay accompanied by the emission of a single massless scalar ($0\nu\beta\beta\phi$), and the neutrinoless double beta decay induced by the capture of a massless scalar with a kinetic energy much smaller than the experimental energy resolution at the end-point of the spectrum $T_\phi \ll \Delta E_{\text{exp}}$. This figure was published in Ref. [3].

within the Standard Model, it does, in fact, allow for a small but strictly non-zero $0\nu\beta\beta$ rate. While this seems to be in direct contradiction to the black-box theorem, this apparent conflict is easily circumvented when considering the discussion provided in the previous section. The Standard Model predicts the existence of a cosmic neutrino background (CνB) [11, 241, 242][1], thereby providing the opportunity for a double-neutrino-capture induced $0\nu\beta\beta$ (2νC$\beta\beta$)

$$2\nu + (A, Z) \longrightarrow (A, Z+2) + 2e^-. \tag{7.5}$$

This process is, of course, not "*neutrinoless*" in the usual sense. It does, however, mimick the standard $0\nu\beta\beta$ signatures in dedicated $0\nu\beta\beta$ experiments. This possibility was studied in Refs. [243, 244] for a hypothetical ton-scale ^{100}Mo $0\nu\beta\beta$ experiment resulting in a expected half-life for the 2νC$\beta\beta$ of

$$\left(T^{1/2}_{\nu\nu\beta\beta}\right) \simeq 7 \times 10^{47}\,\text{yr} \times \left(\frac{\langle n_\nu\rangle}{n_\nu}\right)^2, \tag{7.6}$$

where $\langle n_\nu\rangle = 56\,\text{cm}^{-3}$ is the expected local number density per neutrino type. Therefore, we see that the 2νC$\beta\beta$ generates a tiny albeit strictly non-zero $0\nu\beta\beta$ signal. However,

[1]also referred to as CNB or *relic neutrinos*.

it is evident that even a substantial local clustering is unlikely to provide enough enhancement to result in observable half-lives reducing this to an academically interesting but practically irrelevant feature of the Standard Model. Instead, a direct detection of the CνB via a neutrino-capture induced single beta decay in tritium may be achievable. This is the goal of the PTOLEMY collaboration [245, 246].

Similar fermion capture modes of $0\nu\beta\beta$ may arise in the context of neutralino or gluino CDM in $R\!\!\!/_p$-SUSY models[1, 141, 142, 144] as well as other light fermionic DM models. However, scenarios with sizeable half-lives in reach of current or next-generation $0\nu\beta\beta$ experiments are strongly limited by the Pauli exclusion principle and require the presence of multiple fermion types to circumvent the Pauli exclusion [3, 247, 248].

7.4 Neutrinoless Double Beta Decay via a Dark Scalar Capture – I. The Free Phase

7.4.1 Introducing a Proof-Of-Concept Model

Let us now construct a proof-of-concept model that can generate a $0\nu\beta\beta$ signal with the same kinematics as the usual $0\nu\beta\beta$ scenarios while, simultaneously, restricting the neutrinos to be of Dirac nature. Firstly, this requires the introduction of a right-handed neutrino ν_R, alongside the SM fields, that allows us to write down a Dirac mass term

$$\mathcal{L}_{m_{\nu},D} = -Y^{\nu}_{ij}\overline{L}_i\tilde{H}\nu_{R,j} + \text{h.c.}, \tag{7.7}$$

where $\tilde{H} = i\sigma_2 H^*$ represents the Higgs field and Y^{ν}_{ij} is the corresponding neutrino Yukawa matrix. The Dirac neutrino mass is then given by

$$M^{\nu}_{D,ij} = \frac{v}{\sqrt{2}}Y^{\nu}_{ij}, \tag{7.8}$$

where $v \simeq 246\,\text{GeV}$ represents the Higgs vev. To circumvent the generation of a Majorana mass term for the right-handed neutrinos, which would consequently imply the Majorana nature of active neutrinos via the famous seesaw type-I mechanism, we impose a global $B-L$ symmetry. Additionally, we introduce a complex scalar field ϕ carrying a $B-L$ charge of -2 while being a singlet under all remaining SM symmetries. The relevant parts of the Lagrangian then read [3]

$$\mathcal{L} \supset \left[-Y^{\nu}_{ij}\overline{L}_i\tilde{H}\nu_{R,j} - g_{ij}\overline{\nu}_{R,i}\nu^C_{R,j}\phi + \text{h.c.}\right] - \lambda_{H\phi}(H^\dagger H)(\phi^\dagger\phi) - V(|\phi|^2), \tag{7.9}$$

where the scalar potential is given by the usual ϕ^4 form

$$V(|\phi|^2) = m^2_\phi\phi^\dagger\phi + \lambda_\phi(\phi^\dagger\phi)^2, \tag{7.10}$$

and we require the Higgs portal coupling $\lambda_{H\phi}$ to be negligibly small. The generation of a Majorana mass via a spontaneous breaking of the global $B-L$ symmetry can be avoided

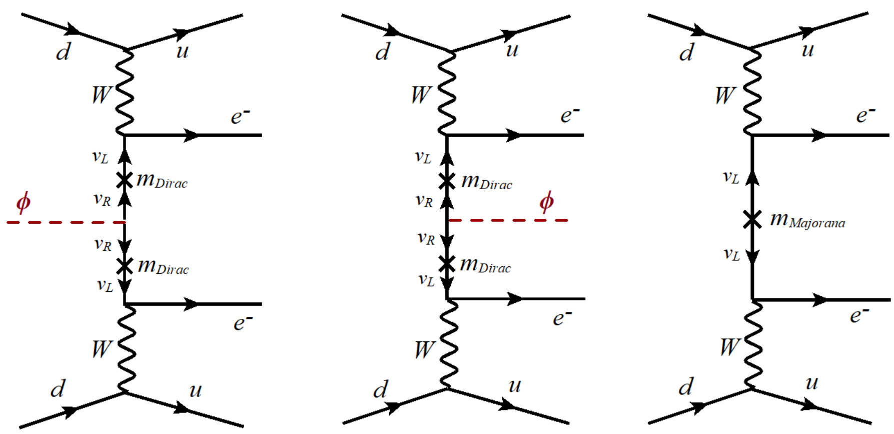

(a) Dark Scalar Capture (b) Scalar Emission (c) Ususal Majorana Mass Insertion for Light Neutrinos

Figure 7.3: Comparison of the relevant Feynman diagrams for a $0\nu\beta\beta$ induced via a scalar capture (a), the corresponding scalar emission (b) as well as the usual light neutrino-exchange mechanism (c). Our proof-of-concept model allows for diagrams (a) and (b) but forbids diagram (c). This figure was published in Ref. [3].

by a suitable choice of m_ϕ^2 and λ_ϕ. At tree-level, it suffices to require $m_\phi^2 \geq 0, \lambda_\phi \geq 0$. It should be noted that, in a theory of quantum gravity, one may expect a spontaneous breaking of global symmetries [249] which, in turn, may reintroduce small Majorana neutrino masses into our proof-of-concept model. In this case, it is straightforward to promote the global $B-L$ symmetry to a local gauge symmetry [250], which is expected to be conserved in a theory of quantum gravity, even at the non-perturbative level. In any case, we are, obviously, not interested in gravity in our proof-of-concept model and may therefore work with a global $B-L$ symmetry.

The proposed model may generate two separate contributions to a $0\nu\beta\beta$ signal. The first one via the capture of the $B-L$ charged complex scalar ϕ from a dark background

$$\phi + (A, Z) \longrightarrow (A, Z+2) + 2e^-, \tag{7.11}$$

which may act either as a dark matter or as a dark radiation component of the energy density of the Universe. The second option is a $0\nu\beta\beta$ accompanied by the emission of a scalar ϕ

$$(A, Z) \longrightarrow (A, Z+2) + 2e^- + \phi^\dagger, \tag{7.12}$$

which may occur whenever ϕ is light enough, i.e., $m_\phi < Q$. In Figure 7.3 we compare the corresponding Feynman diagrams to the standard LνEM. At the same time, the famous black-box theorem cannot be applied here due to the addition of an external scalar field as well as the exact $B-L$ conserving nature of the model. Consequently, the neutrino explicitly remains of Dirac nature. The capture of the complex scalar ϕ from a cosmic background requires stability over cosmological timescales. This can be achieved by kinematically forbidding the $\phi \to 2\nu$ decay, i.e., by setting $m_\phi < 2m_{\nu,\mathrm{min}}$. This requirement will, generally, restrict ϕ to be of sub-eV masses, thus allowing both the capture and the emission processes. In this section, we will consider the scenario in which ϕ acts as an ultralight non-relativistic cold dark matter (CDM) component [251–254]. Let us point out that, in contrast to recent literature discussing the possibility of a $0\nu\beta\beta$ induced by a neutrino-DM interaction [255–257], we assume an explicit $B-L$ conservation via the introduction of a complex $B-L$ charged scalar field that strictly prohibits the generation of a Majorana neutrino mass term of any kind in the vacuum ground-state Lagrangian.

7.4.2 $0\nu\beta\beta$ Half-Lives from Scalar Capture and Emission

Next, we want to calculate the $0\nu\beta\beta$ rates arising from the scalar capture and emission diagrams presented in Figure 7.3 following along the lines of Ref. [3]. Here, we will naively assume ϕ to be in a free phase of cold particles. Due to the requirement that the energy of the absorbed scalar should not exceed the typical energy resolution of $0\nu\beta\beta$ experiments $\Delta E \sim \mathcal{O}(\mathrm{keV})$ [35, 37], and the fact that the energy of the emitted scalar is constrained by the total decay energy $Q \sim \mathcal{O}(\mathrm{MeV})$, we can ignore the scalars four-momentum q_ϕ in both the emission and capture diagrams, as it is small in comparison to the typical momentum transfer which is at the order of the Fermi momentum, i.e., $q_\phi \lesssim \mathcal{O}(\mathrm{MeV}) \ll p_F \sim \mathcal{O}(100\,\mathrm{MeV})$. In this case, crossing symmetry ensures the transition amplitude for the emission and absorption processes to be precisely identical

$$\begin{aligned}\mathcal{A}_{0\nu\beta\beta\phi} = {} & 2G_F^2 V_{ud}^2 \overline{e_L}(p_1)\gamma_\mu \sum_{ij} U_{ei}U_{ej}\frac{g_{ij}m_i m_j}{q^4}\gamma_\nu e_L^C(p_2) \\ & \times \left[J_V^\mu(1) + J_A^\mu(1)\right]\tau_1^+ \left[J_V^\nu(2) + J_A^\nu(2)\right]\tau_2^+ + (p_1 \leftrightarrow p_2),\end{aligned} \tag{7.13}$$

where the nuclear currents $J_{V,A}$ are defined in eq. (4.93). In contrast to the long- and short-range mechanisms of $0\nu\beta\beta$ studied in previous chapters, the scalar emission and capture amplitude $\mathcal{A}_{0\nu\beta\beta\phi}$ exhibits a $1/q^4$ dependence. Consequently, the relevant NMEs cannot be extracted from the sets presented in previous chapters. Instead, we may obtain the relevant NMEs from a comparison with existing literature on Majoron-emitting mechanisms [258, 259]. The remaining parts of the transition amplitude resemble the well-studied LνEM of $0\nu\beta\beta$ discussed in Section 4.7.1. The relevant PSFs can be extracted from existing literature by comparison of the final states, with the capture mode following the same PSFs as the usual LνEM [103], while the scalar emission mode represents the well-studied Majoron-emission scenarios [260]. The relevant NMEs and PSFs are listed in Table 7.1. Note that we use the PSFs derived from the exact solution of the radial Dirac equation for a nucleus of uniform charge density with electron screening [103, 260].

In analogy to the effective Majorana mass $m_{\beta\beta}$ (c.f. eq. (4.112)) which governs the magnitude of the usual LνEM-induced $0\nu\beta\beta$ half-life, it is convenient to define the effective mass

$$m^2_{\beta\beta\phi} = \sum_i U^2_{ei} m^2_i, \tag{7.14}$$

where, for simplicity, we assumed a diagonal and real coupling $g_{ij} = g\delta_{ij}, g \in \mathbb{R}$. At the same time, we will restrict our interest here to the normal neutrino mass ordering with a vanishing minimal neutrino mass $m_{\text{min}} = 0$. The decay rate of the scalar emission mode is then given by

$$\Gamma^{\text{em}}_{0\nu\beta\beta\phi} = g^2 \log(2) \left(\frac{m_{\beta\beta\phi}}{m_e}\right)^4 |\mathcal{M}_{0\nu\beta\beta\phi}|^2 \, G_{0\nu\beta\beta\phi}, \tag{7.15}$$

while the scalar capture rate reads

$$\Gamma^{\text{cap}}_{0\nu\beta\beta\phi} = g^2 \log(2) \frac{\alpha \rho_{\text{DM}}}{2m^2_\phi m^2_e} \left(\frac{m_{\beta\beta\phi}}{m_e}\right)^4 |\mathcal{M}_{0\nu\beta\beta\phi}|^2 \, G_{0\nu\beta\beta}. \tag{7.16}$$

Here, the scalar number density

$$n_\phi = \frac{\alpha \rho_{\text{DM}}}{m_\phi}, \tag{7.17}$$

is parameterized in terms of the local dark matter density $\rho_{\text{DM}} \simeq 0.3\,\text{GeV/cm}^3$ [261], the fraction of the local dark matter density α that ϕ accounts for, and the scalar mass m_ϕ. The factors of m_e^{-4} and m_e^{-2} in eq. (7.15) and (7.16) arise from the definitions of $\mathcal{M}_{0\nu\beta\beta\phi}$ [259] and $G_{0\nu\beta\beta}$, respectively. Note that in the calculation of the capture rate we assumed ϕ to be non-relativistic today by taking $E_\phi \simeq m_\phi$.

Remember that our initial goal was the formulation of a proof-of-concept model that generates the same experimental signature as the usual $0\nu\beta\beta$ mechanisms. In order to achieve this, we need to be sure that the emission mode is properly suppressed compared to the capture mode (c.f. Figure 7.2), as it would otherwise result in a different summed electron spectrum. In the regime corresponding to an ultralight scalar the ratio of the emission and capture rates is given by

$$\frac{\Gamma^{\text{em}}_{0\nu\beta\beta\phi}}{\Gamma^{\text{cap}}_{0\nu\beta\beta\phi}} = \frac{2m^2_\phi m^2_e}{\alpha \rho_{\text{DM}}} \frac{G_{0\nu\beta\beta\phi}}{G_{0\nu\beta\beta}}, \qquad \frac{\Gamma^{\text{em}}_{0\nu\beta\beta\phi}}{\Gamma^{\text{cap}}_{0\nu\beta\beta\phi}} \left({}^{136}\text{Xe}\right) \simeq \frac{6.4 \times 10^{-25}}{\alpha} \left(\frac{m_\phi}{10^{-20}\,\text{eV}}\right)^2, \tag{7.18}$$

and we can write the $0\nu\beta\beta$ half-life induced by the scalar-capture mode as

$$T^{1/2}_{0\nu\beta\beta\phi} = \frac{\log(2)}{\Gamma^{\text{cap}}_{0\nu\beta\beta\phi}}, \qquad T^{1/2}_{0\nu\beta\beta\phi} \left({}^{136}\text{Xe}\right) \simeq \frac{1.4 \times 10^{28}\,\text{yr}}{\alpha g^2} \left(\frac{m_\phi}{10^{-20}\,\text{eV}}\right)^2. \tag{7.19}$$

Using the example of ^{136}Xe, we can see that in the relevant parameter ranges for an ultralight complex scalar field acting as CDM, the emission mode is substantially suppressed. Consequently, the experimental $0\nu\beta\beta$ signature follows the capture mode, thereby mimicking the usual LNV $0\nu\beta\beta$ scenarios.

Isotope	$G_{0\nu\beta\beta}[10^{-14}\,\text{yr}]$ [103]	$G_{0\nu\beta\beta\phi}[10^{-16}\,\text{yr}]$ [260]	$\mathcal{M}_{0\nu\beta\beta\phi}[10^{-3}]$ [259]
^{76}Ge	0.236	0.442	2.556
^{82}Se	1.016	3.610	1.993
^{96}Zr	2.058	9.050	1.668
^{100}Mo	1.592	5.980	1.901
^{110}Pd	0.482	0.941	1.409
^{116}Cd	1.670	5.690	0.945
^{124}Sn	0.904	2.090	1.179
^{128}Te	0.059	0.031	1.527
^{130}Te	1.422	4.130	1.311
^{136}Xe	1.458	4.090	1.113
^{148}Nd	1.010	1.970	0.650
^{150}Nd	6.303	31.00	0.839
^{154}Sm	0.302	0.282	0.859
^{160}Gd	0.956	15.90	1.260
^{198}Pt	0.756	0.607	0.395
^{232}Th	1.393	0.824	0.930
^{238}U	3.361	3.370	1.118

Table 7.1: Phase-space factors and nuclear matrix elements for the scalar capture and emission modes.

We see that our proof-of-concept model can accommodate a significant $0\nu\beta\beta$ rate that reproduces the summed electron spectrum of the usual LNV $0\nu\beta\beta$ mechanisms while, simultaneously, rendering neutrinos to be of Dirac nature. The possible existence of such a scenario complicates the usual interpretation of a $0\nu\beta\beta$ detection as proof of the Majorana nature of neutrinos via the black-box theorem. While, following the previous literature, the quantitative aspects of the famous black-box theorem have already been known to be almost negligibly small [239] with a $0\nu\beta\beta$ observation allowing for a scenario of almost degenerate pseudo-Dirac neutrinos, the qualitative essence of the black-box theorem previously remained intact. It is the existence of such a lepton-number-conserving model, capable of describing a $0\nu\beta\beta$ observation, that challenges the qualitative essence of the long-standing black-box theorem by circumventing its practical application.

7.4.3 Identifying a Scalar Capture Induced $0\nu\beta\beta$

As we have seen in the previous section, a $0\nu\beta\beta$ induced via the capture of an ultralight CDM scalar cannot be distinguished from the usual LNV $0\nu\beta\beta$ mechanisms via a measurement of the summed electron spectrum. However, as we have discussed in Chapter 5, one may be able to distinguish among different $0\nu\beta\beta$ mechanisms via a measurement

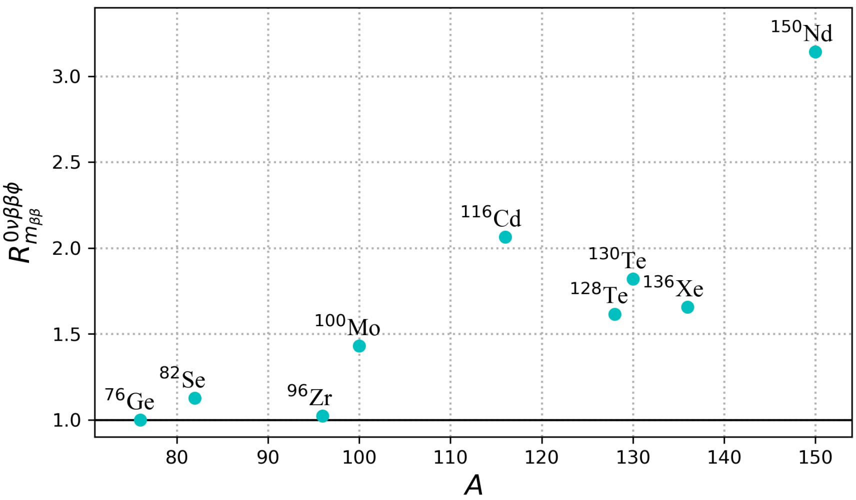

Figure 7.4: Comparison of the half-life ratios generated by the scalar-capture mode and the usual light neutrino-exchange mechanism of $0\nu\beta\beta$.

of the individual electron kinematics, which can be studied in tracking calorimetric experiments, such as NEMO [111, 135] and SuperNEMO [136], or by measuring the $0\nu\beta\beta$ half-life in multiple isotopes and comparing the half-life ratios with the theoretical expectations for individual mechanisms. In the case of our proof-of-concept model defined in the previous section, the additional information on the individual electron kinematics, as provided via tracking calorimetric experiments, cannot be used to identify the $0\nu\beta\beta$ induced via the scalar-capture mode, simply because the final state is equivalent to the usual LνEM. Instead, we should focus on the possibility of an identification via half-life ratios which are sensitive to the differences in NMEs. Again, we define the half-life ratio for a certain isotope $^{\mathrm{A}}$X normalized with respect to ^{76}Ge as [1]

$$R^{\mathcal{O}_i}(^{\mathrm{A}}\mathrm{X}) \equiv \frac{T^{\mathcal{O}_i}_{1/2}(^{\mathrm{A}}\mathrm{X})}{T^{\mathcal{O}_i}_{1/2}(^{76}\mathrm{Ge})}, \tag{7.20}$$

such that the distinguishability of two $0\nu\beta\beta$ mechanisms i, j can be quantified via the ratio

$$R_{ij}(^{\mathrm{A}}\mathrm{X}) = \frac{R^{\mathcal{O}_i}(^{\mathrm{A}}\mathrm{X})}{R^{\mathcal{O}_j}(^{\mathrm{A}}\mathrm{X})}. \tag{7.21}$$

In Figure 7.4 we show the half-life ratios resulting from the scalar-capture mode normalized with respect to the usual LνEM $R^{0\nu\beta\beta\phi}_{m_{\beta\beta}} = R_{0\nu\beta\beta\phi}/R_{m_{\beta\beta}}$ for various isotopes. We can see that the capture mode does, indeed, result in distinct half-life ratios, such that a measurement of the $0\nu\beta\beta$ half-life in multiple isotopes may offer a possibility to unravel it. From Figure 7.4 we can see that the potential to distinguish a scalar capture induced $0\nu\beta\beta$ from the usual mass mechanism is maximized when comparing the $0\nu\beta\beta$ half-life in smaller nuclei, such as ^{76}Ge, with that in larger nuclei, such as ^{150}Nd. This behaviour reflects the naive expectation that the momentum-exchange in the neutrino propagator should be scaling with the nuclear radius as $\mathbf{q} \sim 1/R$, thereby representing the different $\mathbf{q}$-dependence of the LνEM NMEs and the scalar-capture NMEs.

7.4.4 Critique on the Free Phase Approach

By assuming the scalar background to be in a free phase of cold particles, we found that our proof-of-concept model can, indeed, accommodate for significant $0\nu\beta\beta$ rates observable in current and next-generation $0\nu\beta\beta$ experiments. However, this requires substantially large number densities of an ultralight scalar background. In this case, our naive perturbative treatment is expected to break down [72] as diagrams with more than one external scalar become dominant. Indeed, one would expect that ϕ should undergo a phase transition and form a Bose-Einstein Condensate (BEC) when a certain number density is exceeded. As we will see in the following sections, this phase transition has relevant physical consequences, inducing an effective in-medium Majorana mass for the neutrino and substantially increasing the $0\nu\beta\beta$ rate.

7.5 An Introduction to Quantum Field Theory in Thermal Equilibrium

In order to properly describe the $0\nu\beta\beta$ induced via a Bose-Einstein condensed scalar background, we should briefly review the relevant theoretical foundations. Therefore, in this section, we will provide a brief introduction to thermal-equilibrium QFT at finite temperatures and densities. Our primary focus will be to discuss the connection of QFT at finite density (= finite chemical potential) and spontaneous symmetry breaking. We will then apply this phenomenon to introduce a novel way of generating an in-medium seesaw mechanism for neutrino mass generation via the coupling of right-handed neutrinos to a cosmic scalar BEC. In this way, we can describe the non-zero $0\nu\beta\beta$ rate induced by a scalar background while circumventing the problems that arise in the naive free phase approach.

A comprehensive introduction to finite temperature field theory can be found, for example, in the lecture notes of Laine and Vuorinen [262] or Kapusta's textbook [263]. For a general introduction to QFT we recommend the lecture notes by Floerchinger and Wetterich [79, 80], Weigand [264], or the standard textbooks by Schwartz [75] and Peskin and Schroeder [265]. Here, we will mostly follow the textbook by Kapusta [263].

7.5.1 QFT at Finite Temperatures

In the path integral formulation of relativistic QFT, the partition function is given in terms of the Minkowskian action

$$\mathcal{S}_M(\Phi_n) = \int \mathrm{d}^4x\, \mathcal{L}_M(\Phi_n), \tag{7.22}$$

as

$$\mathcal{Z} = \int \prod_n \mathcal{D}\Phi_n \, \exp\{i\mathcal{S}_M(\Phi_n)\}, \tag{7.23}$$

where $\mathcal{D}\Phi$ denotes the functional integral over the field Φ and $\mathcal{L}_M$ is the Minkowskian Lagrange density. Correlation functions are then given by

$$\langle\Omega|T[\Phi_1(x_1)...\Phi_n(x_n)]|\Omega\rangle = \frac{1}{\mathcal{Z}} \int \prod_n \mathcal{D}\Phi_n \, \Phi_1(x_1)...\Phi_n(x_n) \exp\{i\mathcal{S}_M(\Phi_n)\}, \tag{7.24}$$

inferring that any constant prefactor in the partition function drops out when calculating correlation functions and, hence, is not physical.

A finite temperature description of QFT can be introduced by applying a Wick rotation, i.e., going to an imaginary time description

$$x^0 = t \to \tau = it, \tag{7.25}$$

such that we can work in a Euclidean metric

$$\partial^\mu \partial_\mu = \partial_t^2 - \partial_i^2 = -(\partial_\tau^2 + \partial_i^2). \tag{7.26}$$

The imaginary time τ is then associated with the temperature $\beta = T^{-1}$ by restricting it to the interval $\tau \in [0, \beta]$, i.e., by taking

$$\int \mathrm{d}t \to -i \int_0^\beta \mathrm{d}\tau, \tag{7.27}$$

such that the partition function can be written as

$$\mathcal{Z} = \int \prod_n \mathcal{D}\Phi_n \, \exp\{-\mathcal{S}_E\}, \tag{7.28}$$

with the Euclidean action

$$\mathcal{S}_E = \int_0^\beta \mathrm{d}\tau \int \mathrm{d}^3x \mathcal{L}_E, \qquad \mathcal{L}_E = -\mathcal{L}_M(\tau = it). \tag{7.29}$$

In analogy to classical statistical thermodynamics we can now associate the partition function given by the Euclidean action with the canonical partition function

$$\mathcal{Z} = \mathrm{Tr}[\exp\{-\beta\mathcal{H}\}] = \int \prod_n \mathcal{D}\Phi_n \, \exp\{-\mathcal{S}_E\}, \tag{7.30}$$

by requiring periodicity of bosonic fields $\Phi_n \to \Phi$ and anti-periodicity of fermionic fields $\Phi_n \to \Psi$

$$\phi(\tau) = \phi(\tau + \beta), \qquad \Psi(\tau) = -\Psi(\tau + \beta), \tag{7.31}$$

such that the cyclicality of the trace operator is recovered. While this recipe works in general for scalar-, gauge- and fermionic fields [262, 263], we are only interested in the case of scalar fields.

7.5.1.1 The Path Integral at Finite Temperatures

Let us briefly discuss the derivation of eq. 7.30 in the case of a scalar field theory. This will come in handy when discussing aspects of spontaneous symmetry breaking via Bose-Einstein condensation, later on. Again, we will follow along the lines of Ref. [263].

The thermodynamic partition function can be written as

$$\mathcal{Z} = \mathrm{Tr}[\exp\{-\beta H\}] = \sum_n \int \mathrm{d}\phi_n \langle\phi_n| \exp\{-\beta H\}|\phi_n\rangle, \tag{7.32}$$

where the states $|\phi_n\rangle$ are the eigenstates of the scalar field ϕ following the normalization condition

$$\int \mathrm{d}\phi\, |\phi\rangle\langle\phi| = 1, \tag{7.33}$$

and the trace operator is evaluated by summing over all states. By associating the temperature with the imaginary time $\beta = it$ we can identify the transition amplitude $\phi_n \to \phi_n$ after a time t as

$$\langle\phi_n| \exp\{-\beta H\}|\phi_n\rangle = \langle\phi_n| \exp\{-iHt\}|\phi_n\rangle. \tag{7.34}$$

Additionally, we introduce the conjugate momentum field π and its eigenstates $|\pi\rangle$

$$\pi = \frac{\partial\mathcal{L}_M}{\partial(\partial_t\phi)}, \tag{7.35}$$

which are normalized as

$$\int \frac{\mathrm{d}\pi}{2\pi}|\pi\rangle\langle\pi| = 1. \tag{7.36}$$

Using eq. (7.34) as well as the normalization conditions (7.33) and (7.36) we can rewrite the partition function (7.32) by splitting it into infinitesimal timesteps $\Delta t = \lim_{N\to\infty} t/N$

$$\exp\{-iHt\} = \prod_{j=1}^{N} \exp\{-iH\Delta t\}, \tag{7.37}$$

and inserting (alternating) complete sets of ϕ and π states (i.e. unities)

$$\begin{aligned}\mathcal{Z} = &\sum_n \int \mathrm{d}\phi_n \lim_{N\to\infty} \int \left(\prod_{i=1}^{N} \frac{\mathrm{d}\phi_i\, \mathrm{d}\pi_i}{2\pi}\right)\\ &\times \langle\phi_n|\pi_N\rangle\langle\pi_N| \exp\{-iH\Delta t\}|\phi_N\rangle\langle\phi_N|\pi_{N-1}\rangle\langle\pi_{N-1}| \exp\{-iH\Delta t\}|\phi_{N-1}\rangle\\ &\times \ldots\\ &\times \langle\phi_2|\pi_1\rangle\langle\pi_1| \exp\{-iH\Delta t\}|\phi_1\rangle\langle\phi_1|\phi_n\rangle.\end{aligned} \tag{7.38}$$

We can immediately perform the first integral $\int \mathrm{d}\phi_n$ by using the orthogonality condition

$$\langle \phi_1 | \phi_n \rangle = \delta(\phi_1 - \phi_n), \tag{7.39}$$

and by associating $\phi_{N+1} = \phi_n = \phi_1$ we can write the partition function in a short-hand notation as

$$\mathcal{Z} = \sum_n \lim_{N\to\infty} \int \left(\prod_{i=1}^{N} \frac{\mathrm{d}\phi_i \,\mathrm{d}\pi_i}{2\pi} \right) \prod_{j=1}^{N} \langle \phi_{j+1} | \pi_j \rangle \langle \pi_j | \exp\{-iH\Delta t\} | \phi_j \rangle. \tag{7.40}$$

After Taylor expanding the exponential

$$\langle \pi_j | \exp\{-iH\Delta t\} | \phi_j \rangle = \langle \pi_j | 1 - iH\Delta t | \phi_j \rangle + \mathcal{O}(\Delta t^2), \tag{7.41}$$

and using

$$\langle \phi_i | \pi_j \rangle = \exp\left\{ i \int \mathrm{d}^3 x \, \pi_j(x) \phi_i(x) \right\}, \tag{7.42}$$

we can write the partition function in the continuum limit as

$$\mathcal{Z} = \int \mathcal{D}\pi \mathcal{D}\phi \, \exp\left\{ i \int_0^t \mathrm{d}t' \int_x \mathcal{L}(\phi, \pi) \right\} = \int \mathcal{D}\pi \mathcal{D}\phi \, \exp\left\{ - \int_0^\beta \mathrm{d}\tau \int_x \mathcal{L}_E(\phi, \pi) \right\}. \tag{7.43}$$

Here, we inserted the Lagrangian as the Legendre transform of the Hamiltonian

$$\mathcal{H} = \pi \frac{\mathrm{d}\phi}{\mathrm{d}t} - \mathcal{L}. \tag{7.44}$$

By performing the integral over the conjugate fields π eq. (7.30) is recovered.

7.5.2 Spontaneous Symmetry Breaking via Bose-Einstein Condensation - QFT at Finite Density

Remember that our final goal is to induce a $0\nu\beta\beta$ signal in a Dirac-neutrino scenario via the capture of a lepton-number-carrying scalar from some cosmic background. In order to describe such a scenario, we need to describe QFT at finite densities as well. We will see that if the scalar density is high enough, the formation of a Bose-Einstein condensate will introduce a spontaneous symmetry breaking to the theory. The theoretical foundations of this concept have been developed in Refs. [266–268]. Here, we will summarize and describe the basics of this phenomenon.

To study Quantum Field Theories at finite density we start with the grand canonical partition function in classical statistical thermodynamics

$$\mathcal{Z} = \mathrm{Tr}[\exp\{-\beta(H - \mu N)\}], \tag{7.45}$$

where the chemical potential μ is the conjugate to the conserved particle number N. In a relativistic QFT, however, the particle number N is not necessarily a conserved quantum number. Instead, we should define the chemical potential in more general terms as the conjugate of some conserved charge $\mathcal{Q}$ associated to a symmetry of the action via Noether's theorem [75, 265]:

Theorem 7.1. ***Noether's Theorem*** – *If the action $\mathcal{S}$ of a theory is invariant under a continuous symmetry transformation of the fields $\phi_n \to \phi_n + \delta\phi_n$ then, assuming that the equations of motion are satisfied, there exists an associated conserved current*

$$j^\mu = \sum_n \frac{\partial \mathcal{L}}{\partial(\partial_\mu \phi_n)} \frac{\delta\phi_n}{\delta\alpha}, \tag{7.46}$$

such that

$$\partial_\mu j^\mu = 0, \tag{7.47}$$

and a corresponding conserved charge

$$Q = \int \mathrm{d}^3 x j^0 =: \int_x \mathcal{Q}. \tag{7.48}$$

The expectation value of the conserved charge is then related to the chemical potential by taking the derivative of the partition function

$$\langle Q \rangle = \frac{1}{\beta} \frac{\partial \log \mathcal{Z}}{\partial \mu}. \tag{7.49}$$

Let us consider a typical ϕ^4 theory of a complex scalar given by

$$\mathcal{L}_M = \partial^\mu \phi^\dagger \partial_\mu \phi - \mathcal{V}(|\phi|^2), \qquad \mathcal{V}(|\phi|^2) = m^2|\phi|^2 + \lambda|\phi|^4. \tag{7.50}$$

This theory obeys a global $U(1)$ symmetry that transforms $\phi \to \exp\{i\alpha\}\phi$. For convenience, we may describe the complex field ϕ in terms of two real scalars $\phi_{1,2}$ as

$$\phi = \frac{1}{\sqrt{2}}(\phi_1 + i\phi_2), \tag{7.51}$$

with the corresponding conjugate momenta

$$\pi_i = \frac{\partial \mathcal{L}}{\partial(\partial_t \phi_i)}. \tag{7.52}$$

Accordingly, the Hamiltonian is given by

$$\mathcal{H} = \sum_i \frac{1}{2}\pi_i^2 + \frac{1}{2}(\partial_j \phi_i)^2 + \frac{m^2}{2}\phi_i^2 + \frac{\lambda}{4}\phi_i^4, \tag{7.53}$$

and we can write down the partition function in terms of the real scalar fields as [263]

$$\mathcal{Z} = \int \prod_j \mathcal{D}\pi_j \mathcal{D}\phi_j \, \exp\left\{\int_0^\beta \mathrm{d}\tau \int_x \left(\sum_k i\pi_k \frac{\partial \phi_k}{\partial \tau} - \mathcal{H} + \mu \mathcal{Q}\right)\right\}. \tag{7.54}$$

The charge density $\mathcal{Q}$ is simply given by Noether's theorem as

$$\mathcal{Q} = \phi_2 \pi_1 - \phi_1 \pi_2, \tag{7.55}$$

and represents the difference in the number of particles n_ϕ and anti-particles $\overline{n}_\phi$ [264]. We now want to perform the integration over the conjugate fields $\pi_{1,2}$. In order to do so, it is convenient to split the partition function into two parts, one for each conjugate momentum field. The relevant integrals [262]

$$\begin{aligned} \int \mathcal{D}\pi_1 \exp\left\{-\frac{1}{2}\pi_1^2 + \pi_1 \left(i\frac{\partial \phi_1}{\partial \tau} + \mu\phi_2\right)\right\} &\propto \exp\left\{-\frac{1}{2}\left(\frac{\partial \phi_1}{\partial \tau} - i\mu\phi_2\right)^2\right\}, \\ \int \mathcal{D}\pi_2 \exp\left\{-\frac{1}{2}\pi_2^2 + \pi_2 \left(i\frac{\partial \phi_2}{\partial \tau} - \mu\phi_1\right)\right\} &\propto \exp\left\{-\frac{1}{2}\left(\frac{\partial \phi_2}{\partial \tau} + i\mu\phi_1\right)^2\right\}, \end{aligned} \tag{7.56}$$

take a Gaussian form with the general solution presented in eq. (3.10). Again, we have dropped any constant prefactors arising in the Gaussian integration. Notably, we can see that after the Gaussian integration the chemical potential acts as a negative squared mass with terms of $-\mu^2\phi_{1,2}^2$ arising. Indeed, going back to the notation in terms of the complex field ϕ we can write the partition function as [262]

$$\begin{aligned} \mathcal{Z} = \int \mathcal{D}\phi \exp\bigg\{ -\int_0^\beta \mathrm{d}\tau \int_x \Big[&\partial_\tau \phi^\dagger \partial_\tau \phi + \partial_i \phi^\dagger \partial_i \phi + (m^2 - \mu^2)|\phi|^2 + \lambda|\phi|^4 \\ &+ \mu\big(\phi^\dagger \partial_\tau \phi - \big(\partial_\tau \phi^\dagger\big)\phi\big)\Big]\bigg\}. \end{aligned} \tag{7.57}$$

Therefore, we should expect a spontaneous symmetry breaking for $\mu^2 > m^2$. This spontaneous symmetry breaking describes a macroscopic occupation of the ground-state better known as Bose-Einstein condensation [266–268].

7.5.3 Spontaneous Symmetry Breaking at Zero Temperature and Finite Density

We may introduce the effective potential [266, 267]

$$\mathcal{V}_{\text{eff}} = -\frac{1}{\beta V} \log \mathcal{Z}, \tag{7.58}$$

such that the minimum of $\mathcal{V}_{\text{eff}}$ with respect to ϕ describes the system in thermal equilibrium. The relevant thermodynamic quantities, i.e. the pressure P, entropy density

$\mathcal{S} = S/V$, and charge density $\mathcal{Q}$, can be derived by taking the proper derivatives of the effective potential [267, 269]

$$\begin{aligned} P &= \frac{1}{\beta}\frac{\partial \log \mathcal{Z}}{\partial V} = -\mathcal{V}_{\text{eff}}, \\ \mathcal{S} &= \frac{1}{\beta V}\frac{\partial \log \mathcal{Z}}{\partial T} = -\frac{\partial \mathcal{V}_{\text{eff}}}{\partial T}, \\ \mathcal{Q} &= \frac{1}{\beta V}\frac{\partial \log \mathcal{Z}}{\partial \mu} = -\frac{\partial \mathcal{V}_{\text{eff}}}{\partial \mu}, \end{aligned} \tag{7.59}$$

while the total energy density $\mathcal{U} = U/V$ of the system can be calculated via the usual relation

$$\mathcal{U} = T\mathcal{S} - P + \mu\mathcal{Q}, \tag{7.60}$$

and, correspondingly, the equation of state is simply given by $\omega = P/\mathcal{U}$.

At tree-level and zero temperature, the effective potential is given by the classical potential [262, 268]

$$\mathcal{V}_{\text{eff,tree}} = (m^2 - \mu^2)\phi^\dagger\phi + \lambda(\phi^\dagger\phi)^2, \tag{7.61}$$

which for $\mu > m$, acquires the well-known Mexican-hat shape and the scalar field gains a non-zero ground-state expectation value given by the potential minimum as

$$|\langle\phi\rangle|^2 = \frac{\mu^2 - m^2}{2\lambda}. \tag{7.62}$$

In this simple setting, the chemical potential μ is related to the charge density $\mathcal{Q}$ via eq. (7.59) as

$$\mathcal{Q} = 2\mu|\langle\phi\rangle|^2, \tag{7.63}$$

which in the broken phase for $\mu > m$ can be expressed as

$$\mathcal{Q} = \frac{\mu(\mu^2 - m^2)}{\lambda}. \tag{7.64}$$

Obviously, the symmetric phase is by definition characterized by a vanishing charge density $\mathcal{Q} = 0$ stored in the ground-state.

We want to restrict ourselves to the case of a non-interacting ideal gas to provide a simple proof-of-concept scenario. Additionally, this simplification is strongly motivated from a physical standpoint if we want our scalar background field to act as a CDM component of the energy density of the Universe. For ϕ to act as CDM, it needs to have an equation of state that closely follows that of cold dust with $\omega \simeq 0$. However, we can see that even at zero temperature, the interacting scalar theory is characterized by a non-zero pressure in the broken phase. Indeed, the relevant thermodynamic quantities $P, \mathcal{S}, \mathcal{U}$ are given by

$$\begin{aligned}
P &= \begin{cases} 0 & \text{(unbroken phase)}, \\ \frac{(\mu^2-m^2)^2}{4\lambda} & \text{(broken phase)}, \end{cases} \\
\mathcal{S} &\simeq 0, \\
\mathcal{U} &= \begin{cases} 0 & \text{(unbroken phase)}, \\ \frac{3\mu^4-m^4-2\mu^2m^2}{4\lambda} & \text{(broken phase)}. \end{cases}
\end{aligned} \tag{7.65}$$

Hence, the equation of state at zero temperature for the interacting scalar field in the broken phase is given by

$$\omega = \frac{P}{\mathcal{U}} = \frac{(\mu-m)(\mu+m)}{3\mu^2+m^2}. \tag{7.66}$$

Therefore, even at $T = 0$ a pressureless equation of state requires $\mu^2 \to m^2$. From eq. (7.64) we can see that retaining a non-zero ground-state density in the limit $\mu^2 \to m^2$ requires to take $\lambda \to 0$, thus providing another argument for working with a non-interacting ideal gas. In this case, a non-zero ground-state charge density requires $\mu^2 = m^2$ with $\mathcal{Q} = 2m|\langle\phi\rangle|^2$, connecting the ground-state expectation value to the non-zero charge density. Finally, let us parameterize the complex scalar field ϕ in terms of its absolute value and a complex phase

$$\phi = |\phi| \exp\{i\alpha\}. \tag{7.67}$$

The expectation value for $|\phi|$ is fixed by eq. (7.63) and found to be constant. However, from Noether's theorem, the charge density is given in terms of the conjugate fields $\pi = \partial_t\phi$ and therefore a non-zero charge density requires a non-trivial time dependence of ϕ. Since we know the absolute value to be constant in time, this time dependence has to stem from the complex phase α and we may write

$$\mathcal{Q} = -2|\langle\phi\rangle|^2\partial_t\alpha, \tag{7.68}$$

such that we can identify $\partial_t\alpha = -m$ and, thus, find ϕ to be a rotating complex field of constant absolute value

$$\phi = \sqrt{\frac{\mathcal{Q}}{2m_\phi}} \exp\{-im_\phi t\}. \tag{7.69}$$

This result simply resembles the classical-field approximation that is often used in the context of bosonic fields with large occupation numbers [72, 254, 270].

7.5.4 Spontaneous Symmetry Breaking at Finite Temperature and Density

In the context of $0\nu\beta\beta$ we have seen that, at least in the free phase, a significant $0\nu\beta\beta$ rate requires ϕ to be an ultralight CDM component with masses $m \lesssim 10^{-20}$ eV. Usually, in the context of laboratory experiments studying the formation of BECs, the phenomenon of Bose-Einstein condensation is assumed to be a low-temperature phenomenon with $T \ll m$. One may therefore question if the zero-temperature description provided in the previous section is a valid approach in the context of an ultralight scalar field much lighter than, e.g., the temperature of the cosmic microwave background $T_{\mathrm{CMB}} \simeq 2.35 \times 10^{-4}\,\mathrm{eV}$. From an experimental point of view, our naive constraint should be an upper limit on the scalar temperature in the region of the experimental energy resolution $T_\phi \lesssim \Delta E \sim \mathcal{O}(\mathrm{keV})$ which is several orders of magnitude larger than the usual mass region of an ultralight scalar DM field.

At finite temperatures, we may use the periodicity of ϕ in the imaginary time $0 \leq \tau \leq \beta$, $\phi(\tau = 0) = \phi(\tau = \beta)$ to employ a Fourier expansion [267]

$$\phi(\tau, \vec{x}) = \frac{1}{\beta} \sum_{n=-\infty}^{\infty} \int \frac{\mathrm{d}^3 p}{(2\pi)^3} \phi_n \exp\{i(\vec{p} \cdot \vec{x} + \omega_n \tau)\}, \tag{7.70}$$

with the Matsubara frequencies

$$\omega_n = \frac{2\pi n}{\beta}, \quad n \in \mathbb{Z}. \tag{7.71}$$

It is convenient to separate the constant zero mode ρ with $\omega_{n=0} = 0$ from the remaining terms,

$$\phi(\tau, \vec{x}) = \rho + \frac{1}{\beta} \sum_{n \neq 0} \int_p \phi_n \exp\{i(\vec{p} \cdot \vec{x} + \omega_n \tau)\}. \tag{7.72}$$

For simplicity, we may choose ρ to be real. In the ideal gas scenario, the path integral may be solved exactly for $\mu^2 \lesssim m^2$ via a Gaussian integration [266, 267]. The effective potential is then given as

$$\mathcal{V}_{\mathrm{eff}} = \mathcal{V}_{\mathrm{tree}} + \mathcal{V}_{,\mathrm{thermal}} \tag{7.73}$$

where the constant zero-mode gives a contribution of the form of the classical tree-level potential

$$\mathcal{V}_{\mathrm{tree}} = (m^2 - \mu^2)\rho^2, \tag{7.74}$$

and the finite temperature effects carried in the remaining modes are summarized in

$$\mathcal{V}_{\mathrm{thermal}} = \frac{1}{\beta} \int \frac{\mathrm{d}^3 p}{(2\pi)^3} \left(\log\left[1 - \exp\{-\beta(\omega - \mu)\}\right] + \log\left[1 - \exp\{-\beta(\omega + \mu)\}\right] \right). \tag{7.75}$$

Here, $\omega = \sqrt{p^2 + m^2}$ denotes the energy and we ignored a constant, divergent zero-point term which does not affect the thermodynamics of the system [263, 266, 267].

The zero-mode is the lowest energy state ϕ can occupy and therefore describes the ground-state of the system. It is evident that, similar to the zero-temperature case, a non-trivial ground-state expectation value $\rho \neq 0$ can only be realized when taking $\mu^2 = m^2$. In this case, we may separate the total charge density into a ground-state part $\mathcal{Q}_0$ and thermally excited part $\mathcal{Q}^*$, again, by taking the derivative of the effective potential with respect to the chemical potential μ [263]

$$\mathcal{Q} = -\frac{\partial \mathcal{V}_{\text{eff}}}{\partial \mu}\bigg|_{\mu=m} = \mathcal{Q}_0 + \mathcal{Q}^*(T, \mu = m), \tag{7.76}$$

where the charge density stored in the thermally excited modes is given by [263]

$$\mathcal{Q}^*(T, \mu = m) = \int \frac{\mathrm{d}^3 p}{(2\pi)^3} \left(\frac{1}{\exp\{\beta(\omega - m)\} - 1} - \frac{1}{\exp\{\beta(\omega + m)\} - 1} \right), \tag{7.77}$$

and the charge density in the ground state is simply

$$\mathcal{Q}_0 = 2m\rho^2. \tag{7.78}$$

Spontaneous symmetry breaking via the formation of a BEC is realized as long as the ground-state charge density is non-zero, $\mathcal{Q}_0 > 0$, with the expectation value of the zero-momentum mode given by

$$\rho^2 = \frac{\mathcal{Q} - \mathcal{Q}^*(\beta, \mu = m)}{2m}. \tag{7.79}$$

This requirement allows us to define a critical temperature at which the system switches from the free to the condensed phase. The critical temperature T_{crit} is then simply given by the transition point at which all of the conserved charge is stored in the thermal excitations

$$\mathcal{Q}^*(T_{\text{crit}}, \mu = m) = \mathcal{Q}. \tag{7.80}$$

In the limit of high or low charge densities, approximate analytical solutions to the critical temperature are given by [263]

$$T_{\text{crit}} = \begin{cases} \frac{2\pi}{m} \left(\frac{\mathcal{Q}}{\zeta(3/2)} \right)^{2/3} & \mathcal{Q} \ll m^3 \\ \left(\frac{3\mathcal{Q}}{m} \right)^{1/2} & \mathcal{Q} \gg m^3 \end{cases}, \tag{7.81}$$

while exact solutions require a numerical evaluation. For the scenario of an ultralight scalar CDM field, the high-density parameter region with $\mathcal{Q} \gg m^3$ is what is relevant to us. While in the broken phase with temperatures below the critical temperature the chemical potential is fixed to $\mu = m$, charge conservation requires that the chemical potential should decrease at temperatures above T_{crit}. In the high-density regime, we can write the charge density stored in the thermal excitations as [267]

$$\mathcal{Q}^*(T) = \begin{cases} \frac{1}{3}\mu T^2 = Q = \text{const.}, & T > T_{\text{crit}}, \quad \text{unbroken phase} \\ \frac{1}{3} m T^2, & T < T_{\text{crit}}, \quad \text{broken phase} \end{cases}. \tag{7.82}$$

Similarly, the charge density stored in the ground-state is given by $\mathcal{Q}_0 = \mathcal{Q} - \mathcal{Q}^*$ and we may can eq. (7.82) to express it in terms of the total charge density $\mathcal{Q}$, the temperature T and the critical temperature $T_{\rm crit}$ as

$$\mathcal{Q}_0 = 2m\rho^2 = \mathcal{Q}\left(1 - \frac{T^2}{T_{\rm crit}^2}\right), \tag{7.83}$$

such that the ground-state expectation value in the broken phase is given by

$$\rho^2 = \frac{1}{6}T_{\rm crit}^2\left(1 - \frac{T^2}{T_{\rm crit}^2}\right). \tag{7.84}$$

We can see that finite temperature effects on the symmetry breaking nature of the system scale with $T^2/T_{\rm crit}^2$. In the high-density regime of interest, the critical temperature may be expressed as a function of the scalar number density $\mathcal{Q} = n_\phi = \alpha\rho_{\rm DM}/m_\phi$

$$T_{\rm crit} \simeq 2.6 \times 10^{17}\,{\rm eV} \times \alpha^{1/2}\left(\frac{m_\phi}{10^{-20}\,{\rm eV}}\right)^{-1}. \tag{7.85}$$

Thus, in the case of an ultralight scalar CDM field, the critical temperature is many orders of magnitude larger than, e.g., the CMB temperature and thermal effects are strongly suppressed even for $T \gg m_\phi$. Therefore we may, for all practical purposes, resort to the zero-temperature description. A high-temperature $T \gg m$ expansion of the effective potential for both the ideal as well as the interacting scalar field has been obtained in Refs. [267–269] and the relevant thermodynamic properties are given to leading order as

$$\begin{aligned}
P &= \begin{cases} \frac{\pi^2T^4}{45} + \frac{(2\mu^2-m^2)T^2}{12} & \text{(unbroken phase)},\\ \frac{\pi^2T^4}{45} & \text{(broken phase)}, \end{cases}\\
\mathcal{S} &= \begin{cases} \frac{4\pi^2T^3}{45} + \frac{(2\mu^2-m^2)T}{6} & \text{(unbroken phase)},\\ \frac{4\pi^2T^3}{45} & \text{(broken phase)}, \end{cases}\\
\mathcal{U} &= \begin{cases} \frac{\pi^2T^4}{15} + \frac{(2\mu^2-m^2)T^2}{12} + \mu\mathcal{Q} & \text{(unbroken phase)},\\ \frac{\pi^2T^4}{15} + m\mathcal{Q} & \text{(broken phase)}, \end{cases}
\end{aligned} \tag{7.86}$$

such that even at relatively high temperatures comparable to today's CMB temperature, the ideal gas would follow a CDM equation of state of $\omega \simeq 0$. Obviously, for ϕ to act as *the* dark matter candidate, it would have to maintain this role throughout all of the cosmological evolution and a comprehensive cosmological study is beyond what we want to achieve here. In fact, we actually do not care whether ϕ is a dark matter, dark radiation, or even dark energy component, as long as its number density is sufficient to generate a detectable $0\nu\beta\beta$ signal within a lepton-number-conserving theory with Dirac neutrinos. Instead, our main point is that, generally speaking, the $T = 0$ approximation captures the relevant physics for our discussion, even if the ϕ was produced thermally (e.g., through some additional dark sector) and not non-relativistically.

7.6 Neutrinoless Double Beta Decay via a Dark Scalar Capture – II. The BEC Phase

Now that we are equipped with the necessary tools to understand the transition to the BEC phase in a high-density scalar environment, let us focus on the impact of such a scenario on $0\nu\beta\beta$ experiments. As we have seen, in the case of an ultralight scalar with a density in the region of the local CDM density $\rho_{\rm DM} \simeq 0.3\,{\rm GeV/cm^3}$, the critical temperature below which the scalar field is expected to undergo the phase transition to the BEC state is substantially larger than the typical CMB temperature. In the context of $0\nu\beta\beta$ our main concern lies in the magnitude of the scalar fields expectation value and with finite temperature effects scaling as $T^2/T_{\rm crit}^2$ we can simply stick to the $T = 0$ approximation. In this case, we can replace the complex scalar by it's (rotating) expectation value

$$\phi = \sqrt{\frac{n_\phi}{2m_\phi}}\exp\{-im_\phi t\}. \tag{7.87}$$

Thus, from the symmetry breaking nature of the BEC formation we can see that the neutrino-scalar interaction term in the condensate phase

$$\mathcal{L} \supset \sqrt{\frac{n_\phi}{2m_\phi}}\exp\{-im_\phi t\}g_{ij}\overline{\nu_{R,i}}\nu_{R,j}^C + \text{h.c.}, \qquad n_\phi = \frac{\alpha\rho_{\rm DM}}{m_\phi}, \tag{7.88}$$

provides a mechanism for the generation of an effective in-medium Majorana mass for the right-handed neutrinos. Indeed, the condensate acts similar to a vacuum expectation value in a Higgs-like scenario and we may identify the rotating phase as the corresponding Goldstone mode representing a quasi-particle phonon excitation of the condensate. Consequently, in the condensate phase the $0\nu\beta\beta$ triggered by a scalar capture and emission can be perfectly described in terms of the usual LνEM parameterized by the effective Majorana mass $m_{\beta\beta}$ with an additional contribution arising from the exchange of three sterile neutrinos. This simply corresponds to a $0\nu\beta\beta$ induced via the usual seesaw type-I mechanism. Indeed, we can identify the Dirac mass matrix M_D and the right-handed Majorana mass matrix M_R via their respective Yukawa interactions with H and ϕ as

$$M_{D,ij} = Y_{ij}^\nu\frac{v}{\sqrt{2}}, \qquad M_{R,ij} = 2\sqrt{\frac{n_\phi}{2m_\phi}}\exp\{-im_\phi t\}g_{ij}. \tag{7.89}$$

7.6.1 A Bose-Einstein Condensate Seesaw Mechanism

For simplicity, we will assume that the Dirac mass matrix M_D and the effective in-medium right-handed mass matrix M_R can be diagonalized at the same time, i.e., we choose the most simple setting $g_{ij} = g\delta_{ij}$, again, such that we can write

$$M_{D,ij} = m_{D,i}\delta_{ij}, \qquad M_{R,ij} = 2\sqrt{\frac{n_\phi}{2m_\phi}}\exp\{-im_\phi t\}g\delta_{ij}. \tag{7.90}$$

In this case, the diagonalization of the three-generation 6×6 neutrino mass matrix simplifies to three separate one-generation scenarios resembling the usual type-I seesaw scenario [10]. In addition, this scenario has the convenient benefit of forbidding the possible (albeit suppressed) neutrino decay channel $\nu_i \to \phi \nu_j$. By defining the left and right-handed fields

$$n_{R,i} = \begin{pmatrix} \nu_{L,i}^C \\ \nu_{R,i} \end{pmatrix}, \qquad n_{L,i} = n_{R,i}^C, \tag{7.91}$$

we can summarize the neutrino mass terms as

$$\mathcal{L} \supset -\frac{1}{2}\overline{n_{L,i}^C} M_i n_{L,i} + \text{h.c.}, \qquad M_i = \begin{pmatrix} 0 & m_{D,i} \\ m_{D,i} & |m_R| \exp\{-i m_\phi t\} \end{pmatrix}, \tag{7.92}$$

with

$$|m_R| = 2g\sqrt{\frac{n_\phi}{2m_\phi}}. \tag{7.93}$$

The eigenvalues of each mass matrix M_i can be obtained in the usual fashion as

$$m_{\chi,i}^{\pm} = \frac{1}{2}\left(|m_R| \exp\{-i m_\phi t\} \pm \sqrt{|m_R|^2 \exp\{-2i m_\phi t\} + 4m_{D,i}^2}\right), \tag{7.94}$$

and the corresponding diagonalizing matrices V_i can be obtained from the normalized eigenvectors as

$$V_i = \begin{pmatrix} -\frac{m_{\chi,i}^+}{\sqrt{m_{D,i}^2 + \left(m_{\chi,i}^+\right)^2}} & -\frac{m_{\chi,i}^-}{\sqrt{m_{D,i}^2 + \left(m_{\chi,i}^-\right)^2}} \\ \frac{m_{D,i}}{\sqrt{m_{D,i}^2 + \left(m_{\chi,i}^+\right)^2}} & \frac{m_{D,i}}{\sqrt{m_{D,i}^2 + \left(m_{\chi,i}^-\right)^2}} \end{pmatrix}, \qquad V^{-1} = V^T, \tag{7.95}$$

with the mass states $\chi_L = (\chi_L^-, \chi_L^+)^T$ given via

$$\overline{n_{L,i}^C} M_i n_L = \overline{n_{L,i}^C} V_i V_i^T M_i V_i V_i^T n_{L,i} = \overline{\chi_{L,i}^C} M_{i,\text{diag}} \chi_{L,i}, \tag{7.96}$$

as

$$\chi_{L,i} = V_i^T n_{L,i}, \tag{7.97}$$

where we defined the diagonalized mass matrix

$$M_{i,\text{diag}} = \begin{pmatrix} m_{\chi_i}^- & 0 \\ 0 & m_{\chi,i}^+ \end{pmatrix}. \tag{7.98}$$

In general, the eigenvalues $m_{\chi,i}^{\pm}$ of the mass matrices M_i are complex-valued

$$m_{\chi,i}^{\pm} = |m_{\chi,i}^{\pm}| \exp\{i\alpha_i^{\pm}\}, \tag{7.99}$$

and we may apply another basis transformation, to arrive at real-valued and non-negative masses by taking

$$\overline{\chi_{L,i}^C} A_i A_i^\dagger M_{i,\text{diag}} A_i^\dagger A_i \chi_{L,i} = \overline{N_{L,i}^C} \mathcal{M}_i N_{L,i}, \tag{7.100}$$

where the diagonal matrix

$$A_i = \begin{pmatrix} \exp\{\frac{1}{2} i\alpha_i^-\} & 0 \\ 0 & \exp\{\frac{1}{2} i\alpha_i^+\} \end{pmatrix}, \tag{7.101}$$

cancels the phase of the complex eigenvalues $m_{\chi,i}^\pm$. Hence, the final mass matrix

$$\mathcal{M}_i = \begin{pmatrix} m_i^- & 0 \\ 0 & m_i^+ \end{pmatrix}, \qquad m_i^\pm = |m_{\chi,i}^\pm|, \tag{7.102}$$

describes the real-valued physical masses of the corresponding mass states

$$N_{L,i} = A_i V_i^T n_{L,i}. \tag{7.103}$$

Note that, due to the time dependence of the rotating condensate, both the physical masses $|m_{\chi,i}^\pm|$ as well as the corresponding eigenstates $N_{L,i}$ exhibit a time dependence. While this may be counter-intuitive at first, we should remind ourselves that these do not describe fundamental masses, but, instead, effective in-medium masses generated via the interaction of the right-handed neutrinos ν_R with the ϕ BEC. Before we look at the possible consequences of this time dependence, let us first consider the changes in the neutrino mixing and its effects on the weak charged-current interactions with the charged leptons.

The appearance of the additional three sterile states as well as the time dependence requires a correction to the usual PMNS neutrino mixing matrix U [11]. In the standard three-neutrino mixing scenario, the weak charged-current interaction between the left-handed charged leptons of flavor α, $l_{L,\alpha}$, and the neutrino mass states $\nu_{L,i}$ is, ignoring the W-boson as well as coupling constants, given by

$$\overline{l_{L,\alpha}} \gamma^\mu U_{\alpha i}^* \nu_{L,i}, \tag{7.104}$$

where the neutrino mixing matrix is parameterized in terms of the three mixing angles $\theta_{12}, \theta_{13}, \theta_{23}$, the dirac CP phase δ as well as the two Majorana CP phases α_1, α_2 as [11]

$$U = \begin{pmatrix} c_{12}c_{13} & s_{12}c_{13} & s_{13}e^{-i\delta_{cp}} \\ -s_{12}c_{23} - c_{12}s_{23}s_{13}e^{i\delta_{cp}} & c_{12}c_{23} - s_{12}s_{23}s_{13}e^{i\delta_{cp}} & s_{23}c_{13} \\ s_{12}s_{23} - c_{12}c_{23}s_{13}e^{i\delta_{cp}} & -c_{12}s_{23} - s_{12}c_{23}s_{13}e^{i\delta_{cp}} & c_{13}c_{23} \end{pmatrix} \cdot U_M, \tag{7.105}$$

with the Majorana phases being incorporated in

$$U_M = \text{diag}\left(1, e^{i\alpha_1}, e^{i\alpha_2}\right), \tag{7.106}$$

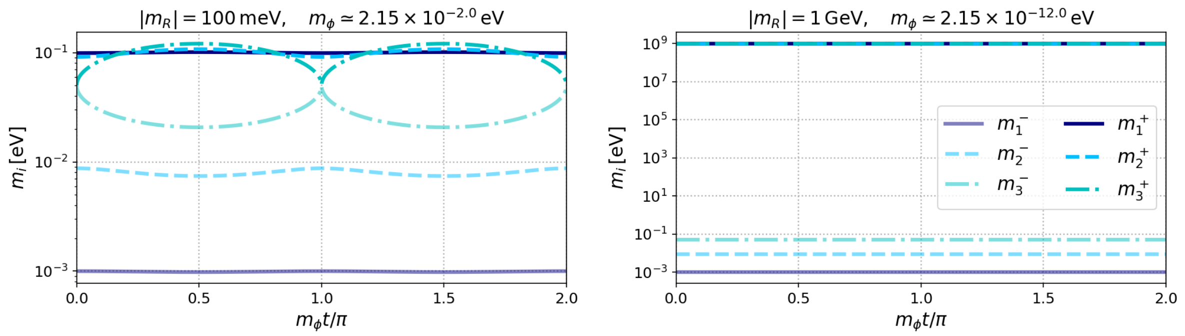

Figure 7.5: Time dependence of the six effective in-medium neutrino masses $m_i^\pm, i \in [1, 2, 3]$ generated from the rotating Bose-Einstein condensate. On the left, we present a low-density scenario with a relatively light effective right-handed neutrino mass of $|m_R| = 100\,\text{meV}$ which generates a significant time dependence of the effective in-medium neutrino masses. On the right, we show a contrasting high-density scenario with a heavy effective right-handed neutrino mass of $|m_R| = 1\,\text{GeV}$, such that the time dependence is strongly suppressed. For each scenario, we present the corresponding scalar masses m_ϕ assuming that $g = \alpha = 1$. The minimal neutrino mass is put to $m_{\text{min}} = 1\,\text{meV}$.

and with the usual abbreviations $\sin\theta_{ij} = s_{ij}$ and $\cos\theta_{ij} = c_{ij}$ employed. We can express eq. (7.104) in terms of the effective in-medium mass states $N_{L,i} = (N_{L,i}^-, N_{L,i}^+)^T$ as

$$\sum_i \overline{l_{L,\alpha}}\gamma^\mu U_{\alpha i}^* \nu_{L,i} = \sum_{i,k} \overline{l_{L,\alpha}}\gamma^\mu U_{\alpha i}^* \left(V_i A_i^\dagger\right)_{0k} (N_{L,i})_k = \sum_i \overline{l_{L,\alpha}}\gamma^\mu \left(\mathcal{U}_{\alpha i}^{-*} N_{L,i}^- + \mathcal{U}_{\alpha i}^{+*} N_{L,i}^+\right), \tag{7.107}$$

with the mixing matrices for the light and heavy states

$$\mathcal{U}_{\alpha i}^{-*} = U_{\alpha i}^*(V_i A_i^\dagger)_{00}, \qquad \mathcal{U}_{\alpha i}^{+*} = U_{\alpha i}^*(V_i A_i^\dagger)_{01}. \tag{7.108}$$

The mixing angles θ_{ij} are fixed from oscillation data [235].

In order to determine the eigenvalues of the effective neutrino mass matrix $\mathcal{M}_i$ we need to fix the model parameters m_ϕ, g, and α which determine the effective right-handed Majorana mass m_R. Additionally, we have to fix the Dirac masses $m_{D,i}$. This can be achieved by requiring that at $t = 0$, i.e., for $m_R = |m_R|$ the three light eigenvalues m_i^- should replicate the squared-mass differences $\Delta m_{ij} = m_i^2 - m_j^2$ that are observed within neutrino oscillation experiments. In this way, only the minimal neutrino mass m_{min} together with the mass ordering and the two Majorana phases remain free.

We may wonder now, whether the time dependence introduced by the rotating condensate may get into conflict with the neutrino oscillation data, or whether it has any other relevant phenomenological implications. Indeed, in previous literature, it was shown that the time dependence introduced by an oscillating real scalar field coupling to neutrinos may have a significant impact on neutrino oscillations [271–274]. This mainly stems from the fact that for an oscillating real scalar field the absolute value of the field is time-dependent, $\Phi = A\sin(m_\Phi t)$, thereby significantly impacting the effective in-medium neutrino masses. In general, this behaviour cannot be blindly assumed to be realized for a complex scalar background field, which has a rotating time-dependent phase but a constant absolute value (c.f. eq. (7.33)). In Figure 7.5 we show the time dependence of the different mass eigenvalues $m_i^\pm$ for a light right-handed mass of $|m_R| = 100\,\mathrm{meV} \sim \mathcal{O}(m_{D,i})$ and for a heavier case of $|m_R| = 1\,\mathrm{GeV} \gg m_{D,i}$. In both scenarios, we put the minimal neutrino mass to $m_{\min} = 1\,\mathrm{meV}$. We can see that, while the time dependence is noticeable for the light m_R scenario, it is unobservably small when going to heavier effective right-handed neutrino masses $|m_R| > 1\,\mathrm{GeV}$. Indeed, in this parameter region, the time dependence of the masses is only at the order of $\Delta m_i/m_i \sim 10^{-10}$. This behaviour is to be expected as heavier sterile neutrinos should, simply, decouple from the remaining degrees of freedom at some point. As in the free phase, we will see that the heavy m_R scenario is the one relevant to our discussion on $0\nu\beta\beta$. From this standpoint, in contrast to the case of a real scalar field, we do not expect the time dependence that is connected to the rotating condensate to leave any observable imprints.

7.6.2 Neutrinoless Double Beta Decay in the Condensate Phase

Let us now return to the phenomenology of the $0\nu\beta\beta$ in the condensate phase. As we have seen in the previous section, the neutrino-scalar interaction in the condensate phase is simply an in-medium realization of a seesaw type-I mechanism, albeit with a time-dependent complex phase which can be relevant when the effective right-handed neutrino mass is of the order of the vacuum Dirac masses. In such seesaw-like scenarios, which have been widely studied in previous literature [176, 275–277], the $0\nu\beta\beta$ is described in terms of the exchange of both light and heavy massive Majorana neutrinos. In contrast to the usual mass mechanism of $0\nu\beta\beta$, we will generally not be able to ignore the neutrino masses within the denominator of the neutrino propagator by taking the $m_\nu^2 \ll p^2$ limit. Instead, the exchange of heavy sterile neutrinos in the $m_\nu \gg p^2$ limit can be matched onto the LEFT operator $\mathcal{O}_{1L}$ (c.f. Table 4.5) by integrating out the heavy neutrinos. The remaining parameter space that describes the exchange of heavy neutrinos with masses similar to the typical momentum exchange of $0\nu\beta\beta$, $m_\nu^2 \sim p^2 \sim \mathcal{O}(100\,\mathrm{MeV})$, can be approximated by defining a mass-dependent NME, $\mathcal{M}(m_\nu)$, which can be obtained via a simple interpolation approach [275, 276]

$$\mathcal{M}_\nu(m_i) = \frac{4m_N^2|\mathcal{M}_\nu^{(9)}|}{\langle p^2\rangle + m_i^2}, \quad \langle p^2\rangle = 4m_N^2\frac{|\mathcal{M}_\nu^{(9)}|}{|\mathcal{M}_\nu^{(3)}|}. \tag{7.109}$$

Here, $\langle p^2\rangle$ describes the typical momentum exchange carried by the propagating neutrino, $\mathcal{M}_\nu^{(3)}$ and $\mathcal{M}_\nu^{(9)}$ are the relevant NMEs for the exchange of light and heavy neutrinos, respectively, and the interpolation formula follows the form of the neutrino propagator to replicate the naive scaling behaviour of the NMEs for different neutrino masses.

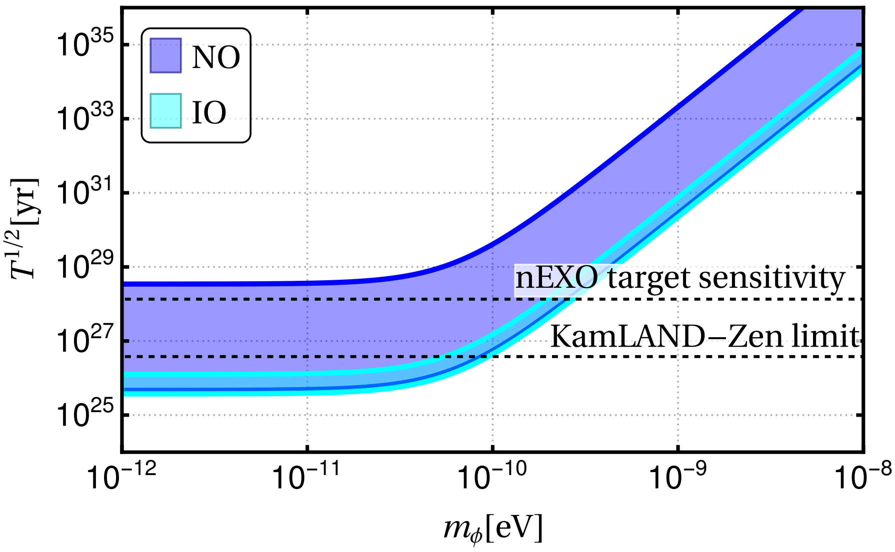

Figure 7.6: $0\nu\beta\beta$ half-life of the scalar-capture mechanism in the Bose-Einstein Condensate phase. As a baseline scenario, we use the current best-fit values of the neutrino mixing parameters, we set $g = \alpha = 1$ and neglect the effect of the unknown Majorana phases. The minimal neutrino mass is varied within the range currently allowed by cosmology imposing the constraint $\sum_i m_i^- \leq 260\,\text{meV}$ [235, 236]. The dark blue area represents the case of normal neutrino mass ordering, $m_1^- < m_2^- < m_3^-$, while the lighter turquoise region shows the inverted mass ordering scenario with $m_3^- < m_1^- < m_2^-$. The isotope of choice is ^{136}Xe and we present the current best limit as obtained by the KamLAND-Zen collaboration [46] as well as the projected target sensitivity of the next-generation nEXO experiment [34]. This plot was published in Ref. [3].

We can now express the $0\nu\beta\beta$ half-life in terms of the effective in-medium neutrino masses $m_i^\pm$ and the corresponding mixing matrices $\mathcal{V}_{ei}^\pm$ as [2, 276]

$$\left(T_{0\nu\beta\beta}^{1/2}\right)^{-1} = g_A^4 G_{0\nu\beta\beta} \left| \sum_{i=1}^{3} (\mathcal{V}_{ei}^-)^2 \frac{m_i^-}{m_e} \mathcal{M}_\nu(0) + (\mathcal{V}_{ei}^+)^2 \frac{m_i^+}{m_e} \mathcal{M}_\nu(m_i^+) \right|^2. \tag{7.110}$$

In Figure 7.6 we show the expected $0\nu\beta\beta$ half-lives over a range of different scalar masses m_ϕ, by setting $g = \alpha = 1$ and varying the minimal neutrino mass within the allowed range constrained by the cosmological limits on the sum of the light neutrino masses, $\sum_i m_i^- \leq 260\,\text{meV}$, as obtained from the Planck CMB data [235, 236]. The mixing angles as well as the Dirac CP-phase of the PMNS matrix are taken as the best-fit values provided by the PDG report [235] and we assume vanishing Majorana phases. We can see that in this baseline scenario, in the high-density regime with $m_\phi \lesssim 10^{-10}\,\text{eV}$, the $0\nu\beta\beta$ half-life approaches the usual range expected from the standard LνEM induced by the exchange of three light Majorana neutrinos. On the contrary, in the low-density regime with $m_\phi \gtrsim 10^{-10}\,\text{eV}$, the expected $0\nu\beta\beta$ half-life increases substantially, as the sterile neutrino masses m_i^+ approach the masses of the active neutrinos m_i^- thereby transitioning to a pseudo-Dirac scenario. This is precisely the behaviour one expects from a seesaw type-I-like mechanism [277]. While we fixed $g = \alpha = 1$, we want to point out that smaller values do not impact the general shape of Figure 7.6, but would instead shift the x-axis towards smaller scalar masses, i.e., larger densities. Therefore, we do not require the scalar field to act as a substantial amount of the observed CDM.

In comparison to the free phase, the $0\nu\beta\beta$ half-lives in the condensate phase approach the sensitivity levels of the current and next-generation $0\nu\beta\beta$ experiments at much lower scalar densities, signifying a substantial enhancement of the $0\nu\beta\beta$ half-life attributed to the phase transition from the free to the BEC phase.

7.6.3 Identifying the Bose-Einstein Condensate Induced $0\nu\beta\beta$

It is evident that, in the high-density parameter region of interest, the BEC-induced $0\nu\beta\beta$ is not distinguishable from the usual LνEM by any means, as it simply leads to an effective in-medium Majorana neutrino mass via a seesaw type-I-like mechanism. While the time dependence attributed to the rotating condensate is, in principle, a distinct feature, it does not result in measurable time variations of the $0\nu\beta\beta$. Consequently, it is impossible to distinguish such a scenario from the usual mass mechanism within $0\nu\beta\beta$ experiments. The same is true when considering its impact on oscillation experiments. In this way, our proof-of-concept model sets itself apart from previous literature, which studied LNV scenarios in the context of a real scalar field background [255, 271].

However, as the effective in-medium neutrino mass is highly dependent on the local scalar number density, it can vary in astrophysical environments situated in different scalar backgrounds of different densities. Additionally, in the free phase, ϕ can act as a mediator of long-range neutrino self-interactions [278]. In the condensate phase, both long-range neutrino self-interactions mediated via a massless phonon excitation of the condensate, as well as short-range neutrino self-interactions mediated by a heavy quasi-particle excitation are present. These self-interactions may impact neutrino free-streaming in astrophysical and cosmological environments of high neutrino-densities such as core-collapse supernovae [279] or during recombination in the early Universe thereby, potentially, providing a solution to the Hubble tension [278, 280–282].

Similarly, the expansion of the cosmos is associated with a larger scalar number density in the early Universe. This would render the effective in-medium neutrino masses to vary on cosmological time-scales with the right-handed effective neutrino mass m_R being larger in the early Universe and, consequently, resulting in smaller active neutrino masses via the seesaw mechanism. Hence, a BEC-induced seesaw mechanism could offer a compelling explanation for a potential future discrepancy between the increasingly stringent cosmological limits on the sum of neutrino masses $\Sigma_i m_i^-$ and the minimal neutrino mass derived from the squared mass differences Δm_{ij} obtained from oscillation data. In fact, the most stringent cosmological limit up to date [283], taking into account the Planck CMB data as well as additional information on the large-scale structure formation and background evolution [235, 283] in combination with the current best-fit oscillation data [235] restricts the sum of the light neutrino masses to the range of

$$82\,\mathrm{meV} > \sum_i m_i^- \gtrsim \begin{cases} 59\,\mathrm{meV}, & \text{normal hierarchy} \\ 100\,\mathrm{meV}, & \text{inverted hierarchy} \end{cases}, \tag{7.111}$$

prompting the need to consider a scenario in which conflicting cosmological and oscillation data may require an explanation in terms of new physics.

For simplicity, we have considered an ultralight scalar background that accommodates for all of the observed CDM. BECs have been extensively studied as potential dark matter candidates in the previous literature [251–254, 284–288]. While it is, obviously, intriguing to explain two phenomena ($0\nu\beta\beta$ and CDM) in a single model, this is by no means a strict requirement and we may simply set $\alpha \ll 1$ such that the scalar condensate only accounts for a tiny fraction of the required CDM in the Universe. Alternatively, ϕ might act as a radiation component of the energy density of the Universe, a scenario that we will study more carefully in Ref. [4].

Considering collider experiments such as the LHC, scalar emission modes can contribute to the decay width of several heavy particles, such as $Z \to \nu\nu\phi$, $W^\pm \to l^\pm\nu\phi$, $H \to \nu\nu\phi$ and others that can decay via a neutrino emitting channel. However, all of these decay modes suffer a substantial suppression from the requirement of light neutrino mass insertions, as ϕ couples only to the right-handed neutrino. We have discussed the suppression of the emission modes earlier in the context of $0\nu\beta\beta$.

As a summarizing statement, the appearance of a lepton-number-carrying complex scalar field coupling to right-handed neutrinos could, in principle, have interesting phenomenological consequences in several contexts. However, in general, its effects on observables related purely to particle physics are expected to be negligible due to the coupling only to right-handed neutrinos and the corresponding suppression of transition amplitudes stemming from the tiny active-sterile mixing. Both in the free phase and in the condensate phase, this tiny mixing can only be compensated by the proposed high number density of the scalar background, which, however, in the condensate phase acts solely through the generation of an effective in-medium Majorana mass for the right-handed neutrinos and the corresponding seesaw mechanism. Therefore, we expect that the most promising ways to uncover such a model will be related to a local or time-dependent variation of the scalar number density in different astrophysical and cosmological environments. Probably *the* smoking gun signature of such a BEC-induced seesaw mechanism would be a future conflict between the minimal neutrino mass measured in today's oscillation experiments and the sum of the light neutrino masses as derived from the early Universe.

7.6.4 Critique on the Bose-Einstein Condensate Approach

As we have done for the free phase approach, we want to discuss whether the description of a high-density scalar background in terms of a BEC is appropriate. The deciding factor here is the application of thermal-equilibrium QFT which, strictly speaking, requires the scalar field to be in a state of thermal and chemical equilibrium. However, with ϕ

coupling to the Standard Model only via the interactions with right-handed neutrinos, it cannot equilibrate via interactions with the Standard Model. Obviously, the reintroduction of the repulsive scalar self-interactions would allow ϕ to self-thermalize at the cost of increasing the pressure of the system thereby conflicting the assumption of ϕ acting as CDM. We may, however, introduce small self-interactions sufficient to account for a self-thermalization of ϕ by allowing ϕ to act as a radiation component to the energy density of the Universe. This scenario does come with stronger constraints on the scalar energy density and we will study it more closely in Ref. [4].

For the ideal gas scenario considered here, gravitational self-interactions can be sufficient for the scalar field to equilibrate [4, 289, 290] if the gravitational relaxation rate

$$\Gamma_g \simeq \frac{Gn}{\delta v^2}, \tag{7.112}$$

is larger than the Hubble rate

$$H^2 = H_0^2(\Omega_\gamma a^{-4} + \Omega_M a^{-3} + \Omega_k a^{-2} + \Omega_\Lambda), \tag{7.113}$$

with the scalar velocity dispersion δ_v, Newton's gravitational constant $G \simeq 6.7 \times 10^{-57}\,\text{eV}$, the cosmological scale factor a, today's Hubble rate $H_0 \simeq 70\,\text{km/s/Mpc}$, and with $\Omega_{\gamma,M,k,\Lambda}$ corresponding to the energy density components of the Universe, i.e., radiation, matter, curvature and the cosmological constant [235], respectively. For a non-relativistically produced scalar field generated at a redshift z_1 with an initial dispersion relation $\delta_v(z_1)$ and an initial number density $n_0 = n(z_1)$, the dispersion relation at later times, i.e., smaller redshift $z < z_1$ may be expressed as [289, 290]

$$\delta v(z) = \delta v(z_1)\frac{a(z_1)}{a(z)} < \frac{a(z_1)}{a(z)}. \tag{7.114}$$

By utilizing this relation, we can put a lower limit on the gravitational relaxation rate at a given redshift z in dependence on the redshift at production z_1 [289]

$$\Gamma_g \gtrsim \frac{Gn_0}{a(z_1)^2 a(z)}. \tag{7.115}$$

It follows that an ultralight scalar field with masses $m_\phi < 10^{-20}\,\text{eV}$ will thermalize instantaneously at production if it is produced at a redshift corresponding to temperatures of $T_1 > 1\,\text{GeV}$. As the Hubble rate in the early Universe is proportional to a^{-2} while the gravitational relaxation rate goes with a^{-1}, such a gravitationally self-thermalized ultralight scalar field will remain in an equilibrium state throughout the cosmological evolution until today and will drop out of equilibrium at some point in the future when the Hubble rate will be dominated by the cosmological constant and, therefore will approach a constant value.

While the existing literature presents convincing arguments in favour of a gravitational self-thermalization of ultralight scalar dark matter [289–291], there is no general agreement on this with opposing arguments appearing as well [292]. In the context of structure formation, gravitational thermalization might only take place locally within DM halos of high scalar number densities without a global thermalization [291]. A self-consistent theoretical description of Bose-Einstein condensation in the context of a self-gravitating scalar field will, generally, require the inclusion of equilibrium QFT in curved space-times [293–300], a task which goes beyond the scope of this work.

Irrespective of this, we have shown that the zero-temperature equilibrium QFT approach does recover the classical field approach that is often used in the context of bosonic fields with large occupation numbers [254, 255, 270]. Therefore, we might argue that the phenomenological consequences should be rather insensitive to the degree of thermalization. Indeed, Refs. [301, 302] provide arguments for a condensation into the zero-momentum mode on time scales much shorter than those required for a full thermalization. Nevertheless, the application of equilibrium QFT methods, specifically modelling non-zero number densities via the introduction of a chemical potential, provides convincing arguments for spontaneous symmetry breaking within the scalar medium. As such, it intuitively provides an explanation for the generation of an effective in-medium Majorana neutrino mass, a feature that is less obvious in the simple classical field treatment.

Finally, as described in Section 7.5, we want to point out that the introduction of a chemical potential requires the existence of an associated conserved charge. While in the simple ϕ^4 theory the scalar number density is conserved due to the corresponding $U(1)_\phi$ symmetry of the scalar potential, this symmetry is broken in our model by the neutrino-scalar interaction term $g\overline{\nu_R}\nu_R^C\phi$. We could recover an approximate $U(1)_\phi$ symmetry by taking $g \ll 1$. However, this is not necessary as number-density-changing processes require incoming or outgoing right-handed neutrinos. While processes involving outgoing right-handed neutrinos can be kinematically forbidden due to the ultralight nature of the scalar field as well as the fact that it mostly occupies the low-energy zero-momentum mode even at relatively large temperatures $T \sim T_{\mathrm{CMB}}$, processes involving incoming right-handed neutrinos are strongly suppressed due to the tiny active-sterile mixing limiting the production of right-handed neutrinos. In this sense, the scalar number density may be treated as a conserved quantity even though the Lagrangian does not reflect the corresponding symmetry.

Chapter 8

Summary & Conclusion

In this work, we have studied various aspects and implications of new lepton-number-violating physics in the context of neutrinoless double beta decay. The basis for our discussion was described in Chapter 4. By utilizing chiral perturbation theory, we have rederived the $0\nu\beta\beta$ half-life master formula developed by Cirigliano et al. in Refs. [44, 45], and expanded it to include the effects of scalar lepton-number-violating neutral-current neutrino-quark LEFT operators, which generate a contribution to the Majorana neutrino mass via the formation of a quark condensate in the low-energy regime of χPT. This interesting feature has been ignored in most of the previous literature. However, we showcased in Chapter 6 that this mechanism sets the strongest limits on such LNV neutral-current neutrino-quark interactions to date, improving the limits obtained in coherent elastic neutrino-nucleus scattering experiments by about 2 orders of magnitude. It should be pointed out that $0\nu\beta\beta$ experiments, of course, cannot put limits on lepton number conserving interactions which are testable in coherent neutrino scattering experiments. The inclusion of these operators provides another essential step towards a complete description of $0\nu\beta\beta$ in a model-independent EFT approach.

In Chapter 5, we applied the chiral EFT approach to $0\nu\beta\beta$, described in Chapter 4, to study the phenomenological implications of different $0\nu\beta\beta$ mechanisms in a model-independent way. In this context, we discussed different possibilities that may allow us to distinguish among the different $0\nu\beta\beta$ operators covering both SMEFT and LEFT operators. While a measurement of the $0\nu\beta\beta$ half-life in multiple isotopes shows the strongest potential for uncovering $0\nu\beta\beta$ induced by higher-dimensional operators, it turns out that, at the current level of accuracy attributed to the nuclear-theory inputs involved in the calculations of the expected $0\nu\beta\beta$ half-lives, this is not practically achievable. We performed a parameter scan over the currently unknown low-energy constants of chiral EFT to estimate the required level of theoretical accuracy in the nuclear theory to be around $\sim \mathcal{O}(10\%)$. This estimate is based on the median values of half-life ratios for various isotopes obtained from the parameter scan and its applicability is of course limited by the current uncertainties of both the nuclear matrix elements as well as the low-energy constants of chiral EFT. Therefore, we also estimated the worst-case scenario given by the least favourable results from the parameter scan, showcasing that, if Nature chooses so, the identification of the underlying $0\nu\beta\beta$ mechanism via half-life measurements in multiple isotopes might turn out to be hopeless. Nevertheless, our estimate of the required accuracy of nuclear matrix elements and LECs can act as a guideline for the ongoing development of ab-initio approaches to nuclear matrix element calculations which aim to improve and quantify the uncertainties involved. A reanalysis of the results presented in Chapter 5 should be performed in the future when significant improvements on the nuclear-theory side have been achieved. Independently of the uncertainties stemming from the nuclear theory, we showed that $0\nu\beta\beta$ experiments utilizing tracking calorimetric techniques such as NEMO and SuperNEMO can help to uncover new lepton-number-violating vector interactions via the measurement of the individual electron kinematics. Despite the fact that tracking calorimeter experiments are, currently, not at the forefront of half-life sensitivities when compared to the next-generation ton-scale experiments such as nEXO or LEGEND, the potential benefit from the measurement of the individual electron kinematics with regards to the identification of non-standard lepton-number-violating mechanisms presents a strong case for the further development of these experiments.

The effective field theory approach summarized in Chapter 4 provides a simple and algorithmic way of calculating $0\nu\beta\beta$ half-lives and other observables in a model-independent as well as model-dependent way. However, the necessary steps, including the matching procedures connecting the different EFTs, are rather complicated and tedious. With ν`DoBe`, we provide a simple and easy-to-access computational Python framework that automates the computational steps and allows users to analyze specific models defined either at the SMEFT or LEFT scales, as well as to derive limits on the individual EFT operators from a given $0\nu\beta\beta$ half-life limit. In Chapter 6 we provided several use-case examples of ν`DoBe` by reanalyzing the recent half-life limit on $0\nu\beta\beta$ in ^{136}Xe as obtained by the KamLAND-Zen collaboration. In this context, we provided a complete list of upper limits on all relevant lepton-number-violating SMEFT and LEFT operators derived from the KamLAND-Zen limit. Additionally, we employed ν`DoBe` to study the constraints on the two-dimensional parameter spaces spanned by the light neutrino-exchange mechanism of $0\nu\beta\beta$, parameterized by $m_{\beta\beta}$, and the higher-dimensional LEFT operators derived by the half-life limits in four different isotopes, ^{76}Ge, ^{100}Mo, ^{130}Te, and ^{136}Xe as given by the GERDA, CUPID-Mo, CUORE, and KamLAND-Zen experiments, respectively. We found that several of the higher-dimensional LEFT operators can lead to a (partial) cancellation of the $0\nu\beta\beta$ half-life when paired with the standard light neutrino-exchange mechanism, leading to unrestricted directions in the parameter space spanned by $m_{\beta\beta}$ and the corresponding higher-dimensional Wilson coefficient. Again, a combination of half-life limits taken from multiple isotopes can help to restrict these regions of cancellation. Particularly, we found that the allowed parameter space derived from the half-life limits in ^{100}Mo tends to be substantially tilted in comparison with the parameter spaces derived from other commonly used isotopes. Consequently, this suggests that the combination of $0\nu\beta\beta$ limits derived in ^{100}Mo and some other commonly used isotope can close these regions of cancellation in the parameter space, thereby making a strong case for next-generation $0\nu\beta\beta$ experiments utilizing ^{100}Mo. Further, by studying $0\nu\beta\beta$ in the context of the mLRSM, we provided a model-dependent use-case example as well, showcasing the potential of ν`DoBe` for the model-building community. In the future, we plan to extend ν`DoBe` to include additional particle physics scenarios, such as light sterile neutrinos and other LNV physics.

Finally, in Chapter 7 we tackled the famous black-box theorem which states that any observation of $0\nu\beta\beta$ implies the Majorana nature of neutrinos via a 4-loop diagram. While the quantitative aspects of the black-box theorem are known to be tiny, such that a pseudo-Dirac scenario cannot be ruled out via a $0\nu\beta\beta$ detection, its qualitative essence, strictly speaking, still remains intact. By proposing a lepton-number-carrying scalar background field, we provided a $B-L$ conserving proof-of-concept model that can accompany a non-zero $0\nu\beta\beta$ rate via a scalar-capture mode that mimics the experimental signature of the usual LNV $0\nu\beta\beta$ mechanisms. Due to the addition of the external scalar field, the application of the black-box theorem is not valid within this scenario. Therefore, the loop generation of a Majorana neutrino mass can be avoided and the Dirac nature of the neutrino is left intact. In this way, the black-box theorem remains true in the sense that any $0\nu\beta\beta$ without additional external fields will generate a Majorana contribution to the neutrino mass, but the application of the black-box theorem to an experimental $0\nu\beta\beta$ signature is, in general, not valid anymore. However, the generation of experimentally testable half-lives via the scalar-capture mode requires the existence of a dark scalar background of substantial number density. In this context, one can expect the scalar field to undergo a phase transition to a Bose-Einstein condensed state which is accompanied by a spontaneous symmetry breaking within the scalar medium, thereby generating an effective in-medium Majorana neutrino mass in a seesaw-like scenario. We applied equilibrium QFT methods to describe the transition of the scalar field to the condensed state. While the thermalization/equilibration of the scalar field via gravitational self-interactions is up for debate, the application of equilibrium QFT methods allowed us to recover the usual classical field approach, which is widely used within the literature when describing bosonic fields of high occupation numbers. At the same time, our approach offers a compelling explanation of the spontaneous symmetry breaking process within the scalar medium, which allows for the generation of an effective in-medium Majorana neutrino mass. In this sense, the neutrino remains a Dirac field only in the zero-density vacuum, while effectively turning into a Majorana state within the scalar medium, showcasing subtleties that need to be addressed in the interpretation of a future $0\nu\beta\beta$ discovery. Interestingly, we found that such an in-medium effective seesaw mechanism for neutrino mass generation could offer an explanation for a potential future discrepancy between the upper limit on the sum of light neutrino masses, obtained from cosmology in the early Universe, and the lower limit on the sum of the light neutrino masses derived from today's oscillation experiments. We will study the cosmological implications of this model in a future publication.

To summarize, the results presented in this work improve our understanding of lepton-number-violating physics beyond the Standard Model in the context of neutrinoless double beta decay. We have achieved this by extending the existing theoretical frameworks to include previously ignored effects, by questioning the implications of long-standing theorems related to $0\nu\beta\beta$, as well as by developing ν`DoBe`, an easily accessible opens-source computational tool, which we believe will be of use to the broad particle physics community and, as such, will help to accelerate scientific progress. In the end, Nature will decide if our efforts will be rewarded by an experimental $0\nu\beta\beta$ discovery. As the closing statement and takeaway, I want to highlight that even if it looks like a duck it might not be a duck[1].

[1]The Wikipedia article on the *Duck Test* may be worth a read.

Appendix A

The Isotopes of Double Beta Decay

In the main text, we have mostly been focusing on the $\beta^-\beta^-$ decay which involves the emission of two electrons. As discussed in the main text as well, crossing symmetry suggests the existence of corresponding decay modes involving the emission of positrons and/or the capture of electrons from the atomic shell. As we discussed, these decay modes, are generally highly suppressed and, therefore, are usually not interesting for practical experimental setups. A recent counter-example is the proposal of the NuDoubt^{++} experiment [138] aiming for a few-kg to ton-scale $2\nu\beta^+\beta^+$ and $0\nu\beta^+\beta^+$ experiment. Similarly, we only covered a small subset of the potential $0\nu\beta^-\beta^-$ candidate isotopes in the main text, due to similar low Q-value suppression. For completeness we provide a complete list of all naturally occurring isotopes that are expected to undergo some sort of double beta decay alongside their natural abundance $\overline{N}$ and corresponding Q-values in Table A.1. The table is obtained by scanning the NIST list of elements [124] for isotopes with a natural abundance $\overline{N} > 0$ that may decay via at least one of the provided double beta channels ($\beta^-\beta^-, \beta^+\beta^+, \beta^+\mathrm{EC}, \mathrm{ECEC}$).

$(2,0)\nu\beta^-\beta^-$			$(2,0)\beta^+\beta^+$			$(2,0)\beta^+$EC			$(2,0)$ECEC		
Isotope	Q[MeV]	$\overline{N}$[%]	Isotope	Q[MeV]	$\overline{N}$[%]	Isotope	Q[MeV]	$\overline{N}$[%]	Isotope	Q[MeV]	$\overline{N}$[%]
^{46}Ca	0.989	0.004	^{78}Kr	0.802	0.355	^{50}Cr	0.147	4.345	^{36}Ar	0.433	0.334
^{48}Ca	4.267	0.187	^{96}Ru	0.670	5.540	^{58}Ni	0.904	68.077	^{40}Ca	0.194	96.941
^{70}Zn	0.997	0.610	^{106}Cd	0.731	1.250	^{64}Zn	0.073	49.170	^{50}Cr	1.169	4.345
^{76}Ge	2.039	7.730	^{124}Xe	0.820	0.095	^{74}Se	0.187	0.890	^{54}Fe	0.680	5.845
^{80}Se	0.134	49.610	^{130}Ba	0.575	0.106	^{78}Kr	1.824	0.355	^{58}Ni	1.926	68.077
^{82}Se	2.996	8.730	^{136}Ce	0.335	0.185	^{84}Sr	0.768	0.560	^{64}Zn	1.095	49.170
^{86}Kr	1.258	17.279				^{92}Mo	0.630	14.530	^{74}Se	1.209	0.890
^{94}Zr	1.142	17.380				^{96}Ru	1.692	5.540	^{78}Kr	2.846	0.355
^{96}Zr	3.349	2.800				^{102}Pd	0.150	1.020	^{84}Sr	1.790	0.560
^{98}Mo	0.110	24.390				^{106}Cd	1.753	1.250	^{92}Mo	1.652	14.530
^{100}Mo	3.034	9.820				^{112}Sn	0.898	0.970	^{96}Ru	2.714	5.540
^{104}Ru	1.301	18.620				^{120}Te	0.708	0.090	^{102}Pd	1.172	1.020
^{110}Pd	2.017	11.720				^{124}Xe	1.842	0.095	^{106}Cd	2.775	1.250
^{114}Cd	0.542	28.730				^{130}Ba	1.597	0.106	^{108}Cd	0.272	0.890
^{116}Cd	2.813	7.490				^{136}Ce	1.357	0.185	^{112}Sn	1.920	0.970
^{122}Sn	0.373	4.630				^{144}Sm	0.760	3.070	^{120}Te	1.730	0.090
^{124}Sn	2.291	5.790				^{156}Dy	0.984	0.056	^{124}Xe	2.864	0.095
^{128}Te	0.867	31.740				^{162}Er	0.825	0.139	^{126}Xe	0.920	0.089
^{130}Te	2.528	34.080				^{168}Yb	0.387	0.123	^{130}Ba	2.619	0.106
^{134}Xe	0.826	10.436				^{174}Hf	0.077	0.160	^{132}Ba	0.844	0.101
^{136}Xe	2.458	8.857				^{184}Os	0.429	0.020	^{136}Ce	2.379	0.185
^{142}Ce	1.417	11.114				^{190}Pt	0.362	0.012	^{138}Ce	0.693	0.251
^{146}Nd	0.070	17.189							^{144}Sm	1.782	3.070
^{148}Nd	1.928	5.756							^{152}Gd	0.056	0.200
^{150}Nd	3.371	5.638							^{156}Dy	2.006	0.056
^{154}Sm	1.251	22.750							^{158}Dy	0.283	0.095
^{160}Gd	1.731	21.860							^{162}Er	1.847	0.139
^{170}Er	0.656	14.910							^{164}Er	0.025	1.601
^{176}Yb	1.089	12.996							^{168}Yb	1.409	0.123
^{186}W	0.492	28.430							^{174}Hf	1.099	0.160
^{192}Os	0.408	40.780							^{180}W	0.143	0.120
^{198}Pt	1.049	7.356							^{184}Os	1.451	0.020
^{204}Hg	0.419	6.870							^{190}Pt	1.384	0.012
^{232}Th	0.838	100.000							^{196}Hg	0.820	0.150
^{238}U	1.144	99.274									

Table A.1: List of naturally occuring double beta isotopes. This list was also published in Ref. [1] and we recalculate it here with updated data from the NIST list of elements [124] with additional information about the natural abundances $\overline{N}$. For each isotope, both the Q-value in MeV and the natural abundance $\overline{N}$ in % are given.

Appendix B

Matching the Standard Model EFT to the Low-Energy EFT

In this appendix, we will provide msome identities and relations that have not been covered in the main text but are very helpful when doing the matching calculations of SMEFT operator onto LEFT. Afterwards, we will provide an example of a matching calculation highlighting the main obstacles in the process.

B.1 Helpful relations

In many scenarios, especially when matching different operator basises onto each other, one has to relate fermionic operators of different bilinear structures onto each other. While the relations are, simply, obtained by taking the transpose of the corresponding bilinear and adhering to the anti-symmetric nature of Dirac spinors, we will provide a comprehensive list of the relations used in the SMEFT-to-LEFT matching discussed in the main text. We hope these may be helpful for future students or any readers of the work presented here:

B.1.1 Scalar Bilinears

$$\begin{aligned}
\overline{\Psi_1}\Psi_2 &= \overline{\Psi_2^C}\Psi_1^C \\
\overline{\Psi_1}\Psi_2^C &= \overline{\Psi_2}\Psi_1^C \\
\left(\overline{\Psi_1}\Psi_2^C\right)^\dagger &= -\overline{\Psi_2^C}\Psi_1 \\
\left(\overline{\Psi_1}\Psi_2\right)^\dagger &= -\overline{\Psi_2}\Psi_1
\end{aligned} \tag{B.1}$$

B.1.2 Pseudoscalar Bilinears

$$\begin{aligned}
\overline{\Psi_1}\gamma_5\Psi_2 &= \overline{\Psi_2^C}\gamma_5\Psi_1^C \\
\overline{\Psi_1}\gamma_5\Psi_2^C &= \overline{\Psi_2}\gamma_5\Psi_1^C \\
\left(\overline{\Psi_1}\gamma_5\Psi_2^C\right)^\dagger &= \overline{\Psi_2^C}\gamma_5\Psi_1 \\
\left(\overline{\Psi_1}\gamma_5\Psi_2\right)^\dagger &= \overline{\Psi_2}\gamma_5\Psi_1
\end{aligned} \tag{B.2}$$

B.1.3 Vector Bilinears

$$\begin{aligned}
\overline{\Psi_1}\gamma^\mu\Psi_2 &= -\overline{\Psi_2^C}\gamma^\mu\Psi_1^C \\
\overline{\Psi_1}\gamma^\mu\Psi_2^C &= -\overline{\Psi_2}\gamma^\mu\Psi_1^C \\
\left(\overline{\Psi_1}\gamma^\mu\Psi_2^C\right)^\dagger &= -\overline{\Psi_2^C}\gamma^\mu\gamma_5\Psi_1 \\
\left(\overline{\Psi_1}\gamma^\mu\Psi_2\right)^\dagger &= -\overline{\Psi_2}\gamma^\mu\gamma_5\Psi_1
\end{aligned} \tag{B.3}$$

B.1.4 Axial-Vector Bilinears

$$\begin{aligned}
\overline{\Psi_1}\gamma^\mu\gamma_5\Psi_2 &= \overline{\Psi_2^C}\gamma^\mu\gamma_5\Psi_1^C \\
\overline{\Psi_1}\gamma^\mu\gamma_5\Psi_2^C &= \overline{\Psi_2}\gamma^\mu\gamma_5\Psi_1^C \\
\left(\overline{\Psi_1}\gamma^\mu\gamma_5\Psi_2^C\right)^\dagger &= -\overline{\Psi_2^C}\gamma^\mu\Psi_1 \\
\left(\overline{\Psi_1}\gamma^\mu\gamma_5\Psi_2\right)^\dagger &= -\overline{\Psi_2}\gamma^\mu\Psi_1
\end{aligned} \tag{B.4}$$

B.1.5 Tensor Bilinears

$$\begin{aligned}
\overline{\Psi_1}\sigma^{\mu\nu}\Psi_2 &= -\overline{\Psi_2^C}\sigma^{\mu\nu}\Psi_1^C \\
\overline{\Psi_1}\sigma^{\mu\nu}\Psi_2^C &= -\overline{\Psi_2}\sigma^{\mu\nu}\Psi_1^C \\
\left(\overline{\Psi_1}\sigma^{\mu\nu}\Psi_2^C\right)^\dagger &= -\overline{\Psi_2^C}\sigma^{\mu\nu}\Psi_1 \\
\left(\overline{\Psi_1}\sigma^{\mu\nu}\Psi_2\right)^\dagger &= -\overline{\Psi_2}\sigma^{\mu\nu}\Psi_1
\end{aligned} \tag{B.5}$$

B.2 An Explicit Matching Example – $\mathcal{O}^{(9)}_{duLLH^2D}$

Here we will perform an explicit SMEFT-to- LEFT matching calculation to provide an example of the general procedure. A prime example is provided by the matching of the SMEFT dimension-9 operator $\mathcal{O}^{(9)}_{duLLH^2D}$ to the relevant LEFT basis for $0\nu\beta\beta$. This specific example maps onto both long- and short-range operators of dimensions $6, 7$, and

9 and includes all relevant steps such as field redefinitions, integration by parts, and integrating out heavy fields.

The operator is given by

$$\mathcal{O}_{duLLH^2D} = C_{duLLH^2D}\epsilon_{ik}\epsilon_{jl}\left[\overline{d_R}\gamma^\mu u_R\right]\left[\overline{L^C}_i\left(iD_\mu L\right)_j\right]\tilde{H}_k H_l.$$

After EWSB the Higgs has gained its non-zero vev. Switching to the unitary gauge we can write

$$H = \frac{1}{\sqrt{2}}\begin{pmatrix}0\\ v+h\end{pmatrix}, \qquad \tilde{H} = i\tau_2 H^* = \frac{1}{\sqrt{2}}\begin{pmatrix}v+h\\ 0\end{pmatrix}, \tag{B.6}$$

fixing the $SU(2)$ indices to $k = 0, l = 1$. Because we are only interested in charged-current processes, we do not need to consider the physical Higgs boson h or the neutral gauge bosons W^3 and B such that the covariant derivative is simply given by

$$\mathcal{D}_\mu L = \begin{pmatrix}\partial_\mu\nu_L - i\frac{g_2}{2}\sqrt{2}W^+_\mu e_L\\ \partial_\mu e_\alpha - i\frac{g_2}{2}\sqrt{2}W^-\nu_\alpha\end{pmatrix} + \mathcal{O}(W^3_\mu, B_\mu). \tag{B.7}$$

The relevant parts of the operator can now be written as

$$\mathcal{O}_{duLLH^2D} = -\frac{v^2}{2}C_{duLLH^2D}\left[\overline{d_R}\gamma^\mu u_R\right]\left[\overline{e^C_L}\left(i\partial_\mu\nu_L + \frac{g_2}{\sqrt{2}}e_L W^+_\mu\right)\right] + \mathcal{O}(W^3, B, h, ...), \tag{B.8}$$

and we will drop the irrelevant parts $\mathcal{O}(...)$ from here on, completely. Next, we notice that the quark current in $\mathcal{O}_{duLLH^2D}$ is a hermitian conjugate of the currents appearing in the LEFT basis (c.f. Tables 4.4 and 4.5) and we should correct this difference by taking the hermitian conjugate

$$\begin{aligned}\mathcal{O}^\dagger_{duLLH^2D} &= \frac{v^2}{2}C^\dagger_{duLLH^2D}\left[\overline{u_R}\gamma^\mu d_R\right]\left(\left[i\partial_\mu\overline{\nu_L}e^C_L - \frac{g_2}{\sqrt{2}}\overline{e_L}e^C_L W^-_\mu\right)\right]\\ &= \frac{v^2}{2}C^\dagger_{duLLH^2D}\left[\overline{u_R}\gamma^\mu d_R\right]\left(\left[\overline{e_L}i\partial_\mu\nu^C_L - \frac{g_2}{\sqrt{2}}\overline{e_L}e^C_L W^-_\mu\right)\right].\end{aligned} \tag{B.9}$$

We are now left with two different terms. Let's focus on the first one as it does not include any heavy fields. Therefore, we are left with the task of transforming it into the correct operator basis utilizing our tool-set of field redefinitions, integration by part (IBP), and general algebra.

First, we notice that the LEFT dimension 7 operators do only involve derivatives of the type $\overleftrightarrow{\partial}$ acting both on the left and right. Let us separate the lepton bilinear into two equal terms

$$\begin{aligned}&\frac{v^2}{2}C^\dagger_{duLLH^2D}\left[\overline{u_R}\gamma^\mu d_R\right]\left[\overline{e_L}i\partial_\mu\nu^C_L\right]\\ =&\frac{v^2}{2}C^\dagger_{duLLH^2D}\left[\overline{u_R}\gamma^\mu d_R\right]\frac{1}{2}\left(\left[\overline{e_L}i\partial_\mu\nu^C_L\right] + \left[\overline{e_L}i\partial_\mu\nu^C_L\right]\right),\end{aligned} \tag{B.10}$$

and perform an IBP on the second lepton bilinear

$$\begin{aligned}
&\frac{v^2}{4}C^{\dagger}_{duLLH^2D}\left[\overline{u_R}\gamma^{\mu}d_R\right]\left(\left[\overline{e_L}i\partial_{\mu}\nu_L^C\right]+\left[\overline{e_L}i\partial_{\mu}\nu_L^C\right]\right)\\
=&\frac{v^2}{4}C^{\dagger}_{duLLH^2D}\Bigg(\left[\overline{u_R}\gamma^{\mu}d_R\right]\left[\overline{e_L}i\overleftrightarrow{\partial}_{\mu}\nu_L^C\right]+\left[\overline{d_R^C}i\partial\!\!\!/ u_R^C\right]\left[\overline{e_L}\nu_L^C\right]-\left[\overline{u_R}i\partial\!\!\!/ d_R\right]\left[\overline{e_L}\nu_L^C\right]\Bigg). \quad \text{(B.11)}
\end{aligned}$$

This provides us with the correct expression for the LEFT operator $\mathcal{O}^{(7)}_{VR}$. However, on the way we also generated two terms that involve derivatives acting on quark fields $\partial\!\!\!/ d_R$ and $\partial\!\!\!/ u_R^C$. By performing appropriate field redefinitions of u_R and d_R we can get rid of these derivatives and write

$$\begin{aligned}
&\frac{v^2}{4}C^{\dagger}_{duLLH^2D}\Bigg(\left[\overline{u_R}\gamma^{\mu}d_R\right]\left[\overline{e_L}i\overleftrightarrow{\partial}_{\mu}\nu_L^C\right]+\left[\overline{d_R^C}m_u u_L^C\right]\left[\overline{e_L}\nu_L^C\right]-\left[\overline{u_R}m_d d_L\right]\left[\overline{e_L}\nu_L^C\right]\Bigg)\\
=&\frac{v^2}{4}C^{\dagger}_{duLLH^2D}\Bigg(\left[\overline{u_R}\gamma^{\mu}d_R\right]\left[\overline{e_L}i\overleftrightarrow{\partial}\nu_L^C\right]+m_u\left[\overline{u_L}d_R\right]\left[\overline{e_L}\nu_L^C\right]-m_d\left[\overline{u_R}d_L\right]\left[\overline{e_L}\nu_L^C\right]\Bigg), \quad \text{(B.12)}
\end{aligned}$$

where we dropped higher order contributions that arise from the field redefinitions but do not contribute to $0\nu\beta\beta$. Hence, we identify contributions from the first term to the LEFT operators $\mathcal{O}^{(6)}_{SL}, \mathcal{O}^{(6)}_{SR}$ and $\mathcal{O}^{(6)}_{VR}$.

The remaining second term can be matched by integrating out the W-boson. At tree-level this is simply done by solving the equations of motion for W (c.f. Chapter 3) giving

$$\begin{aligned}
&-\frac{v^2 g_2}{2\sqrt{2}}C^{\dagger}_{duLLH^2D}\left[\overline{u_R}\gamma^{\mu}d_R\right]\left[\overline{e_L}e_L^C\right]W^-_{\mu}\\
=&\frac{v^2 g_2^2 V_{ud}}{4m_W^2}C^{\dagger}_{duLLH^2D}\left[\overline{u_R}\gamma^{\mu}d_R\right]\left[\overline{e_L}e_L^C\right]\left[\overline{u_L}\gamma_{\mu}d_L\right]\\
=&V_{ud}C^{\dagger}_{duLLH^2D}\left[\overline{u_R}\gamma^{\mu}d_R\right]\left[\overline{e_L}e_L^C\right]\left[\overline{u_L}\gamma_{\mu}d_L\right]. \quad \text{(B.13)}
\end{aligned}$$

Finally, we can combine both terms to find the contributions to the correct LEFT operators

$$\begin{aligned}
&C^{(6)}_{SL}=-\frac{m_d v^4}{4}C^{\dagger}_{duLLH^2D}, \qquad C^{(6)}_{SR}=\frac{m_u v^4}{4}C^{\dagger}_{duLLH^2D}, \qquad C^{(7)}_{VR}=\frac{v^5}{4}C^{\dagger}_{duLLH^2D},\\
&C^{(9)}_{4L}=v^5 V_{ud}C^{\dagger}_{duLLH^2D}. \quad \text{(B.14)}
\end{aligned}$$

B.3 Chiral Power Counting and Matching onto $\mathcal{O}^{(7)}_{VL2,VR2}$

In our main text analysis, we did not include the LEFT operators $\mathcal{O}^{(7)}_{VL2,VR2}$. Here, we want to provide the reasoning for this:

When calculating the SMEFT-to-LEFT matching relations for the SMEFT dimension-9 operator $\mathcal{O}_{deQLH^2D}$, one finds the following matching contributions

$$\begin{aligned}
C_T^{(6)} &= \frac{v^4 m_e}{16} C^\dagger_{deQLH^2D}, \qquad C_{SR}^{(6)} = \frac{v^4 m_e}{8} C^\dagger_{deQLH^2D}, \qquad C_{VL}^{(6)} = -\frac{v^4 m_d}{4} C^\dagger_{deQLH^2D},\\
C_{VR}^{(6)} &= -\frac{v^4 m_u}{4} C^\dagger_{deQLH^2D}, \qquad C_{VR2}^{(7)} = -i\frac{v^5}{4} C^\dagger_{deQLH^2D},\\
C_6^{(9)} &= -\frac{5}{12} v^5 V_{ud} C^\dagger_{deQLH^2D}, \qquad C_7^{(9)} = -V_{ud} v^5 C^\dagger_{deQLH^2D}.
\end{aligned} \tag{B.15}$$

However this is the only matching contribution to any of the two operators $\mathcal{O}^{(7)}_{VL2,VR2}$ and we may therefore disregard the left-handed operator $\mathcal{O}^{(7)}_{VL2}$ already. In order to estimate the relevance of the remaining operator $\mathcal{O}^{(7)}_{VR2}$ we need to map it onto χPT via the external field framework. To achieve this and map it onto the external sources $l_\mu, r_\mu, s, p, t_{\mu\nu}$, we need to get rid of the partial derivative acting on the quark fields. The simplest way to do this is to apply a generalized version of the Gordon decomposition given by

$$\overline{\Psi}_i \gamma^\mu \Psi_j = \frac{1}{m}\left[\overline{\Psi}_i \overset{\leftrightarrow}{\partial}_\mu \Psi_j + \partial_\nu \left(\overline{\Psi}_i \sigma^{\mu\nu}\Psi_j\right)\right], \qquad m = m_i + m_j, \tag{B.16}$$

which is easily derived from the Dirac equations of the two fermions Ψ_{ij}

$$\overline{\Psi}_i \left(i\gamma^\mu \overset{\leftarrow}{\partial}_\mu + m_i\right) = 0, \qquad \left(i\gamma^\mu \partial_\mu - m_j\right)\Psi_j = 0. \tag{B.17}$$

Thus we find contributions to three different external sources

$$\begin{aligned}
l_\mu &= \frac{1}{v^3}\tau^+ C^{(7)}_{VR2} m_d \left[\overline{e_R}\gamma_\mu \nu_L^C\right],\\
r_\mu &= \frac{1}{v^3}\tau^+ C^{(7)}_{VR2} m_u \left[\overline{e_R}\gamma_\mu \nu_L^C\right],\\
t_R^{\mu\nu} &= \frac{1}{v^3}\tau^+ C^{(7)}_{VR2}\left(\left[\partial^\nu \overline{e_R}\gamma^\mu \nu_L^C\right] + \left[\overline{e_R}\gamma^\mu \partial^\nu \nu_L^C\right]\right).
\end{aligned} \tag{B.18}$$

The first two terms, entering via l_μ, r_μ, simply give the same contribution as the dimension-6 vector operators $\mathcal{O}^{(6)}_{VL,VR}$ but with an additional suppression of ϵ_χ^2 due to the small quark masses. The last term, entering via the tensor field $t_R^{\mu\nu}$, only contributes with the NLO parts of the nuclear currents $J_T^{\mu\nu}, J_V^\mu, J_A^\mu$ to the relevant $0^+ \to 0^+$ transition amplitude, with each nuclear current providing a suppression proportional to ϵ_χ. Additionally, we find a suppression of ϵ_χ^2 stemming from the neutrino momentum in the propagator and the derivative acting on ν. The contributions proportional to the electron momenta $k \sim \epsilon_\chi^3 \Lambda_\chi$ via the partial derivative acting on $\overline{e_R}$ are similarly suppressed.

In total, the leading contribution of the operator $\mathcal{O}^{(7)}_{VL2}$ is, therefore, at ϵ_χ^4 and we may ignore it in comparison to the remaining LEFT operators which enter either via the Majorana neutrino mass, which is small but of great phenomenological relevance, or at ϵ_χ^2[1]. In fact, a self-consistent treatment including the operator $\mathcal{O}^{(7)}_{VL2}$ would require the inclusion of χPT terms up to NNLO.

[1]Except for the right-handed vector operator $\mathcal{O}^{(6)}_{VR}$ which contributes at ϵ_χ^3 and, strictly speaking,

requires a treatment up to NNLO. However, it is included due to its phenomenological relevance in connection to left-right symmetric models or other popular scenarios with right-handed vector interactions.

Bibliography

[1] L. Gráf, M. Lindner, and O. Scholer, "Unraveling the $0\nu\beta\beta$ decay mechanisms," *Phys. Rev. D* **106** no. 3, (2022) 035022, arXiv:2204.10845 [hep-ph].

[2] O. Scholer, J. de Vries, and L. Gráf, "νDoBe — A Python tool for neutrinoless double beta decay," *JHEP* **08** (2023) 043, arXiv:2304.05415 [hep-ph].

[3] L. Gráf, S. Jana, O. Scholer, and N. Volmer, "Neutrinoless Double Beta Decay without Vacuum Majorana Neutrino Mass," arXiv:2312.15016 [hep-ph].

[4] L. Gráf, O. Scholer, M. Sen, and N. Volmer, "To be published,".

[5] L. Gráf and O. Scholer, "To be published,".

[6] **Super-Kamiokande** Collaboration, Y. Fukuda *et al.*, "Evidence for oscillation of atmospheric neutrinos," *Phys. Rev. Lett.* **81** (1998) 1562–1567, arXiv:hep-ex/9807003.

[7] **SNO** Collaboration, Q. R. Ahmad *et al.*, "Measurement of the rate of $\nu_e + d \to p + p + e^-$ interactions produced by ^{8}B solar neutrinos at the Sudbury Neutrino Observatory," *Phys. Rev. Lett.* **87** (2001) 071301, arXiv:nucl-ex/0106015.

[8] **KamLAND** Collaboration, K. Eguchi *et al.*, "First results from KamLAND: Evidence for reactor anti-neutrino disappearance," *Phys. Rev. Lett.* **90** (2003) 021802, arXiv:hep-ex/0212021.

[9] **LSND** Collaboration, A. Aguilar *et al.*, "Evidence for neutrino oscillations from the observation of $\bar{\nu}_e$ appearance in a $\bar{\nu}_\mu$ beam," *Phys. Rev. D* **64** (2001) 112007, arXiv:hep-ex/0104049.

[10] E. K. Akhmedov, "Neutrino physics," in *ICTP Summer School in Particle Physics*, pp. 103–164. 6, 1999. arXiv:hep-ph/0001264.

[11] C. Giunti and C. W. Kim, *Fundamentals of Neutrino Physics and Astrophysics*. 2007.

[12] S. L. Glashow, "Partial Symmetries of Weak Interactions," *Nucl. Phys.* **22** (1961) 579–588.

[13] S. Weinberg, "A Model of Leptons," *Phys. Rev. Lett.* **19** (1967) 1264–1266.

[14] A. Salam, "Weak and Electromagnetic Interactions," *Conf. Proc. C* **680519** (1968) 367–377.

[15] M. Gell-Mann, P. Ramond, and R. Slansky, "Complex Spinors and Unified Theories," *Conf. Proc. C* **790927** (1979) 315–321, `arXiv:1306.4669 [hep-th]`.

[16] R. N. Mohapatra and G. Senjanovic, "Neutrino Mass and Spontaneous Parity Nonconservation," *Phys. Rev. Lett.* **44** (1980) 912.

[17] R. N. Mohapatra and G. Senjanovic, "Neutrino Masses and Mixings in Gauge Models with Spontaneous Parity Violation," *Phys. Rev. D* **23** (1981) 165.

[18] M. Magg and C. Wetterich, "Neutrino Mass Problem and Gauge Hierarchy," *Phys. Lett. B* **94** (1980) 61–64.

[19] R. Foot, H. Lew, X. G. He, and G. C. Joshi, "Seesaw Neutrino Masses Induced by a Triplet of Leptons," *Z. Phys. C* **44** (1989) 441.

[20] T. P. Cheng and L.-F. Li, "Neutrino Masses, Mixings and Oscillations in SU(2) x U(1) Models of Electroweak Interactions," *Phys. Rev. D* **22** (1980) 2860.

[21] S. Davidson, E. Nardi, and Y. Nir, "Leptogenesis," *Phys. Rept.* **466** (2008) 105–177, `arXiv:0802.2962 [hep-ph]`.

[22] W. C. Haxton and G. J. Stephenson, "Double beta Decay," *Prog. Part. Nucl. Phys.* **12** (1984) 409–479.

[23] T. Tomoda, "Double beta decay," *Rept. Prog. Phys.* **54** (1991) 53–126.

[24] W. Rodejohann, "Neutrino-less Double Beta Decay and Particle Physics," *Int. J. Mod. Phys. E* **20** (2011) 1833–1930, `arXiv:1106.1334 [hep-ph]`.

[25] F. F. Deppisch, M. Hirsch, and H. Pas, "Neutrinoless Double Beta Decay and Physics Beyond the Standard Model," *J. Phys. G* **39** (2012) 124007, `arXiv:1208.0727 [hep-ph]`.

[26] H. Päs and W. Rodejohann, "Neutrinoless Double Beta Decay," *New J. Phys.* **17** no. 11, (2015) 115010, `arXiv:1507.00170 [hep-ph]`.

[27] M. J. Dolinski, A. W. P. Poon, and W. Rodejohann, "Neutrinoless Double-Beta Decay: Status and Prospects," *Ann. Rev. Nucl. Part. Sci.* **69** (2019) 219–251, `arXiv:1902.04097 [nucl-ex]`.

[28] M. Agostini, G. Benato, J. A. Detwiler, J. Menéndez, and F. Vissani, "Toward the discovery of matter creation with neutrinoless $\beta\beta$ decay," *Rev. Mod. Phys.* **95** no. 2, (2023) 025002, `arXiv:2202.01787 [hep-ex]`.

[29] V. Cirigliano *et al.*, "Neutrinoless Double-Beta Decay: A Roadmap for Matching Theory to Experiment," `arXiv:2203.12169 [hep-ph]`.

[30] K. Fridell, L. Gráf, J. Harz, and C. Hati, "Probing lepton number violation: a comprehensive survey of dimension-7 SMEFT," *JHEP* **05** (2024) 154, `arXiv:2306.08709 [hep-ph]`.

[31] H. V. Klapdor-Kleingrothaus, A. Dietz, H. L. Harney, and I. V. Krivosheina, "Evidence for neutrinoless double beta decay," *Mod. Phys. Lett. A* **16** (2001) 2409–2420, `arXiv:hep-ph/0201231`.

[32] H. V. Klapdor-Kleingrothaus, I. V. Krivosheina, A. Dietz, and O. Chkvorets, "Search for neutrinoless double beta decay with enriched Ge-76 in Gran Sasso 1990-2003," *Phys. Lett. B* **586** (2004) 198–212, `arXiv:hep-ph/0404088`.

[33] **GERDA** Collaboration, M. Agostini *et al.*, "Final Results of GERDA on the Search for Neutrinoless Double-β Decay," *Phys. Rev. Lett.* **125** no. 25, (2020) 252502, `arXiv:2009.06079 [nucl-ex]`.

[34] **nEXO** Collaboration, G. Adhikari *et al.*, "nEXO: neutrinoless double beta decay search beyond 10^{28} year half-life sensitivity," *J. Phys. G* **49** no. 1, (2022) 015104, `arXiv:2106.16243 [nucl-ex]`.

[35] **LEGEND** Collaboration, N. Abgrall *et al.*, "The Large Enriched Germanium Experiment for Neutrinoless $\beta\beta$ Decay: LEGEND-1000 Preconceptual Design Report," `arXiv:2107.11462 [physics.ins-det]`.

[36] **CUPID** Collaboration, A. Armatol *et al.*, "Toward CUPID-1T," `arXiv:2203.08386 [nucl-ex]`.

[37] **CUPID** Collaboration, K. Alfonso *et al.*, "CUPID: The Next-Generation Neutrinoless Double Beta Decay Experiment," *J. Low Temp. Phys.* **211** no. 5-6, (2023) 375–383.

[38] **SNO+** Collaboration, V. Albanese *et al.*, "The SNO+ experiment," *JINST* **16** no. 08, (2021) P08059, `arXiv:2104.11687 [physics.ins-det]`.

[39] J. Schechter and J. W. F. Valle, "Neutrinoless Double beta Decay in SU(2) x U(1) Theories," *Phys. Rev. D* **25** (1982) 2951.

[40] E. Takasugi, "Can the Neutrinoless Double Beta Decay Take Place in the Case of Dirac Neutrinos?," *Phys. Lett. B* **149** (1984) 372–376.

[41] A. V. Manohar, "Effective field theories," *Lect. Notes Phys.* **479** (1997) 311–362, arXiv:hep-ph/9606222.

[42] A. V. Manohar, "Introduction to Effective Field Theories," arXiv:1804.05863 [hep-ph].

[43] R. Penco, "An Introduction to Effective Field Theories," arXiv:2006.16285 [hep-th].

[44] V. Cirigliano, W. Dekens, J. de Vries, M. L. Graesser, and E. Mereghetti, "Neutrinoless double beta decay in chiral effective field theory: lepton number violation at dimension seven," *JHEP* **12** (2017) 082, arXiv:1708.09390 [hep-ph].

[45] V. Cirigliano, W. Dekens, J. de Vries, M. L. Graesser, and E. Mereghetti, "A neutrinoless double beta decay master formula from effective field theory," *JHEP* **12** (2018) 097, arXiv:1806.02780 [hep-ph].

[46] **KamLAND-Zen** Collaboration, S. Abe *et al.*, "Search for Majorana Neutrinos with the Complete KamLAND-Zen Dataset," arXiv:2406.11438 [hep-ex].

[47] J. C. Pati and A. Salam, "Lepton Number as the Fourth Color," *Phys. Rev. D* **10** (1974) 275–289. [Erratum: Phys.Rev.D 11, 703–703 (1975)].

[48] R. N. Mohapatra and J. C. Pati, "A Natural Left-Right Symmetry," *Phys. Rev. D* **11** (1975) 2558.

[49] G. Senjanovic and R. N. Mohapatra, "Exact Left-Right Symmetry and Spontaneous Violation of Parity," *Phys. Rev. D* **12** (1975) 1502.

[50] P. Duka, J. Gluza, and M. Zralek, "Quantization and renormalization of the manifest left-right symmetric model of electroweak interactions," *Annals Phys.* **280** (2000) 336–408, arXiv:hep-ph/9910279.

[51] W. Pauli, "Dear radioactive ladies and gentlemen," *Phys. Today* **31N9** (1978) 27.

[52] J. Chadwick, "Possible Existence of a Neutron," *Nature* **129** (1932) 312.

[53] F. Reines and C. L. Cowan, "Detection of the free neutrino," *Phys. Rev.* **92** (1953) 830–831.

[54] C. L. Cowan, F. Reines, F. B. Harrison, H. W. Kruse, and A. D. McGuire, "Detection of the free neutrino: A Confirmation," *Science* **124** (1956) 103–104.

[55] S. M. Bilenky, "Neutrino. History of a unique particle," *Eur. Phys. J. H* **38** (2013) 345–404, arXiv:1210.3065 [hep-ph].

[56] H. Fritzsch, M. Gell-Mann, and H. Leutwyler, "Advantages of the Color Octet Gluon Picture," *Phys. Lett. B* **47** (1973) 365–368.

[57] F. Gross *et al.*, "50 Years of Quantum Chromodynamics," *Eur. Phys. J. C* **83** (2023) 1125, `arXiv:2212.11107 [hep-ph]`.

[58] P. Langacker, "Structure of the standard model," *Adv. Ser. Direct. High Energy Phys.* **14** (1995) 15–36, `arXiv:hep-ph/0304186`.

[59] Y. Liao and X.-D. Ma, "An explicit construction of the dimension-9 operator basis in the standard model effective field theory," *JHEP* **11** (2020) 152, `arXiv:2007.08125 [hep-ph]`.

[60] P. W. Higgs, "Broken symmetries, massless particles and gauge fields," *Phys. Lett.* **12** (1964) 132–133.

[61] P. W. Higgs, "Broken Symmetries and the Masses of Gauge Bosons," *Phys. Rev. Lett.* **13** (1964) 508–509.

[62] P. W. Higgs, "Spontaneous Symmetry Breakdown without Massless Bosons," *Phys. Rev.* **145** (1966) 1156–1163.

[63] F. Englert and R. Brout, "Broken Symmetry and the Mass of Gauge Vector Mesons," *Phys. Rev. Lett.* **13** (1964) 321–323.

[64] G. S. Guralnik, C. R. Hagen, and T. W. B. Kibble, "Global Conservation Laws and Massless Particles," *Phys. Rev. Lett.* **13** (1964) 585–587.

[65] M. Beuthe, "Oscillations of neutrinos and mesons in quantum field theory," *Phys. Rept.* **375** (2003) 105–218, `arXiv:hep-ph/0109119`.

[66] M. Beuthe, "Towards a unique formula for neutrino oscillations in vacuum," *Phys. Rev. D* **66** (2002) 013003, `arXiv:hep-ph/0202068`.

[67] E. K. Akhmedov and J. Kopp, "Neutrino Oscillations: Quantum Mechanics vs. Quantum Field Theory," *JHEP* **04** (2010) 008, `arXiv:1001.4815 [hep-ph]`. [Erratum: JHEP 10, 052 (2013)].

[68] L. Wolfenstein, "Neutrino Oscillations in Matter," *Phys. Rev. D* **17** (1978) 2369–2374.

[69] S. P. Mikheyev and A. Y. Smirnov, "Resonance Amplification of Oscillations in Matter and Spectroscopy of Solar Neutrinos," *Sov. J. Nucl. Phys.* **42** (1985) 913–917.

[70] S. P. Mikheev and A. Y. Smirnov, "Resonant amplification of neutrino oscillations in matter and solar neutrino spectroscopy," *Nuovo Cim. C* **9** (1986) 17–26.

[71] M. Maltoni and A. Y. Smirnov, "Solar neutrinos and neutrino physics," *Eur. Phys. J. A* **52** no. 4, (2016) 87, `arXiv:1507.05287 [hep-ph]`.

[72] M. Sen and A. Y. Smirnov, "Refractive neutrino masses, ultralight dark matter and cosmology," *JCAP* **01** (2024) 040, arXiv:2306.15718 [hep-ph].

[73] V. A. Kuzmin, V. A. Rubakov, and M. E. Shaposhnikov, "On the Anomalous Electroweak Baryon Number Nonconservation in the Early Universe," *Phys. Lett. B* **155** (1985) 36.

[74] V. A. Rubakov and M. E. Shaposhnikov, "Electroweak baryon number nonconservation in the early universe and in high-energy collisions," *Usp. Fiz. Nauk* **166** (1996) 493–537, arXiv:hep-ph/9603208.

[75] M. D. Schwartz, *Quantum Field Theory and the Standard Model*. Cambridge University Press, 3, 2014.

[76] S. Weinberg, "Effective Field Theory, Past and Future," *PoS* **CD09** (2009) 001, arXiv:0908.1964 [hep-th].

[77] S. Weinberg, "Phenomenological Lagrangians," *Physica A* **96** no. 1-2, (1979) 327–340.

[78] J. Gasser and H. Leutwyler, "Chiral Perturbation Theory to One Loop," *Annals Phys.* **158** (1984) 142.

[79] S. Floerchinger, "Lectures on quantum field theory 1," 2024. https://www.tpi.uni-jena.de/~floerchinger/assets/pdfs/QuantumFieldTheory1.pdf.

[80] S. Floerchinger, "Lectures on quantum field theory 2," 2023. https://www.tpi.uni-jena.de/~floerchinger/assets/pdfs/QuantumFieldTheory2.pdf.

[81] B. Grzadkowski, M. Iskrzynski, M. Misiak, and J. Rosiek, "Dimension-Six Terms in the Standard Model Lagrangian," *JHEP* **10** (2010) 085, arXiv:1008.4884 [hep-ph].

[82] E. E. Jenkins, A. V. Manohar, and M. Trott, "Renormalization Group Evolution of the Standard Model Dimension Six Operators I: Formalism and lambda Dependence," *JHEP* **10** (2013) 087, arXiv:1308.2627 [hep-ph].

[83] E. E. Jenkins, A. V. Manohar, and M. Trott, "Renormalization Group Evolution of the Standard Model Dimension Six Operators II: Yukawa Dependence," *JHEP* **01** (2014) 035, arXiv:1310.4838 [hep-ph].

[84] R. Alonso, E. E. Jenkins, A. V. Manohar, and M. Trott, "Renormalization Group Evolution of the Standard Model Dimension Six Operators III: Gauge Coupling Dependence and Phenomenology," *JHEP* **04** (2014) 159, arXiv:1312.2014 [hep-ph].

[85] L. Lehman, "Extending the Standard Model Effective Field Theory with the Complete Set of Dimension-7 Operators," *Phys. Rev. D* **90** no. 12, (2014) 125023, arXiv:1410.4193 [hep-ph].

[86] I. Brivio and M. Trott, "The Standard Model as an Effective Field Theory," *Phys. Rept.* **793** (2019) 1–98, `arXiv:1706.08945 [hep-ph]`.

[87] Y. Liao and X.-D. Ma, "Renormalization Group Evolution of Dimension-seven Operators in Standard Model Effective Field Theory and Relevant Phenomenology," *JHEP* **03** (2019) 179, `arXiv:1901.10302 [hep-ph]`.

[88] H.-L. Li, Z. Ren, M.-L. Xiao, J.-H. Yu, and Y.-H. Zheng, "Complete set of dimension-nine operators in the standard model effective field theory," *Phys. Rev. D* **104** no. 1, (2021) 015025, `arXiv:2007.07899 [hep-ph]`.

[89] E. E. Jenkins, A. V. Manohar, and P. Stoffer, "Low-Energy Effective Field Theory below the Electroweak Scale: Operators and Matching," *JHEP* **03** (2018) 016, `arXiv:1709.04486 [hep-ph]`. [Erratum: JHEP 12, 043 (2023)].

[90] E. E. Jenkins, A. V. Manohar, and P. Stoffer, "Low-Energy Effective Field Theory below the Electroweak Scale: Anomalous Dimensions," *JHEP* **01** (2018) 084, `arXiv:1711.05270 [hep-ph]`. [Erratum: JHEP 12, 042 (2023)].

[91] Y. Liao, X.-D. Ma, and Q.-Y. Wang, "Extending low energy effective field theory with a complete set of dimension-7 operators," *JHEP* **08** (2020) 162, `arXiv:2005.08013 [hep-ph]`.

[92] S. Weinberg, "Effective chiral Lagrangians for nucleon - pion interactions and nuclear forces," *Nucl. Phys. B* **363** (1991) 3–18.

[93] O. Scholer, "On Distinguishing Different $0\nu\beta\beta$ Mechanisms," Master's thesis, U. Heidelberg, ITP, 2020.

[94] E. Fermi, "An attempt of a theory of beta radiation. 1.," *Z. Phys.* **88** (1934) 161–177.

[95] M. Goeppert-Mayer, "Double beta-disintegration," *Phys. Rev.* **48** (1935) 512–516.

[96] W. H. Furry, "On transition probabilities in double beta-disintegration," *Phys. Rev.* **56** (1939) 1184–1193.

[97] M. G. Inghram and J. H. Reynolds, "Double beta-decay of Te-130," *Phys. Rev.* **78** (1950) 822–823.

[98] T. Bernatowicz, J. Brannon, R. Brazzle, R. Cowsik, C. Hohenberg, and F. Podosek, "Neutrino mass limits for a precise determination of beta-beta decay rates of Te-128 and Te-130," *Phys. Rev. Lett.* **69** (1992) 2341–2344.

[99] H. V. Thomas, R. A. D. Pattrick, S. A. Crowther, D. J. Blagburn, and J. D. Gilmour, "Geochemical constraints on the half-life of ^{130}Te," *Phys. Rev. C* **78** (Nov, 2008) 054606. `https://link.aps.org/doi/10.1103/PhysRevC.78.054606`.

[100] C. F. V. Weizsacker, "Zur Theorie der Kernmassen," *Z. Phys.* **96** (1935) 431–458.

[101] H. A. Bethe and R. F. Bacher, "Nuclear Physics A. Stationary States of Nuclei," *Rev. Mod. Phys.* **8** (1936) 82–229.

[102] E. Majorana, "Teoria simmetrica dell'elettrone e del positrone," *Nuovo Cim.* **14** (1937) 171–184.

[103] J. Kotila and F. Iachello, "Phase space factors for double-β decay," *Phys. Rev. C* **85** (2012) 034316, `arXiv:1209.5722 [nucl-th]`.

[104] **NEMO-3** Collaboration, R. Arnold *et al.*, "Measurement of the double-beta decay half-life and search for the neutrinoless double-beta decay of ^{48}Ca with the NEMO-3 detector," *Phys. Rev. D* **93** no. 11, (2016) 112008, `arXiv:1604.01710 [hep-ex]`.

[105] S. Umehara *et al.*, "Neutrino-less double-beta decay of Ca-48 studied by Ca F(2)(Eu) scintillators," *Phys. Rev. C* **78** (2008) 058501, `arXiv:0810.4746 [nucl-ex]`.

[106] P. Belli, R. Bernabei, F. Cappella, R. Cerulli, F. A. Danevich, S. d'Angelo, A. Incicchitti, V. V. Kobychev, D. V. Poda, and V. I. Tretyak, "Final results of an experiment to search for 2beta processes in zinc and tungsten with the help of radiopure $ZnWO_4$ crystal scintillators," *J. Phys. G* **38** (2011) 115107, `arXiv:1110.3923 [nucl-ex]`.

[107] O. Azzolini *et al.*, "Search for neutrinoless double beta decay of ^{64}Zn and ^{70}Zn with CUPID-0," *Eur. Phys. J. C* **80** no. 8, (2020) 702, `arXiv:2003.10840 [nucl-ex]`.

[108] **GERDA, (GERDA Collaboration)*** Collaboration, M. Agostini *et al.*, "Final Results of GERDA on the Two-Neutrino Double-β Decay Half-Life of Ge76," *Phys. Rev. Lett.* **131** no. 14, (2023) 142501, `arXiv:2308.09795 [nucl-ex]`.

[109] **CUPID** Collaboration, O. Azzolini *et al.*, "Measurement of the $2\nu\beta\beta$ Decay Half-Life of Se82 with the Global CUPID-0 Background Model," *Phys. Rev. Lett.* **131** no. 22, (2023) 222501, `arXiv:2306.14654 [nucl-ex]`.

[110] **CUPID** Collaboration, O. Azzolini *et al.*, "Final Result on the Neutrinoless Double Beta Decay of ^{82}Se with CUPID-0," *Phys. Rev. Lett.* **129** no. 11, (2022) 111801, `arXiv:2206.05130 [hep-ex]`.

[111] **NEMO-3** Collaboration, J. Argyriades *et al.*, "Measurement of the two neutrino double beta decay half-life of Zr-96 with the NEMO-3 detector," *Nucl. Phys. A* **847** (2010) 168–179, `arXiv:0906.2694 [nucl-ex]`.

[112] **CUPID-Mo** Collaboration, C. Augier *et al.*, "Measurement of the $2\nu\beta\beta$ Decay Rate and Spectral Shape of Mo100 from the CUPID-Mo Experiment," *Phys. Rev. Lett.* **131** no. 16, (2023) 162501, `arXiv:2307.14086 [nucl-ex]`.

[113] C. Augier *et al.*, "Final results on the $0\nu\beta\beta$ decay half-life limit of ^{100}Mo from the CUPID-Mo experiment," *Eur. Phys. J. C* **82** no. 11, (2022) 1033, `arXiv:2202.08716 [nucl-ex]`.

[114] P. Belli *et al.*, "Search for double-beta decay processes in Cd-108 and Cd-114 with the help of the low-background CdWO-4 crystal scintillator," *Eur. Phys. J. A* **36** (2008) 167–170.

[115] J. Ebert *et al.*, "Results of a search for neutrinoless double- β decay using the COBRA demonstrator," *Phys. Rev. C* **94** no. 2, (2016) 024603, `arXiv:1509.04113 [nucl-ex]`.

[116] A. S. Barabash *et al.*, "Final results of the Aurora experiment to study 2β decay of ^{116}Cd with enriched ^{116}CdWO$_4$ crystal scintillators," *Phys. Rev. D* **98** no. 9, (2018) 092007, `arXiv:1811.06398 [nucl-ex]`.

[117] **CUORE** Collaboration, D. Q. Adams *et al.*, "New Direct Limit on Neutrinoless Double Beta Decay Half-Life of Te128 with CUORE," *Phys. Rev. Lett.* **129** no. 22, (2022) 222501, `arXiv:2205.03132 [nucl-ex]`.

[118] **CUORE** Collaboration, D. Q. Adams *et al.*, "Measurement of the $2\nu\beta\beta$ Decay Half-Life of ^{130}Te with CUORE," *Phys. Rev. Lett.* **126** no. 17, (2021) 171801, `arXiv:2012.11749 [nucl-ex]`.

[119] **CUORE** Collaboration, D. Q. Adams *et al.*, "Improved Limit on Neutrinoless Double-Beta Decay in ^{130}Te with CUORE," *Phys. Rev. Lett.* **124** no. 12, (2020) 122501, `arXiv:1912.10966 [nucl-ex]`.

[120] **PandaX** Collaboration, X. Yan *et al.*, "Searching for Two-Neutrino and Neutrinoless Double Beta Decay of Xe134 with the PandaX-4T Experiment," *Phys. Rev. Lett.* **132** no. 15, (2024) 152502, `arXiv:2312.15632 [nucl-ex]`.

[121] **KamLAND-Zen** Collaboration, A. Gando *et al.*, "Search for Majorana Neutrinos near the Inverted Mass Hierarchy Region with KamLAND-Zen," *Phys. Rev. Lett.* **117** no. 8, (2016) 082503, `arXiv:1605.02889 [hep-ex]`. [Addendum: Phys.Rev.Lett. 117, 109903 (2016)].

[122] **NEMO-3** Collaboration, R. Arnold *et al.*, "Measurement of the $2\nu\beta\beta$ decay half-life of ^{150}Nd and a search for $0\nu\beta\beta$ decay processes with the full exposure from the NEMO-3 detector," *Phys. Rev. D* **94** no. 7, (2016) 072003, `arXiv:1606.08494 [hep-ex]`.

[123] F. A. Danevich, V. V. Kobychev, O. A. Ponkratenko, V. I. Tretyak, and Y. G. Zdesenko, "Quest for double beta decay of Gd-160 and Ce isotopes," *Nucl. Phys. A* **694** (2001) 375–391, arXiv:nucl-ex/0011020.

[124] J. Coursey, D. Schwab, J. Tsai, and R. Dragoset, "Atomic weights and isotopic compositions (version 4.1).," 2015. [Online] Available: http://physics.nist.gov/Comp [2024, 20, 05] National Institute of Standards and Technology, Gaithersburg, MD.

[125] **GERDA** Collaboration, K. H. Ackermann *et al.*, "The GERDA experiment for the search of $0\nu\beta\beta$ decay in ^{76}Ge," *Eur. Phys. J. C* **73** no. 3, (2013) 2330, arXiv:1212.4067 [physics.ins-det].

[126] **Majorana** Collaboration, N. Abgrall *et al.*, "The Majorana Demonstrator Neutrinoless Double-Beta Decay Experiment," *Adv. High Energy Phys.* **2014** (2014) 365432, arXiv:1308.1633 [physics.ins-det].

[127] **CUORE** Collaboration, C. Arnaboldi *et al.*, "CUORE: A Cryogenic underground observatory for rare events," *Nucl. Instrum. Meth. A* **518** (2004) 775–798, arXiv:hep-ex/0212053.

[128] **CUPID** Collaboration, O. Azzolini *et al.*, "CUPID-0: the first array of enriched scintillating bolometers for $0\nu\beta\beta$ decay investigations," *Eur. Phys. J. C* **78** no. 5, (2018) 428, arXiv:1802.06562 [physics.ins-det].

[129] **AMoRE** Collaboration, M. H. Lee, "AMoRE: A search for neutrinoless double-beta decay of 100Mo using low-temperature molybdenum-containing crystal detectors," *JINST* **15** no. 08, (2020) C08010, arXiv:2005.05567 [physics.ins-det].

[130] **NEXT** Collaboration, F. Granena *et al.*, "NEXT, a HPGXe TPC for neutrinoless double beta decay searches," arXiv:0907.4054 [hep-ex].

[131] **PandaX-III** Collaboration, K. Han, "PandaX-III: Searching for Neutrinoless Double Beta Decay with High Pressure Gaseous Time Projection Chambers," *J. Phys. Conf. Ser.* **1342** no. 1, (2020) 012095, arXiv:1710.08908 [physics.ins-det].

[132] **EXO-200** Collaboration, M. Auger *et al.*, "Search for Neutrinoless Double-Beta Decay in ^{136}Xe with EXO-200," *Phys. Rev. Lett.* **109** (2012) 032505, arXiv:1205.5608 [hep-ex].

[133] **SNO+** Collaboration, S. Andringa *et al.*, "Current Status and Future Prospects of the SNO+ Experiment," *Adv. High Energy Phys.* **2016** (2016) 6194250, arXiv:1508.05759 [physics.ins-det].

[134] **CANDLES** Collaboration, S. Ajimura *et al.*, "Low background measurement in CANDLES-III for studying the neutrino-less double beta decay of ^{48}Ca," *Phys. Rev. D* **103** no. 9, (2021) 092008, `arXiv:2008.09288 [hep-ex]`.

[135] **NEMO** Collaboration, J. Argyriades *et al.*, "Measurement of the Double Beta Decay Half-life of Nd-150 and Search for Neutrinoless Decay Modes with the NEMO-3 Detector," *Phys. Rev. C* **80** (2009) 032501, `arXiv:0810.0248 [hep-ex]`.

[136] **SuperNEMO** Collaboration, R. Arnold *et al.*, "Probing New Physics Models of Neutrinoless Double Beta Decay with SuperNEMO," *Eur. Phys. J. C* **70** (2010) 927–943, `arXiv:1005.1241 [hep-ex]`.

[137] J. Kotila and F. Iachello, "Phase space factors for $\beta^+\beta^+$ decay and competing modes of double-β decay," *Phys. Rev. C* **87** no. 2, (2013) 024313, `arXiv:1303.4124 [nucl-th]`.

[138] **NuDoubt++** Collaboration, M. Böhles *et al.*, "Combining Hybrid and Opaque Scintillator Techniques in the Search for Double Beta Plus Decays," `arXiv:2407.05999 [hep-ex]`.

[139] W.-C. Huang and J. Lopez-Pavon, "On neutrinoless double beta decay in the minimal left-right symmetric model," *Eur. Phys. J. C* **74** (2014) 2853, `arXiv:1310.0265 [hep-ph]`.

[140] G. Li, M. Ramsey-Musolf, and J. C. Vasquez, "Left-Right Symmetry and Leading Contributions to Neutrinoless Double Beta Decay," *Phys. Rev. Lett.* **126** no. 15, (2021) 151801, `arXiv:2009.01257 [hep-ph]`.

[141] M. Hirsch, H. V. Klapdor-Kleingrothaus, and S. G. Kovalenko, "New constraints on R-parity broken supersymmetry from neutrinoless double beta decay," *Phys. Rev. Lett.* **75** (1995) 17–20.

[142] M. Hirsch, H. V. Klapdor-Kleingrothaus, and S. G. Kovalenko, "Supersymmetry and neutrinoless double beta decay," *Phys. Rev. D* **53** (1996) 1329–1348, `arXiv:hep-ph/9502385`.

[143] M. Hirsch, H. V. Klapdor-Kleingrothaus, and S. G. Kovalenko, "New leptoquark mechanism of neutrinoless double beta decay," *Phys. Rev. D* **54** (1996) R4207–R4210, `arXiv:hep-ph/9603213`.

[144] P. D. Bolton, F. F. Deppisch, and P. S. B. Dev, "Neutrinoless double beta decay via light neutralinos in R-parity violating supersymmetry," *JHEP* **03** (2022) 152, `arXiv:2112.12658 [hep-ph]`.

[145] O. Panella and Y. N. Srivastava, "Bounds on compositeness from neutrinoless double beta decay," *Phys. Rev. D* **52** (1995) 5308–5313, `arXiv:hep-ph/9411224`.

[146] O. Panella, C. Carimalo, Y. N. Srivastava, and A. Widom, "Neutrinoless double beta decay with composite neutrinos," *Phys. Rev. D* **56** (1997) 5766–5775, `arXiv:hep-ph/9701251`.

[147] E. Takasugi, "Double beta decay constraint on composite neutrinos," *Prog. Theor. Phys.* **98** (1997) 977–985, `arXiv:hep-ph/9706240`.

[148] C. P. Burgess and J. M. Cline, "Majorons without Majorana masses and neutrinoless double beta decay," *Phys. Lett. B* **298** (1993) 141–148, `arXiv:hep-ph/9209299`.

[149] C. P. Burgess and J. M. Cline, "A New class of Majoron emitting double beta decays," *Phys. Rev. D* **49** (1994) 5925–5944, `arXiv:hep-ph/9307316`.

[150] R. Cepedello, F. F. Deppisch, L. González, C. Hati, and M. Hirsch, "Neutrinoless Double-β Decay with Nonstandard Majoron Emission," *Phys. Rev. Lett.* **122** no. 18, (2019) 181801, `arXiv:1811.00031 [hep-ph]`.

[151] N. Arkani-Hamed, S. Dimopoulos, G. R. Dvali, and J. March-Russell, "Neutrino masses from large extra dimensions," *Phys. Rev. D* **65** (2001) 024032, `arXiv:hep-ph/9811448`.

[152] G. Bhattacharyya, H. V. Klapdor-Kleingrothaus, H. Pas, and A. Pilaftsis, "Neutrinoless double beta decay from singlet neutrinos in extra dimensions," *Phys. Rev. D* **67** (2003) 113001, `arXiv:hep-ph/0212169`.

[153] V. Pleitez and M. D. Tonasse, "Neutrinoless double beta decay in an SU(3)-L x U(1)-N model," *Phys. Rev. D* **48** (1993) 5274–5279, `arXiv:hep-ph/9302201`.

[154] R. M. Fonseca and M. Hirsch, "Gauge vectors and double beta decay," *Phys. Rev. D* **95** no. 3, (2017) 035033, `arXiv:1612.04272 [hep-ph]`.

[155] S. Weinberg, "Effective Gauge Theories," *Phys. Lett. B* **91** (1980) 51–55.

[156] A. Arbey and F. Mahmoudi, "Dark matter and the early Universe: a review," *Prog. Part. Nucl. Phys.* **119** (2021) 103865, `arXiv:2104.11488 [hep-ph]`.

[157] M. Cirelli, A. Strumia, and J. Zupan, "Dark Matter," `arXiv:2406.01705 [hep-ph]`.

[158] A. Kobach, "Baryon Number, Lepton Number, and Operator Dimension in the Standard Model," *Phys. Lett. B* **758** (2016) 455–457, `arXiv:1604.05726 [hep-ph]`.

[159] S. Weinberg, "Baryon and Lepton Nonconserving Processes," *Phys. Rev. Lett.* **43** (1979) 1566–1570.

[160] D. Zhang, "Renormalization group equations for the SMEFT operators up to dimension seven," *JHEP* **10** (2023) 148, `arXiv:2306.03008 [hep-ph]`.

[161] D. Zhang, "Revisiting renormalization group equations of the SMEFT dimension-seven operators," *JHEP* **02** (2024) 133, arXiv:2310.11055 [hep-ph].

[162] M. Fierz, "Zur Fermischen Theorie des β-Zerfalls," *Z. Phys.* **104** no. 7-8, (1937) 553–565.

[163] J. F. Nieves and P. B. Pal, "Generalized Fierz identities," *Am. J. Phys.* **72** (2004) 1100–1108, arXiv:hep-ph/0306087.

[164] J. S. R. Chisholm, "Change of variables in quantum field theories," *Nucl. Phys.* **26** no. 3, (1961) 469–479.

[165] S. Kamefuchi, L. O'Raifeartaigh, and A. Salam, "Change of variables and equivalence theorems in quantum field theories," *Nucl. Phys.* **28** (1961) 529–549.

[166] H. Pas, M. Hirsch, H. V. Klapdor-Kleingrothaus, and S. G. Kovalenko, "Towards a superformula for neutrinoless double beta decay," *Phys. Lett. B* **453** (1999) 194–198.

[167] S. Weinberg, "Why the renormalization group is a good thing," *Asymptotic realms of physics* (1983) 1–19.

[168] J. C. Criado and M. Pérez-Victoria, "Field redefinitions in effective theories at higher orders," *JHEP* **03** (2019) 038, arXiv:1811.09413 [hep-ph].

[169] S. Weinberg, "Nuclear forces from chiral Lagrangians," *Phys. Lett. B* **251** (1990) 288–292.

[170] V. Bernard, N. Kaiser, and U.-G. Meissner, "Chiral dynamics in nucleons and nuclei," *Int. J. Mod. Phys. E* **4** (1995) 193–346, arXiv:hep-ph/9501384.

[171] S. Scherer, "Introduction to chiral perturbation theory," *Adv. Nucl. Phys.* **27** (2003) 277, arXiv:hep-ph/0210398.

[172] S. Scherer and M. R. Schindler, "A Chiral perturbation theory primer," arXiv:hep-ph/0505265.

[173] E. Epelbaum, H.-W. Hammer, and U.-G. Meissner, "Modern Theory of Nuclear Forces," *Rev. Mod. Phys.* **81** (2009) 1773–1825, arXiv:0811.1338 [nucl-th].

[174] S. Scherer, "Chiral Perturbation Theory: Introduction and Recent Results in the One-Nucleon Sector," *Prog. Part. Nucl. Phys.* **64** (2010) 1–60, arXiv:0908.3425 [hep-ph].

[175] O. Cata and V. Mateu, "Chiral perturbation theory with tensor sources," *JHEP* **09** (2007) 078, arXiv:0705.2948 [hep-ph].

[176] V. Cirigliano, W. Dekens, J. de Vries, M. Hoferichter, and E. Mereghetti, "Toward Complete Leading-Order Predictions for Neutrinoless Double β Decay," *Phys. Rev. Lett.* **126** no. 17, (2021) 172002, `arXiv:2012.11602 [nucl-th]`.

[177] M. Rampp, R. Buras, H. T. Janka, and G. Raffelt, "Core-collapse supernova simulations: variations of the input physics," `arXiv:astro-ph/0203493`.

[178] W. Dekens, J. de Vries, K. Fuyuto, E. Mereghetti, and G. Zhou, "Sterile neutrinos and neutrinoless double beta decay in effective field theory," *JHEP* **06** (2020) 097, `arXiv:2002.07182 [hep-ph]`.

[179] E. E. Jenkins and A. V. Manohar, "Baryon chiral perturbation theory using a heavy fermion Lagrangian," *Phys. Lett. B* **255** (1991) 558–562.

[180] G. Prezeau, M. Ramsey-Musolf, and P. Vogel, "Neutrinoless double beta decay and effective field theory," *Phys. Rev. D* **68** (2003) 034016, `arXiv:hep-ph/0303205`.

[181] V. Cirigliano, W. Dekens, E. Mereghetti, and A. Walker-Loud, "Neutrinoless double-β decay in effective field theory: The light-Majorana neutrino-exchange mechanism," *Phys. Rev. C* **97** no. 6, (2018) 065501, `arXiv:1710.01729 [hep-ph]`. [Erratum: Phys.Rev.C 100, 019903 (2019)].

[182] V. Cirigliano, W. Dekens, J. De Vries, M. L. Graesser, E. Mereghetti, S. Pastore, and U. Van Kolck, "New Leading Contribution to Neutrinoless Double-β Decay," *Phys. Rev. Lett.* **120** no. 20, (2018) 202001, `arXiv:1802.10097 [hep-ph]`.

[183] A. Manohar and H. Georgi, "Chiral Quarks and the Nonrelativistic Quark Model," *Nucl. Phys. B* **234** (1984) 189–212.

[184] E. E. Jenkins, A. V. Manohar, and M. Trott, "Naive Dimensional Analysis Counting of Gauge Theory Amplitudes and Anomalous Dimensions," *Phys. Lett. B* **726** (2013) 697–702, `arXiv:1309.0819 [hep-ph]`.

[185] D. B. Kaplan, M. J. Savage, and M. B. Wise, "Nucleon - nucleon scattering from effective field theory," *Nucl. Phys. B* **478** (1996) 629–659, `arXiv:nucl-th/9605002`.

[186] A. Nogga, R. G. E. Timmermans, and U. van Kolck, "Renormalization of one-pion exchange and power counting," *Phys. Rev. C* **72** (2005) 054006, `arXiv:nucl-th/0506005`.

[187] M. Pavón Valderrama and D. R. Phillips, "Power Counting of Contact-Range Currents in Effective Field Theory," *Phys. Rev. Lett.* **114** no. 8, (2015) 082502, `arXiv:1407.0437 [nucl-th]`.

[188] V. Cirigliano, W. Dekens, J. de Vries, M. Hoferichter, and E. Mereghetti, "Determining the leading-order contact term in neutrinoless double β decay," *JHEP* **05** (2021) 289, arXiv:2102.03371 [nucl-th].

[189] R. Wirth, J. M. Yao, and H. Hergert, "Ab Initio Calculation of the Contact Operator Contribution in the Standard Mechanism for Neutrinoless Double Beta Decay," *Phys. Rev. Lett.* **127** no. 24, (2021) 242502, arXiv:2105.05415 [nucl-th].

[190] **Particle Data Group** Collaboration, C. Patrignani *et al.*, "Review of Particle Physics," *Chin. Phys. C* **40** no. 10, (2016) 100001.

[191] A. Nicholson *et al.*, "Heavy physics contributions to neutrinoless double beta decay from QCD," *Phys. Rev. Lett.* **121** no. 17, (2018) 172501, arXiv:1805.02634 [nucl-th].

[192] T. Bhattacharya, V. Cirigliano, S. Cohen, R. Gupta, H.-W. Lin, and B. Yoon, "Axial, Scalar and Tensor Charges of the Nucleon from 2+1+1-flavor Lattice QCD," *Phys. Rev. D* **94** no. 5, (2016) 054508, arXiv:1606.07049 [hep-lat].

[193] A. Babič, S. Kovalenko, M. I. Krivoruchenko, and F. Šimkovic, "Quark condensate seesaw mechanism for neutrino mass," *Phys. Rev. D* **103** no. 1, (2021) 015007, arXiv:1911.12189 [hep-ph].

[194] J. Hyvärinen and J. Suhonen, "Nuclear matrix elements for $0\nu\beta\beta$ decays with light or heavy Majorana-neutrino exchange," *Phys. Rev. C* **91** no. 2, (2015) 024613.

[195] M. Doi, T. Kotani, and E. Takasugi, "Double beta Decay and Majorana Neutrino," *Prog. Theor. Phys. Suppl.* **83** (1985) 1.

[196] S. M. Bilenky and C. Giunti, "Neutrinoless Double-Beta Decay: a Probe of Physics Beyond the Standard Model," *Int. J. Mod. Phys. A* **30** no. 04n05, (2015) 1530001, arXiv:1411.4791 [hep-ph].

[197] F. F. Deppisch, L. Graf, F. Iachello, and J. Kotila, "Analysis of light neutrino exchange and short-range mechanisms in $0\nu\beta\beta$ decay," *Phys. Rev. D* **102** no. 9, (2020) 095016, arXiv:2009.10119 [hep-ph].

[198] J. Menéndez, "Neutrinoless $\beta\beta$ decay mediated by the exchange of light and heavy neutrinos: The role of nuclear structure correlations," *J. Phys. G* **45** no. 1, (2018) 014003, arXiv:1804.02105 [nucl-th].

[199] J. Engel and J. Menéndez, "Status and Future of Nuclear Matrix Elements for Neutrinoless Double-Beta Decay: A Review," *Rept. Prog. Phys.* **80** no. 4, (2017) 046301, arXiv:1610.06548 [nucl-th].

[200] D. Stefanik, R. Dvornicky, F. Simkovic, and P. Vogel, “Reexamining the light neutrino exchange mechanism of the $0\nu\beta\beta$ decay with left- and right-handed leptonic and hadronic currents,” *Phys. Rev. C* **92** no. 5, (2015) 055502, arXiv:1506.07145 [hep-ph].

[201] M. Mirea, T. Pahomi, and S. Stoica, “Phase Space Factors for Double Beta Decay: an up-date,” arXiv:1411.5506 [nucl-th].

[202] L. Naterop and P. Stoffer, “Low-energy effective field theory below the electroweak scale: one-loop renormalization in the 't Hooft-Veltman scheme,” *JHEP* **02** (2024) 068, arXiv:2310.13051 [hep-ph].

[203] K. S. Babu, C. N. Leung, and J. T. Pantaleone, “Renormalization of the neutrino mass operator,” *Phys. Lett. B* **319** (1993) 191–198, arXiv:hep-ph/9309223.

[204] F. Deppisch and H. Pas, “Pinning down the mechanism of neutrinoless double beta decay with measurements in different nuclei,” *Phys. Rev. Lett.* **98** (2007) 232501, arXiv:hep-ph/0612165.

[205] V. M. Gehman and S. R. Elliott, “Multiple-Isotope Comparison for Determining 0 nu beta beta Mechanisms,” *J. Phys. G* **34** (2007) 667–678, arXiv:hep-ph/0701099. [Erratum: J.Phys.G 35, 029701 (2008)].

[206] Y. K. Wang, P. W. Zhao, and J. Meng, “Nuclear matrix elements of neutrinoless double-β decay in the triaxial projected shell model,” *Phys. Rev. C* **104** no. 1, (2021) 014320, arXiv:2105.02649 [nucl-th].

[207] L. Coraggio, A. Gargano, N. Itaco, R. Mancino, and F. Nowacki, “Calculation of the neutrinoless double-β decay matrix element within the realistic shell model,” *Phys. Rev. C* **101** no. 4, (2020) 044315, arXiv:2001.00890 [nucl-th].

[208] D.-L. Fang, A. Faessler, and F. Simkovic, “$0\nu\beta\beta$ -decay nuclear matrix element for light and heavy neutrino mass mechanisms from deformed quasiparticle random-phase approximation calculations for ^{76}Ge, ^{82}Se, ^{130}Te, ^{136}Xe , and ^{150}Nd with isospin restoration,” *Phys. Rev. C* **97** no. 4, (2018) 045503, arXiv:1803.09195 [nucl-th].

[209] M. T. Mustonen and J. Engel, “Large-scale calculations of the double-β decay of $^{76}Ge,^{130}Te,^{136}Xe$, and ^{150}Nd in the deformed self-consistent Skyrme quasiparticle random-phase approximation,” *Phys. Rev. C* **87** no. 6, (2013) 064302, arXiv:1301.6997 [nucl-th].

[210] J. M. Yao, L. S. Song, K. Hagino, P. Ring, and J. Meng, “Systematic study of nuclear matrix elements in neutrinoless double-β decay with a beyond-mean-field covariant density functional theory,” *Phys. Rev. C* **91** no. 2, (2015) 024316, arXiv:1410.6326 [nucl-th].

[211] L. S. Song, J. M. Yao, P. Ring, and J. Meng, "Nuclear matrix element of neutrinoless double-β decay: Relativity and short-range correlations," *Phys. Rev. C* **95** no. 2, (2017) 024305, arXiv:1702.02448 [nucl-th].

[212] N. López Vaquero, T. R. Rodríguez, and J. L. Egido, "Shape and pairing fluctuations effects on neutrinoless double beta decay nuclear matrix elements," *Phys. Rev. Lett.* **111** no. 14, (2013) 142501, arXiv:1401.0650 [nucl-th].

[213] J. M. Yao, B. Bally, J. Engel, R. Wirth, T. R. Rodríguez, and H. Hergert, "*AbInitio* Treatment of Collective Correlations and the Neutrinoless Double Beta Decay of ^{48}Ca," *Phys. Rev. Lett.* **124** no. 23, (2020) 232501, arXiv:1908.05424 [nucl-th].

[214] A. Belley, C. G. Payne, S. R. Stroberg, T. Miyagi, and J. D. Holt, "*AbInitio* Neutrinoless Double-Beta Decay Matrix Elements for ^{48}Ca , ^{76}Ge , and ^{82}Se," *Phys. Rev. Lett.* **126** no. 4, (2021) 042502, arXiv:2008.06588 [nucl-th].

[215] M. Agostini, F. F. Deppisch, and G. Van Goffrier, "Probing the mechanism of neutrinoless double-beta decay in multiple isotopes," *JHEP* **02** (2023) 172, arXiv:2212.00045 [hep-ph].

[216] M. I. Krivoruchenko, F. Simkovic, D. Frekers, and A. Faessler, "Resonance enhancement of neutrinoless double electron capture," *Nucl. Phys. A* **859** (2011) 140–171, arXiv:1012.1204 [hep-ph].

[217] J. Kotila, J. Barea, and F. Iachello, "Neutrinoless double-electron capture," *Phys. Rev. C* **89** no. 6, (2014) 064319, arXiv:1509.01927 [nucl-th].

[218] F. F. Karpeshin, M. B. Trzhaskovskaya, and L. F. Vitushkin, "Nonresonance Shake Mechanism in Neutrinoless Double Electron Capture," *Phys. Atom. Nucl.* **83** no. 4, (2020) 608–612, arXiv:2008.03906 [nucl-th].

[219] K. Blaum, S. Eliseev, F. A. Danevich, V. I. Tretyak, S. Kovalenko, M. I. Krivoruchenko, Y. N. Novikov, and J. Suhonen, "Neutrinoless Double-Electron Capture," *Rev. Mod. Phys.* **92** (2020) 045007, arXiv:2007.14908 [hep-ph].

[220] M. Duerr, M. Lindner, and K. Zuber, "Consistency Test of Neutrinoless Double Beta Decay with one Isotope," *Phys. Rev. D* **84** (2011) 093004, arXiv:1103.4735 [hep-ph].

[221] C. R. Ding, G. Li, and J. M. Yao, "Nuclear matrix elements of neutrinoless double-beta decay in covariant density functional theory with different mechanisms," arXiv:2403.17722 [nucl-th].

[222] C. R. H. others, "Array programming with NumPy," *Nature* **585** no. 7825, (Sept., 2020) 357–362. https://doi.org/10.1038/s41586-020-2649-2.

[223] T. pandas development team, *pandas-dev/pandas: Pandas 1.1.3*, Oct., 2020. `https://doi.org/10.5281/zenodo.4067057`.

[224] Wes McKinney, "Data Structures for Statistical Computing in Python," in *Proceedings of the 9th Python in Science Conference*, Stéfan van der Walt and Jarrod Millman, eds., pp. 56 – 61. 2010.

[225] J. D. Hunter, "Matplotlib: A 2d graphics environment," *Computing in Science & Engineering* **9** no. 3, (2007) 90–95.

[226] P. Virtanen *et al.*, "SciPy 1.0: Fundamental algorithms for scientific computing in python," *Nature Methods* **17** (2020) 261–272.

[227] F. Johansson *et al.*, *mpmath: a Python library for arbitrary-precision floating-point arithmetic (version 1.1.0)*, December, 2013. http://mpmath.org/.

[228] **KamLAND-Zen** Collaboration, S. Abe *et al.*, "Search for the Majorana Nature of Neutrinos in the Inverted Mass Ordering Region with KamLAND-Zen," *Phys. Rev. Lett.* **130** no. 5, (2023) 051801, `arXiv:2203.02139 [hep-ex]`.

[229] J. Terasaki, "Strength of the isoscalar pairing interaction determined by a relation between double-charge change and double-pair transfer for double- β decay," *Phys. Rev. C* **102** no. 4, (2020) 044303, `arXiv:2003.03542 [nucl-th]`.

[230] F. Šimkovic, V. Rodin, A. Faessler, and P. Vogel, "$0\nu\beta\beta$ and $2\nu\beta\beta$ nuclear matrix elements, quasiparticle random-phase approximation, and isospin symmetry restoration," *Phys. Rev. C* **87** no. 4, (2013) 045501, `arXiv:1302.1509 [nucl-th]`.

[231] T. R. Rodriguez and G. Martinez-Pinedo, "Energy density functional study of nuclear matrix elements for neutrinoless $\beta\beta$ decay," *Phys. Rev. Lett.* **105** (2010) 252503, `arXiv:1008.5260 [nucl-th]`.

[232] J. Barea, J. Kotila, and F. Iachello, "$0\nu\beta\beta$ and $2\nu\beta\beta$ nuclear matrix elements in the interacting boson model with isospin restoration," *Phys. Rev. C* **91** no. 3, (2015) 034304, `arXiv:1506.08530 [nucl-th]`.

[233] A. Neacsu and M. Horoi, "Shell model studies of the ^{130}Te neutrinoless double-beta decay," *Phys. Rev. C* **91** (2015) 024309, `arXiv:1411.4313 [nucl-th]`.

[234] J. Menendez, A. Poves, E. Caurier, and F. Nowacki, "Disassembling the Nuclear Matrix Elements of the Neutrinoless beta beta Decay," *Nucl. Phys. A* **818** (2009) 139–151, `arXiv:0801.3760 [nucl-th]`.

[235] **Particle Data Group** Collaboration, R. L. Workman *et al.*, "Review of Particle Physics," *PTEP* **2022** (2022) 083C01.

[236] **Planck** Collaboration, N. Aghanim *et al.*, "Planck 2018 results. VI. Cosmological parameters," *Astron. Astrophys.* **641** (2020) A6, arXiv:1807.06209 [astro-ph.CO]. [Erratum: Astron.Astrophys. 652, C4 (2021)].

[237] S. S. Chatterjee, S. Lavignac, O. G. Miranda, and G. Sanchez Garcia, "Exploring the sensitivity to non-standard and generalized neutrino interactions through coherent elastic neutrino-nucleus scattering with a NaI detector," arXiv:2402.16953 [hep-ph].

[238] **AMoRE** Collaboration, Y. Oh, "AMoRE-II preparation status," *PoS* **TAUP2023** (2024) 214.

[239] M. Duerr, M. Lindner, and A. Merle, "On the Quantitative Impact of the Schechter-Valle Theorem," *JHEP* **06** (2011) 091, arXiv:1105.0901 [hep-ph].

[240] C. D. Carone, "Double beta decay with vector majorons," *Phys. Lett. B* **308** (1993) 85–88, arXiv:hep-ph/9302290.

[241] E. Vitagliano, I. Tamborra, and G. Raffelt, "Grand Unified Neutrino Spectrum at Earth: Sources and Spectral Components," *Rev. Mod. Phys.* **92** (2020) 45006, arXiv:1910.11878 [astro-ph.HE].

[242] D. Scott, "The Cosmic Neutrino Background," in *International School of Physics "Enrico Fermi" in collaboration with the summer schools ISAPP: Neutrino Physics, Astrophysics and Cosmology*. 2, 2024. arXiv:2402.16243 [astro-ph.CO].

[243] R. Hodak, S. Kovalenko, and F. Simkovic, "Capturing relic neutrinos with beta-and double beta-decaying nuclei," *AIP Conf. Proc.* **1180** no. 1, (2009) 50–54.

[244] R. Hodak, F. Simkovic, S. Kovalenko, and A. Faessler, "Towards the detection of light and heavy relic neutrinos," *Prog. Part. Nucl. Phys.* **66** (2011) 452–456.

[245] **PTOLEMY** Collaboration, E. Baracchini *et al.*, "PTOLEMY: A Proposal for Thermal Relic Detection of Massive Neutrinos and Directional Detection of MeV Dark Matter," arXiv:1808.01892 [physics.ins-det].

[246] **PTOLEMY** Collaboration, M. G. Betti *et al.*, "Neutrino physics with the PTOLEMY project: active neutrino properties and the light sterile case," *JCAP* **07** (2019) 047, arXiv:1902.05508 [astro-ph.CO].

[247] S. Tremaine and J. E. Gunn, "Dynamical Role of Light Neutral Leptons in Cosmology," *Phys. Rev. Lett.* **42** (1979) 407–410.

[248] H. Davoudiasl, P. B. Denton, and D. A. McGady, "Ultralight fermionic dark matter," *Phys. Rev. D* **103** no. 5, (2021) 055014, arXiv:2008.06505 [hep-ph].

[249] R. Kallosh, A. D. Linde, D. A. Linde, and L. Susskind, "Gravity and global symmetries," *Phys. Rev. D* **52** (1995) 912–935, arXiv:hep-th/9502069.

[250] J. Heeck, "Unbroken B – L symmetry," *Phys. Lett. B* **739** (2014) 256–262, arXiv:1408.6845 [hep-ph].

[251] S.-J. Sin, "Late time cosmological phase transition and galactic halo as Bose liquid," *Phys. Rev. D* **50** (1994) 3650–3654, arXiv:hep-ph/9205208.

[252] S. U. Ji and S. J. Sin, "Late time phase transition and the galactic halo as a bose liquid: 2. The Effect of visible matter," *Phys. Rev. D* **50** (1994) 3655–3659, arXiv:hep-ph/9409267.

[253] W. Hu, R. Barkana, and A. Gruzinov, "Cold and fuzzy dark matter," *Phys. Rev. Lett.* **85** (2000) 1158–1161, arXiv:astro-ph/0003365.

[254] E. G. M. Ferreira, "Ultra-light dark matter," *Astron. Astrophys. Rev.* **29** no. 1, (2021) 7, arXiv:2005.03254 [astro-ph.CO].

[255] G.-y. Huang and N. Nath, "Neutrino meets ultralight dark matter: $0\nu\beta\beta$ decay and cosmology," *JCAP* **05** no. 05, (2022) 034, arXiv:2111.08732 [hep-ph].

[256] F. Nozzoli and C. Cernetti, "Dark Matter stimulated neutrinoless double beta decay," arXiv:2212.07832 [hep-ph].

[257] J. Herms, S. Jana, V. P. K., and S. Saad, "Light neutrinophilic dark matter from a scotogenic model," *Phys. Lett. B* **845** (2023) 138167, arXiv:2307.15760 [hep-ph].

[258] M. Hirsch, H. V. Klapdor-Kleingrothaus, S. G. Kovalenko, and H. Pas, "On the observability of majoron emitting double beta decays," *Phys. Lett. B* **372** (1996) 8–14, arXiv:hep-ph/9511227.

[259] J. Kotila and F. Iachello, "Nuclear matrix elements for Majoron-emitting double-β decay," *Phys. Rev. C* **103** no. 4, (2021) 044302, arXiv:2104.02327 [nucl-th].

[260] J. Kotila, J. Barea, and F. Iachello, "Phase-space factors and half-life predictions for Majoron-emitting $\beta^-\beta^-$ decay," *Phys. Rev. C* **91** no. 6, (2015) 064310, arXiv:1509.05154 [nucl-th]. [Erratum: Phys.Rev.C 92, 029903 (2015)].

[261] **XENON** Collaboration, E. Aprile *et al.*, "Dark Matter Search Results from a One Ton-Year Exposure of XENON1T," *Phys. Rev. Lett.* **121** no. 11, (2018) 111302, arXiv:1805.12562 [astro-ph.CO].

[262] M. Laine and A. Vuorinen, *Basics of Thermal Field Theory*, vol. 925. Springer, 2016. arXiv:1701.01554 [hep-ph].

[263] J. I. Kapusta and C. Gale, *Finite-temperature field theory: Principles and applications*. Cambridge Monographs on Mathematical Physics. Cambridge University Press, 2011.

[264] T. Weigand, "Quantum Field Theory 1," 2012. `https://www.thphys.uni-heidelberg.de/courses/weigand/QFT1-12-13.pdf`.

[265] M. E. Peskin and D. V. Schroeder, *An Introduction to quantum field theory*. Addison-Wesley, Reading, USA, 1995.

[266] J. I. Kapusta, "Bose-Einstein Condensation, Spontaneous Symmetry Breaking, and Gauge Theories," *Phys. Rev. D* **24** (1981) 426–439.

[267] H. E. Haber and H. A. Weldon, "Finite Temperature Symmetry Breaking as Bose-Einstein Condensation," *Phys. Rev. D* **25** (1982) 502.

[268] K. M. Benson, J. Bernstein, and S. Dodelson, "Phase structure and the effective potential at fixed charge," *Phys. Rev. D* **44** (1991) 2480–2497.

[269] H. E. Haber and H. A. Weldon, "Thermodynamics of an Ultrarelativistic Bose Gas," *Phys. Rev. Lett.* **46** (1981) 1497.

[270] M. H. Mittleman, *Introduction to the theory of laser-atom interactions*. Springer Science & Business Media, 2013.

[271] G.-y. Huang, M. Lindner, P. Martínez-Miravé, and M. Sen, "Cosmology-friendly time-varying neutrino masses via the sterile neutrino portal," *Phys. Rev. D* **106** no. 3, (2022) 033004, `arXiv:2205.08431 [hep-ph]`.

[272] A. Berlin, "Neutrino Oscillations as a Probe of Light Scalar Dark Matter," *Phys. Rev. Lett.* **117** no. 23, (2016) 231801, `arXiv:1608.01307 [hep-ph]`.

[273] G. Krnjaic, P. A. N. Machado, and L. Necib, "Distorted neutrino oscillations from time varying cosmic fields," *Phys. Rev. D* **97** no. 7, (2018) 075017, `arXiv:1705.06740 [hep-ph]`.

[274] A. Dev, P. A. N. Machado, and P. Martínez-Miravé, "Signatures of ultralight dark matter in neutrino oscillation experiments," *JHEP* **01** (2021) 094, `arXiv:2007.03590 [hep-ph]`.

[275] A. Faessler, M. González, S. Kovalenko, and F. Šimkovic, "Arbitrary mass Majorana neutrinos in neutrinoless double beta decay," *Phys. Rev. D* **90** no. 9, (2014) 096010, `arXiv:1408.6077 [hep-ph]`.

[276] P. D. Bolton, F. F. Deppisch, and P. S. Bhupal Dev, "Neutrinoless double beta decay versus other probes of heavy sterile neutrinos," *JHEP* **03** (2020) 170, `arXiv:1912.03058 [hep-ph]`.

[277] W. Dekens, J. de Vries, E. Mereghetti, J. Menéndez, P. Soriano, and G. Zhou, "Neutrinoless double-β decay in the neutrino-extended standard model," *Phys. Rev. C* **108** no. 4, (2023) 045501, arXiv:2303.04168 [hep-ph].

[278] J. M. Berryman *et al.*, "Neutrino self-interactions: A white paper," *Phys. Dark Univ.* **42** (2023) 101267, arXiv:2203.01955 [hep-ph].

[279] P.-W. Chang, I. Esteban, J. F. Beacom, T. A. Thompson, and C. M. Hirata, "Toward Powerful Probes of Neutrino Self-Interactions in Supernovae," *Phys. Rev. Lett.* **131** no. 7, (2023) 071002, arXiv:2206.12426 [hep-ph].

[280] E. Di Valentino, O. Mena, S. Pan, L. Visinelli, W. Yang, A. Melchiorri, D. F. Mota, A. G. Riess, and J. Silk, "In the realm of the Hubble tension—a review of solutions," *Class. Quant. Grav.* **38** no. 15, (2021) 153001, arXiv:2103.01183 [astro-ph.CO].

[281] C. D. Kreisch, F.-Y. Cyr-Racine, and O. Doré, "Neutrino puzzle: Anomalies, interactions, and cosmological tensions," *Phys. Rev. D* **101** no. 12, (2020) 123505, arXiv:1902.00534 [astro-ph.CO].

[282] M. Berbig, S. Jana, and A. Trautner, "The Hubble tension and a renormalizable model of gauged neutrino self-interactions," *Phys. Rev. D* **102** no. 11, (2020) 115008, arXiv:2004.13039 [hep-ph].

[283] S. Brieden, H. Gil-Marín, and L. Verde, "Model-agnostic interpretation of 10 billion years of cosmic evolution traced by BOSS and eBOSS data," *JCAP* **08** no. 08, (2022) 024, arXiv:2204.11868 [astro-ph.CO].

[284] C. G. Boehmer and T. Harko, "Can dark matter be a Bose-Einstein condensate?," *JCAP* **06** (2007) 025, arXiv:0705.4158 [astro-ph].

[285] S. Das and R. K. Bhaduri, "Dark matter and dark energy from a Bose–Einstein condensate," *Class. Quant. Grav.* **32** no. 10, (2015) 105003, arXiv:1411.0753 [gr-qc].

[286] A. Sharma, J. Khoury, and T. Lubensky, "The Equation of State of Dark Matter Superfluids," *JCAP* **05** (2019) 054, arXiv:1809.08286 [hep-th].

[287] E. Castellanos, C. Escamilla-Rivera, and J. Mastache, "Is a Bose–Einstein condensate a good candidate for dark matter? A test with galaxy rotation curves," *Int. J. Mod. Phys. D* **29** no. 09, (2020) 2050063, arXiv:1910.03791 [gr-qc].

[288] D. Antypas *et al.*, "New Horizons: Scalar and Vector Ultralight Dark Matter," arXiv:2203.14915 [hep-ex].

[289] P. Sikivie and Q. Yang, "Bose-Einstein Condensation of Dark Matter Axions," *Phys. Rev. Lett.* **103** (2009) 111301, arXiv:0901.1106 [hep-ph].

[290] O. Erken, P. Sikivie, H. Tam, and Q. Yang, "Cosmic axion thermalization," *Phys. Rev. D* **85** (2012) 063520, `arXiv:1111.1157 [astro-ph.CO]`.

[291] A. H. Guth, M. P. Hertzberg, and C. Prescod-Weinstein, "Do Dark Matter Axions Form a Condensate with Long-Range Correlation?," *Phys. Rev. D* **92** no. 10, (2015) 103513, `arXiv:1412.5930 [astro-ph.CO]`.

[292] S. Davidson and M. Elmer, "Bose Einstein condensation of the classical axion field in cosmology?," *JCAP* **12** (2013) 034, `arXiv:1307.8024 [hep-ph]`.

[293] M.-H. Lee, H.-C. Kim, and J. K. Kim, "Bose-Einstein condensation for a selfinteracting theory in curved space-time," `arXiv:hep-th/9310036`.

[294] D. J. Toms, "Bose-Einstein condensation as symmetry breaking in curved space-time and in space-times with boundaries," *Phys. Rev. D* **47** (1993) 2483–2496.

[295] K. Kirsten and D. J. Toms, "Bose-Einstein condensation for interacting scalar fields in curved space-time," *Phys. Rev. D* **51** (1995) 6886–6900, `arXiv:hep-th/9501093`.

[296] D. J. Toms, "The Effective action at finite temperature and density with application to Bose-Einstein condensation," 12, 1996. `arXiv:cond-mat/9612003`.

[297] J. D. Smith and D. J. Toms, "Bose-Einstein condensation as symmetry breaking in compact curved space-times," *Phys. Rev. D* **53** (1996) 5771–5780, `arXiv:hep-th/9602046`.

[298] E. Castellanos, C. Escamilla-Rivera, A. Macías, and D. Núñez, "Scalar Field as a Bose-Einstein Condensate?," *JCAP* **11** (2014) 034, `arXiv:1310.3319 [gr-qc]`.

[299] E. Castellanos, C. Escamilla-Rivera, C. Lämmerzahl, and A. Macías, "Scalar field as a Bose–Einstein condensate in a Schwarzschild–de Sitter spacetime," *Int. J. Mod. Phys. D* **26** no. 04, (2016) 1750032, `arXiv:1512.03118 [gr-qc]`.

[300] E. Castellanos, J. C. Degollado, C. Lämmerzahl, A. Macías, and V. Perlick, "Bose-Einstein Condensates in Charged Black-Hole Spacetimes," *JCAP* **01** (2018) 043, `arXiv:1708.09057 [gr-qc]`.

[301] J. Berges and D. Sexty, "Bose condensation far from equilibrium," *Phys. Rev. Lett.* **108** (2012) 161601, `arXiv:1201.0687 [hep-ph]`.

[302] J. Berges and J. Jaeckel, "Far from equilibrium dynamics of Bose-Einstein condensation for Axion Dark Matter," *Phys. Rev. D* **91** no. 2, (2015) 025020, `arXiv:1402.4776 [hep-ph]`.

Acknowledgements

This work would not have been possible without the invaluable support of many individuals to whom I owe my deepest gratitude.

First of all, I want to thank my PhD supervisor Prof. Dr. Dr. h.c. Manfred Lindner, who led me starting from my bachelor's thesis, through my master's degree, and my PhD phase until today. You provided valuable advice when necessary and gave me the freedom and trust to follow my own interests. It was an honour to be part of your research group.

Furthermore, I would like to thank my co-supervisor Dr. Lukáš Gráf for his support, patience, and the many fruitful discussions in and beyond physics. Working and sharing an office with you was always a pleasure.

Additional thanks go to my collaborators of past and ongoing projects, Dr. Jordy de Vries, Ana Martín Galán, Dr. Lukáš Gráf, Dr. Rasmus S.L. Hansen, Dr. Chandan Hati, Dr. Sudip Jana, Dr. Manibrata Sen, and Nele Volmer.

To both Prof. Dr. Dr. h.c. Manfred Lindner and Prof. Dr. Tilman Plehn I want to express my gratitude for sacrificing their summer break time to read and review my dissertation. Additionally, I want to thank the other members of the examination committee Prof. Dr. Loredana Gastaldo and Prof. Dr. Björn Malte Schäfer for their time.

A special thanks is directed to Anja Berneiser and Britta Schwarz for their immense help regarding bureaucratic issues which are probably my greatest weakness.

For proofreading this dissertation I want to thank Lukáš Gráf and Nele Volmer for spending their valuable time.

During my time at the MPIK, I was lucky to get to know and spend time with many interesting, friendly, and overall great people. I enjoyed many interesting discussions about physics, politics, and life while sharing an office with Christina Benso, Ingolf Bischer, Christian Döring, Thomas Hugle, Carlos Jaramillo, Moritz Platscher, and Thomas Rink during my bachelor's and master's time. The same is true for my office mates Frederik Depta and Tim Herbermann later during my PhD. Though oftentimes skipped in favour of work, I will always remember the interesting and fun discussions at the coffee table and in the MPIK hallways, in the context of which I want to mention Andreas Trautner, Philipp Saake, Thede de Boer, and Nele Volmer as well. I am doomed to miss some people here and I am truly sorry for that. I genuinely enjoyed my time with all of you at MPIK!

As without my studies at Heidelberg University I could not have pursued my PhD, I want to thank my fellow students Alex Matskevych, Kian Tadjalli Mehr, Paul Oppelt, Jakob Stegmann, Fritz Schelten, and Martin Weinreich.

A special shout-out goes to Sam for keeping me sane during the period of writing this dissertation by forcing me to get out of my cave and go outside every day.

Last but not least, I want to express my deep gratitude towards my family, my mother Birgit Scholer, my father Hermann Scholer, and my sister Viktoria Demmer, for their support throughout all of these years. Additionally, I want to thank Sybille and Thomas Michelsen for their support. Finishing a dissertation with a newborn baby has its own challenges and I want to sincerely thank Sybille Michelsen for your support during this time. Finally, I cannot express how grateful I am to Ina Michelsen for your loving support, your patience with me, and everything you are. You are the love of my life and without you this would not have been possible.